Cavitation Control for Enhanced Comminution of Renal Calculi

by

Alexander P. Duryea

A dissertation submitted in partial fulfillment
of the requirements for the degree of
Doctor of Philosophy
(Biomedical Engineering)
in the University of Michigan
2015

Doctoral Committee:

Professor Charles A. Cain, Co-Chair
Assistant Research Scientist Timothy L. Hall, Co-Chair
Associate Professor William W. Roberts
Assistant Professor Zhen Xu

Table of Contents

List of Figures

Abstract

Shock wave lithotripsy (SWL) revolutionized the treatment of kidney stones when first introduced three decades ago. Instead of open stone surgery, ultrasonic shock waves could be applied from outside the body to fragment stones *in-situ*, offering a non-invasive approach to stone therapy. Although still widely utilized for the treatment of stones, SWL has yet to realize its full potential. Incomplete stone fragmentation and damage to surrounding tissues are common problems plaguing SWL procedures, and despite the fact that much progress has been made in understanding the mechanisms underlying these phenomena, implementation of this knowledge to improve clinical outcomes has been minimal.

One of the fundamental components underlying stone fragmentation in SWL is the energetic formation and collapse of microscopic bubbles. This behavior—known as cavitation—can be incited by extremely intense ultrasound pulses such as the shock waves administered in lithotripsy procedures. The role of cavitation in SWL is twofold: violent collapse of bubbles generated at the stone surface confers large stresses to the structure of the stone, and is a crucial component of fragmentation; contrastingly, bubbles generated away from the stone along the acoustic propagation path can block energy from reaching the stone and compromise comminution efficacy.

The work in this dissertation seeks to augment conventional SWL procedures through strategic control of the cavitation environment surrounding a kidney stone. This is achieved by way of two ultrasonic pulsing strategies designed to either enhance or suppress cavitation activity:

1) Histotripsy sequences, developed previously as a non-invasive therapeutic ultrasound technology for the mechanical fractionation of tissue structures, utilize very intense bursts of ultrasound to initiate and control a cavitational bubble cloud. 2) Bubble removal sequences, developed herein to mitigate unwanted cavitation activity, utilize low amplitude ultrasound bursts to stimulate the consolidation and *de facto* removal of cavitation bubble nuclei. Through appropriate application of these modalities for cavitation control, it is possible to enhance the comminution process for faster, more complete stone treatments. Ultimately, it is our hope that the concepts developed in this dissertation will provide the foundation for an enhanced first-line treatment for the non-invasive removal of kidney stones.

Chapter 1

Introduction

The main objective of this dissertation is to explore the strategic manipulation of the cavitation environment surrounding a kidney stone for improved comminution. More specifically, this work investigates how cavitation-enhancing histotripsy pulses and cavitation-suppressing bubble removal pulses can provide an adjunct to traditional shock wave lithotripsy protocols. We begin with an examination of the basic characteristics associated with histotripsy stone comminution, followed by an exploration of how these qualities can complement those associated with shock wave lithotripsy procedures. Next, we develop an ultrasonic pulsing strategy for the removal of unwanted cavitation bubbles (i.e. residual nuclei) that have been implicated in limiting the efficacy of stone comminution. Finally, these bubble removal pulses are incorporated in both shock wave lithotripsy and histotripsy treatments in an effort to enhance their therapeutic outcomes.

This chapter will give a brief introduction to the major therapeutic modalities explored in this dissertation, namely shock wave lithotripsy and histotripsy. A discussion of the effects of residual cavitation bubbles in these respective therapies is also presented, as it is a crucial theme that emerges over the duration of this work. Lastly, this chapter concludes with an outline of this dissertation, providing an overview of each individual chapter.

1.1 Shock Wave Lithotripsy

Extracorporeal shock wave lithotripsy (SWL) revolutionized the treatment of urinary stones when first introduced three decades ago. Instead of open stone surgery, acoustic energy could be applied from outside the body to fragment stones *in-situ*. Although widely utilized for treatment of stones, SWL has not realized its full potential. Incomplete fragmentation of stones is a common problem resulting in significant pain (when stone fragments migrate down the ureter and impede urine outflow) and a high rate of residual fragments that may need additional therapy to prevent them from acting as a nidus for additional stone formation. In studies using the Dornier HM-3 lithotripter with a low rate (< 10%) of retreatment, reported stone free rates at 3 months are about 70-80% [1-3]. Similar rates have been reported for other lithotripters but often include much higher retreatment rates (up to 50%) [4-6]. Comparing more fairly with ureteroscopy, the actual long term stone free rate for a single typical SWL session could be as low as 50%. Additionally, many patients considered successfully treated still experience pain as fragments migrate down the ureter. The research in this dissertation aims to address the barriers preventing SWL from realizing its full potential to provide patients with high stone free rates following a single treatment session and minimal pain from clearance of fragmented stone material.

Stone fragmentation in SWL is a dynamic process in which cracks initiate, grow, and coalesce within the stone matrix. It is well established that mechanical stresses induced directly by a lithotripter shock wave play a critical role in this subdivision [7-16]. Mechanisms proposed to explain the contribution of these direct stresses include the superposition of longitudinal waves within the stone (spalling) [7-9, 11, 14], circumferential stresses generated by the portion of the shock wave traveling in fluid adjacent to the stone boundary (squeezing) [12], and shear waves generated at stone corners that are reinforced by the squeezing wave (dynamic squeezing) [15].

These direct stress mechanisms do not act in isolation, however, and there is a great deal of evidence suggesting that cavitation produced by the trailing tensile tail of the shock wave is a crucial component of the stone comminution process [13-27]. Studies in which the cavitational component of shock waves was suppressed through shock wave modification [17], viscous fluids [13, 14, 18], or static overpressure [19, 20] have yielded a drastic reduction in stone fragmentation. Conversely, Xi and Zhong demonstrated that an auxiliary shock wave timed such as to intensify the collapse of shock wave induced bubbles can markedly enhance comminution [21]. The damage conferred by cavitation activity is typified by numerous minute pittings on the stone surface, which are likely the result of localized stress created by the impact of fluid jets or secondary shock waves produced by bubble collapse [21-23, 25, 27]. Additionally, the work of Sass, *et al.* suggests that cavitation may act to facilitate the growth of fissures in the stone material induced by the direct stress wave component of shock waves [16].

While the past 30 years of lithotripsy research have produced a basic understanding of the mechanisms involved in stone comminution, little improvement has been achieved in clinical devices [28, 29]. In fact, lithotripters subsequent to the HM-3 are widely regarded as having lower performance [30-32]. The protocols for modern lithotripters and the acoustic fields they produce remain largely unchanged from the HM-3, except for the focal zone dimensions. Modifications have been made primarily to improve patient tolerance and provider convenience. In order to drive the development and adoption of a new clinical device, any new technique must be significantly more effective or produce a dramatic reduction in procedure length. We believe that both these objectives can be accomplished with the methods explored in this dissertation.

1.2 Histotripsy

Histotripsy is a platform therapeutic ultrasound technology for the non-invasive treatment of tissue structures. Through the use of very short (< 20 cycles), high peak negative pressure (> 10 MPa), low duty cycle (< 1%) pulses, histotripsy directs the control of a cavitational bubble cloud for the mechanical destruction of a targeted tissue. Histotripsy uses much higher pulse repetition rates in comparison to SWL (often ≥ 100 Hz, compared to 1 – 2 Hz in SWL). As such, a far greater number of individual cavitation events are generated in a given amount of time. Over the course of many pulses, targeted tissue is progressively mechanically fractionated resulting in complete cellular destruction. To generate high amplitudes, the sound fields must be tightly focused. This, combined with the fact that the initiation of cavitation is a threshold phenomenon, leads to precise lesions with sharp margins.

Numerous studies have demonstrated the feasibility of mechanical tissue fractionation via cavitation control with histotripsy [33-43]. When applied at a fluid-tissue interface, histotripsy can produce controlled tissue erosion, which has been utilized to remove cardiac tissue and create intracardiac flow channels for congenital heart disease [34, 37, 38]. When applied within bulk tissue, histotripsy can generate well demarcated volumes of homogenized structure. This has been employed for prostate ablation as a treatment for benign prostatic hyperplasia (BPH) [33, 39-42], as well as hepatic tissue ablation for treatment of liver tumors [43].

The ability of histotripsy to generate and modulate purely cavitational activity offers an important tool to further study the role of cavitation in the kidney stone comminution process, and stands to provide a potential adjunct to conventional SWL procedures. While the cavitation produced by standard lithotripters has been documented as a crucial component of stone subdivision and subsequent fragment reduction, its role in the process is not completely understood. This is in large part due to the inability to isolate the cavitational component of shock waves from the direct mechanical stresses induced by the positive phase of the waveform. Furthermore, lithotripters produce steady, unvarying outputs that would only be optimal if SWL were a constant process. As previous work has demonstrated that SWL stone comminution progresses through multiple phases in which the dependence on cavitation varies [13], the ability to controllably enhance cavitation at strategic points in the stone treatment could markedly augment the therapeutic outcome. Clearly, histotripsy affords us with a novel tool to study kidney stone comminution in ways not previously possible. It is our hope that these efforts will result in a therapy for the non-invasive treatment of kidney stones that alleviates the limitations associated with current SWL procedures.

1.3 Implications of Remnant Bubble Nuclei in Therapeutic Ultrasound

While cavitation is a crucial component of the stone comminution process, when not appropriately controlled it can compromise the therapeutic outcome. Specifically, remnant cavitation nuclei that persist following primary cavitation collapse can limit the efficacy of both SWL and histotripsy therapies, and as such are an important consideration in this work on strategic cavitation control for enhanced stone comminution. A major portion of this dissertation will be devoted to developing a novel ultrasound pulsing strategy to mitigate the effects of these remnant bubbles. The present section offers a preliminary introduction to this important topic.

The collapse of primary cavitation bubbles generated by a high intensity acoustic pulse can produce an extensive population of residual bubble nuclei [44-52]. A single primary bubble can give rise to dozens of residual daughters, as its collapse is typically accompanied by fission into numerous remnant fragments [44, 49, 50, 51]. The resulting daughter bubbles are microscopic in size (<10 µm) [53, 54] and can persist for tens of milliseconds [49, 55] or even full seconds [46, 50, 51, 56], depending on the conditions under which they were generated. If additional acoustic pulses are applied prior to the dissolution of these residual bubbles, they can serve as nuclei to seed subsequent cavitation activity [44-46, 48, 49]. As such, residual bubble nuclei impart a cavitation memory to their host medium, influencing the threshold, extent, and distribution of ensuing cavitation events [52, 57-61].

Residual bubble nuclei that persist from one pulse to the next can limit the efficiency of cavitation-based ultrasound therapies. In SWL the efficacy of stone comminution is highly dependent on the rate of shock wave delivery, with testing both *in-vitro* [59, 62-65] and *in-vivo* [66] demonstrating a decrease in per-shock fragmentation efficiency with increasing shock rate. This is a result of extensive cavitation generated along the shock wave propagation path, the collapse of which produces a large population of residual nuclei [50, 51]. When a shock wave propagates through a medium containing these residual bubbles, the tensile component of the waveform causes them to expand—a process that selectively attenuates the shock wave's negative tail and reduces the energy that ultimately reaches the stone [53, 59, 61, 67]. At high shock rates residual nuclei have less time to passively dissolve between successive shocks, leading to more severe attenuation of the negative phase and compromised comminution efficacy. Similar bubble shielding effects are expected to be present in histotripsy stone treatments, as will be investigated in this dissertation work.

Rate-dependent efficiency has also been observed in histotripsy fractionation of soft tissue [52]. In this case it is cavitation memory—i.e., the repetitive initiation of cavitation at a discrete set of sites within the focal zone—that is the primary source of less efficient lesion formation at high pulse repetition frequencies [52]. Residual nuclei that persist between histotripsy pulses can seed this cavitation memory effect, resulting in inhomogeneous tissue fractionation and requiring an excess number of pulses to achieve complete homogenization of the targeted volume. It has been demonstrated that by increasing the time between successive histotripsy pulses such that remnant nuclei can more completely dissolve, cavitation bubbles are generated at a more randomized set of sites within the focal zone and complete homogenization is achieved using fewer pulses [52].

1.4 Outline

This dissertation is organized into nine chapters documenting our exploration of strategic cavitation control for enhanced kidney stone comminution. A brief summary of each chapter follows.

The present chapter introduces the objective of this dissertation and motivates the work in the context of one of the current first-line non-invasive therapies for kidney stones: shock wave lithotripsy. Histotripsy, which is a platform therapeutic ultrasound technology enabling much of the work included in this dissertation, is also introduced.

Chapter 2 examines the feasibility of kidney stone treatment using histotripsy through the use of model stones sonicated *in-vitro*. The characteristics of histotripsy stone erosion are evaluated and compared to those observed previously in SWL. Additionally, the mechanism of histotripsy stone erosion is evaluated by monitoring cavitation activity—both optically and acoustically—and correlating to the observed therapeutic effect.

Chapter 3 demonstrates how the characteristics of histotripsy stone comminution observed in Chapter 2 can provide an adjunct to traditional SWL procedures. Model stones are treated *in-vitro* using a research system that permits the application of histotripsy and SWL therapies in a confocal manner. The effect of histotripsy-controlled cavitation on SWL treatment is evaluated at strategic time points in the stone comminution process. In addition to demonstrating the highly complementary nature of histotripsy and SWL, this study offers further insight into the role of cavitation in SWL procedures.

Chapter 4 investigates a novel strategy for the active removal of unwanted cavitation activity (residual bubble nuclei produced by primary cavitation collapse) that can limit the efficacy of both SWL and histotripsy therapies. A unique pulse sequence is developed utilizing low amplitude ultrasound bursts to eliminate remnant bubbles from the field. These sequences—which we term bubble removal pulses—are shown to promote the aggregation and subsequent coalescence of cavitation nuclei.

Chapter 5 extends the preliminary feasibility study presented in Chapter 4, investigating the effect of pulse frequency on the bubble removal process. Bubble removal pulses ranging from 0.5 – 2 MHz are explored, and the results are examined in the context of Bjerknes theory to develop a working hypothesis for the physical mechanism underlying nuclei consolidation.

Chapter 6 incorporates the bubble removal strategy developed in the preceding chapters in SWL treatment of model kidney stones *in-vitro*. This study serves to corroborate previous work regarding the ill-effects of residual cavitation nuclei in SWL—specifically, their manifestation in a rate-dependent comminution efficacy. It is demonstrated that high per-shock efficiency can be maintained at high shock rates when remnant bubbles are actively removed between successive shock waves.

Chapter 7 examines the effects of bubble removal sequences in histotripsy stone erosion, again through the *in-vitro* treatment of model stones. Analogous to the study with SWL presented in Chapter 6, actively removing remnant cavitation nuclei between successive histotripsy pulses is shown to augment the per-pulse comminution efficiency when high pulse rates are used. Optical monitoring of the cavitation activity produced under the various exposure conditions in this study also provides an assessment of the cavitation characteristics that are paramount to efficacious stone erosion with histotripsy.

Chapter 8 offers a preliminary investigation of the application of bubble removal sequences to soft tissue, examining their effect on histotripsy treatment of a red blood cell tissue-mimicking phantom. Here, the active removal of remnant bubble nuclei alleviates the cavitation memory effect that has previously been documented to limit the efficiency of histotripsy lesion development in soft tissue when high pulse rates are utilized. In a broader context, the results of this work serve as a foundation for the use of bubble removal sequences to provide active protection of tissues in SWL and histotripsy stone treatments.

Lastly, Chapter 9 provides a summary of the findings and contributions of this dissertation, and discusses future work that will be required to enable these strategies for cavitation control to augment SWL stone comminution in a clinical setting.

1.5 References

[1] Cass AS. Comparison of first generation (Dornier HM3) and second generation (Medstone STS) lithotriptors: treatment results with 13,864 renal and ureteral calculi. *J Urol*. Vol. 153 (3 Pt 1), pp. 588-92. Mar 1995.

[2] Lingeman JE, Smith LH and Wood JR. Bioeffects and long term effects of ESWL. In: Urinary Calculi: ESWL, Endourology and Medical Therapy. Philadelphia: Lea & Febiger, 285, 1989.

[3] Politis G and Griffith DP. ESWL: Stone free efficacy based upon the stone size and location. *World J Urol*, vol. 5, pp. 255-258, 1987.

[4] Mobley TB, Myers DA, Grine WB, Jenkins JM and Jordan WR. Low energy lithotripsy with the Lithostar: treatment results with 19,962 renal and ureteral calculi. *J Urol*, vol. 149(6), pp. 1419-24, Jun 1993.

[5] Liston TG, Montgomery BS, Bultitude MI and Tiptaft RC. Extracorporeal shock wave lithotripsy with the Storz Modulith SL20: the first 500 patients. *Br J Urol*, vol. 69(5), pp. 465-9, May 1992.

[6] Coz F, Orvieto M, Bustos M, Lyng R, Stein C, Hinrichs A and San Francisco I. Extracorporeal shockwave lithotripsy of 2000 urinary calculi with the modulith SL-20: success and failure according to size and location of stones. *J Endourol*, vol. 14(3), pp. 239-46, Apr 2000.

[7] C. Chaussy, E. Schmiedt, D. Jocham, V. Walther, W. Brendel, B. Forssmann and W. Hepp, "Extracorporeal shock wave lithotripsy: New aspects in the treatment of kidney stone disease.," *Basel: Karger*, 1982.

[8] S. R. Khan, R. L. Hackett and B. Finlayson, "Morphology of urinary stone particles resulting from ESWL Treatment," *J Urol*, vol. 136, pp. 1367-1372, 1986.

[9] J. P. Whelan and B. Finlayson, "An experimental model for the systematic investigation of stone fracture by extracorporeal shock wave lithotripsy," *J. Urol*, vol. 140, pp. 395-400, 1988.

[10] S. M. Gracewski, G. Dahake, Z. Ding, S. J. Burns and E. C. Everbach, "Internal stress wave measurements in solids subjected to lithotripster pulses," *J Acoust Soc Am*, vol. 94, pp. 652-661, 1993.

[11] X. F. Xi and P. Zhong, "Dynamic photoelastic study of the transient stress field in solids during shock wave lithotripsy," *J Acoust Soc Am*, vol. 109, pp. 1226-1239, 2001.

[12] W. Eisenmenger, "The mechanisms of stone fragmentation in ESWL," *Ultrasound Med Biol*, vol. 27, pp. 683-693, 2001.

[13] S. Zhu, F. H. Cocks, G. M. Preminger and P. Zhong, "The role of stress waves and cavitation in stone comminution in shock wave lithotripsy," *Ultrasound in Med. & Biol.*, vol. 28, no. 5, pp. 661-671, 2002.

[14] M. Delius, G. Heine and W. Brendel, "A mechanism of gallstone destruction by extracorporeal shock waves," *Naturwiss*, vol. 75, pp. 200-201, 1988.

[15] O. A. Sapozhnikov, A. D. Maxwell, B. MacConaghy and M. R. Bailey, "A mechanistic analysis of stone fracture in lithotripsy," *J Acoust Soc Am*, vol. 121, no. 2, pp. 1190-1202, 2007.

[16] W. Sass, M. Braunlich, H. Dreyer and E. Matura, "The mechanisms of stone disintegration by shock waves," *Ultrasound Med Biol*, vol. 17, no. 3, pp. 239-243, 1991.

[17] M. R. Bailey, "Control of acoustic cavitation with application to lithotripsy," Technical Report No. ARL-TR-97-1, Applied Research Laboratories, The University of Texas at Austin, Austin, TX, pp.1-210, 1997.

[18] N. Vakil and E. C. Everbach, "Transient acoustic cavitation in gallstone fragmentation: A study of gallstones fragmented in vivo," *Ultrasound Med Biol*, vol. 19, pp. 331-342, 1993.

[19] M. Delius, "Minimal static excess pressure minimises the effect of extracorporeal shock waves on cells and reduces it on gallstones," *Ultrasound Med Biol*, vol. 23, pp. 611-617, 1997.

[20] M. R. Bailey, R. O. Cleveland, T. Colonius, L. A. Crum, A. P. Evan, J. E. Lingeman, J. A. McAteer, O. A. Sapozhnikov and J. C. Williams, "Cavitation in shock wave lithotripsy: the critical role of bubble activity in stone breakage and kidney trauma," *in 2003 IEEE Ultrasonics Symposium*, 2003.

[21] X. F. Xi and P. Zhong, "Improvement of stone fragmentation during shock wave lithotripsy using a combined EH/PEAA shock wave generator- In vitro experiments," *Ultrasound Med Biol*, vol. 6, pp. 457-467, 2000.

[22] A. J. Coleman, J. E. Saunders, L. A. Crum and M. Dyson, "Acoustic cavitation generated by an extracorporeal shockwave lithotripter," *Ultrasound Med Biol*, vol. 13, pp. 69-76, 1987.

[23] L. A. Crum, "Cavitation microjets as a contributory mechanism for renal calculi disintegration in ESWL," *J Urol*, vol. 140, pp. 1587-1590, 1988.

[24] P. Zhong and C. J. Chuong, "Propagation of shock waves in elastic solids caused by the impact of cavitation microjets: Part I. Theoretical formulation," *J Acoust Soc Am*, vol. 94, pp. 19-28, 1993.

[25] P. Zhong, C. J. Chuong and G. M. Preminger, "Propagation of shock waves in elastic solids caused by the impact of cavitation microjets: Part II. Application to extracorporeal shock wave lithotripsy," *J Acoust Soc Am*, vol. 94, pp. 29-36, 1993.

[26] K. Rink, G. Delacretaz, G. Pittomvils, R. Boving and J. P. Lafaut, "Incidence of cavitation in the fragmentation process of extracorporeal shock wave lithotripters," *Appl Phys Lett*, vol. 64, no. 19, pp. 2596-2598, 1994.

[27] A. Philipp and W. Lauterborn, "Cavitation erosion by single laser-produced bubbles," *J Fluid Mech*, vol. 361, pp. 75-116, 1998.

[28] Leighton TG and Cleveland RO. Lithotripsy. *Proc Inst Mech Eng H*, vol. 224(2), pp. 317-42, 2010.

[29] Lingeman JE, Kim SC, Kuo RL, McAteer JA and Evan AP. Shockwave lithotripsy: anecdotes and insights. *J Endourol*, vol. 17(9), pp. 687-93. Nov 2003.

[30] Chan SL, Stothers L, Rowley A, Perler Z, Taylor W and Sullivan LD. A prospective trial comparing the efficacy and complications of the modified Dornier HM3 and MFL 5000 lithotriptors for solitary renal calculi. *J Urol*, vol. 153(6), pp. 1794-7, Jun 1995.

[31] Portis AJ, Yan Y, Pattaras JG, Andreoni C, Moore R and Clayman RV. Matched pair analysis of shock wave lithotripsy effectiveness for comparison of lithotriptors. *J Urol*, vol. 169(1), pp. 58-62, Jan 2003.

[32] Gerber R, Studer UE and Danuser H. Is newer always better? A comparative study of 3 lithotriptor generations. *J Urol*, vol. 173(6), pp. 2013-6, Jun 2005.

[33] J. E. Parsons, C. A. Cain, G. D. Abrams, and J. B. Fowlkes, "Pulsed cavitational ultrasound therapy for controlled tissue homogenization," *Ultrasound Med Biol,* vol. 32, pp. 115-29, Jan 2006.

[34] Z. Xu, A. Ludomirsky, L. Y. Eun, T. L. Hall, B. C. Tran, J. B. Fowlkes, *et al.*, "Controlled ultrasound tissue erosion," *IEEE Trans Ultrason Ferroelectr Freq Control,* vol. 51, pp. 726-36, Jun 2004.

[35] Z. Xu, J. B. Fowlkes, E. D. Rothman, A. M. Levin, and C. A. Cain, "Controlled ultrasound tissue erosion: the role of dynamic interaction between insonation and microbubble activity," *J Acoust Soc Am,* vol. 117, pp. 424-35, Jan 2005.

[36] Z. Xu, T. L. Hall, J. B. Fowlkes, and C. A. Cain, "Effects of acoustic parameters on bubble cloud dynamics in ultrasound tissue erosion (histotripsy)," *J Acoust Soc Am,* vol. 122, pp. 229-36, Jul 2007.

[37] Z. Xu, G. Owens, D. Gordon, C. Cain, and A. Ludomirsky, "Noninvasive creation of an atrial septal defect by histotripsy in a canine model," *Circulation,* vol. 121, pp. 742-9, Feb 16 2010.

[38] G. E. Owens, R. M. Miller, G. Ensing, K. Ives, D. Gordon, A. Ludomirsky, *et al.*, "Therapeutic ultrasound to noninvasively create intracardiac communications in an intact animal model," *Catheter Cardiovasc Interv,* vol. 77, pp. 580-8, Mar 1 2011.

[39] W. W. Roberts, "Focused ultrasound ablation of renal and prostate cancer: current technology and future directions," *Urol Oncol,* vol. 23, pp. 367-71, Sep-Oct 2005.

[40] A. M. Lake, T. L. Hall, K. Kieran, J. B. Fowlkes, C. A. Cain, and W. W. Roberts, "Histotripsy: minimally invasive technology for prostatic tissue ablation in an in vivo canine model," *Urology,* vol. 72, pp. 682-6, Sep 2008.

[41] C. R. Hempel, T. L. Hall, C. A. Cain, J. B. Fowlkes, Z. Xu, and W. W. Roberts, "Histotripsy fractionation of prostate tissue: local effects and systemic response in a canine model," *J Urol,* vol. 185, pp. 1484-9, Apr 2011.

[42] G. R. Schade, T. L. Hall, and W. W. Roberts, "Urethral-sparing histotripsy of the prostate in a canine model," *Urology,* vol. 80, pp. 730-5, Sep 2012.

[43] E. Vlaisavljevich, Y. Kim, S. Allen, G. Owens, S. Pelletier, C. Cain, *et al.*, "Image-guided non-invasive ultrasound liver ablation using histotripsy: feasibility study in an in vivo porcine model," *Ultrasound Med Biol,* vol. 39, pp. 1398-409, Aug 2013.

[44] H. G. Flynn and C. C. Church, "A mechanism for the generation of cavitation maxima by pulsed ultrasound," *J Acoust Soc Am,* vol. 76, pp. 505-12, Aug 1984.

[45] J. B. Fowlkes and L. A. Crum, "Cavitation threshold measurements for microsecond length pulses of ultrasound," *The Journal of the Acoustical Society of America,* vol. 83, pp. 2190-2201, 1988.

[46] P. Huber, K. Jochle, and J. Debus, "Influence of shock wave pressure amplitude and pulse repetition frequency on the lifespan, size and number of transient cavities in the field of an electromagnetic lithotripter," *Phys Med Biol,* vol. 43, pp. 3113-28, Oct 1998.

[47] C. E. Brennen, "Fission of collapsing cavitation bubbles," *Journal of Fluid Mechanics,* vol. 472, pp. 153-166, 2002.

[48] M. Arora, L. Junge, and C. D. Ohl, "Cavitation cluster dynamics in shock-wave lithotripsy: part 1. Free field," *Ultrasound Med Biol,* vol. 31, pp. 827-39, Jun 2005.

[49] Z. Xu, T. L. Hall, J. B. Fowlkes, and C. A. Cain, "Optical and acoustic monitoring of bubble cloud dynamics at a tissue-fluid interface in ultrasound tissue erosion," *The Journal of the Acoustical Society of America,* vol. 121, pp. 2421-2430, 2007.

[50] Y. A. Pishchalnikov, J. A. McAteer, I. V. Pishchalnikova, J. C. Williams, M. R. Bailey, and O. A. Sapozhnikov, "Bubble proliferation in shock wave lithotripsy occurs during inertial collapse," in *18th International Symposium on Nonlinear Acoustics,* 2008, pp. 460-463.

[51] Y. A. Pishchalnikov, J. C. Williams, and J. A. McAteer, "Bubble proliferation in the cavitation field of a shock wave lithotripter," *J Acoust Soc Am,* vol. 130, pp. EL87-93, Aug 2011.

[52] T. Y. Wang, Z. Xu, T. L. Hall, J. B. Fowlkes, and C. A. Cain, "An efficient treatment strategy for histotripsy by removing cavitation memory," *Ultrasound Med Biol,* vol. 38, pp. 753-66, May 2012.

[53] Y. A. Pishchalnikov, J. A. McAteer, and J. C. Williams, Jr., "Effect of firing rate on the performance of shock wave lithotriptors," *BJU Int,* vol. 102, pp. 1681-6, Dec 2008.

[54] R. Mettin, I. Akhatov, U. Parlitz, C. D. Ohl, and W. Lauterborn, "Bjerknes forces between small cavitation bubbles in a strong acoustic field," *Physical Review E,* vol. 56, pp. 2924-2931, 09/01/ 1997.

[55] W. S. Chen, T. J. Matula, and L. A. Crum, "The disappearance of ultrasound contrast bubbles: observations of bubble dissolution and cavitation nucleation," *Ultrasound Med Biol,* vol. 28, pp. 793-803, Jun 2002.

[56] P. S. Epstein and M. S. Plesset, "On the stability of gas bubbles in liquid-gas solutions," *The Journal of Chemical Physics,* vol. 18, pp. 1505-1509, 1950.

[57] M. Arora, C. D. Ohl, and D. Lohse, "Effect of nuclei concentration on cavitation cluster dynamics," *J Acoust Soc Am,* vol. 121, pp. 3432-6, Jun 2007.

[58] O. Yavas, P. Leiderer, H. K. Park, C. P. Grigoropoulos, C. C. Poon, and A. C. Tam, "Enhanced acoustic cavitation following laser-induced bubble formation: Long-term memory effect," *Physical Review Letters,* vol. 72, pp. 2021-2024, 03/28/ 1994.

[59] Y. A. Pishchalnikov, J. A. McAteer, J. C. Williams, Jr., I. V. Pishchalnikova, and R. J. Vonderhaar, "Why stones break better at slow shockwave rates than at fast rates: in vitro study with a research electrohydraulic lithotripter," *J Endourol,* vol. 20, pp. 537-41, Aug 2006.

[60] O. A. Sapozhnikov, V. A. Khokhlova, M. R. Bailey, J. C. Williams, Jr., J. A. McAteer, R. O. Cleveland, *et al.*, "Effect of overpressure and pulse repetition frequency on cavitation in shock wave lithotripsy," *J Acoust Soc Am,* vol. 112, pp. 1183-95, Sep 2002.

[61] Y. A. Pishchalnikov, O. A. Sapozhnikov, M. R. Bailey, I. V. Pishchalnikova, J. C. Williams, and J. A. McAteer, "Cavitation selectively reduces the negative-pressure phase of lithotripter shock pulses," *Acoust Res Lett Online,* vol. 6, pp. 280-286, Nov 3 2005.

[62] G. Vallancien, R. Munoz, M. Borghi, B. Veillon, J. M. Brisset, and M. Daudon, "Relationship between the frequency of piezoelectric shock waves and the quality of renal stone fragmentation. In vitro study and clinical implications," *Eur Urol,* vol. 16, pp. 41-44, 1989.

[63] H. Wiksell and A. C. Kinn, "Implications of cavitation phenomena for shot intervals in extracorporeal shock wave lithotripsy," *Br J Urol,* vol. 75, pp. 720-3, Jun 1995.

[64] A. Greenstein and H. Matzkin, "Does the rate of extracorporeal shock wave delivery affect stone fragmentation?," *Urology,* vol. 54, pp. 430-432, 1999.

[65] M. J. Weir, N. Tariq, and R. J. Honey, "Shockwave frequency affects fragmentation in a kidney stone model," *J Endourol,* vol. 14, pp. 547-50, Sep 2000.

[66] R. F. Paterson, D. A. Lifshitz, J. E. Lingeman, A. P. Evan, B. A. Connors, N. S. Fineberg, *et al.*, "Stone fragmentation during shock wave lithotripsy is improved by slowing the shock wave rate: studies with a new animal model," *J Urol,* vol. 168, pp. 2211-5, Nov 2002.

[67] Y. A. Pishchalnikov, J. A. McAteer, M. R. Bailey, I. V. Pishchalnikova, J. C. Williams, and A. P. Evan, "Acoustic shielding by cavitation bubbles in shock wave lithotripsy (SWL)," in *17th International Symposium on Nonlinear Acoustics* 2005, pp. 319-322.

Chapter 2

Histotripsy Erosion of Model Urinary Calculi

A majority component of this chapter has been published in *IEEE Transactions on Ultrasonics, Ferroelectrics, and Frequency Control*. © 2011 IEEE. Reprinted, with permission, from [1].

2.1 Introduction

As overviewed in Chapter 1, shock wave lithotripsy (SWL) has been in clinical use for nearly 30 years, representing one of several first-line therapies for the treatment of stones located in the kidneys and ureter. This technique utilizes focused shock waves to shatter stones into smaller fragments that are subsequently passed in the urine. It is likely that a combination of stress waves and cavitational effects are involved in stone comminution, with stress waves predominating for the initial subdivision of a primary calculus into large pieces [2, 3]. Cavitation has been shown to play an important role in subsequent fragment reduction, as studies of lithotripsy under over-pressure [4] and in cavitation suppressing fluids [2] have displayed reduced stone comminution.

Although effective, SWL suffers from the fact that it can produce stone fragments of significant size [5-8]. Traditional clinical perspective deems residual fragments less than 2 mm as clinically insignificant, since they are likely to pass with minimal difficulty [9]. Fragments in excess of 2 mm can lead to ureteral obstruction during passage, and when retained, may serve as a nidus for recurrent stone growth [10]. The production of such fragments is a relatively common occurrence; in studies using the Dornier HM-3 lithotripter with a low rate (< 10%) of retreatment, reported stone free rates at 3 months are approximately 70-80% [8, 11, 12]. Similar rates have been reported for other lithotripters, but often include much higher rates of retreatment (up to 50%) [5-7].

Novel forms of lithotripsy have been the subject of recent investigative work. Ikeda and Yoshizawa have explored the use of high intensity focused ultrasound (HIFU) lithotripsy with cavitating microbubbles [13, 14]. This technique utilizes the collapse of a cavitation cloud to fragment stones. In order to control cloud cavitation, the group has designed a two-frequency waveform consisting of a high frequency ultrasound burst to initiate a cavitation cloud followed by a low frequency burst to force the cloud into collapse. Results indicate that application of HIFU lithotripsy to natural stones produces small stone fragments (< 1 mm) as a result of localized cavitation on the stone surface. This characteristic of comminution via cavitation erosion is an attractive outcome with respect to minimizing the size of stone fragments produced during treatment.

Histotripsy, as introduced in Chapter 1, is a technique for the mechanical fractionation of tissue structures which utilizes focused ultrasound pulses to control cavitation activity. Previous work with histotripsy has demonstrated the feasibility of mechanical tissue fractionation via controlled cavitation [15-18], resulting in tiny acellular debris after several minutes of treatment. The initiation and maintenance of a cavitational bubble cloud can be directed via proper ultrasound pulse sequences, which typically include very short (< 20 cycles), high peak negative pressure (> 10 MPa), nonlinear pulses delivered at low duty cycles (< 1%). In contrast to thermal HIFU ablation, the low duty cycle in histotripsy manifests in the damage being mechanical rather than thermal in nature. Considering previous work that indicates the importance of cavitation in producing fine debris during the stone comminution process [2, 4, 13, 14], we hypothesize that cavitation control with histotripsy may provide a potential adjunct to conventional SWL procedures. The present chapter evaluates the feasibility of using histotripsy to treat urinary calculi through the use of an Ultracal-30 model.

2.2 Methods

The preliminary feasibility of using histotripsy to treat renal calculi was evaluated with model stones composed of Ultracal-30 gypsum cement. Statically anchored stones were sonicated for five minutes, and the resulting erosion rate and fragment sizes were assessed. The mechanism of histotripsy-induced stone damage was investigated by correlating stone erosion with cavitation activity. In order to examine the characteristics of stone comminution distinguishable on an ultrasound image, stone treatments were monitored in real time via B-mode ultrasound imaging.

2.2.1 Preparation of Model Urinary Stones

Artificial stones were cast from Ultracal-30 gypsum-based cement (U.S. Gypsum, Chicago, Illinois), which was selected as a model material for urinary stones due to its previous implementation in a number of in-vitro lithotripsy assessments [19-27]. This model has been shown to have acoustic and mechanical properties near the median of those reported for naturally occurring urinary stones [19]. Dry Ultracal-30 powder was mixed 1:1 (g:ml) with tap water for 10 minutes using a magnetic stir bar. Subsequently, 0.8 ml aliquots of the slurry were distributed into the cylindrical wells of an aluminum suppository mold (Gallipot Inc., St. Paul, Minnesota) using a 1 ml syringe. Each well was 10 mm in diameter, resulting in cylindrical stones of 7.9 ± 0.2 mm (mean ± standard deviation; n= 56) in height and 932.0 ± 14.1 mg in weight in the hydrated state. As specified by McAteer, *et al*. [19], the slurry was allowed to solidify for one hour, at which time additional tap water was added to each well in order to prevent dehydration of the cement. The following day, after a minimum solidification time of 12 hours, stones were removed from the mold and immersed in a covered beaker of tap water. Each stone was treated within 48 hours of removal from the mold.

2.2.2 Experimental Setup

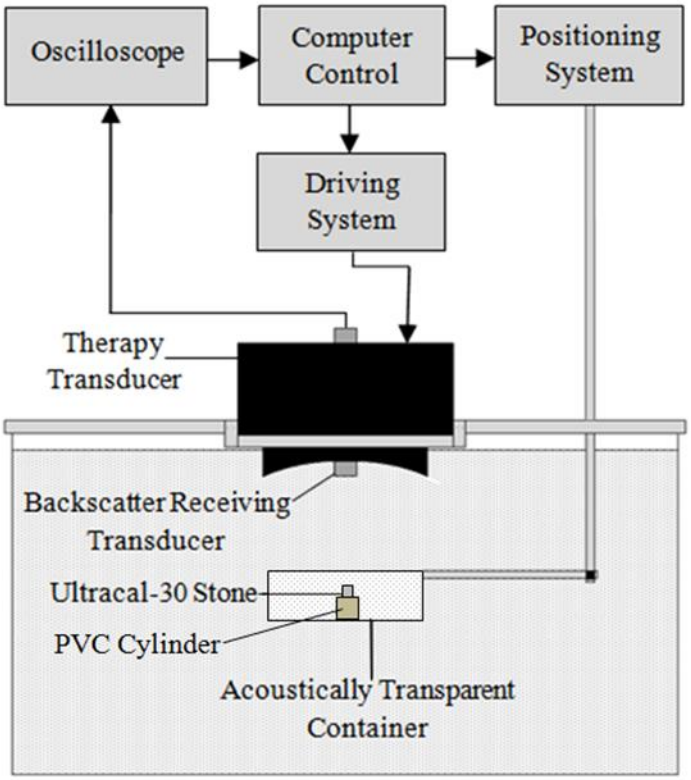

Fig. 2.1 The experimental setup for the treatment of Ultracal-30 model kidney stones consisted of a 1 MHz therapy transducer positioned at the top of a water tank, focused downward onto the stone surface. The cylindrical stones were statically anchored within a container in order to allow for collection of fragments generated during treatment. Acoustic backscatter was passively collected using a 5 MHz backscatter-receiving transducer positioned within the central hole of the therapy array.

The experimental setup used for the treatment of Ultracal-30 model stones is displayed in Fig. 2.1. In order to collect stone debris, each stone was statically anchored within a polypropylene container of dimensions 13 cm x 13 cm x 6 cm (length x width x height). An 11 cm x 11 cm x 0.013 cm (length x width x thickness) polycarbonate window located in the top face of the container allowed ultrasound to be transmitted to the stone with minimal attenuation. Direct measurement of the signal propagating through this window indicated that the attenuation was negligible (< 1%). Stones were kept stationary via the application of a small amount of silicon sealant (DAP Inc., Baltimore, Maryland) to the bottom face of each cylindrical stone. This face was then adhered to a PVC cylinder within the treatment container in order to elevate the stone from the container's bottom surface. The container was filled with water degassed to a dissolved oxygen content of 79% ± 2% in order to mimic that of urine [28], and was subsequently placed into a larger water tank of dimensions 76 cm x 30 cm x 32 cm which also contained water of 80% ± 1% dissolved oxygen. These dissolved oxygen levels were measured at the beginning and end of each treatment day (n=8) using a YSI 5000 Dissolved Oxygen Meter (YSI Inc., Yellow Springs, Ohio). A therapy transducer was mounted at the top of the tank and focused downward. It contained a central hole measuring 4 cm in diameter through which a backscatter-receiving transducer was placed. Alignment of the therapy transducer focus to the stone surface was accomplished using a PC-controlled 3-axis positioning system (Velmex Inc., Bloomfield, New York) to which the stone container was mounted. Two lasers laterally positioned near the therapy transducer focus ensured that stone position was maintained on an inter-trial basis.

2.2.3 Ultrasound Generation and Treatment

Histotripsy treatment was delivered to the Ultracal-30 stones using a piezocomposite spherically-focused 1 MHz transducer measuring 15 cm in diameter and having a 15 cm focal length (Imasonic, S.A., Voray sur l'Ognon, France). The transducer was driven using a class D amplifier developed in-house. All stones were sonicated using 5-cycle pulses delivered at a pulse repetition frequency (PRF) of 1 kHz. In order to investigate the correlation between stone erosion and cavitation cloud activity, ultrasound was applied to stones at different peak negative pressures (P-) of 3, 7, 9, 12, 14, and 21 MPa, which were measured using a fiber optic hydrophone developed in our lab [29]. The corresponding peak positive pressure (P+) values were 4, 13, 24, 34, 45, and 76 MPa, respectively. Representative pressure waveforms are displayed in Fig. 2.2. The lateral and axial -6-dB beamwidths were measured on the P- and P+ pressure profiles at P-/P+ of 10/29 MPa. The lateral -6-dB beamwidths for P- and P+ were 2.0 mm and 0.7 mm, respectively; the axial -6-dB beamwidths for P- and P+ were 19.0 mm and 7.5 mm. Beamwidths at higher pressures could not be successfully measured due to the occurrence of cavitation damage to the fiber tip during the pressure profile scan.

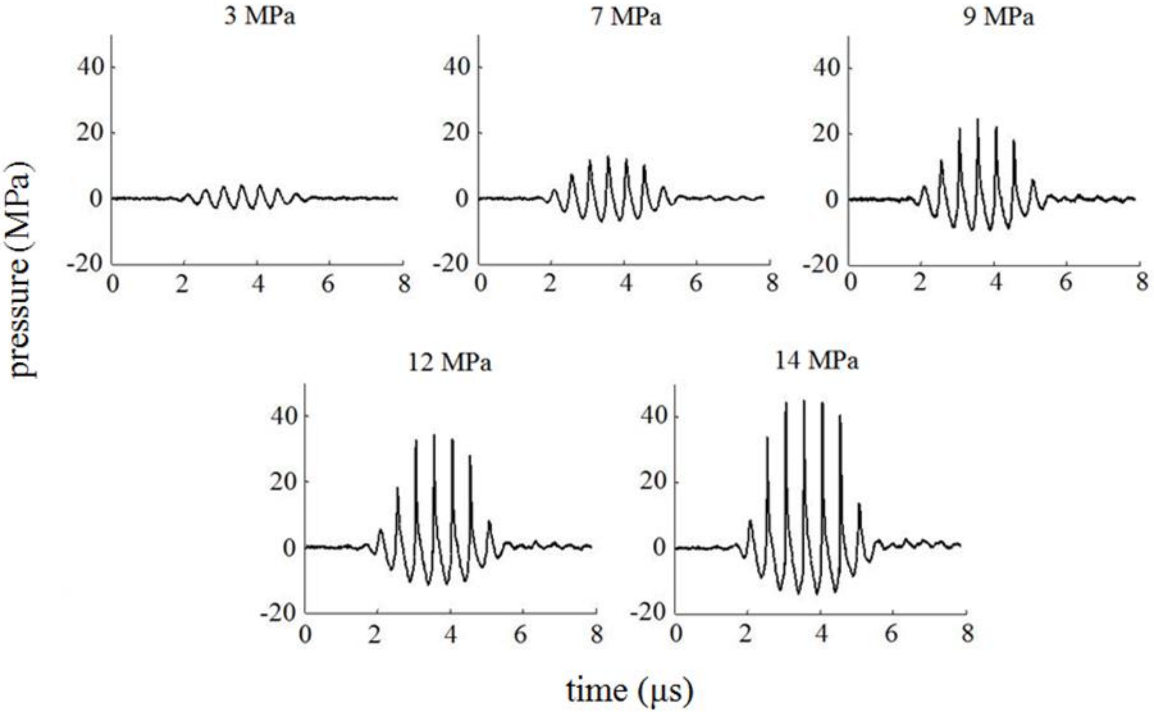

Fig. 2.2 Representative pressure waveforms as recorded from a fiber optic hydrophone. The signals shown have been averaged over 1000 pulses, and are labeled corresponding to their peak negative pressure (P-). At our maximum treatment intensity (P- = 21 MPa), cavitation occurred on the fiber tip after only several pulses; as such, an averaged waveform at this intensity is not presented.

In each treatment, the top face of the stone cylinder was positioned coincident with the uppermost portion of the ellipsoidal cavitational bubble cloud produced at the therapy transducer focus (the portion closest to the therapy transducer, approximately 5 mm pre-focal relative to the geometric focus at maximum intensity). All stones were sonicated for 300 seconds, with both the transducer focus and stone fixed in place throughout the duration of the treatment. Eight stones were treated at each pressure level, and all treatments were performed at room temperature (21° C).

2.2.4 Measurement of Stone Erosion Rate and Fragment Size

The average rate of stone erosion over a treatment period was calculated as the difference in the initial and final mass of the stone, divided by the treatment time (5 minutes). Due to the fact that Ultracal-30 stones must remain hydrated in order to retain their desired acoustic and mechanical properties [19], the stone weights measured pre- and post-treatment represent the hydrated weights of the stones. To ensure accurate comparison between treatments, masses were measured after all standing water was gently blotted off the stone surface with tissue paper.

The size distribution of residual stone fragments following treatment is of primary clinical concern, due to the fact that fragments of substantial size (>2 mm) can result in post-operative complications within the urinary tract. To evaluate the size of the fragments produced by histotripsy, suspended debris collected in the stone container was sequentially sieved through 2 mm, 1 mm, and 100 μm filters. The dry weight of each filter was measured both prior to and 3 days following sieving, and the dry mass of the stone debris trapped on each respective filter was calculated as the difference in these two measurements. To obtain a meaningful comparison between this dry mass and the original weight of an Ultracal-30 stone (hydrated), a conversion factor between the hydrated and dehydrated states was determined by allowing eight Ultracal-30 cylindrical stones to dry at room temperature for 72 hours. It was found that the dehydrated stone mass represents 79% ± 1% of its hydrated counterpart.

2.2.5 Cavitation Monitoring Using Acoustic Backscatter

To monitor cavitation activity, acoustic backscatter of the therapy pulses from the cavitating microbubbles was collected for each treatment. It has been previously documented that a spatially/temporally changing backscatter signal corresponds to a cluster of cavitating microbubbles (a bubble cloud) [17, 30, 31]. Passive detection of the backscatter signal employed a 5 MHz single-element transducer with a 2.5 cm aperture and 15 cm focal length (Olympus NDT, Waltham, Massachusetts). This backscatter-receiving transducer was positioned within the central hole of the therapy transducer, and the two were confocally aligned. Range-gaited backscatter signals were collected every 150 ms throughout the 300 second treatment using an oscilloscope (Lecroy 9354 TM, Chestnut Ridge, New York), and subsequent analysis was performed in MATLAB (MathWorks, Natick, Massachusetts).

Previous work has shown increased spatial variability in the backscatter signal to be an excellent indicator of a cavitating bubble cloud and tissue homogenate production with histotripsy [32]. Quantification of this spatial variability was achieved using the algorithm detailed by Parsons, *et al*. [32]: first, the cross-correlation for adjacent A-lines of the backscatter signal is computed, and the lag value which yields maximum correlation between the two is determined. Next, the difference between neighboring lags is taken, and each spatial variability value is defined as the mean of five consecutive lag differences.

The bubble cloud on the surface of the stone was also imaged directly using a Photron Fastcam SA1.1 high speed camera (Photron USA, San Diego, California). Images were acquired immediately following the arrival of a therapy pulse at the transducer focus (101 μs following transducer firing, corresponding to the propagation time for a 15 cm focal length). A frame rate of 1000 fps was used so that one image was collected per pulse (PRF= 1 kHz), and images were exposed for 20 µs. These parameters allowed for visualization of the bubble cloud near its maximum spatial extent, as the maximum cloud size in histotripsy has been found to occur at the end of a therapy pulse [33, 34]. A total of 201 frames were captured for each imaged treatment.

2.2.6 Ultrasound Imaging Feedback

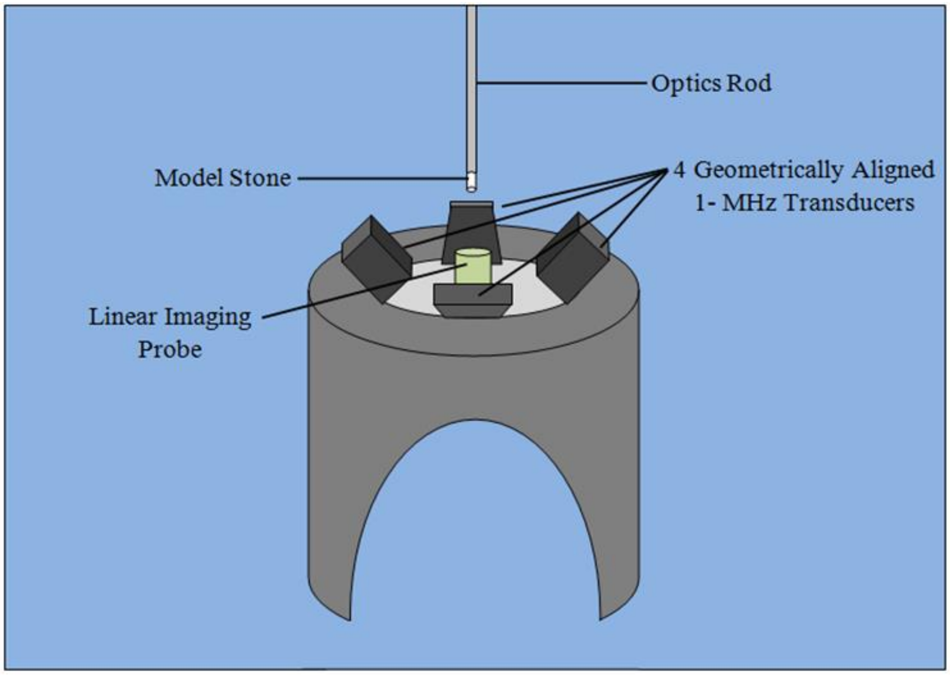

Fig. 2.3 B-mode imaging of stone treatments utilized a therapy system composed of four geometrically aligned 1 MHz transducers. A linear imaging probe positioned at the center of the array was also aligned to the focus. Ultracal-30 model stones were statically adhered to the end of an inverted optics rod during treatment.

An additional set of stone experiments was performed in which erosion progress was monitored in real-time using a LOGIQ P6 ultrasound imaging system (GE Healthcare, USA). Stones were treated with a therapy system consisting of four geometrically-aligned 1 MHz piezocomposite transducers (Imasonic, S.A., Voray sur l'Ognon, France) driven by a custom driving network. Each measured 5 cm x 5 cm in size and had a focal length of 7 cm. The resulting -6-dB beamwidth measured on the P- pressure profile for the overall system was 1.1 mm x 1.2 mm in the lateral dimension and 3.5 mm in the axial direction; the -6-dB beamwidth measured on the P+ pressure profile was 0.7 mm x 0.9 mm in the lateral dimension and 2.5 mm in the axial direction. These measurements were made at a P-/P+ of 21/31 MPa. A centrally-located 10 MHz linear imaging probe was also aligned to the focus of the therapy system. For this experiment, Ultracal-30 stones were statically adhered to the end of an optics rod using a small amount of silicon sealant (Fig. 2.3). To target the stone, prior to treatment a bubble cloud was generated at the therapy system focus in the empty water tank. This bubble cloud was visible as a hyperechoic zone on the ultrasound image, and the portion of the ellipsoidal cloud closest to the transducer was marked as the focus on the imager screen. Next, each cylindrical stone was aligned such that its top face was coincident with the focal marker. Stones were sonicated using 3-cycle pulses delivered at a PRF of 1 kHz and P-/P+ in excess of 23/35 MPa. Pressure values at higher intensity could not be determined due to instantaneous cavitation on the tip of the fiber optic hydrophone. B-mode ultrasound images were recorded before, during, and after histotripsy treatment.

2.3 Results

Results show that histotripsy is capable of effectively mechanically eroding the Ultracal-30 stone model. Significant stone erosion occurred only in the presence of a dense cavitating bubble cloud. In such cases, the side of the stone facing the therapy transducer was eroded to tiny particulates from the onset of treatment. Eroded material was ejected from the stone surface in a plume of debris that was visible immediately upon application of histotripsy. Such characteristics were never observed in the absence of cavitation activity. Real-time ultrasound imaging showed that both the stone and the cavitational bubble cloud appear distinctly as hyperechoic regions on a B-mode image.

2.3.1 Stone Erosion Rate vs. Pressure

The stone erosion rate plotted as a function of peak negative pressure (P-) is displayed in Fig. 2.4, and the representative damage morphology at each respective pressure level is presented in Fig. 2.5. Control group stones (P- = 0 MPa) were handled in the same way as stones that received histotripsy treatment, but were not exposed to ultrasound. No visible damage to control stones was observed with the naked eye, although they did display an average erosion rate of 1.68 ± 0.68 mg/min assuming a 5 minute treatment period. This loss of mass is likely the result of simply handling the stone. Stones treated at a P- of 3 MPa did not display a statistically significant variation in the rate of erosion relative to control, with a value of 1.43 ± 0.23 mg/min (*t-test*, P = 0.35), and visible damage was not readily observable on the stone surface with the naked eye. There was an increase in erosion rate with peak negative pressure between 7-21 MPa (*t-test*, P < 0.03). Stones treated at a P- of 7, 9, and 12 MPa all displayed statistically significant increases in erosion rate relative to control, with values of 2.23 ± 0.43 mg/min, 3.45 ± 1.13 mg/min, and 5.05 ± 0.50 mg/min, respectively (*t-test*, P = 0.04, 0.001, 0.0007). Stone damage was only observed on the surface of the stone facing the therapy transducer. The typical damage area, as can be seen in Fig. 2.5, increased with increasing the magnitude of the peak negative pressure.

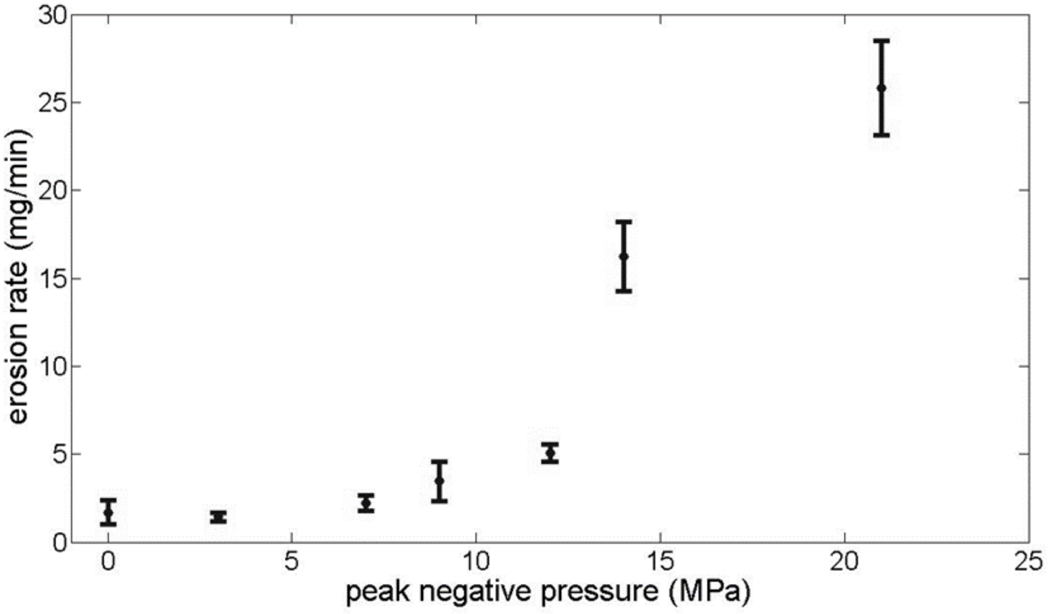

Fig. 2.4 Stone erosion rate plotted as a function of peak negative pressure (P-). Stones treated at P- of 3 MPa did not exhibit an erosion rate significantly different from control, while there was an increase in erosion rate with P- between 7-21 MPa. Drastic rate increases were observed at the upper-most pressures of 14 and 21 MPa.

At P- = 14 and 21 MPa, statistically significant increases in the erosion rate relative to the control were observed (*t-test*, $P < 0.0001$). Treatments performed at a P- of 14 MPa yielded an erosion rate of 16.23 ± 1.99 mg/min, while those at 21 MPa resulted in a rate of 25.80 ± 2.68 mg/min. Visually, treatment at these intensity levels resulted in damage regions that encompassed nearly the entire face of the 10 mm diameter cylindrical stone (Fig. 2.5).

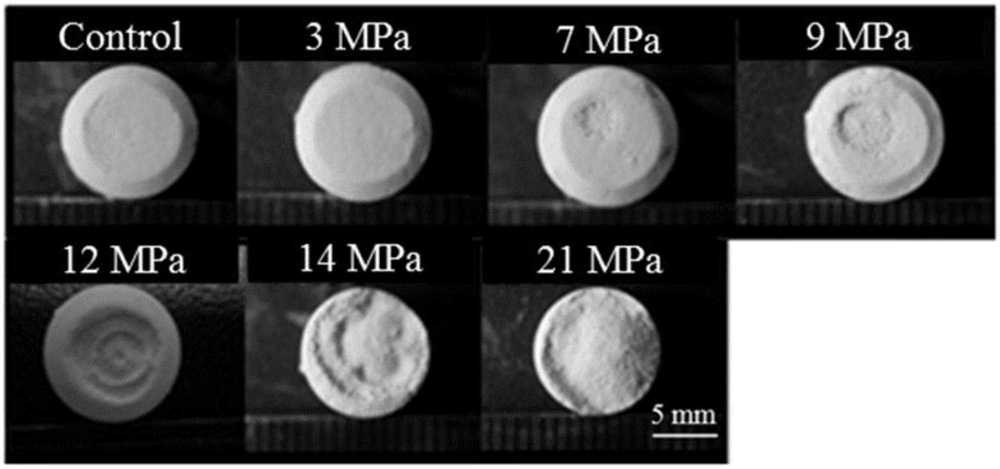

Fig. 2.5 The stone damage morphology was observed to be dependent on the pressure level employed for treatment. No visually apparent damage was observed in either the case of the control or 3 MPa treatments. At intensities corresponding to P- from 7-22 MPa, the typical area of damage on the face of the stone was found to increase with P-. Damage morphologies were not perfectly centered on the top surface of the stone due to slight targeting misalignments.

2.3.2 Stone Fragment Size Distribution

The size distribution of stone fragments resulting from histotripsy was evaluated by sequentially sieving suspended debris through 2 mm, 1 mm, and 100 μm filters. The change in dry weight of each filter was measured in order to assess the fraction of stone fragments corresponding to a given pore size. In all cases, no fragments were observed to be trapped by the filters with the naked eye, and the weight change of the filters did not display a statistically significant difference between control (untreated) samples and those which received ultrasound exposure (*t-test*, $P > 0.15$). This result suggests that stone fragments generated by histotripsy are smaller than 100 μm, and as such were not trapped by the filters used in this study.

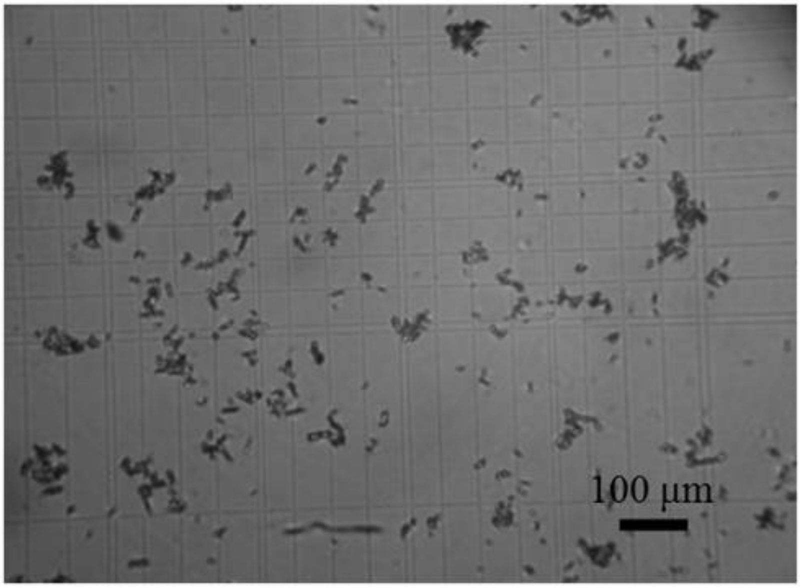

Fig. 2.6 Microscope imaging of Ultracal-30 stone debris placed on a hemocytometer helped to confirm that fragments generated by histotripsy treatment were smaller than 100 µm.

To help verify the fragment size results indicated by sieving, samples of stone debris collected during histotripsy treatments were placed on a hemocytometer and observed using microscopy. An example of such a sample is displayed in Fig. 2.6. As can be viewed in the image, the particulates are all smaller than 100 µm. This result is consistent with the outcome of sieving.

2.3.3 Cavitation Monitoring

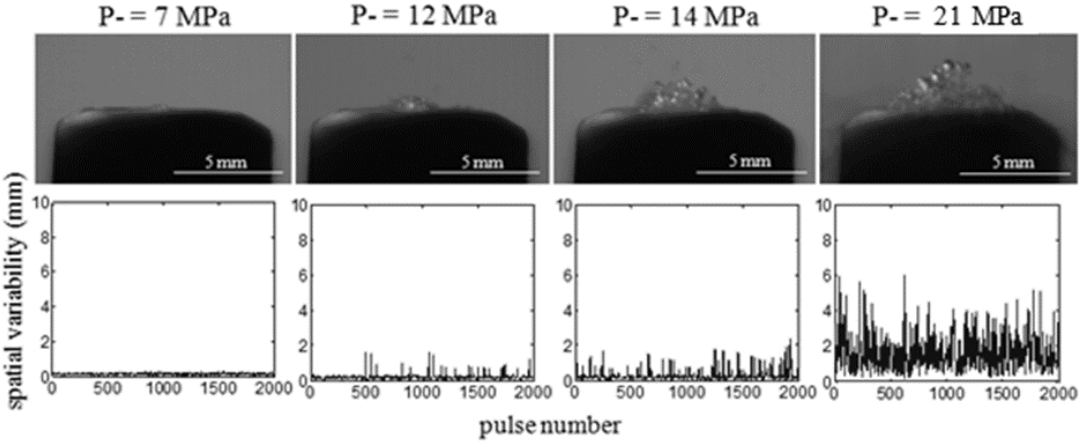

Fig. 2.7 Bubble activity at the stone surface. The calculated spatial variability in the acoustic backscatter signal acquired during histotripsy treatments (lower panel) was observed to increase with peak negative pressure (P-), indicating that the extent of the bubble cloud activity on the surface of the stone increases with P-. These results were confirmed via direct imaging of the bubble activity (top panel).

The spatial variability in the acoustic backscatter signal was calculated in order to quantify cavitation activity. Typical results at select pressure levels are presented in the lower panel of Fig. 2.7. In general, the magnitude of the spatial variability increased with increasing pressure, implying that the bubble cloud action on the stone surface increased as a function of pressure. Direct imaging of the cavitation activity on the surface of the stone confirmed these results, showing larger bubble clouds at higher pressures (Fig. 2.7, top panel).

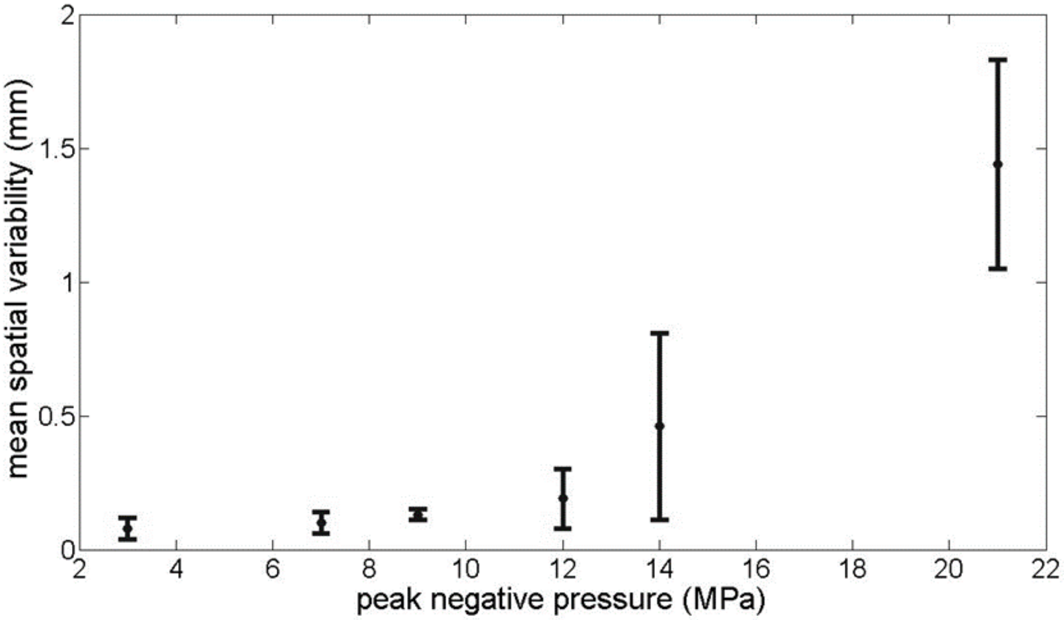

Fig. 2.8 The mean spatial variability (MSV) is plotted as a function of peak negative pressure. Statistically significant increases in MSV above the baseline level were observed for P- of 9 MPa and greater, with the most significant increases occurring for the upper-most pressure levels of 14 and 21 MPa.

The mean spatial variability (MSV) was also calculated for the set of treatments performed at each pressure level (Fig. 2.8). At P- of 3 and 7 MPa, the resulting MSV was low, and no/minimal bubble cloud activity was observed with imaging. At a P- of 9 MPa and above, MSV increased significantly relative to that observed at 7 MPa (*t-test*, $P < 0.01$) and substantial bubble activity was visualized via imaging. Most notably, treatments at P- of 14 and 21 MPa resulted in MSVs of 0.46 ± 0.35 mm and 1.44 ± 0.39 mm, respectively. These values are approximately an order of magnitude greater than those associated with the lower intensities used in this study.

Correspondingly, imaging showed that bubble cloud activity is enhanced at these uppermost pressure levels. These results are consistent with the trends in damage morphology displayed in Fig. 2.5.

2.3.4 Ultrasound Imaging Feedback

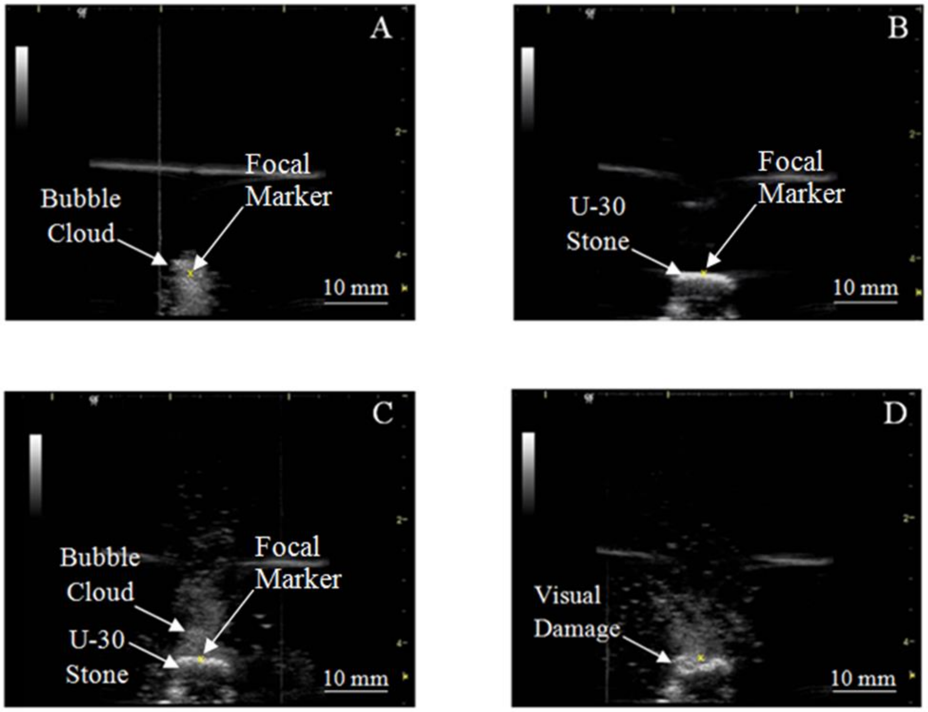

Fig. 2.9 B-mode images are presented from the real-time monitoring of Ultracal-30 stone treatment. The therapy transducer and imaging probe are located adjacent the top side of the images. (A) The bubble cloud showed clearly on the ultrasound image as a temporally changing hyperechoic zone. (B) Placement of a targeting marker near the proximal end of the bubble cloud facilitated alignment of the stone cylinder, which also showed clearly as a hyperechoic region on the image. (C) During treatment, accurate alignment could be confirmed by noting the positions of the stone and bubble cloud relative to one another. (D) A visually apparent reduction in stone size could be observed as treatment progressed, discernable by the change in shape of the stone face adjacent to the bubble cloud.

The important events associated with the real-time monitoring of stone treatment using B-mode imaging are displayed in Fig. 2.9. Prior to treatment, targeting of the therapy transducer was accomplished by first generating a cavitational bubble cloud at its focus. This cloud showed as a dynamic hyperechoic zone on the ultrasound image (Fig. 2.9(A)), with temporally changing characteristics corresponding to the activity of the bubble cloud. Placement of a targeting marker near the end of the cloud closest to the therapy transducer allowed for consistent targeting of the stone, which was also visible as a hyperechoic region on the ultrasound image (Fig. 2.9(B)). Upon application of histotripsy treatment, accurate alignment of the stone was confirmed by noting the position of the hyperechoic bubble cloud relative to the stone itself (Fig. 2.9(C)). A visually apparent reduction in stone size could be observed as treatment progressed, discernable by the change in shape of the stone face adjacent to the bubble cloud (Fig. 2.9(D)).

2.4 Discussion

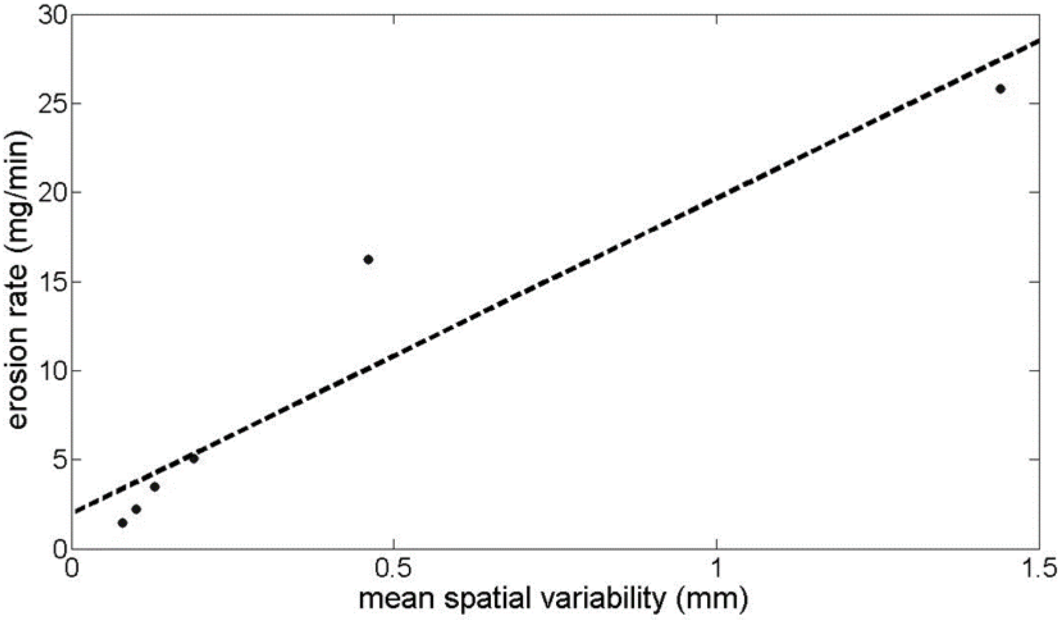

Fig. 2.10 The erosion rate achieved with histotripsy is plotted as a function of the mean spatial variability in the acoustic backscatter signal. Linear regression analysis yielded a correlation coefficient of R=0.95, indicating a strong correlation between the two variables. Recalling that the mean spatial variability in the backscatter signal is a measure of the bubble activity, it is concluded that the stone erosion rate is highly correlated to the degree of cavitation activity on the stone surface.

In this chapter the metric of spatial variability was used to quantify the cavitation activity at the surface of the Ultracal-30 model stones. Fig. 2.8 displays the mean spatial variability (MSV) resulting from treatment at each respective pressure level. Comparing this result with the plot of the stone erosion rate as a function of peak negative pressure (Fig. 2.4), it is apparent that a correlation between the MSV in the backscatter signal and the erosion rate exists. Both are observed to increase as functions of peak negative pressure, and both display drastic increases at P- of 14 and 21 MPa. In order to further assess this correlation, the erosion rate was plotted as a function of mean spatial variability (Fig. 2.10); subsequent linear regression analysis yielded a correlation coefficient (R) of 0.95, suggesting that the stone erosion rate is highly correlated to the degree of cavitation activity on the stone surface. It is therefore concluded that the primary mechanism of stone damage with histotripsy is cavitation-induced erosion.

Further examination of Fig. 2.10 reveals a systematic deviation from the proposed linear relationship between stone erosion rate and MSV. If a line is fitted using only the first three data points (MSV < 0.15 mm), the resulting slope (ΔRate/ΔMSV) is 40.4 mg/mm·min; contrastingly, fitting a line to just the last three data points (MSV > 0.15 mm) produces a reduced slope of 14.8 mg/mm·min. The complex physics involved in the stone erosion process make it difficult to assess the validity of a mathematical model for this situation, and it is possible that a second-order polynomial may be more appropriate. Here a linear model was used for the sole purpose of assessing the correlation between erosion rate and MSV. Physically, this observation suggests that there may be a shielding phenomenon at play as a result of the high pulse repetition frequency (PRF = 1 kHz) used in this study. Shielding is well documented in shock wave lithotripsy, and multiple studies have demonstrated that stone breakage is improved with lowering the shock rate [35-37]. The physical phenomenon underlying this observation was investigated by Pishchalnikov, *et al.* [38]. In their study, it was concluded that an axial distribution of microscopic bubbles—i.e. cavitation nuclei—can persist between lithotripsy pulses. The negative pressure phase of subsequent pulses can then stimulate these bubbles to grow, detracting energy from the negative pressure phase of the shock wave. Hence, the shock wave reaching the stone surface will have an attenuated P-. With respect to histotripsy, it is probable that this shielding phenomenon becomes more pronounced as the size of the bubble cloud increases in the axial dimension. This is consistent with the fact that the empirical erosion rate is lower than expected when MSV is high. It also suggests that there is a large potential for optimizing the histotripsy parameters utilized for stone treatment, with a decrease in PRF likely leading to more efficient erosion. Optimization work in subsequent chapters will focus on evaluating the trade-off between treatment rate (high PRF) and treatment efficiency (low PRF).

An assessment of how the histotripsy stone comminution rate compares to that of conventional SWL is of obvious clinical interest. A full lithotripsy dose traditionally consists of 2000 shocks delivered at a rate of 2 Hz, corresponding to a treatment duration of 16.7 minutes. The average stone erosion rate observed at maximum treatment intensity with histotripsy was approximately 26 mg/min. Assuming that this rate is constant—as would be expected with a surface erosion phenomenon—it would take roughly 36 minutes to fully erode one of the model stones used in this study. This treatment length is slightly over twice that of traditional SWL. However, it should be noted that the histotripsy parameters utilized in this chapter have not yet been optimized. Because histotripsy is a surface erosion phenomenon, having a larger focal region to encompass the entire stone would be desirable. It is therefore hypothesized that using lower frequency transducers will greatly enhance the rate of stone erosion; future work will examine this effect.

Fragments generated upon application of histotripsy to Ultracal-30 model kidney stones were measured to be smaller than 100 μm. It is important to distinguish this debris—which is generated *from the onset* of histotripsy treatment—from the stone fragments one would expect following shock wave lithotripsy. With respect to SWL, the shock waves imparted to the stone result in a distribution of fragment sizes that is very much dependent on treatment time. Zhu, *et al*.

[39] demonstrated that stone phantoms break up in a progressive manner as more and more shock waves are delivered. Specifically, following 25 to 50 shocks, it was observed that the treated stone had broken into several large pieces. The application of subsequent shocks produced more medium and small fragments, indicating progressive comminution of the initial large pieces. This mechanism of fragmentation presents the potential for the generation of residual fragments of significant size, which includes anything in excess of 2 mm in diameter by urological standards. In contrast, one of the profound characteristics of erosion induced by cavitating microbubbles in histotripsy is the fact that the stone fragments generated are of clinically insignificant size from the onset of treatment. This result is consistent with the work of Ikeda and Yoshizawa, who found that using HIFU to treat natural stones resulted in the production of small stone fragments (<1 mm) via cavitation erosion [13, 14].

From a clinical standpoint, the production of ultra-fine debris is much preferred relative to sizeable stone fragments. Residual stone pieces >2 mm may lead to ureteral obstruction, and have been shown to place patients at a higher risk for recurrent stone formation and growth [10]. Contrastingly, those <2 mm are expected to pass spontaneously without further treatment, although passage may often take several weeks [40]. It is certainly possible that in some cases these clinically insignificant residual fragments may be retained and seed new stones [41]; however, study examining patients at 12 month follow-up has shown that the probability of eliminating residual lithiasis is significantly greater in patients with "dust" than in those with significant residual fragments [42].

Targeting is of inherent importance for safe and effective stone comminution. One potential advantage of histotripsy is the fact that it offers real-time image guidance of treatments. It was shown that both the bubble cloud and the stone itself are visible as hyperechoic zones on a B-mode image (Fig. 2.9(A-C)), presenting the opportunity for focal tracking mechanisms. Such tracking capability was not necessary in this preliminary feasibility study, as model stones were statically anchored in place; however, the ability to track the motion of a mobile stone and adjust the therapy transducer focus accordingly may be essential when histotripsy stone erosion is evaluated in more physiologically-relevant settings.

Finally, one inherent limitation of the initial feasibility study presented in this chapter is the fact that it utilized model stones. Ultracal-30 is a commonly accepted stone model within the lithotripsy community; however, the extent to which it is capable of mimicking naturally-occurring renal calculi is obviously limited. For this reason, the results of this study should be regarded as relative trends as opposed to absolute in nature.

2.5 Conclusion

This chapter presents a preliminary assessment of the feasibility of using histotripsy to treat renal calculi, and it was shown that histotripsy can mechanically erode Ultracal-30 model kidney stones into fine fragments. At the maximum tested treatment intensity corresponding to a peak negative pressure of 21 MPa, histotripsy was able to achieve an average erosion rate of approximately 26 mg/min. Substantial stone erosion was only observed in the presence of a dense cavitating bubble cloud, as indicated by both optical imaging and the spatial variability metric. Residual stone fragments generated by histotripsy treatment appeared to be smaller than 100 μm, and both the stone and the cavitational bubble cloud were visible as hyperechoic zones on B-mode images. These results suggest that cavitation control with histotripsy may offer a potential adjunct to SWL procedures, and it is possible that a synergistic combination of the two modalities could eventually lead to faster and more complete stone comminution. Subsequent chapters will explore these potential synergies, as well as evaluate strategies for maximizing the efficiency of histotripsy stone erosion.

2.6 References

[1] A. P. Duryea, A. D. Maxwell, W. W. Roberts, Z. Xu, T. L. Hall, and C. A. Cain, "In vitro comminution of model renal calculi using histotripsy," *IEEE Trans Ultrason Ferroelectr Freq Control,* vol. 58, pp. 971-80, May 2011.

[2] S. Zhu, F.H. Cocks, G.M. Preminger, and P. Zhong, “The role of stress waves and cavitation in stone comminution in shock wave lithotripsy,” *Ultrasound Med Biol*, vol. 28, pp. 661-71, 2002.

[3] O.A. Sapozhnikov, A.D. Maxwell, B. MacConaghy, and M.R. Bailey, “A mechanistic analysis of stone fracture in lithotripsy,” *J Acoust Soc Am*, vol. 121, pp. 1190-202, Feb 2007.

[4] M. Delius, “Minimal static excess pressure minimizes the effect of extracorporeal shock waves on cells and reduces it on gallstones,” *Ultrasound Med Biol*, vol. 23, pp.611-7, 1997.

[5] T.B. Mobley, D.A. Myers, W.B. Grine, J.M. Jenkins, and W.R. Jordan, “Low energy lithotripsy with the Lithostar: treatment results with 19,962 renal and ureteral calculi,” *J Urol*, vol. 149, pp. 1419-24, Jun 1993.

[6] T.G. Liston, B.S. Montgomery, M.I. Bultitude, and R.C. Tiptaft, “Extracorporeal shock wave lithotripsy with the Storz Modulith SL20: the first 500 patients,” *Br J Urol*, vol. 69, pp. 465-9, May 1992.

[7] F. Coz, M. Orvieto, M. Bustos, R. Lyng, C. Stein, A. Hinrichs, and I. San Francisco, “Extracorporeal shockwave lithotripsy of 2000 urinary calculi with the Modulith SL-20: success and failure according to size and location of stones,” *J Endourol*, vol. 14, pp. 239-46, Apr 2000.

[8] A.S. Cass, “Comparison of first generation (Dornier HM3) and second generation (Medstone STS) lithotripters: treatment results with 13,864 renal and ureteral calculi,” *J Urol*, vol. 153, pp. 588-92, Mar 1995.

[9] C. Chaussy, E. Schmiedt, D. Jocham, V. Walther, W. Brendel, B. Forssmann, and W. Hepp, "Extracorporeal shock wave lithotripsy: New aspects in the treatment of kidney stone disease," *Basel, Karger,* 1982.

[10] J.K. Fine, C.Y. Pak, and G.M. Preminger, "Effect of medical management and residual fragments on recurrent stone formation following shock wave lithotripsy," *J Urol,* vol. 153, pp. 27-32; discussion 32-3, Jan 1995.

[11] J.E. Lingeman, L.H. Smith, and J.R. Wood, "Bioeffects and long term effects of ESWL. In: Urinary Calculi: ESWL, Endourology and Medical Therapy, Philadelphia: Lea & Febiger, 1989: 285.

[12] G. Politis and D.P. Griffith, "ESWL: Stone free efficacy based upon the stone size and location," *World J Urol*, vol. 5, pp. 255-8, 1987.

[13] T. Ikeda, S. Yoshizawa, M. Tosaki, J.S. Allen, S. Takagi, N. Ohta, T. Kitamura, and Y. Matsumoto, "Cloud cavitation control for lithotripsy using high intensity focused ultrasound," *Ultrasound Med Biol*, vol. 32, pp. 1383-97, Sept 2006.

[14] S. Yoshizawa, T. Ikeda, A. Ito, R. Ota, S. Takagi, and Y. Matsumoto, "High intensity focused ultrasound lithotripsy with cavitating microbubbles," *Med Biol Eng Comput*, vol. 47, pp. 851-60, 2009.

[15] J.E. Parsons, C.A. Cain, G.D. Abrams, and J.B. Fowlkes, "Pulsed cavitational ultrasound therapy for controlled tissue homogenization," *Ultrasound Med Biol*, vol. 32, pp. 115-29, 2006.

[16] Z. Xu, A. Ludomirsky, L.Y. Eun, T.L. Hall, B.C. Tran, J.B. Fowlkes, and C.A. Cain, "Controlled ultrasound tissue erosion," *IEEE Trans Ultrason Ferroeletr Freq Control*, vol. 51, pp. 726-36, 2004.

[17] Z. Xu, J.B. Fowlkes, E.D. Rothman, A.M. Levin, and C.A. Cain, "Controlled ultrasound tissue erosion: the role of dynamic interaction between insonation and microbubble activity," *J Acoust Soc Am*, vol. 117, pp. 424-35, 2005.

[18] Z. Xu, J.B. Fowlkes, C.A. Cain, "Effects of acoustic parameters on bubble cloud dynamics in ultrasound tissue erosion (histotripsy)," *J Acoust Soc Am*, vol. 122, pp. 229-36, 2007.

[19] J.A. McAteer, J.C. Williams, Jr., R.O. Cleveland, J. Van Cauwelaert, M.R. Bailey, D.A. Lifshitz, and A.P. Evan, "Ultracal-30 gypsum artificial stones for research on the mechanisms of stone breakage in shock wave lithotripsy," *Urol Res*, vol. 33, pp. 429-34, Dec 2005.

[20] R.L. Kuo, R.F. Paterson, T.M. Siqueira, Jr., A.P. Evan, J.A. McAteer, J.C. Williams, Jr., and J.E. Lingeman, "In vitro assessment of ultrasonic lithotriptors," *J Urol*, vol. 170, pp. 1101-4, Oct 2003.

[21] R.F. Paterson, D.A. Lifshitz, J.E. Lingeman, A.P. Evan, B.A. Connors, N.S. Fineberg, J.C. Williams, Jr., and J.A. McAteer, "Stone fragmentation during shock wave lithotripsy is improved by slowing the shock wave rate: studies with a new animal model," *J Urol*, vol. 168, pp. 2211-5, Nov 2002.

[22] P.V. Chitnis and R.O. Cleveland, "Quantitative measurements of acoustic emissions from cavitation at the surface of a stone in response to a lithotripter shock wave," *J Acoust Soc Am*, vol. 119, pp. 1929-32, Apr 2006.

[23] O.A. Sapozhnikov, L.A. Trusov, N.R. Owen, M.R. Bailey, and R.O. Cleveland, "Detecting fragmentation of kidney stones in lithotripsy by means of shock wave scattering," in *AIP Conf Proc*, vol. 829, pp. 308-312, May 2006.

[24] J.A. McAteer, R.O. Cleveland, R.F. Paterson, D.L. Rietjens, A.P. Evan, B.A. Connors, J.E. Lingeman, Y.A. Pishchalnikov, I.V. Pishchalnikova, and J.C. Williams, Jr., "Evidence that cavitation and spall contribute to stone failure in an animal model of kidney stone fragmentation by shock wave lithotripsy (SWL)," *Proceedings 17th International Congress on Acoustics*, vol. VII, pp. 202-3, 2002.

[25] A. Mota, J. Knap, and M. Ortiz, "Three-dimensional fracture and fragmentation of artificial kidney stones," *Journal of Physics: Conference Series*, vol. 46, pp. 299-303, 2006.

[26] Y.A. Pishchalnikov, J.A. McAteer, R.J. VonDerHaar, I.V. Pishchalnikova, and J.C. Williams, Jr., "The characteristics of broad and narrow focal zone lithotripters," *AIP Conf Proc*, vol. 1049, pp. 238-242, 2008.

[27] Y.A. Pishchalnikov, O.A. Sapozhnikov, M.R. Bailey, J.C. Williams, Jr., R.O. Cleveland, T. Colonius, L.A. Crum, A.P. Evan, and J.A. McAteer, "Cavitation bubble cluster activity in the breakage of kidney stones by lithotripter shockwaves," *J Endourol*, vol. 17, pp. 435-46, Sep 2003.

[28] E.A. Gardner, J.B. Fowlkes, P.L. Carson, J.A. Ivey, and D.A. Ohl, "Bubble Generation in Excised Canine Urinary Bladders Using an Electrohydraulic Lithotripter," *1993 IEEE Ultrasonics Symposium*, pp. 905-908, 1993.

[29] J.E. Parsons, C.A. Cain, and J.B. Fowlkes, "Cost-effective assembly of a basic fiber-optic hydrophone for measurement of high-amplitude therapeutic ultrasound fields," *J Acoust Soc Am*, vol. 119, pp. 1432-40, 2006.

[30] Z. Xu, T.L. Hall, J.B. Fowlkes, and C.A. Cain, "Optical and acoustic monitoring of bubble cloud dynamics at a tissue-fluid interface in ultrasound tissue erosion," *J Acoust Soc Am*, vol. 121, pp. 2421-30, 2007.

[31] Z. Xu, M. Raghavan, T.L. Hall, C.W. Chang, M.A. Mycek, J.B. Fowlkes, and C.A. Cain, "High speed imaging of bubble clouds generated in pulsed ultrasound cavitational therapy-histotripsy," *IEEE Trans Ultrason Ferroelectr Freq Control*, vol. 54, pp. 2091-101, 2007.

[32] J.E. Parsons, C.A. Cain, and J.B. Fowlkes, "Spatial Variability in Acoustic Backscatter as an Indicator of Tissue Homogenate Production in Pulsed Cavitational Ultrasound Therapy," *IEEE Trans Ultrason Ferroelctr Freq Control*, vol. 54, pp. 576-90, 2007.

[33] Z. Xu, M. Raghavan, T.L. Hall, M.A. Mycek, J.B. Fowlkes, and C.A. Cain, "Evolution of bubble clouds induced by pulsed cavitational ultrasound therapy - histotripsy," *IEEE Trans Ultrason Ferroelectr Freq Control*, vol. 55, pp. 1122-32, May 2008.

[34] T.-Y. Wang, A.D. Maxwell, S. Park, Z. Xu, J.B. Fowlkes, and C.A. Cain, "Why are short pulses more efficient in tissue erosion using pulsed cavitational ultrasound (histotripsy)?" in *Int Symp Therapeutic Ultrasound,* Aix en Provence, France, 2009.

[35] G. Vallancien, R. Munoz, M. Borghi, B. Veillon, J.M. Brisset, and M Daudon, "Relationship between the frequency of piezoelectric shock waves and the quality of renal stone fragmentation. In vitro study and clinical implications," *Eur Urol,* vol. 16, pp. 41-4, 1989.

[36] M.J. Weir, N. Tariq, and R.J. Honey, "Shockwave frequency affects fragmentation in a kidney stone model," *J Endourol,* vol. 14, pp. 547-50, 2000.

[37] A. Greenstein and H. Matzkin, "Does the rate of extracorporeal shock wave delivery affect stone fragmentation," *Urology,* vol. 54, pp. 430-2, 1999.

[38] Y.A. Pishchalnikov, J.A. McAteer, J.C. Williams, Jr., I.V. Pishchalnikova, and R.J. Vonderhaar, "Why stones break better at slow shockwave rates than at fast rates: in vitro study with a research electrohydraulic lithotripter," *J Endourol,* vol. 20, pp. 537-41, Aug 2006.

[39] S. Zhu, F.H. Cocks, G.M. Preminger, and P. Zhong, "The role of stress waves and cavitation in stone comminution in shock wave lithotripsy," *Ultrasound Med Biol,* vol. 28, pp. 661-71, May 2002.

[40] C. Candau, C. Saussine, H. Lang, C. Roy, F. Faure, and D. Jacqmin, “Natural history of residual renal stone fragments after SWL,” *Eur Urol*, vol. 37, pp. 18-22, 2000.

[41] M.M. Osman, Y. Alfano, S. Kamp, A. Haecker, P. Alken, M.S. Michel, and T. Knoll, “5-year-follow-up of patients with clinically insignificant residual fragments after extracorporeal shockwave lithotripsy,” *Eur Urol*, vol. 47, pp. 860-4, Jan 2005.

[42] G. Zanetti, M. Seveso, E. Montanari, A. Guarneri, A. Del Nero, R. Nespoli, and A. Trinchieri, “Renal Stone fragments following shock wave lithotripsy,” *J Urol*, vol. 158, pp. 352-5, Aug 1997.

Chapter 3

Histotripsy to Augment Shock Wave Lithotripsy Stone Comminution

A majority component of this chapter has been published in *IEEE Transactions on Ultrasonics, Ferroelectrics, and Frequency Control*. © 2013 IEEE. Reprinted, with permission, from [1].

3.1 Introduction

As introduced in Chapter 1, stone fragmentation in shock wave lithotripsy (SWL) is a dynamic process in which cracks initiate, grow, and coalesce within the stone matrix. It is well established that mechanical stresses induced directly by a lithotripter shock wave (LSW) play a critical role in this subdivision [2-11]. Mechanisms proposed to explain the contribution of these direct stresses include the superposition of longitudinal waves within the stone (spalling) [2-4, 6, 9], circumferential stresses generated by the portion of the LSW traveling in fluid adjacent to the stone boundary (squeezing) [7], and shear waves generated at stone corners that are reinforced by the squeezing wave (dynamic squeezing) [10].

These direct stress mechanisms do not act in isolation, however, and there is a great deal of evidence suggesting that cavitation produced by the trailing tensile tail of the LSW is a crucial component of the stone comminution process [8-22]. Studies in which the cavitational component of LSWs was suppressed through shock wave modification [12], viscous fluids [8, 9, 13], or static overpressure [14, 15] have yielded a drastic reduction in stone fragmentation. Conversely, Xi and

Zhong demonstrated that an auxiliary shock wave timed such as to intensify the collapse of LSW-induced bubbles can markedly enhance comminution [16]. The damage conferred by cavitation activity is typified by numerous minute pittings on the stone surface, which are likely the result of localized stress created by the impact of fluid jets or secondary shock waves produced by bubble collapse [16-18, 20, 22]. Additionally, the work of Sass, *et al.* suggests that cavitation may act to facilitate the growth of fissures in the stone material induced by the direct stress wave component of LSWs [11].

In contrast to these studies demonstrating the vital role played by cavitation in stone subdivision, additional work has established that the persistence of cavitational microbubbles from one LSW to the next can hinder the comminution process. Enhanced stone subdivision with decreasing rate of LSW delivery has been demonstrated both *in-vitro* [23, 24] and *in-vivo* [25]. These studies are corroborated by clinical trials in which higher success rates were observed for patients treated with LSWs at a rate of 1 Hz in comparison to those at 2 Hz [26]. Such outcomes are demonstrative of the "shielding" phenomenon commonly associated with SWL, in which a population of prefocal cavitation nuclei—here, remnant bubbles created by the preceding LSWs—act to attenuate the tensile component of the waveform and reduce the efficacy of cavitation at the stone surface [27, 28]. Treatment strategies to minimize the degree of this undesirable cavitation and maximize stone fragmentation have been the subject of recent investigative work [29, 30].

In this chapter, the role of cavitation in SWL is further explored by applying controlled cavitation at strategic time points in the stone comminution process. This was accomplished using histotripsy to control the activity of a cavitational bubble cloud. As discussed in Chapters 1 and 2, previous work with histotripsy has demonstrated the feasibility of mechanical tissue fractionation via controlled cavitation [31-34], as well as the ability of histotripsy to readily erode model stones to fine particulate debris [35, 36]. Our ultimate goal in the present chapter is to investigate how cavitationally-based histotripsy stone erosion can be synchronized with LSWs to augment the stone comminution process.

3.2 Methods

3.2.1 Preparation of Model Urinary Stones

Composite stone phantoms formulated to mimic the mid-range tensile fracture strength of naturally occurring cystine calculi were cast from a mixture of BegoStone plaster (BEGO USA, Smithfield, RI), albumin (Carolina Biological Supply Company, Burlington, NC), and tap water. Following the procedures detailed by Simmons, *et al*. [37] the constituents were mixed rigorously by hand for 4 minutes; a mass ratio of 73% BegoStone, 24.5% water, and 2.5% albumin was used to achieve the desired stone properties. Subsequently, 0.6 mL aliquots of the slurry were distributed into the 1 cm diameter cylindrical wells of a Delrin plastic mold and allowed to cure overnight. Following this initial setting, stone phantoms were removed from the mold and slowly heated to 90º C in a low temperature oven (Model 10GC, Quincy Lab Inc., Chicago, IL). Stones were held at this temperature for 12 hours to permit albumin polymerization, then removed and allowed to cool to room temperature before being submersed in a beaker of tap water to hydrate. Prior to treatment, phantoms in the hydrated state were degassed in a vacuum desiccator (Bel-Art Products, Wayne, NJ) overnight to minimize any air trapped in the stone material. The end result of this process was the production of cylindrical model stones measuring 1 cm in diameter and having a hydrated mass of 1.03 ± 0.03 g (mean ± SD, n= 50).

3.2.2 Experimental Setup

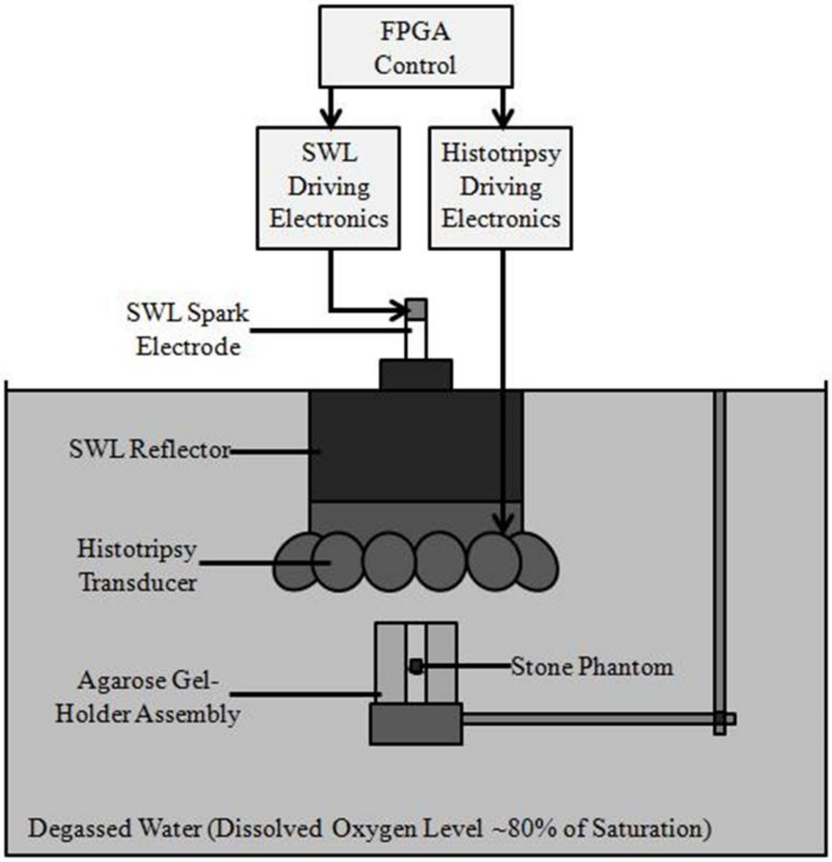

Fig. 3.1 Experimental setup used for the treatment of composite stone phantoms. Stones were held within a channel in an agarose hydrogel, while ultrasound was delivered from the electrohydraulic lithotripter and/or histotripsy transducer positioned above.

The experimental setup used for the treatment of composite stone phantoms is displayed in Fig. 3.1. During sonication stones were held within a channel in an optically transparent 1% agarose hydrogel (Sigma Type VII, Sigma-Aldrich Co., St. Louis, Missouri), the construction of which is detailed in Fig. 3.2. Briefly, this gel-holder is composed of an Accura-60 plastic bottom that was fabricated on a stereolithography machine. A concave "basket" containing 2 mm holes extends up from the bottom and serves as the surface on which the stone sample was ultimately placed (Fig. 3.2(A)). Next, the agarose gel was cast surrounding this basket, creating a channel measuring 15 mm in diameter and 40 mm in height (Fig. 3.2(B)). Stone fragments were free to move about within this channel during sonication, with debris reduced to sub-2 mm size able to pass through the basket into a collecting dish placed below (Fig. 3.2(C)). The entire gel-holder assembly was positioned within a treatment tank measuring 58 x 43 x 45 cm (L x W x H) that was filled with deionized water at room temperature degassed to a dissolved oxygen content of 77% ± 2% (n= 10) to mimic that of urine [38]. These levels were measured at the beginning and end of each treatment day using a Traceable Digital Oxygen Meter (Control Company, Friendswood, TX). Additionally, sodium chloride was added to the treatment tank in order to achieve a water conductivity of 600 µS/cm, which is a typical value used for electrohydraulic shock wave sources such as the one used in this study. Both the LSW source and the histotripsy therapy transducer were positioned at the top of the tank focused downward. Alignment of the therapy focus to the stone was maintained on an inter-trial basis via two lasers laterally positioned at the known geometric focal location.

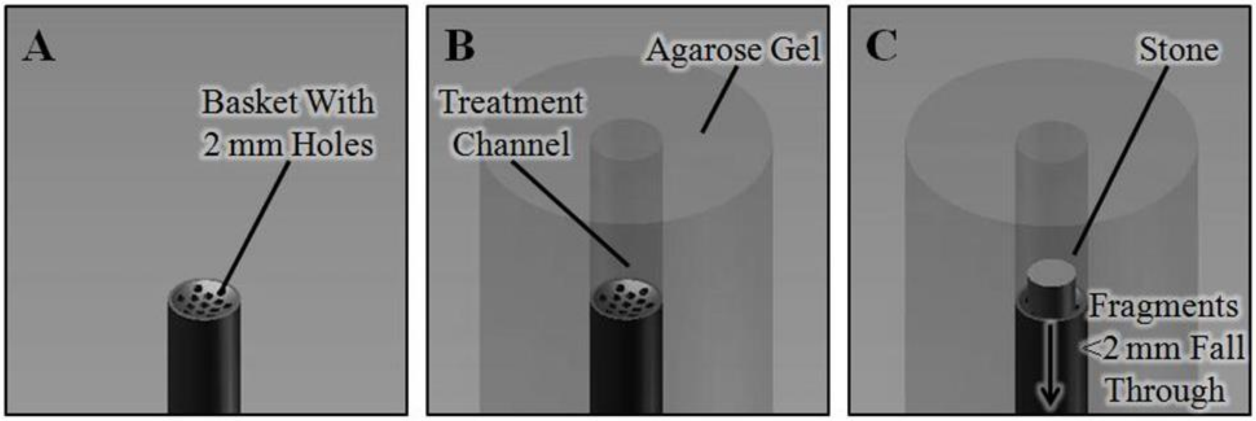

Fig. 3.2 Gel-holder assembly used to position composite stone phantoms during sonication. (A) The bottom portion of the holder (not pictured in its entirety) was fabricated from Accura-60 plastic. It contains a concave basket with 2 mm holes that served as the surface on which model stones were ultimately placed. (B) 1% agarose hydrogel was cast surrounding the basket, creating a channel in which stone fragments were free to move. (C) During treatment, debris reduced to sub-2 mm size was able to pass through the basket into a collecting dish placed below (not pictured).

3.2.3 Ultrasound Generation and Treatment

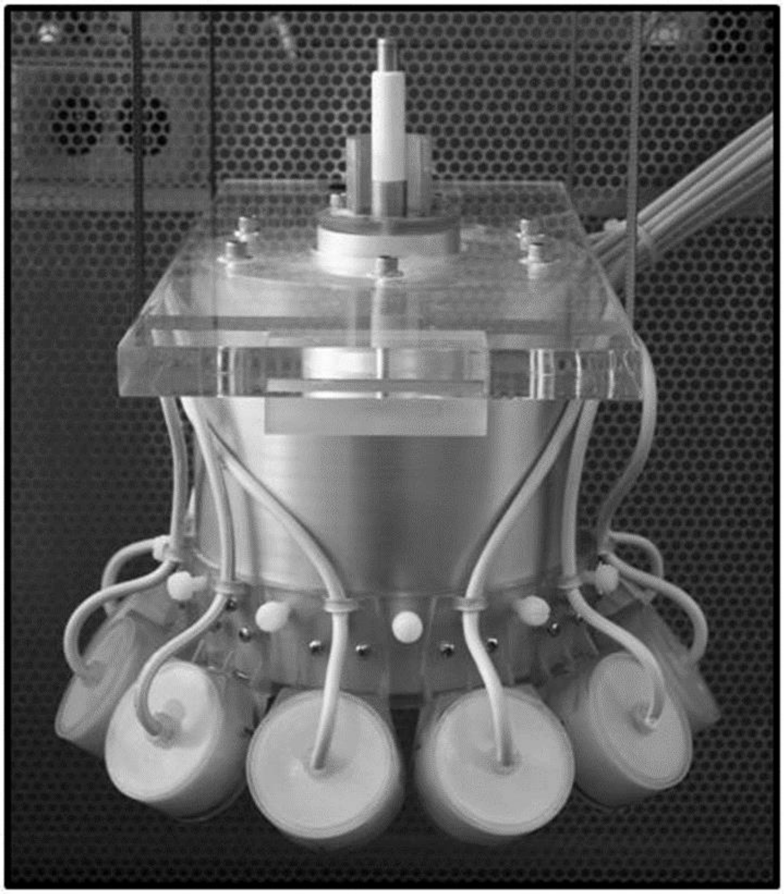

Fig. 3.3 Research system capable of delivering electrohydraulic SWL and histotripsy therapy confocally (driving electronics not pictured). The histotripsy transducer consists of an array of eleven 500 kHz PZT-8 discs sealed in water-tight housing/lens assemblies. Individual housings are geometrically aligned by a scaffold that surrounds the ellipsoidal reflector of the electrohydraulic lithotripter.

Stones were sonicated using a system built in-house that is capable of delivering both electrohydraulic SWL and histotripsy therapy in a confocal manner (Fig. 3.3). The electrohydraulic SWL portion of the system has been described previously [39], and is based on prior research lithotripters designed to simulate the acoustic field generated by the Dornier HM3 [40, 41]. Briefly, a high voltage capacitor charging power supply (TDK-Lambda Americas, Inc., Neptune, NJ) is used to charge an 80 nF high voltage capacitor (General Atomics Energy Products, San Diego, CA), which is subsequently triggered to discharge across an underwater spark electrode via optical input to a solid state switch (Applied Pulsed Power, Inc., Freeville, NY). Consistent with traditional electrohydraulic SWL design, this spark electrode is positioned at one of the foci of an ellipsoidal reflector; upon firing, acoustic energy is focused by the ellipse to the distal focus at which the target sample is positioned. The capacitor charging power supply utilized here is a current drive system that produces a series of voltage ramps, and as such must be coupled to an additional 100 nF high voltage filter capacitor (Maxwell Laboratories, Inc., San Diego, CA) to smooth the output voltage. Finally, a resistor bank composed of fifteen 25 kΩ, 225 W resistors (Vishay Intertechnology, Inc., Shelton, CT) is incorporated at the power supply output for isolation and prevention of internal damage to the supply when the output becomes negative. All SWL treatments were conducted at a shock rate of 1 Hz and charging voltage of 20 kV. This generates an acoustic shock wave having a peak positive pressure (P+) of 34 MPa and a peak negative pressure (P-) of 8 MPa, as calibrated by an optical hydrophone constructed in our lab [42, 43]. Prior to treatment, electrohydraulic SWL electrodes were preconditioned with 200 shocks; each electrode was replaced after the generation of 2,000 shocks.

The histotripsy portion of the system consists of an annular array of 11 PZT-8 disc elements (Channel Industries, Santa Barbara, CA), each measuring 2” in diameter and having a center frequency of 500 kHz. Water-tight housings designed to hold the individual elements were fabricated from Accura-60 plastic using a stereolithography machine. The front face of each housing contains an acoustic lens with a focal length of 15 cm; PZT-8 elements were matched to this lens using a mixture of tungsten powder (74MR-0005, Inframat Advanced Materials, Farmington, CT) and epoxy adhesive (Hysol E-120HP, Loctite Corporation, Rocky Hill, CT). Individual housing/lens assemblies were aligned such that their geometric focus was coincident with that of the lithotripter. This was accomplished using a stereolithography-fabricated scaffold surrounding the lithotripter’s ellipsoidal reflector. In this case, Accura Peak plastic was utilized due to the fact that it has excellent moisture resistance and is therefore less likely to deform under the weight of the housings over time.

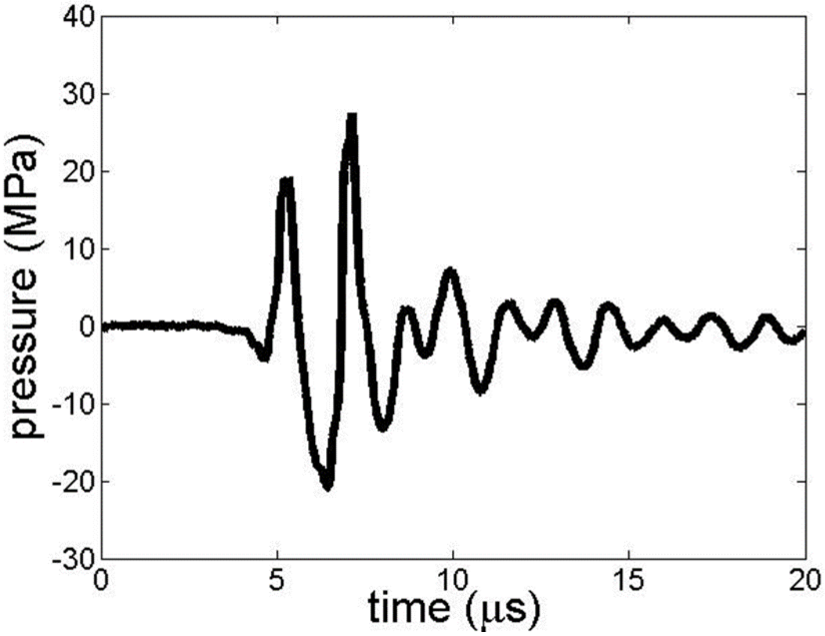

Fig. 3.4 Example histotripsy pressure waveform as recorded by a fiber optic hydrophone. The signal shown has been averaged over 300 pulses and was taken at a sub-therapy driving voltage of 1700 $V_{pk\text{-}pk}$ to prevent cavitation damage to the fiber tip. It can be seen that the histotripsy pulse amplifier produces relatively short pulses, roughly 2 cycles in length.

The histotripsy array was driven using a pulse amplifier developed in our lab. All histotripsy treatments were conducted at a pulse repetition frequency (PRF) of 100 Hz and a power setting such that the peak-peak voltage applied to the PZT-8 elements was roughly 2900 V. This corresponds to a P- of 33 MPa based on calibration with a fiber optic hydrophone developed in-house [44]. An example acoustic output from the system is displayed in Fig. 3.4. This waveform was acquired at a lower peak-peak driving voltage of approximately 1700 V, due to the fact that higher intensities resulted in cavitation damage to the fiber tip after only several pulses and prevented us from obtaining a clean averaged waveform. The P- of 33 MPa at our therapy intensity was determined via linear extrapolation on the basis of the observation that the P- of the waveform increases extremely linearly with driving voltage. The lateral and axial -6-dB beamwidths were measured on the P- and P+ pressure profiles at P-/P+ of 10/11 MPa. It was found that the lateral -6-dB beamwidths for P- and P+ were 2.2 and 2.1 mm, respectively, while the corresponding values in the axial direction were 16.0 and 12.3 mm. Again, an intensity well below that used for stone treatments was utilized for these scans in order to prevent cavitation damage to the hydrophone tip. For comparison, it has been previously reported that the -6-dB beamwidth of the lateral field of an HM3-mimicking research lithotripter is approximately 10 mm, while the -6-dB length of the axial field is approximately 60 mm [41].

Table 3.1 Summary of Treatment Schemes used to Evaluate the Influence of Controlled Cavitation on Shock Wave Lithotripsy Stone Comminution

Treatment Scheme	Description	Shock Wave Total	Histotripsy Pulse Total	Treatment Time (min)
A	Interleaved	600	42,000	10
B	SWL followed by Histotripsy	600	42,000	20
C	Histotripsy followed by SWL	600	42,000	20
D	SWL Only	600	0	10
E	Histotripsy Only	0	42,000	10

Model stones were sonicated with one of five treatment schemes, as summarized in Table 3.1. In scheme **A**, stones were exposed to 10 minutes of SWL (600 LSWs) with 0.7 seconds of histotripsy (70 pulses) interleaved between successive LSWs (totaling to 42,000 pulses). The duration of interleaved histotripsy was selected based on a preliminary investigation to minimize the shielding effects of remnant histotripsy nuclei on subsequent LSWs. Additionally, a delay of

1 ms was imposed between the arrival time of a LSW and the first histotripsy pulse of a burst. This ensured that histotripsy pulses did not arrive prior to the collapse of LSW-induced cavitation bubbles surrounding the stone, as determined by high speed imaging. A representation of this pulse scheme is displayed in the top panel of Fig. 3.5. In scheme **B**, stones received 10 minutes of SWL followed by 10 minutes of histotripsy. Consistent with the interleaved scheme, histotripsy was delivered in 70 pulse bursts (PRF= 100 Hz), with one burst applied per second. The middle and bottom panels of Fig. 3.5 display the timing utilized for SWL and histotripsy, respectively. In scheme **C**, stones were sonicated with 10 minutes of histotripsy followed by 10 minutes of lithotripsy; pulse timing in this case was again consistent with the representations presented in the lower-most panels of Fig. 3.5. Treatment schemes **D** and **E** acted as controls, with stones receiving 10 minutes of SWL only or 10 minutes of histotripsy only, respectively. Ten model stones were treated with each respective scheme.

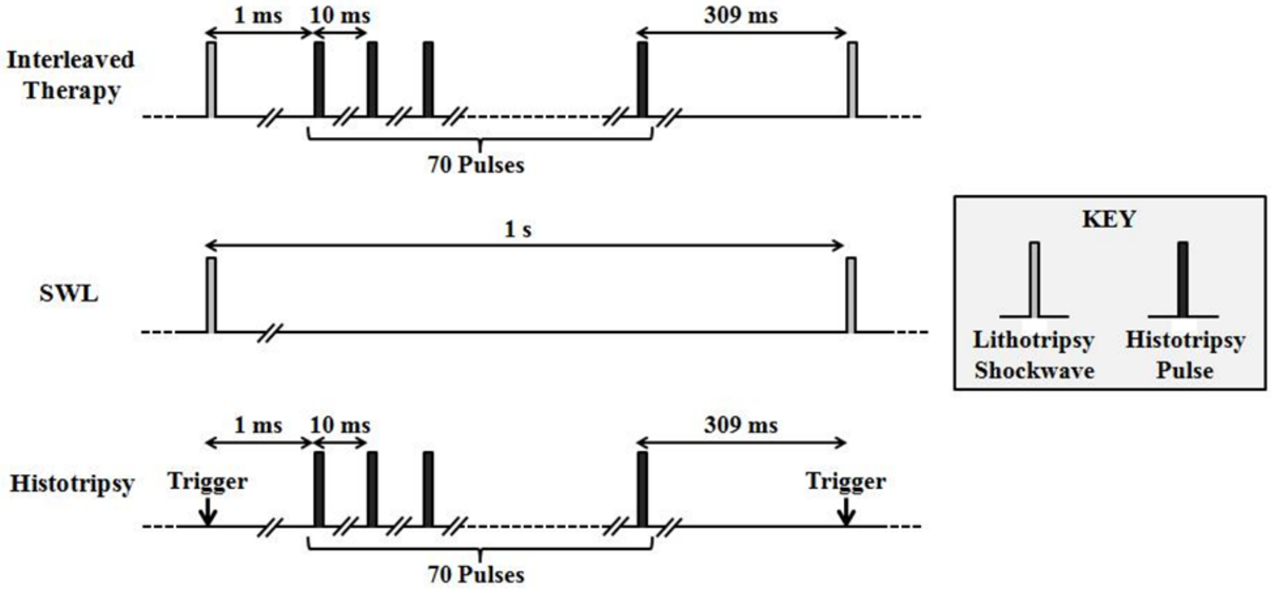

Fig. 3.5 Pulse timing schemes for the interleaved therapy, SWL, and histotripsy. A one-second duration is shown for each. SWL was applied at a shock rate of 1 Hz, while histotripsy was administered in 70 pulse bursts at a PRF of 100 Hz. The five treatment schemes investigated in this study were composed of combinations of these three therapies, as describe in both the text and Table 3.1.

3.2.4 Evaluation of Fragment Size

Following sonication, stone fragments remaining in the treatment channel were collected and sequentially sieved through 8, 6, 4, and 2 mm filters. The hydrated mass of stone debris trapped on each respective filter was measured immediately following sieving, with care taken to gently blot any standing water off the surface of the fragments with tissue paper. The mass of stone debris <2 mm in size was calculated by subtracting the sum of the debris trapped on the filters from the initial mass of the hydrated stone (measured prior to treatment). Quantification of debris size distributions utilized the metric of 'stone mass fraction,' which was calculated as the hydrated mass of debris trapped on a given filter divided by the initial mass of the hydrated stone.

The filter pore sizes utilized in this study were selected based on clinical literature describing the fate of residual stone fragments following SWL treatment. It has been documented that residual fragments >4 mm carry a statistically higher risk for causing complication and becoming clinically significant during follow-up [45]. Contrastingly, those ≤4 mm are expected to pass spontaneously without further treatment and are referred to as clinically insignificant residual fragments (CIRF). It is certainly possible that, in some cases, even these CIRF may be retained and seed recurrent stone growth [46]. For this reason it is preferable to minimize the size of such residual debris; indeed, study has shown that the probability of eliminating residual lithiasis is significantly greater in patients with "dust" in comparison to those with significant residual fragments [47]. With respect to the study detailed in this chapter, it is important to remember that all treatments are truncated and designed for the sole purpose of investigating comminution mechanism rather than achieving a complete clinical outcome. Nevertheless, the author feels it is important that the reader have a basic understanding regarding the clinical perspective of fragment size in order to frame the context of the results.

3.2.5 High Speed Imaging

A potential limitation to interleaving histotripsy pulses between successive LSWs is shielding. It is possible that remnant microbubbles that persist following the collapse of the histotripsy bubble cloud may reduce the efficacy of subsequent shock waves. The interleaved pulse scheme utilized in this study was selected based on a preliminary investigation to minimize these shielding effects; however, it is quite possible that some degree of shielding is still present in comparison to the LSWs in isolation (scheme **D**). To further investigate this phenomenon, high speed images were acquired during schemes **A** and **D** using a Phantom v210 camera (Vision Research, Inc., Wayne, NJ). In each case, a single image with 2-μs exposure time was taken 20-μs following the arrival of the LSW at the stone surface. Backlighting was used to produce a projection of the cavitation activity in the axial-lateral plane of the lithotripter. The extent of bubble excitation induced by LSWs with and without histotripsy pulses interleaved was compared.

3.3 Results

3.3.1 Histotripsy and Shock Wave Lithotripsy in Isolation

The stone fragment size distributions resulting from each respective treatment scheme are displayed in Fig. 3.6. Application of 600 LSWs (scheme **D**) resulted in stone subdivision to a broad range of fragment sizes, with an average of 14.9 ± 24.1% of the original stone mass remaining >8 mm. In contrast, sonication with histotripsy (scheme **E**) only eroded the surface of stones to tiny particulate debris that was small enough to pass through the finest filter used in this study (<2 mm). Following the truncated histotripsy sonication session, an average of 14.9 ± 1.6% of the original stone mass was eroded from the surface, leaving behind a single primary stone piece (>8 mm) with mass 85.1 ± 1.6% of the original.

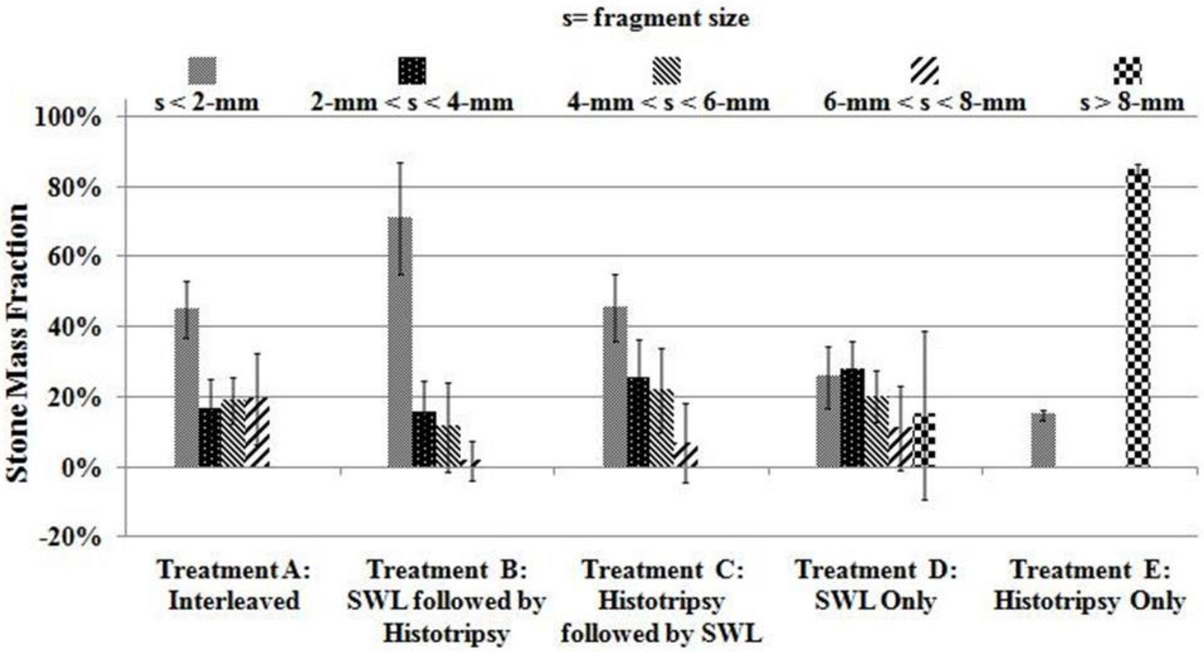

Fig. 3.6 Stone fragment size distributions. Following sonication, stone debris remaining in the treatment channel was sequentially sieved through 8, 6, 4, and 2 mm filters. It was found that SWL alone produced a broad range of fragment sizes, while histotripsy only eroded the stone surface to fine particulate debris (<2 mm). The combination of SWL and histotripsy (**A**, **B**, and **C**) resulted in a shift in the distributions toward smaller fragments and complete elimination of all debris >8 mm.

3.3.2 Histotripsy and Shock Wave Lithotripsy in Combination

The combination of SWL and histotripsy (schemes **A**, **B**, and **C**) resulted in a shift in the size distributions toward smaller fragments and complete elimination of all debris >8 mm. The highest degree of stone comminution was achieved using SWL followed by histotripsy (scheme **B**), in which 71.1 ± 16.0% of the original stone mass was reduced to fragments <2 mm in size. This represents a statistically significant increase in sub-2 mm fragments in comparison to all other treatment schemes (*t-test*, $P < 0.01$). Correspondingly, the mass fraction of fragments falling in the 2-8 mm range showed a statistically significant decrease in comparison to treatment schemes **A**, **C**, and **D** (*t-test*, $P < 0.01$). Visually, during the SWL phase of scheme **B** the stone was subdivided to a range of fragment sizes, consistent with the results of the SWL-only therapy. During the subsequent histotripsy phase no further subdivision of the fragments was observed; rather, their surfaces were eroded to fine particulate debris <2 mm in size. Histotripsy cavitation erosion of these subdivided stones displayed an increase in efficacy relative to histotripsy erosion of whole stones (scheme **E**). This is a result of the subdivided stones having a greater exposed surface area, providing the cavitational bubble cloud with more material over which to erode. Correspondingly, the final treatment outcome in scheme **B** was highly dependent on the degree of stone subdivision achieved during the initial SWL phase.

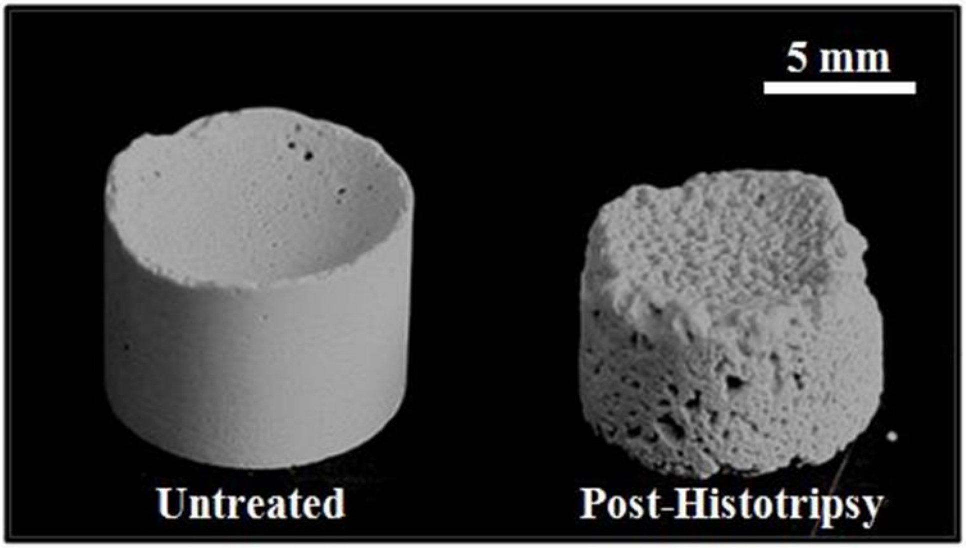

Fig. 3.7 Representative model stones prior to treatment (left) and following sonication with histotripsy (right). Histotripsy cavitation erosion was observed to produce extensive pitting on the surface of the stone.

Histotripsy followed by SWL (scheme **C**) and the interleaved therapy (scheme **A**) also produced an increase in sub-2 mm debris relative to SWL or histotripsy in isolation (*t-test*, $P < 0.01$), with 45.6 ± 9.6% and 44.9 ± 8.1% of the original stone mass passing through the 2 mm filter, respectively. Although these sub-2 mm mass fractions are not statistically different from one another (*t-test*, $P = 0.87$), histotripsy followed by SWL appears to achieve a higher degree of comminution in comparison to the interleaved therapy; examining fragments 6-8 mm in size, histotripsy followed by SWL achieved a reduced mass fraction of 6.8 ± 11.3% in comparison to the 19.3 ± 13.0% of the interleaved scheme. This represents a statistically significant reduction in debris of this size (*t-test*, P = 0.03). Visually, following the histotripsy phase of scheme **C** extensive pitting was induced on the stone surface (Fig. 3.7), and during the subsequent SWL phase the onset of stone subdivision was observed to require a reduced number of LSWs in comparison to SWL-only (scheme **D**). Conversely, during the interleaved therapy the onset of stone subdivision was observed to require a greater number of LSWs relative to SWL-only. This suggests that remnant cavitational nuclei from the histotripsy burst may indeed be acting to shield the stone from subsequent LSWs. Fig. 3.8 displays five representative images captured 20 μs after LSW arrival for the interleaved and SWL-only pulse schemes. A higher degree of LSW-induced bubble excitation is apparent for the interleaved case.

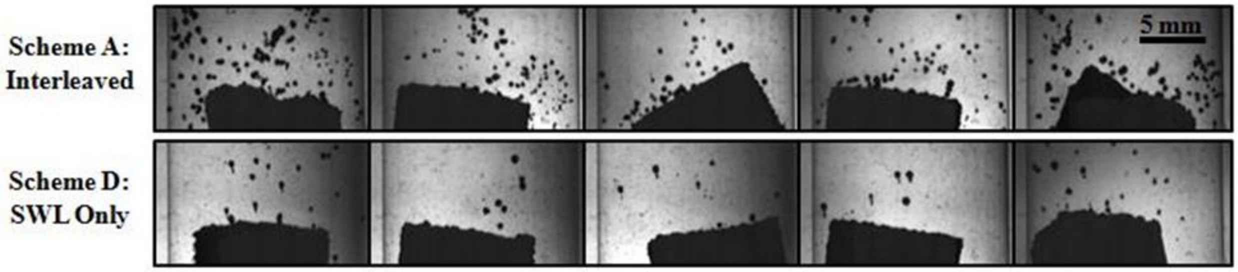

Fig. 3.8 High speed images showing LSW-induced cavitation surrounding the stone. The direction of ultrasound propagation is top-bottom in each image, and the stone was free to move within the treatment channel (as described previously). A single image was captured 20 μs after the arrival of each LSW. The top panel presents five representative images for the interleaved treatment (scheme A), while the bottom panel displays representative images for the SWL only treatment (scheme D). An increase in bubble excitation is observable in the former case.

3.4 Discussion

The importance of cavitation in SWL stone comminution has been documented in numerous studies. Work in which the cavitational component of LSWs was suppressed has resulted in drastically reduced fragmentation [8, 9, 12-15], while actively intensifying the collapse of LSW-induced bubbles has been shown to enhance the comminution process [16]. The physical mechanisms underlying the role of cavitation in SWL remain somewhat weakly defined, however, in part due to the fact that it is difficult to isolate the cavitational component of LSWs. In the work presented in this chapter histotripsy was utilized to temporally and spatially direct the activity of a cavitational bubble cloud, allowing for further exploration of the relationship between cavitation and LSW stone comminution in a way that was not previously possible. Through the application of controlled cavitation at specific time points relative to LSWs, we aimed to further elucidate the role of cavitation in SWL and demonstrate the ability of histotripsy to provide an adjunct to the SWL stone comminution process.

The highest degree of stone comminution in this study was achieved using pulse scheme **B**, in which histotripsy controlled cavitation was applied following SWL (Fig. 3.6). This treatment demonstrates a major point of synergy between SWL stone subdivision and histotripsy cavitation erosion: when a minimal number of LSWs are first used to subdivide a stone into multiple pieces, the efficacy of cavitation erosion is enhanced as a result of an increase in exposed stone surface area. Further adding to this synergistic interaction is the fact that the direct stress (spalling) mechanism of LSW stone subdivision displays an inherent size limitation in the fragments it generates [8, 10]. Zhu, *et al*. found that both model and natural kidney stones immersed in castor oil cannot be fragmented into passable pieces, and it was concluded that while stone subdivision via stress waves is important for the initial fragmentation of a stone, cavitation is essential for the production of fine passable debris [8]. This suggests that SWL stone comminution may be viewed as a two-phase process. During the first phase, the direct stress wave component of LSWs dominates to produce the initial subdivision of a stone. As these fragments are further comminuted to smaller and smaller size, the efficacy of the stress waves attenuates and the cavitational component of the LSW becomes the primary means of fragment reduction. Thus, the application of controlled cavitation at this point in the comminution process should be expected to provide an adjunct to SWL therapy, as was observed in treatment scheme **B**.

Application of histotripsy cavitation erosion prior to SWL (scheme **C**) was also found to increase the degree of stone comminution relative to the control (SWL-only) case (Fig. 3.6). This suggests that sonicating a stone with histotripsy preconditions it for LSW subdivision. As displayed in Fig. 3.7, following the histotripsy phase of the therapy extensive pitting was produced on the stone surface. Such pitting is commonly associated with cavitation damage, and is attributed to localized stress created by the impact of fluid jets or secondary shock waves produced by bubble collapse [16-18, 20-22]. It is likely that these surface defects provide sites for crack initiation and propagation during the subsequent SWL phase of this treatment scheme—a concept that has been suggested previously in SWL literature. Zhu, *et al.* showed that when the cavitational component of LSWs is isolated by positioning stone phantoms off the shock wave axis, the resulting damage is primarily surface erosion that is likely to weaken the surface structure and increase susceptibility to LSWs [8]. Cleveland and van Cauweleart used computed tomography to demonstrate that when model stones are exposed to LSWs, fractures first form at the surface and then grow inward [48]. It has been postulated that following the generation of such crevices, liquid enters the stone material and is cavitated upon the application of subsequent LSWs [11]. Crack propagation is then likely to result as enormous stresses are generated within the fissure [14, 49]. Sapozhnikov, *et al.* found that model stones could only be fractured in a cavitation suppressing medium when they contained an etched band to simulate cavitation damage, suggesting that cavitation-induced surface cracks play an important role in stone subdivision [10]. These studies corroborate the idea that the application of histotripsy cavitation erosion prior to SWL increases the susceptibility of a stone to LSW subdivision.

During the interleaved treatment (scheme **A**), one would expect both the aforementioned phenomena to be at play. In the initial stages, surface defects induced by histotripsy cavitation erosion are likely to facilitate the formation and growth of cracks within the stone matrix. Following primary stone subdivision, the increase in exposed surface area should augment histotripsy therapy and enhance the cavitation erosion process. However, the degree of stone comminution resulting from this interleaved treatment was reduced in comparison to schemes in which histotripsy and SWL were applied in isolation subsequent to one another (**B** and **C**, see Fig. 3.6). Furthermore, it was visually observed that the onset of stone subdivision required a greater number of LSWs during this interleaved scheme in comparison to SWL-only. We hypothesize that this outcome is a result of shielding caused by remnant bubble nuclei that persist following a histotripsy burst. The phenomenon of shielding is well established in SWL, in which a population of prefocal cavitation nuclei generated by a LSW act to attenuate the tensile component of subsequent LSWs and reduce the efficacy of cavitation at the stone surface [27, 28]. This effect can be passively mitigated by increasing the time between successive LSWs, and enhanced stone subdivision with decreasing shock rate has been demonstrated both *in-vitro* [23, 24] and *in-vivo* [25]. Additionally, clinical trials have yielded higher success rates for patients treated with SWL at a rate of 1 Hz in comparison to those at 2 Hz [26].

The interleaved pulse scheme utilized in the work detailed in this chapter was selected based on preliminary investigation to minimize the shielding effects of remnant histotripsy nuclei on subsequent LSWs. However, regardless of the timing, generation of a cavitational bubble cloud between successive LSWs is likely to amplify the extent of shielding to some degree. This can be seen in Fig. 3.8, in which it is apparent that LSW-induced bubble activity increases when LSWs are preceded by a histotripsy burst. The interleaved therapy then becomes an optimization problem in which the added benefit of histotripsy cavitation erosion must be considered against the propensity for remnant cavitation nuclei to induce shielding. As suggested by previous SWL studies, passively increasing the wait-time between a histotripsy burst and subsequent LSW can afford residual nuclei with sufficient time to dissolve and mitigate the extent of shielding. However, we would like to interleave a maximal amount of histotripsy therapy between successive LSWs in order to accentuate the positive effects of cavitation erosion in a minimal amount of time. For this reason, one of the primary aims of the subsequent work presented in this dissertation is the development of a pulse sequence for actively mitigating the bubble shielding effect.

Finally, it should be noted that for the purpose of the study presented in this chapter, histotripsy therapy was used solely to explore the *trends* associated with the interaction between cavitation and LSW stone comminution. The histotripsy parameters utilized in this study were selected following a coarse preliminary investigation, and a full parametric optimization remains for future work.

3.5 Conclusion

In this chapter, histotripsy ultrasound therapy was used to explore the role of cavitation in the SWL stone comminution process. When applied prior to SWL, histotripsy cavitation erosion produced extensive pitting on the stone surface. It is likely that this damage acts to precondition stones for LSW subdivision by providing sites from which cracks can nucleate. The application of histotripsy cavitation erosion following SWL resulted in the greatest degree of stone comminution. This treatment scheme takes advantage of a major point of synergy between LSW stone subdivision and cavitation erosion: whereas the direct stress wave (spalling) component of LSWs has an intrinsic size limitation to the fragments it can produce, the efficacy of cavitation erosion increases as a stone is comminuted and has a greater exposed surface area. When histotripsy pulses are interleaved between successive LSWs, one would expect both the aforementioned effects to contribute to stone comminution. At the onset of treatment, histotripsy-induced pitting on the stone surface should accelerate LSW fragmentation; following primary stone subdivision, the increase in exposed surface area should enhance the cavitation erosion process. However, the degree of stone comminution produced by the interleaved treatment was reduced in comparison to applying SWL and histotripsy separately and subsequent to one another. It is likely that this is a result of shielding induced by remnant histotripsy bubble nuclei, and bubble-removing pulse sequences designed to mitigate this effect will be the subject of subsequent chapters of this dissertation. Nevertheless, the work in this chapter confirms that cavitation plays a critical role in kidney stone comminution, and demonstrates the fact that application of controlled cavitation at strategic points in the fragmentation process can provide an adjunct to SWL therapy.

3.6 References

[1] A. P. Duryea, W. W. Roberts, C. A. Cain, and T. L. Hall, "Controlled cavitation to augment SWL stone comminution: mechanistic insights in vitro," IEEE Trans Ultrason Ferroelectr Freq Control, vol. 60, pp. 301-9, Feb 2013.

[2] C. Chaussy, E. Schmiedt, D. Jocham, V. Walther, W. Brendel, B. Forssmann and W. Hepp, "Extracorporeal shock wave lithotripsy: New aspects in the treatment of kidney stone disease.," *Basel: Karger*, 1982.

[3] S. R. Khan, R. L. Hackett and B. Finlayson, "Morphology of urinary stone particles resulting from ESWL Treatment," *J Urol*, vol. 136, pp. 1367-1372, 1986.

[4] J. P. Whelan and B. Finlayson, "An experimental model for the systematic investigation of stone fracture by extracorporeal shock wave lithotripsy," *J. Urol*, vol. 140, pp. 395-400, 1988.

[5] S. M. Gracewski, G. Dahake, Z. Ding, S. J. Burns and E. C. Everbach, "Internal stress wave measurements in solids subjected to lithotripster pulses," *J Acoust Soc Am*, vol. 94, pp. 652-661, 1993.

[6] X. F. Xi and P. Zhong, "Dynamic photoelastic study of the transient stress field in solids during shock wave lithotripsy," *J Acoust Soc Am*, vol. 109, pp. 1226-1239, 2001.

[7] W. Eisenmenger, "The mechanisms of stone fragmentation in ESWL," *Ultrasound Med Biol*, vol. 27, pp. 683-693, 2001.

[8] S. Zhu, F. H. Cocks, G. M. Preminger and P. Zhong, "The role of stress waves and cavitation in stone comminution in shock wave lithotripsy," *Ultrasound in Med. & Biol.*, vol. 28, no. 5, pp. 661-671, 2002.

[9] M. Delius, G. Heine and W. Brendel, "A mechanism of gallstone destruction by extracorporeal shock waves," *Naturwiss*, vol. 75, pp. 200-201, 1988.

[10] O. A. Sapozhnikov, A. D. Maxwell, B. MacConaghy and M. R. Bailey, "A mechanistic analysis of stone fracture in lithotripsy," *J Acoust Soc Am*, vol. 121, no. 2, pp. 1190-1202, 2007.

[11] W. Sass, M. Braunlich, H. Dreyer and E. Matura, "The mechanisms of stone disintegration by shock waves," *Ultrasound Med Biol*, vol. 17, no. 3, pp. 239-243, 1991.

[12] M. R. Bailey, "Control of acoustic cavitation with application to lithotripsy," Technical Report No. ARL-TR-97-1, Applied Research Laboratories, The University of Texas at Austin, Austin, TX, pp.1-210, 1997.

[13] N. Vakil and E. C. Everbach, "Transient acoustic cavitation in gallstone fragmentation: A study of gallstones fragmented in vivo," *Ultrasound Med Biol*, vol. 19, pp. 331-342, 1993.

[14] M. Delius, "Minimal static excess pressure minimises the effect of extracorporeal shock waves on cells and reduces it on gallstones," *Ultrasound Med Biol*, vol. 23, pp. 611-617, 1997.

[15] M. R. Bailey, R. O. Cleveland, T. Colonius, L. A. Crum, A. P. Evan, J. E. Lingeman, J. A. McAteer, O. A. Sapozhnikov and J. C. Williams, "Cavitation in shock wave lithotripsy: the critical role of bubble activity in stone breakage and kidney trauma," *in 2003 IEEE Ultrasonics Symposium*, 2003.

[16] X. F. Xi and P. Zhong, "Improvement of stone fragmentation during shock wave lithotripsy using a combined EH/PEAA shock wave generator- In vitro experiments," *Ultrasound Med Biol*, vol. 6, pp. 457-467, 2000.

[17] A. J. Coleman, J. E. Saunders, L. A. Crum and M. Dyson, "Acoustic cavitation generated by an extracorporeal shockwave lithotripter," *Ultrasound Med Biol*, vol. 13, pp. 69-76, 1987.

[18] L. A. Crum, "Cavitation microjets as a contributory mechanism for renal calculi disintegration in ESWL," *J Urol*, vol. 140, pp. 1587-1590, 1988.

[19] P. Zhong and C. J. Chuong, "Propagation of shock waves in elastic solids caused by the impact of cavitation microjets: Part I. Theoretical formulation," *J Acoust Soc Am*, vol. 94, pp. 19-28, 1993.

[20] P. Zhong, C. J. Chuong and G. M. Preminger, "Propagation of shock waves in elastic solids caused by the impact of cavitation microjets: Part II. Application to extracorporeal shock wave lithotripsy," *J Acoust Soc Am*, vol. 94, pp. 29-36, 1993.

[21] K. Rink, G. Delacretaz, G. Pittomvils, R. Boving and J. P. Lafaut, "Incidence of cavitation in the fragmentation process of extracorporeal shock wave lithotripters," *Appl Phys Lett*, vol. 64, no. 19, pp. 2596-2598, 1994.

[22] A. Philipp and W. Lauterborn, "Cavitation erosion by single laser-produced bubbles," *J Fluid Mech*, vol. 361, pp. 75-116, 1998.

[23] M. J. Weir, N. Tariq and R. J. Honey, "Shockwave frequency affects fragmentation in a kidney stone model," *J Endourol*, vol. 14, pp. 547-550, 2000.

[24] A. Greenstein and H. Matzkin, "Does the rate of extracorporeal shock wave delivery affect stone fragmentation?," *Urology*, vol. 54, pp. 430-432, 1999.

[25] R. F. Paterson, D. A. Lifshitz, J. E. Lingeman, A. P. Evan, B. A. Connors, N. S. Fineberg, J. C. Williams Jr. and J. A. McAteer, "Stone fragmentation during shock wave lithotripsy is improved by slowing the shock wave rate: Studies with a new animal model," *J Urol*, vol. 168, pp. 2211-2215, 2002.

[26] M. J. Semins, B. J. Trock and B. R. Matlaga, "The effect of shock wave rate on the outcome of shock wave lithotripsy: A meta-analysis," *J Urol*, vol. 179, pp. 194-197, 2008.

[27] Y. A. Pishchalnikov, J. A. McAteer, J. C. Williams Jr., I. V. Pishchalnikova and R. J. Vonderhaar, "Why stones break better at slow shockwave rates than at fast rates: In vitro study with a research electrohydraulic lithotripter," *J Endourol*, vol. 20, pp. 537-541, 2006.

[28] Y. A. Pishchalnikov, J. A. McAteer and J. C. Williams Jr., "Effect of firing rate on the performance of shock wave lithotriptors," *BJU Int*, vol. 102, pp. 1681-1686, 2008.

[29] Y. Zhou, F. H. Cocks, G. M. Preminger and P. Zhong, "The effect of treatment strategy on stone comminution efficiency in shock wave lithotripsy," *J Urol*, vol. 172, pp. 349-354, 2004.

[30] D. Z. Yong, M. E. Lipkin, W. N. Simmons, G. Sankin, D. M. Albala, P. Zhong and G. M. Preminger, "Optimization of treatment strategy used during shockwave lithotripsy to maximize stone fragmentation efficiency," *J Endo*, vol. 25, no. 9, pp. 1507-1511, 2011.

[31] J. E. Parsons, C. A. Cain, G. D. Abrams and J. B. Fowlkes, "Pulsed cavitational ultrasound therapy for controlled tissue homogenization," *Ultrasound Med Biol*, vol. 32, no. 1, pp. 115-129, 2006.

[32] Z. Xu, A. Ludomirsky, L. Y. Eun, T. L. Hall, B. C. Tran, J. B. Fowlkes and C. A. Cain, "Controlled ultrasound tissue erosion," *IEEE Trans Ultrason Ferroelectr Freq Control*, vol. 51, no. 6, pp. 726-736, 2004.

[33] Z. Xu, J. B. Fowlkes, E. D. Rothman, A. M. Levin and C. A. Cain, "Controlled ultrasound tissue erosion: The role of dynamic interaction between insonation and microbubble activity," *J Acoust Soc Am*, vol. 117, no. 1, pp. 424-435, 2005.

[34] Z. Xu, J. B. Fowlkes and C. A. Cain, "Effects of acoustic parameters on bubble cloud dynamics in ultrasound tissue erosion (histotripsy)," *J Acoust Soc Am*, vol. 122, no. 1, pp. 229-236, 2007.

[35] A. P. Duryea, A. D. Maxwell, W. W. Roberts, Z. Xu, T. L. Hall and C. A. Cain, "In-vitro comminution of model renal calculi using histotirpsy," *IEEE Trans Ultrason Ferroelectr Freq Control*, vol. 58, no. 5, pp. 971-980, 2011.

[36] A. P. Duryea, T. L. Hall, A. D. Maxwell, Z. Xu, C. A. Cain and W. W. Roberts, "Histotirpsy erosion of model urinary calculi," *J Endo*, vol. 25, no. 2, pp. 341-344, 2011.

[37] W. N. Simmons, F. H. Cocks, P. Zhong and G. Preminger, "A composite kidney stone phantom with mechanical properties controllable over the range of human kidney stones," *J Mech Behav Biomed Mater*, vol. 3, pp. 130-133, 2010.

[38] E. A. Gardner, J. B. Fowlkes, P. L. Carson, J. A. Ivey and D. A. Ohl, "Bubble generation in excised canine urinary bladders using an electrohydraulic lithotripter," *in IEEE Ultrasonics Symp.*, 1993.

[39] A. P. Duryea, W. W. Roberts, C. A. Cain and T. L. Hall, "Optically triggered solid state driver for shock wave therapy," *in 2011 International Society for Therapeutic Ultrasound Symposium*, New York, 2012.

[40] A. J. Coleman, J. E. Saunders and M. J. Choi, "An experimental shock wave generator for lithotripsy studies," *Phys Med Biol*, vol. 34, no. 11, pp. 1733-1742, 1989.

[41] R. O. Cleveland, M. R. Bailey, N. Fineberg, B. Hartenbaum, M. Lokhandwalla, J. A. McAteer and B. Sturtevant, "Design and characterization of a research electrohydraulic lithotripter patterned after the Dornier HM3," *Rev Sci Instrum*, vol. 71, no. 6, pp. 2514-2525, 2000.

[42] G. Paltauf and H. Schmidt-Kloiber, "Measurement of laser-induced acoustic waves with a calibrated optical transducer," *J Appl Phys*, vol. 82, no. 4, pp. 1525-1531, 1997.

[43] B. Granz, R. Nanke, J. Fehre, P. Thorsten and R. Engelbrecht, "Light spot hydrophone, innovation in lithotripsy," *Medical Solutions*, pp. 86-87, 2004.

[44] J. E. Parsons, C. A. Cain and J. B. Fowlkes, "Cost-effective assembly of a basic fiber-optic hydrophone for measurment of high-amplitude therapeutic ultrasound fields," *J Acoust Soc Am*, vol. 119, no. 3, pp. 1432-1440, 2006.

[45] A. R. El-Nahas, A. M. El-Assmy, K. Madbouly and K. Z. Sheir, "Predictors of clinical signifcance of residual fragments after extracorporeal shockwave lithotripsy for renal stones," *J Endourol*, vol. 20, no. 11, pp. 870-874, 2006.

[46] M. M. Osman, Y. Alfano, S. Kamp, A. Haecker, P. Alken, M. S. Michel and T. Knoll, "5-year-follow-up of patients with clinically insignificant residual fragments after extracorporeal shockwave lithotripsy," *Eur Urol*, vol. 47, no. 6, pp. 860-864, 2005.

[47] G. Zanetti, M. Seveso, E. Montanari, A. Guarneri, A. Del Nero, R. Nespoli and A. Trinchieri, "Renal stone fragments following shock wave lithotripsy," *J Urol*, vol. 158, pp. 352-355, 1997.

[48] R. O. Cleveland and J. van Cauweleart, "Fragmentation mechanisms of kidney stones in shock wave lithotripsy can be detected with microCT X-ray imaging," *in Proceedings of the Joint German Convention on Acoustics and Congres Francais d'Acoustique (CFA)*, Strasbourg, France, 2004.

[49] J. E. Field, "The physics of liquid impact, shock wave interactions with cavities, and the implications to shock wave lithotripsy," *Phys Med Biol*, vol. 36, pp. 1475-1484, 1991.

Chapter 4

Active Removal of Residual Nuclei Following a Cavitation Event

A majority component of this chapter has been published in *IEEE Transactions on Ultrasonics, Ferroelectrics, and Frequency Control*.

4.1 Introduction

The implications of remnant cavitation bubbles in ultrasound therapy were introduced in Chapter 1. To reiterate, collapse of the primary cavitation bubbles generated by a high intensity acoustic pulse can produce an extensive population of residual bubble nuclei [2-10]. A single primary bubble can give rise to dozens of residual daughters, as its collapse is typically accompanied by fission into numerous remnant fragments [2, 5, 8, 9]. The resulting daughter bubbles are microscopic in size (<10 μm) [11, 12] and can persist for tens of milliseconds [7, 13] or even full seconds [4, 8, 9, 14], depending on the conditions under which they were generated. If additional acoustic pulses are applied prior to the dissolution of these residual bubbles, they can serve as nuclei to seed subsequent cavitation activity [2-4, 6, 7]. As such, residual bubble nuclei impart a cavitation memory to their host medium, influencing the threshold, extent, and distribution of ensuing cavitation events [10, 15-19].

Residual bubble nuclei that persist from one pulse to the next can limit the efficiency of cavitation-based ultrasound therapies. In shock wave lithotripsy (SWL) the efficacy of stone comminution is highly dependent on the rate of shock wave (SW) delivery, with testing both *in-vitro* [17, 20-23] and *in-vivo* [24] demonstrating a decrease in per-shock fragmentation efficiency with increasing shock rate. This is a result of extensive cavitation generated along the SW propagation path, the collapse of which produces a large population of residual nuclei [8, 9]. When a SW propagates through a medium containing these residual bubbles, the tensile component of the waveform causes them to expand—a process that selectively attenuates the SW's negative tail and reduces the energy that ultimately reaches the stone [11, 17, 19, 25]. At high shock rates residual nuclei have less time to passively dissolve between successive SWs, leading to more severe attenuation of the negative phase and compromised comminution efficacy. An analogous effect was observed in Chapter 3 of this dissertation, in which interleaving histotripsy pulses between successive SWs was found to seed increased prefocal cavitation and limit the per-shock fragmentation efficiency. Furthermore, in Chapter 2 the per-pulse efficiency of histotripsy model stone erosion was hypothesized to suffer as a result of the ill-effects of remnant bubble nuclei.

Rate-dependent efficiency has also been observed in histotripsy fractionation of soft tissue [10]. In this case it is cavitation memory—i.e., the repetitive initiation of cavitation at a discrete set of sites within the focal zone—that is the primary source of less efficient lesion formation at high pulse repetition frequencies [10]. Residual nuclei that persist between histotripsy pulses can seed this cavitation memory effect, resulting in inhomogeneous tissue fractionation and requiring an excess number of pulses to achieve complete homogenization of the targeted volume. It has been demonstrated that by increasing the time between successive histotripsy pulses such that remnant nuclei can more completely dissolve, cavitation bubbles are generated at a more randomized set of sites within the focal zone and complete homogenization is achieved using fewer pulses [10].

The ability to manipulate residual bubble nuclei following primary cavitation collapse would be of great benefit to ultrasound therapies such as SWL and histotripsy. In the present chapter a strategy for the active removal of these residual bubbles is explored, using low amplitude ultrasound bursts to stimulate nuclei coalescence. It has been well documented that when microscopic bubbles are exposed to a sound field, forces develop that can promote either their aggregation or dispersion [29-35]. These, collectively referred to as the Bjerknes forces, offer a means of manipulating the population of residual bubble nuclei following cavitation collapse. Here we investigate acoustic sequences that permit the Bjerknes forces to act in concert to stimulate the aggregation and subsequent coalescence of cavitation nuclei—effectively removing them from the field.

4.2 Methods

4.2.1 Experimental Setup

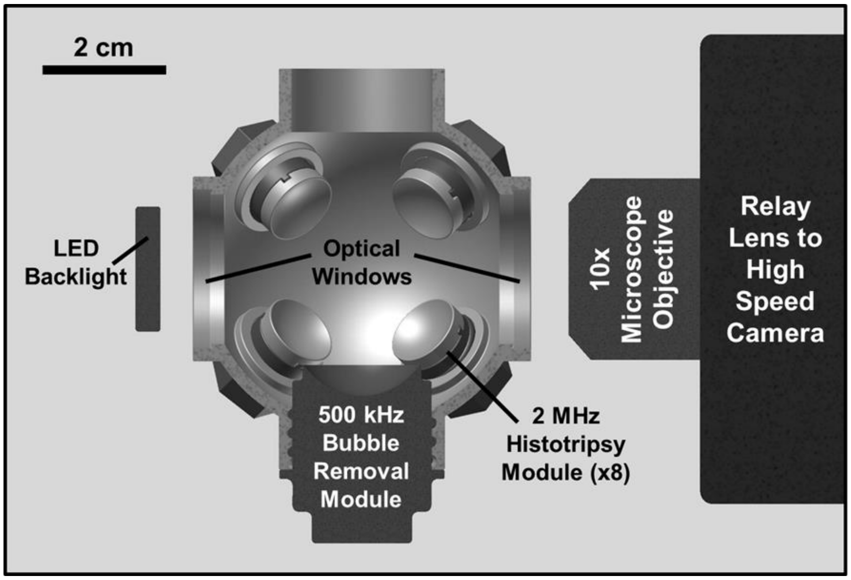

Fig. 4.1 Half-section view of the experimental setup used to study effects of low-amplitude acoustic bursts on residual cavitation bubble nuclei. Primary cavitation was initiated by an array of eight 2 MHz histotripsy modules arranged in a spherical pattern, while bubble removal pulses were delivered from a separate 500 kHz module aligned confocally. All transducer modules were held within an Accura 60 plastic scaffold that also served as the water tank for the experiments. Optical windows in the front and rear of the scaffold allowed for the use of backlit high speed photography to monitor the bubble removal process.

The experimental setup used to study the effect of low-amplitude acoustic bursts on residual bubble nuclei is displayed in Fig. 4.1. All experiments were conducted in deionized water degased to physiologically relevant levels (dissolved oxygen content of 7.3 ± 0.6 mg/L at 20.3 ± 3.5 ˚C (mean ± SD), corresponding to 79 ± 1% of saturation); this mimics the dissolved gas content of human urine, for example [33-35]. Each experiment was monitored using a Photron Fastcam SA1.1 high speed camera (Photron USA Inc., San Diego, CA) at a frame rate of 20 kfps and exposure time of 49 µs. A 10X super-long working distance microscope objective (T Plan SLWD 10X/0.20, Nikon Instruments Inc., Tokyo, Japan) coupled to a 70 mm macro lens (Sigma 70 mm 1:2:8 DG Macro, Sigma Corporation of America, Ronkonkoma, NY) provided the optical power to resolve the microscopic residual nuclei of interest in this study. The theoretical resolution limit of this optical setup is 1.3 µm, while the theoretical depth of field is 18.3 µm. A large area, high power LED light source (BXRA-50C9000, Bridgelux Inc., Livermore, CA) was used to backlight the experiments such that bubbles generated in the field were visible as dark shadows on the optical images.

A 2 MHz histotripsy transducer constructed in-house was used to initiate primary cavitation activity (a cavitational bubble cloud). It consisted of eight PZT-4 disc elements (Steiner & Martins Inc., Miami, FL), measuring 10 mm in diameter and 1 mm in thickness. Water-tight modules designed to hold individual elements were fabricated from Accura 60 plastic (3D Systems Inc., Rock Hill, SC) using a stereolithography machine. The front face of each module contained an Accura 60 acoustic lens with a focal length of 20 mm; PZT-4 elements were matched to this lens using an epoxy (1C-LV Hysol, Loctite Corporation, Rocky Hill, CT) filled 100 mesh copper screen (McMaster-Carr, Aurora, OH) to achieve the proper thickness and impedance. The eight individual histotripsy modules were aligned confocally in a spherical arrangement using a plastic scaffold, also fabricated via stereolithography from Accura 60. This scaffold doubled as the water tank for the experiments, and had optical windows in the front and rear to permit the use of backlit high speed photography. The spherical geometry of this transducer produced a highly confined focal zone, with the -6-dB beamwidths measuring approximately 500 µm in both the lateral and axial dimensions. These measurements were conducted at a pressure amplitude of 6 MPa (linear regime) using a fiber optic hydrophone with a 100 µm diameter sensing tip [36]. The histotripsy transducer was driven using a pulse amplifier developed in our lab, which was designed to produce very short intense bursts. More details regarding the acoustic output generated by this setup are provided in the subsequent section.

A separate 500 kHz transducer—which we denote as the bubble removal module—was used to sonicate residual cavitation nuclei produced by collapse of the histotripsy bubble cloud. Similar to the histotripsy modules, this transducer was constructed in-house using a stereolithography-fabricated Accura 60 housing and acoustic lens, in this case having a focal length of 25 mm. Two 1 MHz Pz36 disc elements (Ferroperm Piezoceramics A/S, Kvistgaard, Denmark) measuring 20 mm in diameter and 1.6 mm in thickness were stacked and driven in unison to produce a 500 kHz equivalent source. The front face of this Pz36 stack was mated directly to the Accura 60 acoustic lens using epoxy adhesive (Hysol E-120 HP, Loctite Corporation, Rocky Hill, CT); a copper screen matching layer was not utilized in this case due to the low acoustic impedance of Pz36 (specified at 14 MRayl by the manufacturer). The bubble removal module was held within the same spherical scaffold used to position the histotripsy modules and aligned coincident with their geometric focus (Fig. 4.1). It produced an acoustic field with -6-dB beamwidths measuring 4.3 mm in the lateral dimension and exceeding 20 mm in the axial; as such, the bubble removal field was much broader than the 500 µm wide focal zone of the histotripsy transducer, encompassing the full extent of histotripsy-induced cavitation bubbles. These field scans were performed at a pressure amplitude of 500 kPa (linear regime) using an HNR-0500 needle hydrophone (Onda Corporation, Sunnyvale, CA). The bubble removal module was driven using a 500 kHz sinusoid from an ENI AP400B controllable power amplifier (Electronic Navigation Industries Inc., Rochester, NY); further details on the acoustic output are presented in the subsequent section.

4.2.2 Acoustic Pulse Sequence

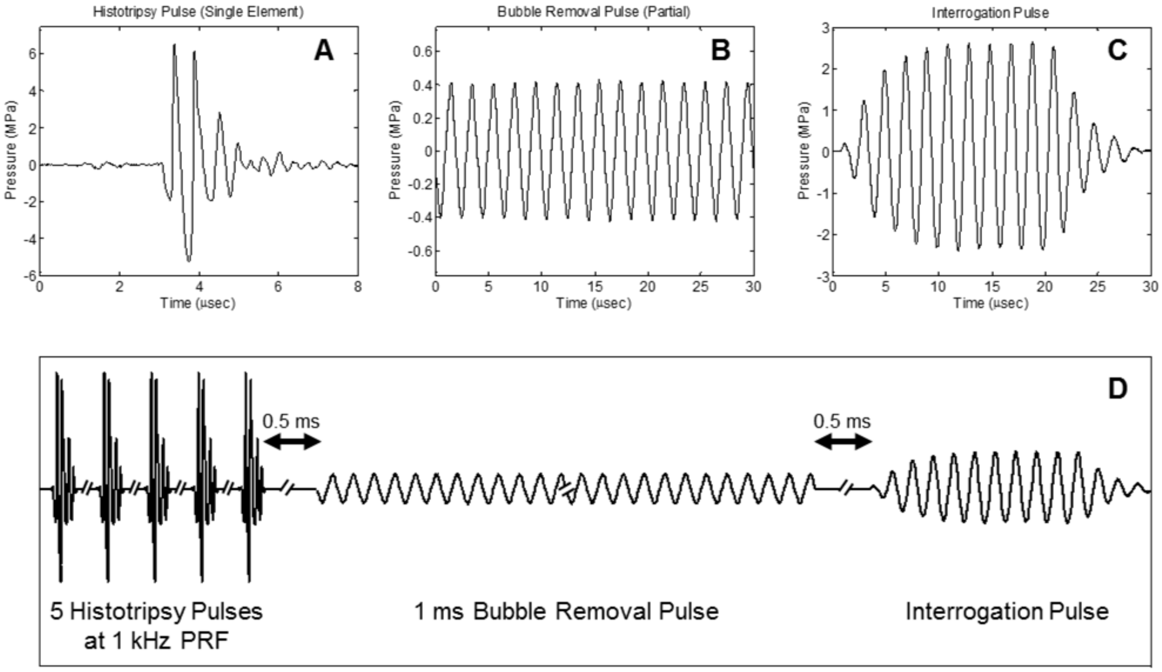

Fig. 4.2 General pulse scheme used to study the effect of low-amplitude acoustic bursts on residual cavitation bubble nuclei. (**A**) Representative waveform acquired from a single 2 MHz histotripsy module; the histotripsy pulse amplitude at the focal location can be estimated as the linear sum of the waveforms from all eight histotripsy modules, suggesting a focal peak negative pressure of approximately 40 MPa. (**B**) Partial segment of the 1 ms bubble removal pulse; all bubble removal pulses had a center frequency of 500 kHz, while the amplitude was varied from 0 to 1.7 MPa. (**C**) Interrogation pulse used to expand residual bubble nuclei remaining in the field; all interrogation pulses were generated by the 500 kHz bubble removal module, had duration of 10 cycles, and amplitude of 2.5 MPa. (**D**) Overall timing of experimental pulse scheme. Further details can be found in the text.

Three general types of acoustic pulses were utilized in this study, as represented in Fig. 4.2(A-C): (1) Histotripsy pulses generated by the 2 MHz histotripsy transducer were used to initiate cavitation activity in the form of a cavitational bubble cloud; (2) Bubble removal pulses produced by the 500 kHz bubble removal module were used to sonicate residual bubble nuclei following primary cavitation collapse, stimulating their coalescence and de facto removal from the field; (3) An interrogation pulse, also delivered from the 500 kHz bubble removal module, was used to probe the field for the presence of residual nuclei following bubble removal. This pulse caused remaining microscopic nuclei to expand and be more easily detected via high speed imaging. The overall timing of this pulse scheme is summarized in Fig. 4.2(D), with specifics provided henceforth.

The initiation of primary cavitation activity in this study was achieved using a train of five histotripsy pulses delivered at a pulse repetition frequency (PRF) of 1 kHz. Histotripsy pulses were very short (approximately 2 µs) and intense. The acoustic output from a single histotripsy module is displayed in Fig. 4.2(A), measured using the same fiber optic hydrophone used to perform histotripsy field scans. Due to the sparse and spherical distribution of the modules that compose the histotripsy transducer, there is minimal superposition of individual waveforms until they reach the geometric focal location; as such, we estimate the output of the histotripsy transducer as the linear sum of the outputs from the eight individual modules [37]—suggesting a peak negative pressure of approximately 40 MPa. This overall output exceeds the intrinsic cavitation threshold in water [37], permitting the histotripsy transducer to initiate a cavitational bubble cloud with each pulse. A train of five histotripsy pulses in rapid succession was utilized to maximize the extent of cavitation. Similar to the bubble proliferation phenomenon observed in SWL [8, 9], this arrangement of histotripsy pulses was empirically determined to enhance cavitation activity as residual daughter bubbles persisting between pulses seeded additional sites for cavitation inception.

Following collapse of the final histotripsy-induced bubble cloud, residual cavitation nuclei were sonicated with a 1 ms long bubble removal pulse to stimulate their removal from the field via bubble coalescence. A partial segment of a representative bubble removal pulse is displayed in Fig. 4.2(B), acquired using the same HNR-0500 needle hydrophone used to perform bubble removal module field scans. All bubble removal pulses had a center frequency of 500 kHz and were applied at a delay of 500 µs following the final histotripsy pulse; the later allowed the histotripsy bubble cloud to collapse and produce residual nuclei in an unimpeded manner. To investigate the influence of acoustic pulse amplitude on the bubble removal process, bubble removal pulse amplitudes of 0, 80, 150, 180, 230, 310, 400, 570, 750, 1100, and 1700 kPa were tested. As the bubble removal pulses were observed to have some amplitude variation across their 1 ms duration (~10%), these reported values represent the mean amplitude over all 500 cycles of the pulse. It should be noted that the bubble removal pulse parameters utilized in the study presented in this chapter have not yet been optimized, and were selected following a very coarse parametric investigation. As such, these pulses are intended solely for introducing the concept of removing residual nuclei following a cavitation event. Chapter 5 of this dissertation will extend this work and investigate the effect of sonication frequency on the bubble removal process.

The presence of residual nuclei remaining in the field following the bubble removal pulse was probed for using a second, much shorter, pulse from the 500 kHz bubble removal module, which we denote as the interrogation pulse. In a separate set of experiments detailed in Chapter 5, the individual residual bubble nuclei produced by the 2 MHz histotripsy transducer were observed to fall in a tight size distribution with a mean diameter of approximately 6 µm. Although this is larger than the 1.3 µm theoretical resolution limit of our optical setup, these individual microscopic residual nuclei may fall out of the depth of field imaging plane (estimated at 18 µm) and therefore be difficult to detect and quantify. For this reason, the interrogation pulse was used to expand any bubble nuclei remaining in the field such that they could be more easily detected via high speed imaging. Fig. 4.2(C) displays the interrogation pulse waveform used for all experiments in this chapter, as calibrated by the HNR-0500 needle hydrophone. In all cases, a 10 cycle pulse with amplitude of 2.5 MPa was used to interrogate the field at 500 μs following the completion of the bubble removal pulse. This interrogation pulse was found not to initiate any cavitation bubbles independently (i.e., when not preceded by the generation of a population of cavitation bubble nuclei).

4.2.3 Quantification of Bubble Removal Pulse Efficacy

To quantify the efficacy of bubble removal, the backlit area of shadow of remnant nuclei expanded by the interrogation pulse was calculated. The entire duration of each pulse sequence was imaged using high speed photography at 20 kfps, and it was empirically determined that the 120th frame in the image sequence corresponded to the time point of maximal bubble expansion induced by the interrogation pulse. The backlit area of bubble shadow in this frame was calculated for all experiments using Matlab (MathWorks Inc., Natick, MA) to sum the pixels that resided below a threshold value. Ten trials were performed at each bubble removal pulse amplitude tested.

4.3 Results

Representative image sequences showing the activity of residual bubble nuclei over the course of the bubble removal and interrogation pulses are displayed for select cases in Fig. 4.3, while the backlit area of shadow from bubbles expanded by the interrogation pulse is quantified for all cases in Fig. 4.4. Collapse of the final histotripsy bubble cloud was observed to produce an extensive set of microscopic residual bubble nuclei. In the control case (bubble removal pulse amplitude set to 0) these residual bubbles persisted over the entirety of the 1 ms bubble removal pulse duration, gradually dispersing with time (Fig. 4.3, row 1). Applying the interrogation pulse to this bubble population facilitated its visualization with the high speed camera (Fig. 4.3, row 1, column 7); the average interrogated bubble shadow area resulting from the ten control trials was used to normalize all values presented in Fig. 4.4.

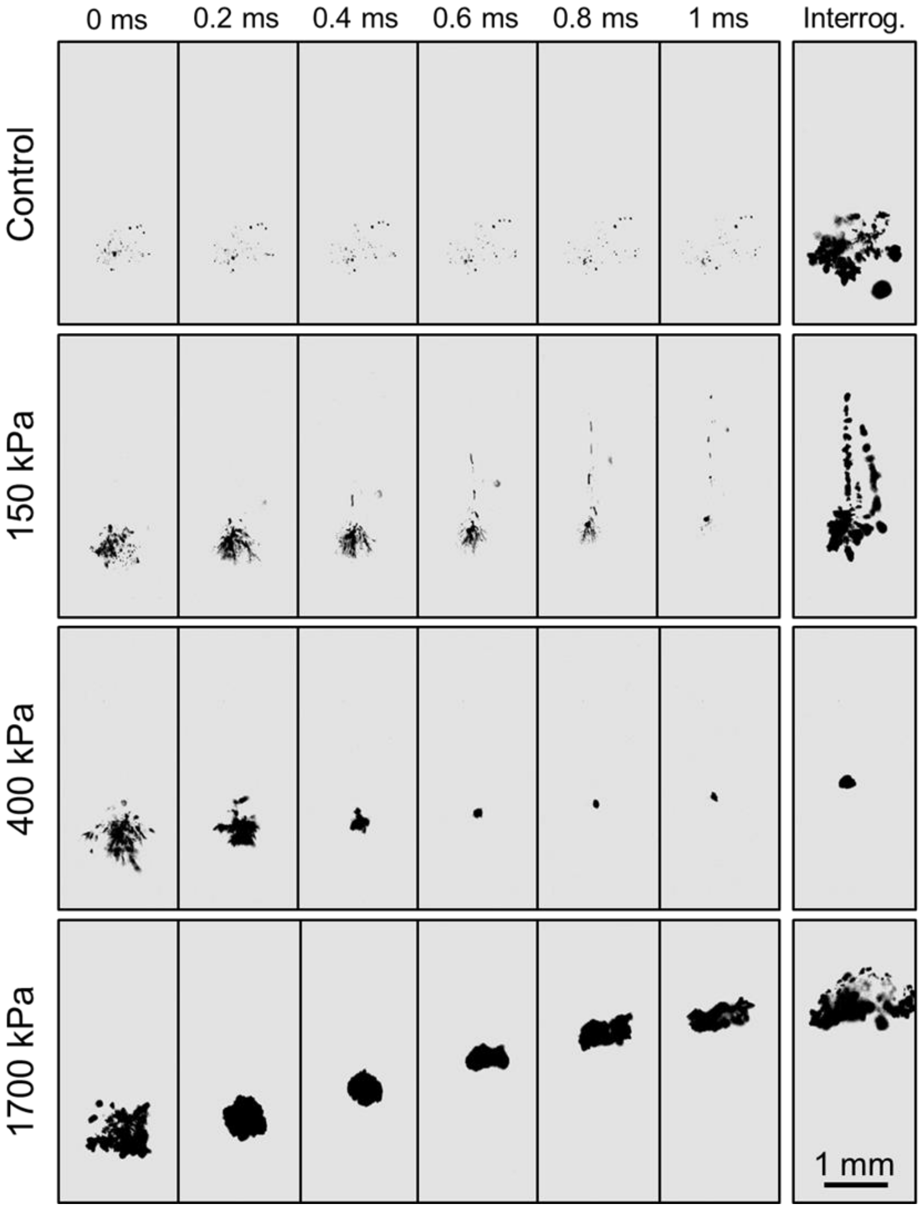

Fig. 4.3 Representative backlit images of nuclei activity over the course of bubble removal and interrogation. Ultrasound propagates from bottom to top in each frame, and t= 0 ms corresponds to the arrival of the bubble removal pulse. Four distinct cases are presented, including bubble removal pulse amplitudes of 0 (control), 150, 400, and 1700 kPa. For each, the activity of residual bubble nuclei is displayed at 0.2 ms intervals over the duration of the 1 ms bubble removal pulse; the last frame in each row shows the result of the corresponding interrogation pulse.

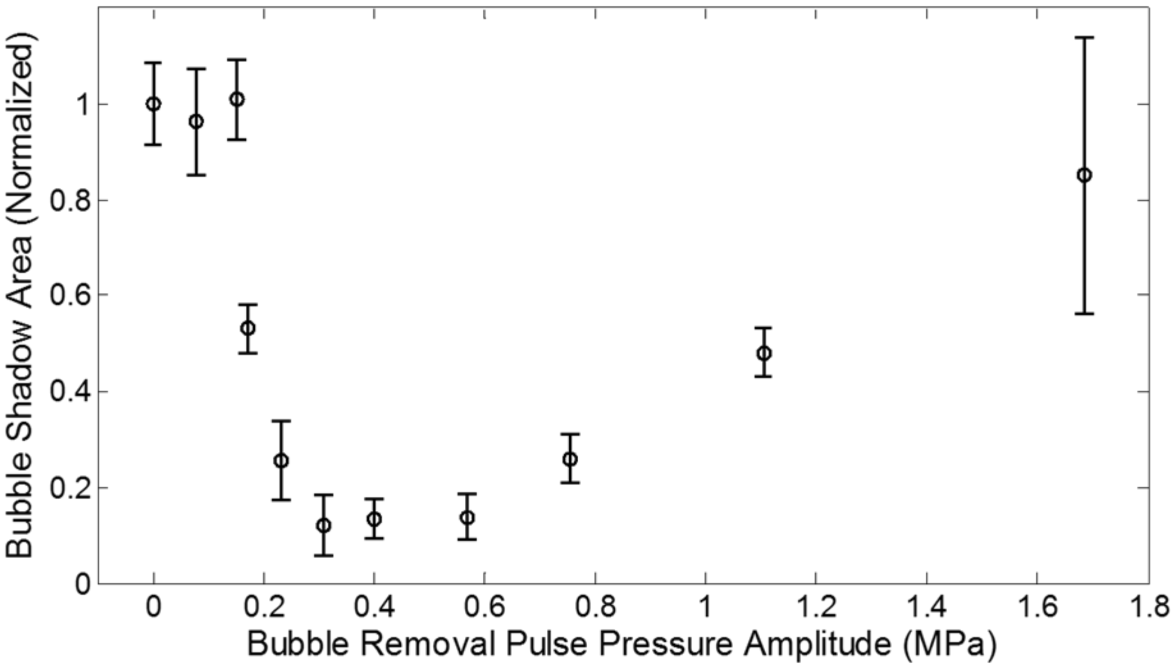

Fig. 4.4 Backlit area of shadow (mean ± SD) from bubbles expanded by the interrogation pulse (normalized to the control case). Bubble removal pulses with amplitudes of 80, 150, and 1700 kPa did not produce a statistically significant change in interrogated bubble shadow area relative to control, while those with amplitudes ranging from 150 – 1100 kPa resulted in a statistically significant reduction. Within the later range, interrogated bubble shadow area was observed to decrease with increasing bubble removal pulse amplitude until reaching a minimum in the vicinity of 310 – 570 kPa. Further increase in bubble removal pulse amplitude resulted in an increase in interrogated bubble shadow area. These trends are correlated to observations from high speed photography in the text.

4.3.1 Regime I: Bubble Nuclei Dispersion

At the lowest bubble removal pulse amplitudes of 80 and 150 kPa minimal bubble coalescence was observed. Instead, dispersion of the residual bubbles was stimulated, with a portion of the nuclei population migrating in the direction of bubble removal pulse propagation. This phenomenon can be observed in the second row of images displayed in Fig. 4.3. Correspondingly, the backlit area of shadow of interrogated bubbles did not show a statistically significant deviation from the control case at these amplitudes (*t-test*, $P > 0.42$), with respective normalized values (mean ± SD) of 0.96 ± 0.11 and 1.01 ± 0.08 (Fig. 4.4).

4.3.2 Regime II: Bubble Nuclei Coalescence

Intermediate bubble removal pulse amplitudes of 180 – 570 kPa were found to stimulate the aggregation and subsequent coalescence of residual bubble nuclei, as can be observed in the third row of Fig. 4.3. In these cases the residual bubble population was consolidated from a very large number of remnant nuclei down to a countably small number of residual bubbles. Correspondingly, a statistically significant reduction in the interrogated bubble shadow area relative to control (Fig. 4.4) was observed for all bubble removal pulse amplitudes in this range (*t-test*, $P < 1E-10$). The extent of the coalescence process was observed to become more pronounced as the bubble removal pulse amplitude was increased from 180 to 570 kPa; this translated to a progressive reduction in interrogated bubble shadow area (*t-test*, $P < 0.001$) until reaching a minimum in the vicinity of 310 – 570 kPa. Specifically, bubble removal pulses with amplitudes of 180, 230, and 310 kPa were found to produce normalized interrogated bubble shadow areas of 0.53 ± 0.05, 0.25 ± 0.08, and 0.12 ± 0.06, respectively. No further reduction was observed for bubble removal pulses greater than 310 kPa, with amplitudes of 400 and 570 kPa producing normalized interrogated bubble shadow areas of 0.14 ± 0.04 and 0.14 ± 0.05 (*t-test*, $P > 0.50$).

4.3.3 Regime III: Bubble Nuclei Excitation

Further increasing the bubble removal pulse amplitude above 570 kPa did not maintain or enhance the extent of bubble coalescence; rather, the highest tested amplitudes of 750, 1100, and 1700 kPa showed a reduction in the efficacy of the coalescence process. While pulses in this amplitude range continued to stimulate the aggregation of residual bubble nuclei, coalescence was compromised by the fact that these higher amplitude pulses re-excited residual bubbles and caused them to undergo violent cavitation—the collapse of which produced additional residual daughter nuclei (Fig. 4.3, row 4). As a result, interrogated bubble shadow area (Fig. 4.4) was observed to increase with increasing bubble removal pulse amplitude from 750 to 1700 kPa (*t-test*, $P < 0.001$), with removal pulse amplitudes of 750, 1100, and 1700 kPa resulting in normalized values of 0.26 ± 0.05, 0.48 ± 0.05, and 0.85 ± 0.29, respectively. The later result at the highest tested bubble removal pulse amplitude of 1700 kPa did not deviate significantly from the control case (*t-test*, $P = 0.14$).

4.4 Discussion

This chapter introduces a unique strategy for mitigating the effects of residual bubble nuclei produced by cavitation collapse, using low-amplitude acoustic bursts to stimulate their removal from the field via bubble coalescence. It was shown that these bubble removal pulses produce three distinct regimes of remnant nuclei behavior depending on the pulse amplitude utilized: (1) When sonicated at low amplitudes (150 kPa and below), residual bubbles experience minimal coalescence, although some dispersion of the nuclei is observed; (2) At intermediate amplitudes (180 – 570 kPa), the aggregation and subsequent coalescence of nuclei is stimulated—effectively removing them from the field; (3) High amplitudes (750 kPa and above) show a decrease in the efficacy of coalescence, resulting from the re-excitation of remnant nuclei and production of additional residual daughter bubbles.

We hypothesize that the primary and secondary Bjerknes forces are the major facilitators of the bubble coalescence phenomenon of interest in this study. Briefly, bubbles oscillating in an acoustic field will experience two major sets of forces [26-32, 38, 39]. The first, the primary Bjerknes force, describes the effect of the acoustic field on individual bubbles [29-31, 38, 39]. Theory dictates that bubbles smaller than the resonant size of the sonication frequency will be stimulated to migrate up the pressure gradient and congregate at antinodes, while those larger than the resonant size of the sonication frequency are stimulated to migrate down the pressure gradient and congregate at nodes. The second major force on acoustically driven bubbles, the secondary Bjerknes force, describes the effect of neighboring bubbles on one another [29, 30, 32, 39]. In this case theory suggests that bubbles that are of similar size such that their phase difference of oscillation is less than $\pi/2$ will experience an attractive force. Conversely, bubbles that are very different in size such that their phase difference of oscillation is greater than $\pi/2$ will experience a repulsive force. Overall, the Bjerknes forces can manifest in the aggregation or dispersion of acoustically driven bubbles, depending on the bubble size distribution relative to the sonication frequency. This fact has been observed experimentally in numerous studies [29-32, 38, 40, 41], including more recent work in the field of ultrasound contrast agent imaging [42-45].

In the study detailed in this chapter, 500 kHz bubble removal pulses delivered at intermediate amplitudes were found to stimulate the most effective coalescence of residual bubble nuclei. Based on the Minnaert formula [46], the frequency of 500 kHz corresponds to an equilibrium bubble diameter of 12 µm. Our high speed imaging (further detailed in Chapter 5) suggests that the remnant nuclei produced by collapse of the histotripsy bubble cloud were smaller than this resonant size, falling in a very tight size distribution with equilibrium diameter of approximately 6 µm. As such, it is likely that the primary and secondary Bjerknes forces act in concert to stimulate the bubble coalescence observed in this study: the primary force stimulates the migration of residual bubble nuclei up the pressure gradient toward the antinode of the bubble removal transducer, while the secondary force facilitates the attraction of individual bubbles to one another. Ultimately, this synergistic manipulation of residual nuclei manifests in their aggregation and subsequent coalescence. Optimization work presented in Chapter 5 aims to verify this hypothesis through an experimental investigation of the effect of bubble removal pulse frequency.

The fact that different regimes of bubble nuclei behavior were observed as the bubble removal pulse amplitude was increased suggests that the relative contributions of the primary and secondary Bjerknes forces have an amplitude dependence. Indeed, it has been previously documented that the secondary Bjerknes force increases with intensity more significantly than the primary [47-49]. This suggests that the efficacious aggregation and coalescence of residual nuclei observed at intermediate bubble removal pulse amplitudes has a strong dependence on the magnitude of this secondary force. A similar conclusion was presented by Hatanaka, *et al*. [47], who determined that bubble clustering observed at excessive ultrasonic intensity is predominantly due to the secondary Bjerknes force. This theory is consistent with the fact that, at the lower bubble removal pulse amplitudes tested in this study, minimal coalescence was observed. Instead, prominent dispersion of residual nuclei occurred. It is possible that these residual bubbles grew to sizes greater than the 12 μm resonant size of the isonification frequency, either by some limited degree of coalescence or rectified diffusion, at which point they migrated down the pressure gradient of the bubble removal sound field. Such behavior would give rise to the distribution of nuclei depicted in the second row of Fig. 4.3. As the bubble removal pulse amplitude was increased and the secondary Bjerknes force became more dominant, this behavior was likely offset by the stronger degree of inter-bubble attraction.

As discussed previously, the ability to actively remove residual bubble nuclei from the field has the potential to markedly enhance the efficacy of cavitation-based ultrasound therapies. In SWL the efficiency of stone comminution has been documented to decrease as the rate of SW application increases [17, 20-24]—a phenomenon attributed to remnant cavitation nuclei that persist from one SW to the next. When SWs propagate through a field containing these residuals, they experience a selective attenuation of their negative phase [11, 17, 19, 25] that compromises fragmentation of the stone. As discussed in Chapter 2, a similar bubble shielding effect is likely to limit the efficiency of histotripsy model stone erosion when high pulse rates a used. Furthermore, the results of Chapter 3 indicate that interleaving histotripsy pulses between successive lithotripsy shock waves may reduce the per-shock efficiency of SWL by seeding the field with remnant bubbles. Finally, rate dependent efficiency is also observed in histotripsy treatment of soft tissue, albeit due to cavitation memory rather than direct attenuation of the acoustic waveform [10]. In this case residual bubble nuclei that persist between histotripsy pulses can seed repetitive cavitation at a discrete set of sites within the focal volume, leading to inhomogeneous tissue fractionation and requiring an excess number of pulses to achieve complete homogenization of the targeted volume. Clearly, the strategic manipulation of residual bubble nuclei following the collapse of primary acoustic cavitation could be of great benefit in many cavitation-based therapy applications. The work presented in the subsequent chapters of this dissertation will focus on further optimization of the bubble removal process, as well as its incorporation in SWL stone comminution, histotripsy stone erosion, and histotripsy soft tissue fractionation.

4.5 Conclusion

In this chapter it was demonstrated that acoustic pulses can actively remove residual cavitation bubble nuclei from the field by stimulating their aggregation and subsequent coalescence. We hypothesize that the primary and secondary Bjerknes forces act in concert to facilitate this process, with the secondary force playing a more dominant role. Application of bubble removal pulse sequences to cavitation-based ultrasound therapies such as SWL and histotripsy will likely mitigate the rate dependent limitations that stem from the persistence of residual bubbles. The work presented in the remainder of this thesis will focus on the optimization of these bubble removal sequences, as well as their implementation in SWL and histotripsy treatments.

4.6 References

[1] A. P. Duryea, C. A. Cain, H. A. Tamaddoni, W. W. Roberts, and T. L. Hall, "Removal of Residual Nuclei Following a Cavitation Event using Low-Amplitude Ultrasound," *IEEE Trans Ultrason Ferroelectr Freq Control,* vol. 61, pp. 1619-26, Oct 2014.

[2] H. G. Flynn and C. C. Church, "A mechanism for the generation of cavitation maxima by pulsed ultrasound," *J Acoust Soc Am,* vol. 76, pp. 505-12, Aug 1984.

[3] J. B. Fowlkes and L. A. Crum, "Cavitation threshold measurements for microsecond length pulses of ultrasound," *The Journal of the Acoustical Society of America,* vol. 83, pp. 2190-2201, 1988.

[4] P. Huber, K. Jochle, and J. Debus, "Influence of shock wave pressure amplitude and pulse repetition frequency on the lifespan, size and number of transient cavities in the field of an electromagnetic lithotripter," *Phys Med Biol,* vol. 43, pp. 3113-28, Oct 1998.

[5] C. E. Brennen, "Fission of collapsing cavitation bubbles," *Journal of Fluid Mechanics,* vol. 472, pp. 153-166, 2002.

[6] M. Arora, L. Junge, and C. D. Ohl, "Cavitation cluster dynamics in shock-wave lithotripsy: part 1. Free field," *Ultrasound Med Biol,* vol. 31, pp. 827-39, Jun 2005.

[7] Z. Xu, T. L. Hall, J. B. Fowlkes, and C. A. Cain, "Optical and acoustic monitoring of bubble cloud dynamics at a tissue-fluid interface in ultrasound tissue erosion," *The Journal of the Acoustical Society of America,* vol. 121, pp. 2421-2430, 2007.

[8] Y. A. Pishchalnikov, J. A. McAteer, I. V. Pishchalnikova, J. C. Williams, M. R. Bailey, and O. A. Sapozhnikov, "Bubble proliferation in shock wave lithotripsy occurs during inertial collapse," in *18th International Symposium on Nonlinear Acoustics*, 2008, pp. 460-463.

[9] Y. A. Pishchalnikov, J. C. Williams, and J. A. McAteer, "Bubble proliferation in the cavitation field of a shock wave lithotripter," *J Acoust Soc Am,* vol. 130, pp. EL87-93, Aug 2011.

[10] T. Y. Wang, Z. Xu, T. L. Hall, J. B. Fowlkes, and C. A. Cain, "An efficient treatment strategy for histotripsy by removing cavitation memory," *Ultrasound Med Biol,* vol. 38, pp. 753-66, May 2012.

[11] Y. A. Pishchalnikov, J. A. McAteer, and J. C. Williams, Jr., "Effect of firing rate on the performance of shock wave lithotriptors," *BJU Int,* vol. 102, pp. 1681-6, Dec 2008.

[12] R. Mettin, I. Akhatov, U. Parlitz, C. D. Ohl, and W. Lauterborn, "Bjerknes forces between small cavitation bubbles in a strong acoustic field," *Physical Review E,* vol. 56, pp. 2924-2931, 09/01/ 1997.

[13] W. S. Chen, T. J. Matula, and L. A. Crum, "The disappearance of ultrasound contrast bubbles: observations of bubble dissolution and cavitation nucleation," *Ultrasound Med Biol,* vol. 28, pp. 793-803, Jun 2002.

[14] P. S. Epstein and M. S. Plesset, "On the stability of gas bubbles in liquid-gas solutions," *The Journal of Chemical Physics,* vol. 18, pp. 1505-1509, 1950.

[15] M. Arora, C. D. Ohl, and D. Lohse, "Effect of nuclei concentration on cavitation cluster dynamics," *J Acoust Soc Am,* vol. 121, pp. 3432-6, Jun 2007.

[16] O. Yavas, P. Leiderer, H. K. Park, C. P. Grigoropoulos, C. C. Poon, and A. C. Tam, "Enhanced acoustic cavitation following laser-induced bubble formation: Long-term memory effect," *Physical Review Letters,* vol. 72, pp. 2021-2024, 03/28/ 1994.

[17] Y. A. Pishchalnikov, J. A. McAteer, J. C. Williams, Jr., I. V. Pishchalnikova, and R. J. Vonderhaar, "Why stones break better at slow shockwave rates than at fast rates: in vitro study with a research electrohydraulic lithotripter," *J Endourol,* vol. 20, pp. 537-41, Aug 2006.

[18] O. A. Sapozhnikov, V. A. Khokhlova, M. R. Bailey, J. C. Williams, Jr., J. A. McAteer, R. O. Cleveland, *et al.*, "Effect of overpressure and pulse repetition frequency on cavitation in shock wave lithotripsy," *J Acoust Soc Am,* vol. 112, pp. 1183-95, Sep 2002.

[19] Y. A. Pishchalnikov, O. A. Sapozhnikov, M. R. Bailey, I. V. Pishchalnikova, J. C. Williams, and J. A. McAteer, "Cavitation selectively reduces the negative-pressure phase of lithotripter shock pulses," *Acoust Res Lett Online,* vol. 6, pp. 280-286, Nov 3 2005.

[20] G. Vallancien, R. Munoz, M. Borghi, B. Veillon, J. M. Brisset, and M. Daudon, "Relationship between the frequency of piezoelectric shock waves and the quality of renal stone fragmentation. In vitro study and clinical implications," *Eur Urol,* vol. 16, pp. 41-44, 1989.

[21] H. Wiksell and A. C. Kinn, "Implications of cavitation phenomena for shot intervals in extracorporeal shock wave lithotripsy," *Br J Urol,* vol. 75, pp. 720-3, Jun 1995.

[22] A. Greenstein and H. Matzkin, "Does the rate of extracorporeal shock wave delivery affect stone fragmentation?," *Urology,* vol. 54, pp. 430-432, 1999.

[23] M. J. Weir, N. Tariq, and R. J. Honey, "Shockwave frequency affects fragmentation in a kidney stone model," *J Endourol,* vol. 14, pp. 547-50, Sep 2000.

[24] R. F. Paterson, D. A. Lifshitz, J. E. Lingeman, A. P. Evan, B. A. Connors, N. S. Fineberg, *et al.*, "Stone fragmentation during shock wave lithotripsy is improved by slowing the shock wave rate: studies with a new animal model," *J Urol,* vol. 168, pp. 2211-5, Nov 2002.

[25] Y. A. Pishchalnikov, J. A. McAteer, M. R. Bailey, I. V. Pishchalnikova, J. C. Williams, and A. P. Evan, "Acoustic shielding by cavitation bubbles in shock wave lithotripsy (SWL)," in *17th International Symposium on Nonlinear Acoustics* 2005, pp. 319-322.

[26] V. Bjerknes, *Fields of Force*, 1906.

[27] V. Bjerknes, *Die Kraftfelder*, 1909.

[28] M. Kornfeld and L. Suvorov, "On the destructive action of cavitation," *Journal of Applied Physics,* vol. 15, pp. 495-506, 1944.

[29] F. G. Blake, "Bjerknes Forces in Stationary Sound Fields," *The Journal of the Acoustical Society of America,* vol. 21, pp. 551-551, 1949.

[30] E. A. Neppiras, "Subharmonic and Other Low-Frequency Emission from Bubbles in Sound-Irradiated Liquids," *The Journal of the Acoustical Society of America,* vol. 46, pp. 587-601, 1969.

[31] L. A. Crum and A. I. Eller, "Motion of Bubbles in a Stationary Sound Field," *The Journal of the Acoustical Society of America,* vol. 48, pp. 181-189, 1970.

[32] L. A. Crum, "Bjerknes forces on bubbles in a stationary sound field," *The Journal of the Acoustical Society of America,* vol. 57, pp. 1363-1370, 1975.

[33] M. Chaigneau and G. Le Moan, "On the composition of gas dissolved in human urine," *C R Acad Sci Hebd Seances Acad Sci D,* vol. 267, pp. 1893-5, Nov 25 1968.

[34] J. B. Fowlkes, P. L. Carson, E. H. Chiang, and J. M. Rubin, "Acoustic generation of bubbles in excised canine urinary bladders," *J Acoust Soc Am,* vol. 89, pp. 2740-4, Jun 1991.

[35] E. Y. Hwang, J. B. Fowlkes, and P. L. Carson, "Variables controlling contrast generation in a urinary bladder model," *J Acoust Soc Am,* vol. 103, pp. 3706-16, Jun 1998.

[36] J. E. Parsons, C. A. Cain, and J. B. Fowlkes, "Cost-effective assembly of a basic fiber-optic hydrophone for measurement of high-amplitude therapeutic ultrasound fields," *J Acoust Soc Am,* vol. 119, pp. 1432-40, Mar 2006.

[37] A. D. Maxwell, C. A. Cain, T. L. Hall, J. B. Fowlkes, and Z. Xu, "Probability of Cavitation for Single Ultrasound Pulses Applied to Tissues and Tissue-Mimicking Materials," *Ultrasound in Medicine & Biology,* vol. 39, pp. 449-465, 3// 2013.

[38] L. A. Crum, "The motion of bubbles in a stationary sound field," *The Journal of the Acoustical Society of America,* vol. 46, p. 1411, 1969.

[39] T. G. Leighton, *The Acoustic Bubble*. San Diego, CA: Academic Press Inc, 1997.

[40] D. E. Goldman and G. R. Ringo, "Determination of Pressure Nodes in Liquids," *The Journal of the Acoustical Society of America,* vol. 21, pp. 270-270, 1949.

[41] W. L. Nyborg and D. E. Hughes, "Bubble annihilation in cavitation streamers," *The Journal of the Acoustical Society of America,* vol. 42, pp. 891-894, 1968.

[42] P. Dayton, A. Klibanov, G. Brandenburger, and K. Ferrara, "Acoustic radiation force in vivo: a mechanism to assist targeting of microbubbles," *Ultrasound Med Biol,* vol. 25, pp. 1195-201, Oct 1999.

[43] P. A. Dayton, J. S. Allen, and K. W. Ferrara, "The magnitude of radiation force on ultrasound contrast agents," *J Acoust Soc Am,* vol. 112, pp. 2183-92, Nov 2002.

[44] S. Zhao, M. Borden, S. H. Bloch, D. Kruse, K. W. Ferrara, and P. A. Dayton, "Radiation-force assisted targeting facilitates ultrasonic molecular imaging," *Mol Imaging,* vol. 3, pp. 135-48, Jul 2004.

[45] K. Ferrara, R. Pollard, and M. Borden, "Ultrasound microbubble contrast agents: fundamentals and application to gene and drug delivery," *Annu Rev Biomed Eng,* vol. 9, pp. 415-47, 2007.

[46] M. Minnaert, "XVI. On musical air-bubbles and the sounds of running water," *Philosophical Magazine Series 7,* vol. 16, pp. 235-248, 1933/08/01 1933.

[47] S. Hatanaka, K. Yasui, T. Kozuka, T. Tuziuti, and H. Mitome, "Influence of bubble clustering on multibubble sonoluminescence," *Ultrasonics,* vol. 40, pp. 655-60, May 2002.

[48] W. Lauterborn, T. Kurz, R. Mettin, and C. D. Ohl, "Experimental and theoretical bubble dynamics," *Adv. Chem. Phys.,* vol. 110, pp. 295-380, 1999.

[49] R. Mettin, S. Luther, C. D. Ohl, and W. Lauterborn, "Acoustic cavitation structures and simulations by a particle model," *Ultrasonics Sonochemistry,* vol. 6, pp. 25-29, 1999.

Chapter 5

Active Removal of Residual Nuclei Following a Cavitation Event: A Parametric Study

A majority component of this chapter is in-press in *IEEE Transactions on Ultrasonics, Ferroelectrics, and Frequency Control*. © 2015 IEEE. Reprinted, with permission, from [1].

5.1 Introduction

Chapter 4 presented a strategy for the active removal of the remnant bubble nuclei produced by primary cavitation collapse [2], with the ultimate goal of mitigating the ill-effects of residual bubbles in cavitation-based ultrasound therapies [3-9]. It was shown that the application of appropriately designed low amplitude ultrasound pulses can stimulate the aggregation and subsequent coalescence of residual bubble nuclei, in effect removing them from the field. These acoustic sequences, which we denote as bubble removal pulses, were hypothesized to operate via a synergistic interplay between the primary and secondary Bjerknes forces. Microscopic residual bubble nuclei, being smaller than the resonant size of the 500 kHz bubble removal pulse previously utilized, tend to move up the pressure gradient and congregate at the antinode of the bubble removal field (primary Bjerknes force) [10-14]. When brought into close proximity with one another, bubbles that are of similar size experience an attractive force, further promoting their consolidation (secondary Bjerknes force) [10, 11, 14, 15]. The results presented in Chapter 4 indicate that the secondary Bjerknes force is likely the dominant facilitator of the bubble consolidation process, with a select set of acoustic parameters producing optimal aggregation and coalescence [2].

The optimization of bubble removal pulses to manipulate residual nuclei following primary cavitation collapse could lead to a pronounced adjunct for ultrasound therapies such as SWL and histotripsy. In the present chapter, we further explore this phenomenon through an investigation of the effect of frequency on the bubble removal process. The work presented in Chapter 4 considered only a single frequency (500 kHz) to sonicate remnant cavitation bubbles. Here we extend the parameter space and examine bubble removal pulses of 0.5, 1, and 2 MHz, investigating if previously observed trends hold across frequency. The acoustic implications of residual nuclei remaining in the field following bubble removal are also explored by measuring the transmission of a secondary pulse through the volume of interest.

5.2 Methods

5.2.1 Experimental Setup

The experimental setup used to investigate the effects of bubble removal pulse frequency was the same as that described in Chapter 4, with the addition of a needle hydrophone (Müller-Platte Needle Probe 100-100-1, Dr. Müller Instruments, Oberursel, Germany) positioned adjacent to the histotripsy transducer focus at an offset distance of 2 mm, distal relative to the bubble removal module (Fig. 5.1). Once again, all experiments were conducted in deionized water degased to physiologically relevant levels (dissolved oxygen content of 7.1 ± 0.1 mg/L at 21.1 ± 0.4 ˚C (mean ± SD), corresponding to 78 ± 1% of saturation); this mimics the dissolved gas content of human urine, for example [16-18]. Each experiment was monitored using a Photron Fastcam SA1.1 high speed camera (Photron USA Inc., San Diego, CA) at a frame rate of 20 kfps and exposure time of 49 µs. A 10X super-long working distance microscope objective (T Plan SLWD

10X/0.20, Nikon Instruments Inc., Melville, NY) coupled to a 70 mm macro lens (Sigma 70 mm 1:2:8 DG Macro, Sigma Corporation of America, Ronkonkoma, NY) provided the optical power to resolve the microscopic residual nuclei of interest in this study. The theoretical resolution limit of this optical setup is 1.3 µm, while the theoretical depth of field is 18.3 µm. A large area, high power LED light source (BXRA-50C9000, Bridgelux Inc., Livermore, CA) was used to backlight the experiments such that bubbles generated in the field were visible as dark shadows on the optical images.

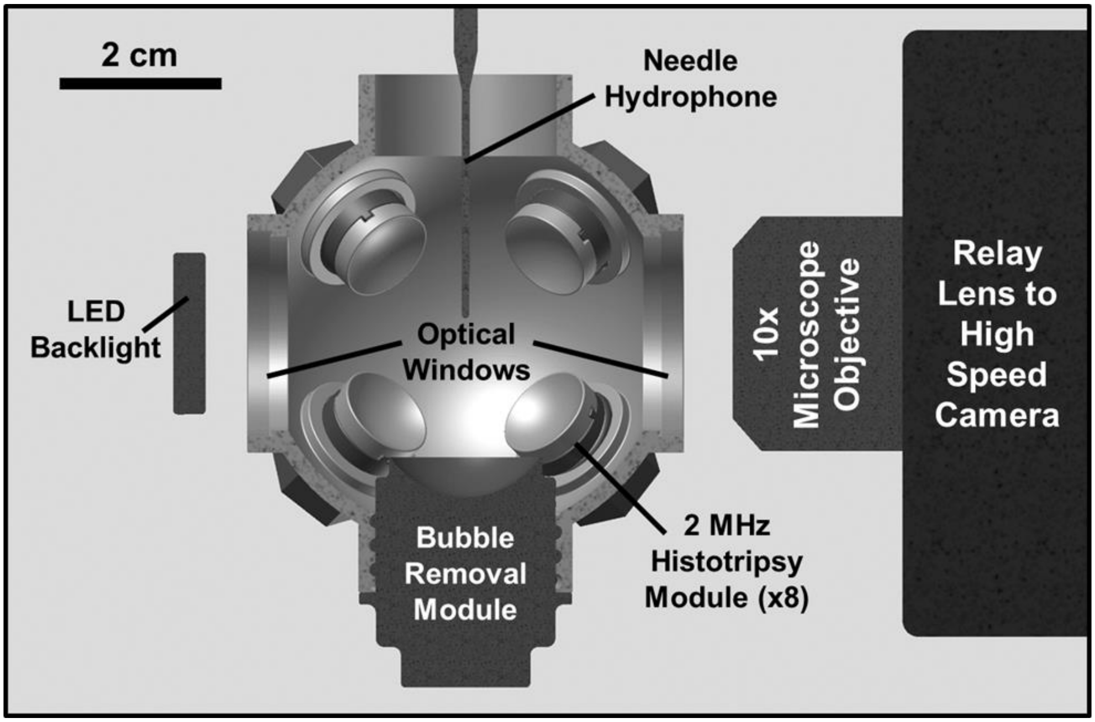

Fig. 5.1 Half-section view of the experimental setup used to study effects of sonication frequency on the bubble removal process. Primary cavitation was initiated by an array of eight 2 MHz histotripsy modules arranged in a spherical pattern, while bubble removal pulses were delivered from a separate bubble removal module (0.5, 1, or 2 MHz) aligned at a predetermined offset relative to the histotripsy focus (see text). All transducer modules were held within an Accura 60 plastic scaffold that also served as the water tank for the experiments. Optical windows in the front and rear of the scaffold permitted the use of backlit high speed photography to monitor the bubble removal process. A needle hydrophone positioned adjacent to the histotripsy focus, at an offset 2 mm distal relative to the bubble removal module, was used to measure the transmission of interrogation pulses propagating through the field.

The 2 MHz histotripsy transducer described in Chapter 4 was used to initiate primary cavitation activity (a cavitational bubble cloud). Again, it consisted of eight PZT-4 disc elements

(Steiner & Martins Inc., Miami, FL), measuring 10 mm in diameter and 1 mm in thickness. Water-tight modules designed to hold individual elements were fabricated from Accura 60 plastic (3D Systems Inc., Rock Hill, SC) using a stereolithography machine. The front face of each module contained an Accura 60 acoustic lens with a focal length of 20 mm; PZT-4 elements were matched to this lens using an epoxy (1C-LV Hysol, Loctite Corporation, Rocky Hill, CT) filled 100 mesh copper screen (McMaster-Carr, Aurora, OH) to achieve the proper thickness and impedance. The eight individual histotripsy modules were aligned confocally in a spherical arrangement using a plastic scaffold, also fabricated via stereolithography from Accura 60. This scaffold doubled as the water tank for the experiments, and had optical windows in the front and rear to permit the use of backlit high speed photography. The spherical geometry of this transducer produced a highly confined focal zone conducive to the high optical magnification required to resolve remnant bubble nuclei, with the -6-dB beamwidths measuring approximately 500 µm in both the lateral and axial dimensions. These measurements were conducted at a pressure amplitude of 6 MPa (linear regime) using a fiber optic hydrophone with a 100 µm diameter sensing tip [19]. The histotripsy transducer was driven using a pulse amplifier developed in our lab, which was designed to produce very short intense bursts. More details regarding the acoustic output generated by this setup are provided in section 5.2.3.

A separate set of transducers—which we collectively refer to as the bubble removal modules—were used to sonicate residual cavitation nuclei produced by collapse of the histotripsy bubble cloud. Similar to the histotripsy modules, these transducers were constructed in-house using a stereolithography-fabricated Accura 60 housing and acoustic lens. To test the effect of frequency on the bubble removal process, three distinct module designs were utilized, which included those with center frequencies of 0.5, 1, and 2 MHz. All bubble removal modules were constructed using Pz36 disc elements (Ferroperm Piezoceramics A/S, Kvistgaard, Denmark). For a given module, the front face of the Pz36 element was mated directly to the Accura 60 acoustic lens using epoxy adhesive (Hysol E-120 HP, Loctite Corporation, Rocky Hill, CT); a copper screen matching layer was not utilized in these cases due to the low acoustic impedance of Pz36 (specified at 14 MRayl by the manufacturer). The 0.5 MHz bubble removal module was constructed from two 1 MHz Pz36 disc elements measuring 20 mm in diameter and 1.6 mm in thickness, which were stacked and driven in unison to produce a 0.5 MHz equivalent source. The 1 MHz bubble removal module was constructed from a single 1 MHz Pz36 disc element, also measuring 20 mm in diameter and 1.6 mm in thickness. Lastly, the 2 MHz bubble removal module was constructed from a single 2 MHz Pz36 disc element, measuring 10.2 mm in diameter and 0.8 mm in thickness. For a given experiment, the bubble removal module of interest was held within the same spherical scaffold used to position the histotripsy modules (Fig. 5.1). All bubble removal modules were driven using a sinusoid at their respective center frequency from an ENI AP400B controllable power amplifier (Electronic Navigation Industries Inc., Rochester, NY); further details on the acoustic outputs are presented in the subsequent sections.

5.2.2 Bubble Removal Module Design

To investigate the consequences of sonication frequency on the bubble removal process, it is desirable to keep all other exposure conditions constant. This includes the dimensions of the acoustic field produced by a given bubble removal module, as the pressure gradients strongly influence the behavior of acoustically driven bubbles. For this reason we took care to ensure that the acoustic field dimensions produced by each respective bubble removal module were as similar as possible in the vicinity in which the residual bubble nuclei were produced (i.e., the histotripsy focus). This design process was conducted using a Fast Object-Oriented C++ Ultrasound

Simulator (FOCUS, developed by McGough, *et al*. [20-23]), which is a cross-platform freeware that consists of a Matlab (MathWorks Inc., Natick, MA) user interface and object-oriented C++ computation core. Linear transient simulations were performed to predict the field dimensions generated by a particular set of module parameters. These included the source's center frequency, size, acoustic lens power, and offset relative to the histotripsy transducer focus. The ultimate parameter sets implemented for the three bubble removal modules characterized in this study are as follows: (1) 0.5 MHz source measuring 20 mm in diameter, mated to an acoustic lens with a 25 mm focal length and offset a distance of 18 mm from the histotripsy transducer focus; (2) 1 MHz source measuring 20 mm in diameter, mated to an acoustic lens with a 25 mm focal length and offset 35 mm from the histotripsy transducer focus; (3) 2 MHz source measuring 10.2 mm in diameter, mated to an acoustic lens with a 20 mm focal length and offset 35 mm from the histotripsy transducer focus. The lateral and axial beam profiles generated by these bubble removal modules are displayed in Fig. 5.2, measured using an HNR-0500 needle hydrophone (Onda Corporation, Sunnyvale, CA) at a pressure amplitude of 500 kPa for each. As specified by the manufacturer, this hydrophone has a measurement uncertainty of 1.5 dB in the frequency range 0.5 – 1 MHz and 1 dB in the frequency range 1 – 15 MHz. In the lateral dimension, the -6-dB beamwidths measured on the pressure amplitude were found to be 4.1 mm, 6.2 mm, and 4.2 mm for the 0.5, 1, and 2 MHz modules, respectively. Corresponding values in the axial dimension were observed to exceed 8 mm in all cases. It should be noted, however, that the population of residual bubble nuclei generated by the histotripsy transducer was empirically observed to reside within a zone measuring approximately 1 x 1 x 1 mm centered at the histotripsy transducer focus. This region is represented by the gray bars included in Fig. 5.2, and it can be seen that the acoustic field dimensions produced by the three bubble removal modules used in this study are extremely similar over this zone of interest.

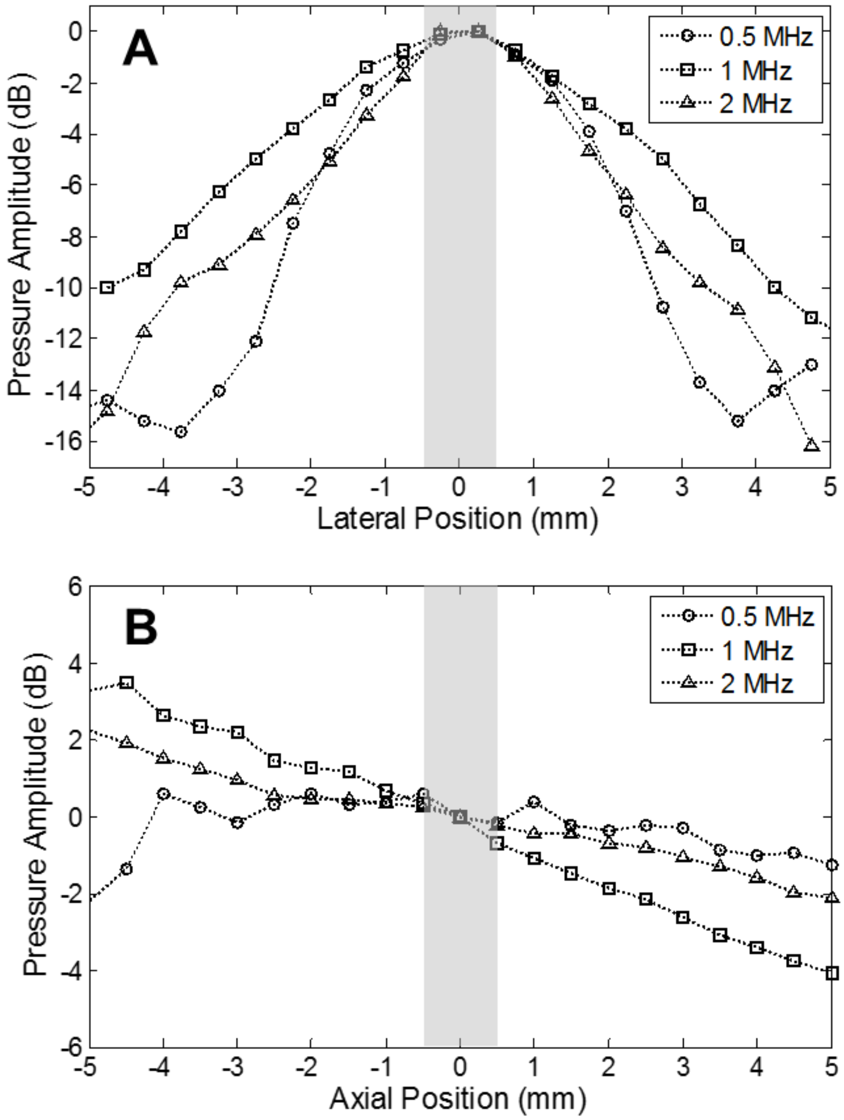

Fig. 5.2 Bubble removal module field scans performed in the (**A**) lateral and (**B**) axial dimensions using an HNR-0500 needle hydrophone. Position 0 corresponds to the point of overlap with the histotripsy transducer focus. In all cases, the pressures are normalized to their respective values at this location. Gray bars represent the region over which residual bubble nuclei generated by the histotripsy transducer generally occur, empirically observed to be an approximate 1 x 1 x 1 mm volume centered at the histotripsy transducer focus. The field dimensions of the bubble removal modules are quite consistent over this region of interest.

5.2.3 Acoustic Pulse Sequence

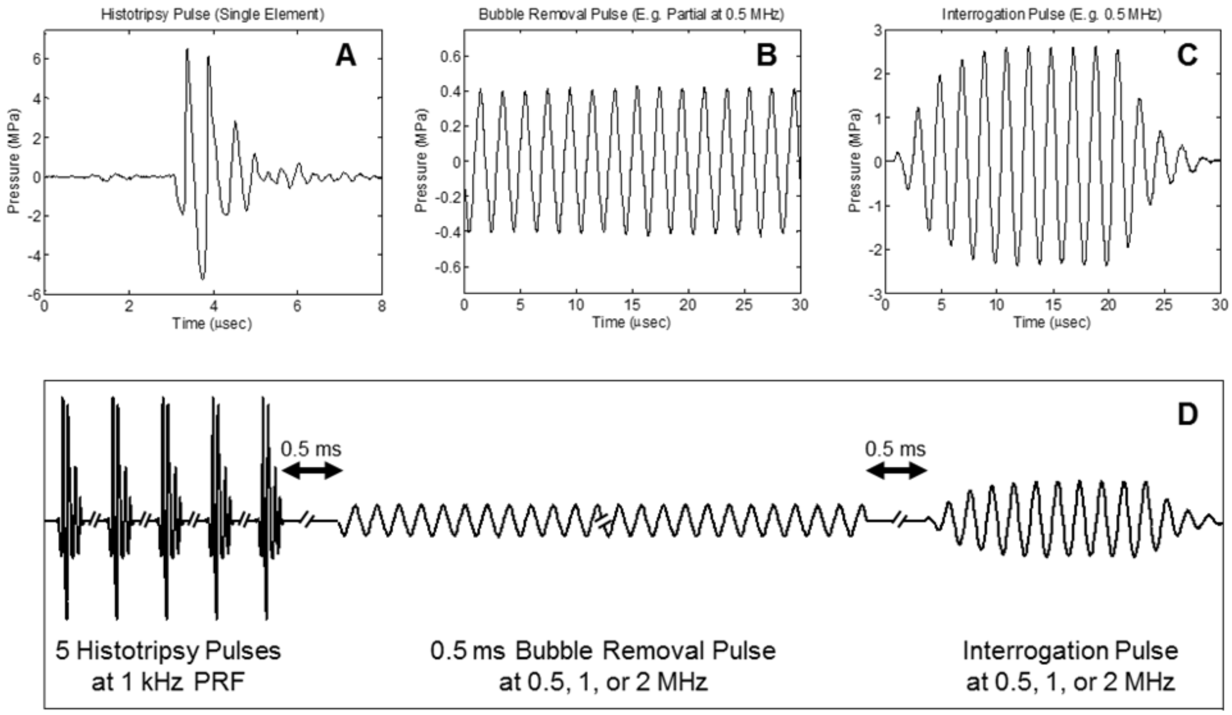

Fig. 5.3 General pulse scheme used to study the effect of sonication frequency on the bubble removal process. (**A**) Representative waveform acquired from a single 2 MHz histotripsy module; the histotripsy pulse amplitude at the focal location can be estimated as the linear sum of the waveforms from all eight histotripsy modules, suggesting a focal peak negative pressure of approximately 40 MPa. (**B**) Example segment of a 0.5 ms bubble removal pulse at 0.5 MHz; bubble removal pulses with center frequencies of 0.5, 1, and 2 MHz were investigated, while the amplitude was varied from 0 to approximately 2 MPa at a given frequency. (**C**) Example interrogation pulse at 0.5 MHz; interrogation pulses were generated by the bubble removal module utilized in a given experiment and had a constant duration of 10 cycles, while the amplitude was frequency-dependent (see text). (**D**) Overall timing of experimental pulse scheme.

Consistent with the work presented in Chapter 4, three general types of acoustic pulses were utilized in the present study. These are represented in Fig. 5.3(A-C): (1) Histotripsy pulses generated by the 2 MHz histotripsy transducer were used to initiate cavitation activity in the form of a cavitational bubble cloud; (2) Bubble removal pulses produced by the bubble removal modules (0.5, 1, or 2 MHz) were used to sonicate residual bubble nuclei following primary cavitation collapse, stimulating their coalescence and removal from the field; (3) An interrogation pulse, also delivered from the bubble removal module utilized in a given experiment, was used to probe the field for the presence of residual nuclei following bubble removal. The function of this interrogation pulse was twofold. Firstly, it caused remaining microscopic nuclei to expand and be more easily detected via high speed imaging. Secondly, it provided a measure of the acoustic ramifications of bubble nuclei remaining in the field, as its transmission was measured by the needle hydrophone positioned just distal to the histotripsy focus (Fig. 5.1). The overall timing of this pulse scheme is summarized in Fig. 5.3(D), with specifics provided henceforth.

The initiation of primary cavitation activity in this study was achieved using a train of five histotripsy pulses delivered at a pulse repetition frequency (PRF) of 1 kHz. Histotripsy pulses were very short (approximately 2 μs) and intense. The acoustic output from a single histotripsy module is displayed in Fig. 5.3(A), measured using the same fiber optic hydrophone used to perform histotripsy field scans. Due to the sparse and spherical distribution of the modules that compose the histotripsy transducer, there is minimal superposition of individual waveforms until they reach the geometric focal location; as such, we estimate the output of the histotripsy transducer as the linear sum of the outputs from the eight individual modules [24]—suggesting a peak negative pressure of approximately 40 MPa. This overall output exceeds the intrinsic cavitation threshold in water [24], permitting the histotripsy transducer to initiate a cavitational bubble cloud with each pulse. A train of five histotripsy pulses in rapid succession was utilized to maximize the extent of cavitation. Similar to the bubble proliferation phenomenon observed in SWL [25, 26], this arrangement of histotripsy pulses was empirically determined to enhance cavitation activity as residual daughter bubbles persisting between pulses seeded additional sites for cavitation inception.

Following collapse of the final histotripsy-induced bubble cloud, residual cavitation nuclei were sonicated with a 0.5 ms long bubble removal pulse at a given frequency (0.5, 1, or 2 MHz) to stimulate their removal from the field via bubble coalescence. A partial segment of a representative bubble removal pulse at 0.5 MHz is displayed in Fig. 5.3(B), acquired using the same HNR-0500 needle hydrophone used to perform bubble removal module field scans. All bubble removal pulses were applied at a delay of 0.5 ms following the final histotripsy pulse, which allowed the histotripsy bubble cloud to collapse and produce residual nuclei in an unimpeded manner. To investigate the influence of acoustic pulse amplitude on the bubble removal process at a given frequency, bubble removal pulses with mechanical indices (MIs) ranging from 0 to approximately 1.5 were tested. Specifically, bubble removal pulses at 0.5 MHz were applied at amplitudes of 0, 80, 150, 230, 310, 400, 570, 750, and 1100 kPa. Those at 1 MHz were applied at amplitudes of 0, 80, 210, 280, 360, 430, 660, 890, 1300, 1600, and 1900 kPa. Finally, bubble removal pulses at 2 MHz were applied at amplitudes of 0, 100, 160, 220, 290, 430, 570, 790, 1100, 1300, 1700, 2100, and 2400 kPa. As the bubble removal pulses were observed to have some amplitude variation across their 0.5 ms duration (~10%), these reported values represent the mean amplitude over all cycles composing the pulse.

The presence of residual nuclei remaining in the field following the bubble removal pulse was probed for using a second, much shorter, pulse from the bubble removal module, which we denote as the interrogation pulse. Because the microscopic remnant bubble nuclei of interest in this study are likely on the order of the of the 1.3 µm theoretical resolution limit of our optical setup, they can be difficult to detect and quantify; furthermore, they may fall out of the depth of field imaging plane (estimated at 18 µm). For these reasons the interrogation pulse was used to expand any bubble nuclei remaining in the field such that they could be more easily detected via high speed imaging. The interrogation pulse also provided a measure of the acoustic consequences of residual bubbles that persist in the field, as its transmission through the volume of interest was measured by the needle hydrophone positioned just distal to the histotripsy focus (Fig. 5.1).

Interrogation pulses propagating through the field experienced an attenuation commensurate with the extent of residual bubble nuclei remaining, providing an acoustic metric for quantifying the effectiveness of bubble removal. Fig. 5.3(C) displays a representative interrogation pulse waveform generated by the 0.5 MHz bubble removal module, as calibrated by the HNR-0500 needle hydrophone. For all bubble removal frequencies, a 10 cycle pulse was used to interrogate the field at 0.5 ms following the completion of bubble removal. Interrogation pulses generated by the 0.5 MHz module had peak-positive/peak-negative (P+/P-) pressures of 2.6/2.4 MPa, those generated by the 1 MHz module had P+/P- of 2.3/1.5 MPa, and those from the 2 MHz module P+/P- of 3.0/1.5 MPa. These values were selected based on the empirical observation that they yield the same baseline level of P- attenuation across frequency, as is shown in section 5.3 of this chapter. Interrogation pulses were found not to initiate any cavitation bubbles independently (i.e., when not preceded by the generation of a population of cavitation bubble nuclei).

5.2.4 Quantification of Bubble Removal Pulse Efficacy

Two distinct metrics were utilized to quantify the efficacy of bubble removal in this study. First, the backlit area of shadow of remnant nuclei expanded by the interrogation pulse was calculated. The entire duration of each pulse sequence was imaged using high speed photography at 20 kfps, and it was empirically determined that the 110th frame in the image sequence corresponded to the time point of maximal bubble expansion induced by the interrogation pulse. This is consistent with the interrogation pulse arrival at 5.5 ms depicted in Fig. 5.3. The backlit area of bubble shadow in this frame was calculated for all experiments using Matlab to sum the pixels that resided below a threshold value, nominally set to 15 standard deviations from the background mean and then scaled on a per-pixel basis to account for variations in light intensity across the field of view. Secondly, the transmission of the interrogation pulse was detected by the needle hydrophone located 2 mm distal to the histotripsy transducer focus. The degree of attenuation of this received pulse is indicative of the extent of residual nuclei remaining in the field, thus providing a practical metric for the effectiveness of the bubble removal process. Interrogation pulse transmission was quantified using the transmitted peak-negative pressure, based on the observation that this metric displays a uniform baseline attenuation across the frequency range investigated (see section 5.3). For each frequency ten trials were performed at each bubble removal pulse amplitude in a randomized fashion, with a minimum rest time of one minute imposed between successive trials. All statistical analysis was performed using a Student's t-Test with $P < 0.05$ considered significant.

5.2.5 Residual Bubble Nuclei Sizing

In a separate set of experiments, the size distribution of residual bubble nuclei generated by histotripsy bubble cloud collapse was investigated via optical imaging. The same setup described in section 5.2.1 was utilized for these experiments, with the exception of the camera and its associated optics. In this case images were acquired using a Point Grey Chameleon camera (Point Grey Research Inc., Richmond, BC, Canada), which was selected based on its smaller pixel size of 3.75 µm affording increased resolution relative to the Photron SA1.1 high speed camera used in the previous portion of this study (20 µm pixels). A 20X super-long working distance microscope objective (T Plan SLWD 20X/0.30, Nikon Instruments Inc., Melville, NY) coupled to a 200 mm macro lens (AF Micro-Nikkor 200mm f/4D IF-ED, Nikon Corporation, Tokyo, Japan) provided the optical power in this case. The theoretical resolution limit of this optical setup is 0.4 µm, while the theoretical depth of field is 6.7 µm. Again, the initiation of primary cavitation was generated using a train of five histotripsy pulses delivered at a PRF of 1 kHz and estimated peak negative pressure of 40 MPa. In this case no bubble removal or interrogation pulses were applied, and a single image of the remnant bubble nuclei was exposed for 2 µs at a delay of 0.5 ms following the final histotripsy pulse. This sequence was repeated 1000 times with a delay of 10 seconds imposed between successive trials to allow for complete dissolution of remnant bubbles. Resulting images were processed in Matlab using the native function ‘imfindcircles’ to detect and size bubbles that were in focus.

5.3 Results

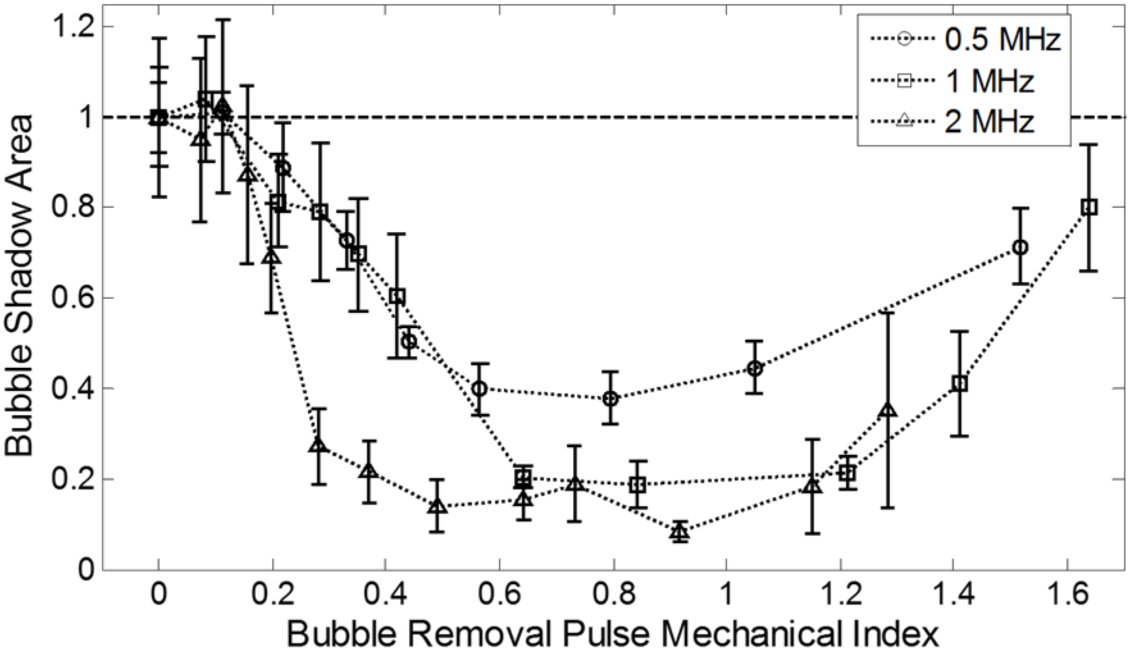

Fig. 5.4 Backlit area of shadow (mean ± SD, n= 10) from bubbles expanded by the interrogation pulse. Data at all frequencies has been normalized to its corresponding baseline value (bubble removal pulse amplitude set to 0). When evaluated as a function of MI, three distinct regimes of behavior are apparent across all frequencies tested (with provided cutoffs being approximate values): (1) MI < 0.2: Minimal bubble coalescence is observed and bubble shadow area does not deviate significantly from its baseline value; (2) 0.2 < MI < 1: Bubble coalescence becomes more pronounced with increasing MI, and bubble shadow area decreases and trends toward a minimum; (3) MI > 1: Bubble coalescence is compromised as removal pulses incite violent cavitation and bubble shadow area increases.

The backlit area of shadow from bubbles expanded by the interrogation pulse is displayed in Fig. 5.4, while transmission of interrogation pulse peak-negative pressure is shown in Fig. 5.5. Data in each of these plots has been normalized to its respective baseline case. For the backlit area of bubble shadow, this baseline is defined as the interrogated bubble shadow area when the bubble removal pulse amplitude is set to 0 (i.e., when no removal of residual nuclei is stimulated). For interrogation pulse transmission, the baseline is defined as the transmitted peak-negative pressure when the histotripsy pulse amplitude is set to 0 (i.e., when no cavitation bubbles are generated prior to interrogation). In this way, when bubble removal pulses eliminate residual nuclei from the field, it produces a decrease in the interrogated bubble shadow area relative to its baseline value; correspondingly, attenuation of the interrogation pulse is relieved and transmission recovers toward its respective baseline.

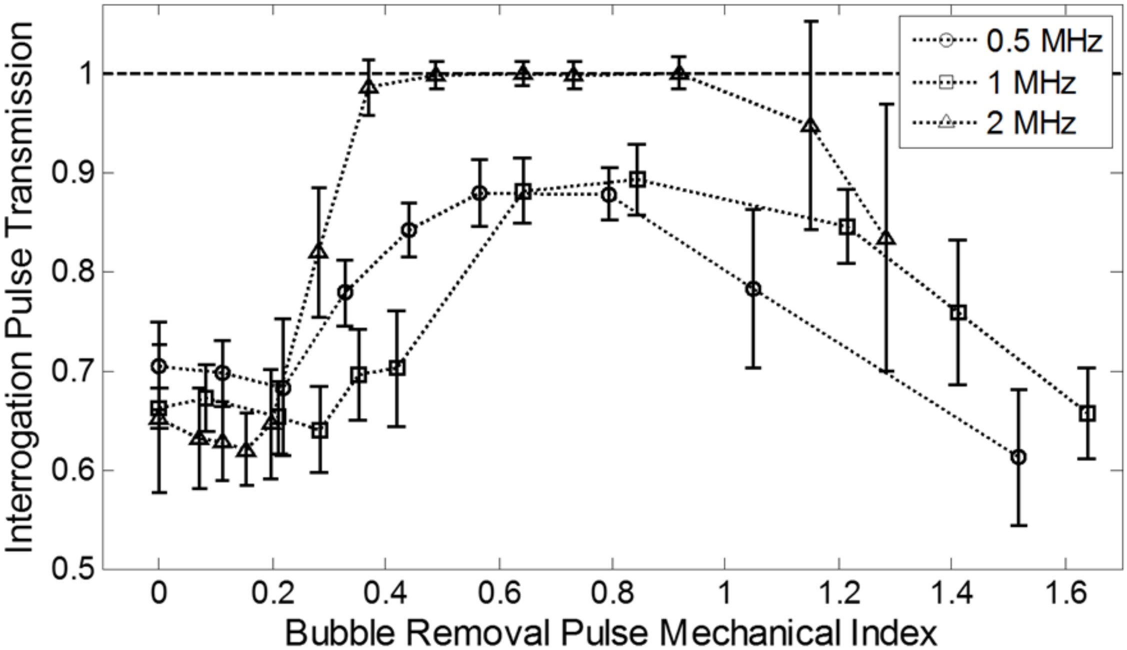

Fig. 5.5 Transmission of interrogation pulse peak-negative pressure (mean ± SD, n= 10). Data at all frequencies has been normalized to its corresponding baseline value (histotripsy pulse amplitude set to 0—i.e., no cavitation bubbles generated prior to interrogation). When evaluated as a function of MI, three distinct regimes of behavior are apparent across all frequencies tested (with provided cutoffs being approximate values): (1) MI < 0.2: Minimal bubble coalescence is observed and interrogation pulse transmission does not deviate significantly from its baseline value; (2) 0.2 < MI < 1: Bubble coalescence becomes more pronounced with increasing MI, and interrogation pulse transmission increases and trends toward a maximum; (3) MI > 1: Bubble coalescence is compromised as removal pulses incite violent cavitation and interrogation pulse transmission decreases.

Collapse of the final histotripsy bubble cloud was observed to produce an extensive set of microscopic residual bubble nuclei. Based on our optical sizing experiment, bubbles in this population fell within a size distribution of 5.6 ± 1.1 µm diameter (mean ± SD). With the bubble removal pulse amplitude set to 0, these residual nuclei persisted over the entirety of the 0.5 ms bubble removal pulse duration, gradually dispersing with time within an approximate 1 x 1 x 1 mm volume centered at the histotripsy transducer focus. Propagation of the interrogation pulse through this population of residual bubbles produced pronounced attenuation of the waveform, with peak-negative pressure transmission from the 0.5, 1, and 2 MHz modules measured at 0.70 ± 0.04, 0.66 ± 0.02, and 0.65 ± 0.03 relative to their baseline values, respectively.

Increasing the bubble removal pulse amplitude from 0 resulted in three distinct regimes of residual nuclei behavior, consistent with the work presented in Chapter 4 at the single sonication frequency of 500 kHz [2]. When evaluated as a function of bubble removal pulse mechanical index (MI), these regimes are markedly consistent across the 0.5 – 2 MHz frequency range investigated in this study. More specifically, at a given bubble removal sonication frequency the following general behavior is observed (with provided cutoffs being approximate values): (1) MI < 0.2: Minimal bubble coalescence with some dispersion of residual nuclei stimulated; (2) 0.2 < MI < 1.0: The aggregation and subsequent coalescence of residual nuclei becomes more pronounced with increasing MI, reaching an optimum in the vicinity of MI = 0.8; (3) MI > 1.0: The efficacy of bubble coalescence is compromised as bubble removal pulses induce high magnitude inertial cavitation, the collapse of which produces additional residual daughter nuclei. The results of optical high speed imaging documenting this behavior for bubble removal pulses at 500 kHz can be found in Chapter 4, and as such are not reproduced here.

5.3.1 Regime I: Bubble Nuclei Dispersion

At MIs of approximately 0.2 and below, minimal bubble coalescence was observed on high speed imaging; rather, these ultra-low bubble removal intensities stimulated a minimal degree of translation of the residual nuclei within the bubble removal focal volume. Correspondingly, bubble removal pulses applied at MI < 0.2 did not produce a statistically significant variation in interrogated bubble shadow area (Fig. 5.4) relative to the respective baseline cases in which the bubble removal amplitude was set to 0 (*t-test*, $P > 0.16$). An analogous result was observed for interrogation pulse transmission in this range (Fig. 5.5), with values found not to deviate from that produced with the bubble removal pulse set to 0 at each respective frequency (*t-test*, $P > 0.13$).

5.3.2 Regime II: Bubble Nuclei Coalescence

Bubble removal pulses with MIs ranging from approximately 0.2 to 1 stimulated the aggregation and subsequent coalescence of residual nuclei, the extent of which was observed to increase with increasing MI over this range. A corresponding decrease in interrogated bubble shadow area (Fig. 5.4) was generated relative to baseline for each bubble removal frequency when $MI \geq 0.2$ (*t-test*, $P < 0.02$), with this decrease becoming more pronounced and trending toward a minimum value as the bubble removal pulse MI was increased. Interrogation pulse transmission (Fig. 5.5) showed an analogous trend, as pulse attenuation was lessened and transmission observed to increase for all frequencies relative to their respective values when bubble removal was set to 0. For 0.5, 1, and 2 MHz, statistically significant increases in transmission were observed above MIs of 0.22, 0.28, and 0.20, respectively (*t-test*, $P < 0.04$). The extent of this increase became more pronounced with increasing bubble removal pulse MI, ultimately reaching a maximum for each given frequency.

The extrema observed for both the bubble shadow area and interrogation pulse transmission metrics displayed distinct characteristics based on bubble removal pulse frequency. In each case, bubble removal pulses applied at 2 MHz trended toward the extremum more rapidly in comparison to 0.5 or 1 MHz, with the value of this extremum being more pronounced. With respect to bubble shadow area, bubble removal at 2 MHz generated a rapid decrease, falling to a normalized value of 0.27 ± 0.08 by MI = 0.28. Further increases in MI within this range produced moderate reductions in bubble shadow area below this level, with the absolute minimum having a value of 0.08 ± 0.02 at an MI of 0.92. Minimums in bubble shadow area generated by 0.5 and 1 MHz bubble removal pulses had normalized values of 0.38 ± 0.06 and 0.19 ± 0.05, respectively. The minimum at 0.5 MHz fell within the range $0.57 \leq MI \leq 0.80$ (*t-test*, $P > 0.47$), while that for 1 MHz occurred in the vicinity $0.64 \leq MI \leq 1.21$ (*t-test*, $P > 0.23$). Interrogation pulse transmission in the 2 MHz case fully recovered to its baseline value by MI = 0.37, maintaining this level through MI = 0.92 (*t-test*, $P > 0.12$). Interrogation pulse transmissions at 0.5 and 1 MHz were never observed to fully recover to their respective baselines, reaching peak values of 0.88 ± 0.03 and 0.89 ± 0.04, respectively. At 0.5 MHz this transmission maximum was maintained over the range $0.57 \leq MI \leq 0.80$ (*t-test*, $P > 0.90$), while the corresponding range at 1 MHz was $0.64 \leq MI \leq 0.84$ (*t-test*, $P > 0.49$). Optical observation via high speed imaging corroborated these trends in the bubble shadow area and interrogation pulse transmission metrics, with bubble removal pulses delivered at a given intermediate MI value observed to produce more complete consolidation of residual nuclei at 2 MHz relative to that produced at 0.5 or 1 MHz.

5.3.3 Regime III: Bubble Nuclei Excitation

Bubble removal pulses with MIs exceeding approximately 1 showed a decrease in the efficacy of the bubble coalescence process with increasing MI. High speed imaging indicated that, while pulses in this range continued to stimulate the aggregation of nuclei, coalescence was compromised as a result of residual nuclei undergoing high magnitude inertial cavitation—the collapse of which produced additional residual daughter bubbles. Measurements of interrogated bubble shadow area (Fig. 5.4) show a corresponding increase in this range. At 0.5 and 2 MHz, all bubble removal pulses tested with MI > 1 produced an increase in bubble shadow area relative to the respective minimum values observed at intermediate amplitude (*t-test*, $P < 0.02$). At 1 MHz, the minimum in bubble shadow area persists to a slightly higher MI of 1.21, with bubble removal pulses applied above this value producing an increase in area consistent with the other frequencies tested (*t-test*, $P < 0.001$). Compromised bubble coalescence at high MI generated an analogous trend in interrogation pulse transmission (Fig. 5.5), with all bubble removal pulses of MI > 1 producing a reduction in transmission relative to their respective maximums observed at intermediate amplitudes. This reduction was statistically significant in all cases (*t-test*, $P < 0.01$), with the exception of 2 MHz bubble removal at an MI of 1.15 (*t-test*, $P = 0.12$). The large error bars in this later case are a result of the fact that residual nuclei were more prone to being displaced large distances (i.e., out of the path of attenuation measured by the hydrophone) at the high pressures required to achieve an MI > 1 at this highest frequency.

5.4 Discussion

The work presented in this chapter further develops a unique strategy for mitigating effects of the residual bubble nuclei produced by cavitation collapse, using low-amplitude acoustic bursts to stimulate their removal from the field via bubble coalescence. Expanding upon our preliminary work detailed in Chapter 4, here we investigated the implications of bubble removal pulse frequency on the nuclei consolidation process. It was found that all tested frequencies (0.5 – 2 MHz) were capable of stimulating the coalescence of remnant nuclei, with markedly similar trends emerging when the process is evaluated as a function of bubble removal pulse MI. The major distinction came for bubble removal pulses applied at the highest tested frequency of 2 MHz, which were observed to stimulate the most effective coalescence of residual nuclei. This is evidenced by both the backlit area of shadow (Fig. 5.4) and interrogation pulse transmission (Fig. 5.5) metrics, and corroborated by direct optical observation of the bubble coalescence process via high speed photography.

In Chapter 4 it was hypothesized that the primary and secondary Bjerknes forces are the major facilitators of the bubble coalescence process, with the secondary force being the dominant contributor. Briefly, when a bubble is driven in an acoustic field it will experience a force generated by the field itself (the primary Bjerknes force), as well as a force generated by adjacent oscillating bubbles (the secondary Bjerknes force) [10-15, 27-29]. The magnitude and direction of the primary Bjerknes force is dependent upon the phase of oscillation of the bubble relative to that of the acoustic field—which we denote as θ_s—while the magnitude and direction of the secondary Bjerknes force is dependent upon the phase of oscillation of two bubbles relative to one another—denoted as θ_b (where $\theta_b = \theta_{s2} - \theta_{s1}$). When evaluated as a function of equilibrium bubble size θ_s displays a sigmoidal-shaped dependence, with the extreme cases of bubbles being much smaller or much larger than resonant size corresponding to phase differences θ_s of 0 or π, respectively. This result can be obtained from the equations of motion when a bubble is modeled as a damped forced oscillator [14, 30].

It is an informative exercise to examine the theoretical behavior of residual bubble nuclei in this study in the framework provided by Bjerknes theory. Based on the Minnaert formula [31], the 0.5, 1, and 2 MHz bubble removal pulses evaluated here correspond to resonant bubble diameters of 12, 6, and 3 µm, respectively. The equilibrium diameter of the remnant bubble nuclei produced by the histotripsy transducer was optically sized to fall within a distribution measuring 5.6 ± 1.1 µm (mean ± SD). As such, at the lowest tested bubble removal pulse frequency of 0.5 MHz (12 µm resonant diameter) we would expect the residual nuclei to be smaller than the resonant size of the sonication frequency. This manifests in a phase difference of oscillation relative to the sound field of $0 \leq \theta_s < \pi/2$, inducing their migration up the pressure gradient and congregation at antinodes [14, 32]. Furthermore, because the size distribution of nuclei is relatively tight—residing entirely to one side of resonance—we expect the phase difference of oscillation between adjacent bubbles to fall within the range $0 \leq |\theta_b| < \pi/2$ such that the secondary Bjerknes force is attractive [10, 14, 15]. Conversely, at the highest tested bubble removal pulse frequency of 2 MHz (3 µm resonant diameter) residual nuclei should be larger than resonant size. Thus, we expect a phase difference of oscillation relative to the sound field of $\pi/2 < \theta_s \leq \pi$, promoting their migration down the pressure gradient and congregation at nodes [14, 32]. Because the size distribution of nuclei is again relatively tight and resides to one side of resonance, we expect the phase difference of oscillation of adjacent bubbles to fall within the range $0 \leq |\theta_b| < \pi/2$ such that the secondary Bjerknes force remains attractive. Lastly, at the intermediate bubble removal pulse frequency of 1 MHz the size distribution of remnant bubble nuclei is likely to be bisected by the 6 µm equilibrium diameter corresponding to resonance. As such, migration both up and down the pressure gradient could be expected as a result of the primary Bjerknes force, while all nuclei remain in a tight size distribution such that $0 \leq |\theta_b| < \pi/2$ and an attractive secondary Bjerknes force develops.

The observed behavior of residual nuclei in this study gives further support to the theory that the secondary Bjerknes force is the dominant facilitator of the bubble consolidation process. While the primary Bjerknes force is likely a contributor to the initial aggregation of nuclei at the lowest tested frequency of 0.5 MHz, its effect on consolidation is potentially counterproductive at the higher frequencies investigated in this study. Furthermore, as residual nuclei coalesce, the average equilibrium diameter of bubbles present in the field will increase. This is likely to further diminish any positive aggregative effects generated by the primary force, as bubbles further exceed resonant size and are subject to a force oriented down the pressure gradient away from the axis of consolidation. Nevertheless, pronounced aggregation and coalescence of residual nuclei was observed for all frequencies tested, implying that the secondary Bjerknes force is the major contributor to the process. The fact that bubble consolidation did not become pronounced until intermediate MIs is also consistent with this theory, as previous studies have demonstrated that the secondary Bjerknes force increases with intensity more significantly than the primary [33-35]. Finally, the dominance of the secondary Bjerknes force provides an explanation as to why the highest tested bubble removal frequency of 2 MHz generates the most effective nuclei coalescence. When residual bubble nuclei begin to coalesce and their average equilibrium diameter increases beyond the initial measured value, the resulting bubble size population will reside the farthest from resonance when sonicated at 2 MHz (relative to the other frequencies tested). As such, the phase difference of oscillation (θ_b) of bubbles within the population will be the smallest for this highest frequency, leading to a more pronounced secondary Bjerknes force (which has a dependence on $\cos(\theta_b)$ [14]).

As is discussed further in Chapter 9, future work will include the development of a mathematical simulation to verify both the relative contributions of the Bjerknes forces and the implications of bubble removal pulse frequency. Based on the empirical results presented in this chapter, we expect higher bubble removal frequencies to generate the most effective nuclei consolidation for remnant bubbles of this size. It remains to be seen if ultrasound therapy sources of different frequencies (be it histotripsy or SWL) generate remnant cavitation nuclei of varying mean size, and this will be an important consideration in determining the optimal bubble removal frequency for a given application. Furthermore, as it will be desirable for the bubble removal sound field to encompass the entire population of residual bubble nuclei, there will be practical tradeoffs between the bubble removal sonication frequency and the resulting focal dimensions. One important point in this regard is the fact that—while Chapters 4 and 5 aimed to investigate the bubble removal mechanism in a simplified environment—application of this process *in-vivo* is likely to be more complex with tissue structures influencing the distribution and mobility of remnant bubbles. The porosity of tissue with respect to these micron-sized bubbles is currently unknown. However, we expect this approach to translate directly to the fluid-filled space of the kidney's collecting system in which renal stones typically reside. As such, this bubble removal strategy is investigated as an adjunct to SWL and histotripsy kidney stone treatments in Chapters 6 and 7, respectively. A preliminary investigation regarding its application to soft tissue is detailed in Chapter 8.

5.5 Conclusion

In this chapter we further developed a novel strategy for mitigating effects of the residual bubble nuclei produced by cavitation collapse, exploring the implications of bubble removal pulse frequency on the nuclei consolidation process. It was found that, when evaluated as a function of bubble removal pulse MI, the efficacy of bubble removal shows markedly similar trends across the frequency range tested (0.5 – 2 MHz). At low bubble removal pulse MIs (approximately $MI < 0.2$) minimal effect was produced, at intermediate MIs (approximately $0.2 < MI < 1$) pronounced aggregation and coalescence of residual nuclei was generated, and at high MI (approximately $MI > 1$) residual cavitation nuclei were re-excited and the coalescence process was compromised. The main distinction in these trends was the fact that, at a given intermediate bubble removal pulse MI, the highest tested frequency of 2 MHz generated the most effective consolidation of remnant nuclei. We attribute this result to the likelihood that the secondary Bjerknes force is the major facilitator of the consolidation process, and plan to further investigate the phenomenon with the aid of mathematical simulation. It is our hope that these efforts will result in an adjunct for cavitationally based ultrasound therapies such as histotripsy and SWL, enhancing efficiencies that are currently limited by the effects of residual cavitation bubbles. The application of bubble removal pulses to SWL kidney stone comminution, histotripsy kidney stone erosion, and histotripsy soft tissue homogenization is explored in Chapters 6, 7, and 8 of this dissertation.

5.6 References

[1] A. P. Duryea, H. A. Tamaddoni, C. A. Cain, W. W. Roberts, and T. L. Hall, "Removal of residual nuclei following a cavitation event: a parametric study," *IEEE Trans Ultrason Ferroelectr Freq Control,* In-Press.

[2] A. P. Duryea, C. A. Cain, H. A. Tamaddoni, W. W. Roberts, and T. L. Hall, "Removal of Residual Nuclei Following a Cavitation Event using Low-Amplitude Ultrasound," *IEEE Trans Ultrason Ferroelectr Freq Control,* vol. 61, pp. 1619-26, Oct 2014.

[3] Y. A. Pishchalnikov, O. A. Sapozhnikov, M. R. Bailey, I. V. Pishchalnikova, J. C. Williams, and J. A. McAteer, "Cavitation selectively reduces the negative-pressure phase of lithotripter shock pulses," *Acoust Res Lett Online,* vol. 6, pp. 280-286, Nov 3 2005.

[4] Y. A. Pishchalnikov, J. A. McAteer, J. C. Williams, Jr., I. V. Pishchalnikova, and R. J. Vonderhaar, "Why stones break better at slow shockwave rates than at fast rates: in vitro study with a research electrohydraulic lithotripter," *J Endourol,* vol. 20, pp. 537-41, Aug 2006.

[5] Y. A. Pishchalnikov, J. A. McAteer, M. R. Bailey, I. V. Pishchalnikova, J. C. Williams, and A. P. Evan, "Acoustic shielding by cavitation bubbles in shock wave lithotripsy (SWL)," in *17th International Symposium on Nonlinear Acoustics* 2005, pp. 319-322.

[6] Y. A. Pishchalnikov, J. A. McAteer, and J. C. Williams, Jr., "Effect of firing rate on the performance of shock wave lithotriptors," *BJU Int,* vol. 102, pp. 1681-6, Dec 2008.

[7] J. Lautz, G. Sankin, and P. Zhong, "Turbulent water coupling in shock wave lithotripsy," *Phys Med Biol,* vol. 58, pp. 735-48, Feb 7 2013.

[8] H. Wiksell and A. C. Kinn, "Implications of cavitation phenomena for shot intervals in extracorporeal shock wave lithotripsy," *Br J Urol,* vol. 75, pp. 720-3, Jun 1995.

[9] T. Y. Wang, Z. Xu, T. L. Hall, J. B. Fowlkes, and C. A. Cain, "An efficient treatment strategy for histotripsy by removing cavitation memory," *Ultrasound Med Biol,* vol. 38, pp. 753-66, May 2012.

[10] F. G. Blake, "Bjerknes Forces in Stationary Sound Fields," *The Journal of the Acoustical Society of America,* vol. 21, pp. 551-551, 1949.

[11] E. A. Neppiras, "Subharmonic and Other Low-Frequency Emission from Bubbles in Sound-Irradiated Liquids," *The Journal of the Acoustical Society of America,* vol. 46, pp. 587-601, 1969.

[12] L. A. Crum and A. I. Eller, "Motion of Bubbles in a Stationary Sound Field," *The Journal of the Acoustical Society of America,* vol. 48, pp. 181-189, 1970.

[13] L. A. Crum, "The motion of bubbles in a stationary sound field," *The Journal of the Acoustical Society of America,* vol. 46, p. 1411, 1969.

[14] T. G. Leighton, *The Acoustic Bubble*. San Diego, CA: Academic Press Inc, 1997.

[15] L. A. Crum, "Bjerknes forces on bubbles in a stationary sound field," *The Journal of the Acoustical Society of America,* vol. 57, pp. 1363-1370, 1975.

[16] M. Chaigneau and G. Le Moan, "On the composition of gas dissolved in human urine," *C R Acad Sci Hebd Seances Acad Sci D,* vol. 267, pp. 1893-5, Nov 25 1968.

[17] J. B. Fowlkes, P. L. Carson, E. H. Chiang, and J. M. Rubin, "Acoustic generation of bubbles in excised canine urinary bladders," *J Acoust Soc Am,* vol. 89, pp. 2740-4, Jun 1991.

[18] E. Y. Hwang, J. B. Fowlkes, and P. L. Carson, "Variables controlling contrast generation in a urinary bladder model," *J Acoust Soc Am,* vol. 103, pp. 3706-16, Jun 1998.

[19] J. E. Parsons, C. A. Cain, and J. B. Fowlkes, "Cost-effective assembly of a basic fiber-optic hydrophone for measurement of high-amplitude therapeutic ultrasound fields," *J Acoust Soc Am,* vol. 119, pp. 1432-40, Mar 2006.

[20] R. J. McGough, T. V. Samulski, and J. F. Kelly, "An efficient grid sectoring method for calculations of the near-field pressure generated by a circular piston," *J Acoust Soc Am,* vol. 115, pp. 1942-54, May 2004.

[21] R. J. McGough, "Rapid calculations of time-harmonic nearfield pressures produced by rectangular pistons," *J Acoust Soc Am,* vol. 115, pp. 1934-41, May 2004.

[22] J. F. Kelly and R. J. McGough, "A time-space decomposition method for calculating the nearfield pressure generated by a pulsed circular piston," *IEEE Trans Ultrason Ferroelectr Freq Control,* vol. 53, pp. 1150-9, Jun 2006.

[23] D. Chen and R. J. McGough, "A 2D fast near-field method for calculating near-field pressures generated by apodized rectangular pistons," *J Acoust Soc Am,* vol. 124, pp. 1526-37, Sep 2008.

[24] A. D. Maxwell, C. A. Cain, T. L. Hall, J. B. Fowlkes, and Z. Xu, "Probability of Cavitation for Single Ultrasound Pulses Applied to Tissues and Tissue-Mimicking Materials," *Ultrasound in Medicine & Biology,* vol. 39, pp. 449-465, 3// 2013.

[25] Y. A. Pishchalnikov, J. A. McAteer, I. V. Pishchalnikova, J. C. Williams, M. R. Bailey, and O. A. Sapozhnikov, "Bubble proliferation in shock wave lithotripsy occurs during inertial collapse," in *18th International Symposium on Nonlinear Acoustics*, 2008, pp. 460-463.

[26] Y. A. Pishchalnikov, J. C. Williams, and J. A. McAteer, "Bubble proliferation in the cavitation field of a shock wave lithotripter," *J Acoust Soc Am,* vol. 130, pp. EL87-93, Aug 2011.

[27] V. Bjerknes, *Fields of Force*, 1906.

[28] V. Bjerknes, *Die Kraftfelder*, 1909.

[29] M. Kornfeld and L. Suvorov, "On the destructive action of cavitation," *Journal of Applied Physics,* vol. 15, pp. 495-506, 1944.

[30] P. M. Morse, *Theoretical Acoustics*: Princeton University Press, 1986.

[31] M. Minnaert, "XVI. On musical air-bubbles and the sounds of running water," *Philosophical Magazine Series 7,* vol. 16, pp. 235-248, 1933/08/01 1933.

[32] T. G. Leighton, A. J. Walton, and M. J. W. Pickworth, "Primary Bjerknes forces," *European Journal of Physics,* vol. 11, p. 47, 1990.

[33] S. Hatanaka, K. Yasui, T. Kozuka, T. Tuziuti, and H. Mitome, "Influence of bubble clustering on multibubble sonoluminescence," *Ultrasonics,* vol. 40, pp. 655-60, May 2002.

[34] W. Lauterborn, T. Kurz, R. Mettin, and C. D. Ohl, "Experimental and theoretical bubble dynamics," *Adv. Chem. Phys.,* vol. 110, pp. 295-380, 1999.

[35] R. Mettin, S. Luther, C. D. Ohl, and W. Lauterborn, "Acoustic cavitation structures and simulations by a particle model," *Ultrasonics Sonochemistry,* vol. 6, pp. 25-29, 1999.

Chapter 6

Active Removal of Residual Nuclei to Enhance SWL Efficacy at High Rate

A majority component of this chapter has been published in the *Journal of Endourology*.

© 2014 J Endourol. Reprinted, with permission, from [1].

6.1 Introduction

As introduced in the preceding chapters, the efficacy of stone comminution in shock wave lithotripsy (SWL) is highly influenced by the rate of shock wave (SW) delivery. Extensive testing, both *in-vitro* [2-6] and *in-vivo* [7], has demonstrated that the efficiency of stone fragmentation decreases with increasing SW rate. This work is corroborated by numerous human studies [8-14], in which it was observed that slow rates (60-90 SW/min) yield more successful outcomes than high rate (120 SW/min). Mechanistically, cavitation is postulated to be the primary source of rate-dependent efficacy in SWL. It is well documented that SWs can generate extensive cavitation activity along their propagation path, with the size and density of the bubble population increasing with increasing shock rate [2, 15-17]. The lifespan of SW-induced bubbles has been reported to be on the order of 1 ms [18-21], implying that they will undergo inertial collapse well before the arrival of the subsequent SW. However, recent work has shown that collapse of these primary bubbles produces a large population of smaller daughter bubbles—i.e. cavitation nuclei—that can persist on the order of 1 second [22, 23].

A SW that propagates through a medium containing residual cavitation nuclei will experience selective attenuation of its negative phase [2, 17, 24, 25]. Because the cavitation nuclei are very small (<10 μm [25]) they do not affect the compressional portion of the waveform. However, the tensile component of the SW will cause bubble nuclei to grow—a process that removes energy from the negative tail of the SW and transfers it to the propagation medium in the form of kinetic and potential energy of the fluid surrounding the bubbles [17]. As such, the negative phase of the SW that ultimately reaches the stone is attenuated both in time and amplitude, leading to decreased efficacy of stone comminution. This effect is more pronounced at high shock rates, as residual cavitation nuclei have less time to passively dissolve between successive SWs.

In Chapters 4 and 5 we examined a novel approach for the active removal of the residual bubble nuclei produced by primary cavitation collapse, using low-amplitude ultrasound pulses to stimulate their aggregation and subsequent coalescence. Here, we incorporate these bubble removal pulses in SWL treatment of model kidney stones *in-vitro* in an effort to mitigate the rate dependent efficacy resulting from remnant bubbles.

6.2 Methods

6.2.1 Experimental Setup

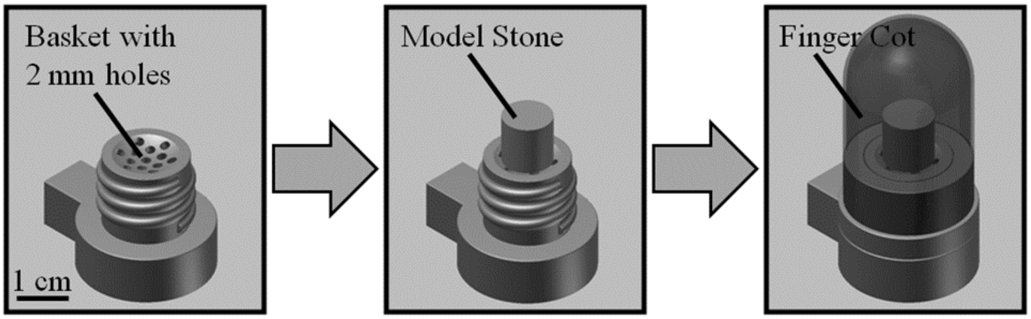

Fig. 6.1 Finger cot assembly used to hold model kidney stones during SWL treatment. The base of the structure contains a concave basket with 2 mm holes onto which stones were placed. A vinyl finger cot was used to enclose the assembly and ensure that both stone debris and cavitation nuclei remained in the treatment zone. Complete comminution was defined as the point at which all stone fragments had been reduced to <2 mm and passed through the basket.

Model stones formulated to mimic the tensile fracture strength of naturally occurring cystine calculi were cast from a mixture of BegoStone plaster (BEGO USA, Smithfield, RI), albumin (Carolina Biological Supply Co., Burlington, NC), and tap water [26]. A Delrin (DuPont, Wilmington, DE) plastic mold was used to create stone cylinders measuring 1 cm in diameter and having an initial hydrated mass of 1.02 ± 0.03 g (mean ± SD, $n = 30$). During treatment, stone phantoms were held within a finger cot assembly (Fig. 6.1). The base of this structure is composed of Accura-60 (3D Systems Inc., Rock Hill, SC) plastic fabricated on a stereolithography machine. It contains a concave basket with 2 mm holes on which the stone was placed for treatment; when stone debris was reduced to sub-2 mm size, it was able to pass through the basket and was considered treated. A vinyl finger cot (Wesco Enterprises Inc., Santa Fe Springs, CA) measuring approximately 2 cm in diameter and 3 cm in height was used to enclose the assembly and ensure that both the stone and cavitation nuclei remained in the treatment zone. The finger cot assembly was filled with deionized water degassed to a dissolved oxygen level 80% ± 2% of saturation in order to mimic that of urine [27]. It was subsequently placed into a larger treatment tank measuring 60 x 30 x 45 cm (L x W x H) that contained degassed water (dissolved oxygen level <15 % of saturation) with a conductivity of 600 µS/cm (Fig. 6.2).

SWL was delivered using an electrohydraulic research system designed to simulate the acoustic field generated by the Dornier HM3 [28-30]. A charging voltage of 20 kV was used for all treatments, which was calibrated to produce an acoustic shock wave having a peak positive pressure (P+) of 34 MPa and a peak negative pressure (P-) of 8 MPa. Electrohydraulic SWL electrodes were preconditioned using 200 SWs at 60 SW/min, and each electrode was replaced following the generation of 2000 SWs.

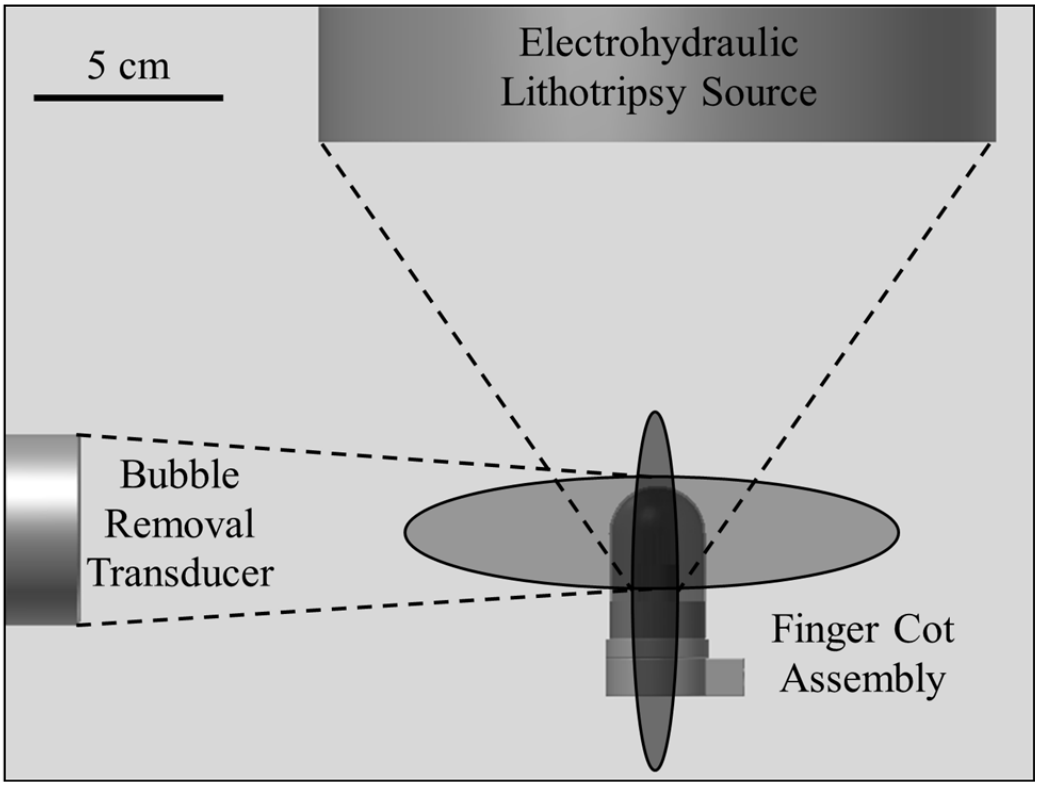

Fig. 6.2 Experimental setup used to assess SWL comminution efficacy. The finger cot assembly used to hold model stones was filled with deionized water degassed to a dissolved oxygen level 80% of saturation to mimic that of urine; it was subsequently placed into a larger treatment tank containing degassed water (dissolved oxygen level <15 % of saturation) with a conductivity of 600 µS/cm. SWs were delivered from a research electrohydraulic lithotripter patterned after the Dornier HM3, while bubble removal pulses were generated by a separate piezoelectric transducer oriented orthogonal to the axis of SW propagation.

Bubble removal pulses were generated by a separate piezoelectric transducer (Steiner & Martins Inc., Miami, FL) firing orthogonal to the SW propagation axis (Fig. 6.2). This transducer was composed of a flat disc with an active area measuring 5 cm in diameter, and generated a natural focal zone with -6-dB beamwidths measuring 2.5 cm in the lateral dimension and 14 cm in the axial; this natural focus was centered coincident with that of the electrohydraulic lithotripter. The bubble removal transducer was driven using an ENI AP400B controllable power amplifier (Electronic Navigation Industries Inc., Rochester, NY) with 100 ms pulses at 370 kHz. A driving voltage of 470 $V_{pk\text{-}pk}$ was utilized, which was calibrated to generate an acoustic output amplitude of 500 kPa. The timing scheme used for incorporating bubble removal pulses between successive

SWs is displayed in Fig. 6.3. Following a given SW, a 500 μs delay was imposed before the arrival of the 100 ms bubble removal pulse. This allowed primary cavitation induced by the SW to undergo an unimpeded growth-collapse cycle prior to the sonication of remnant bubble nuclei.

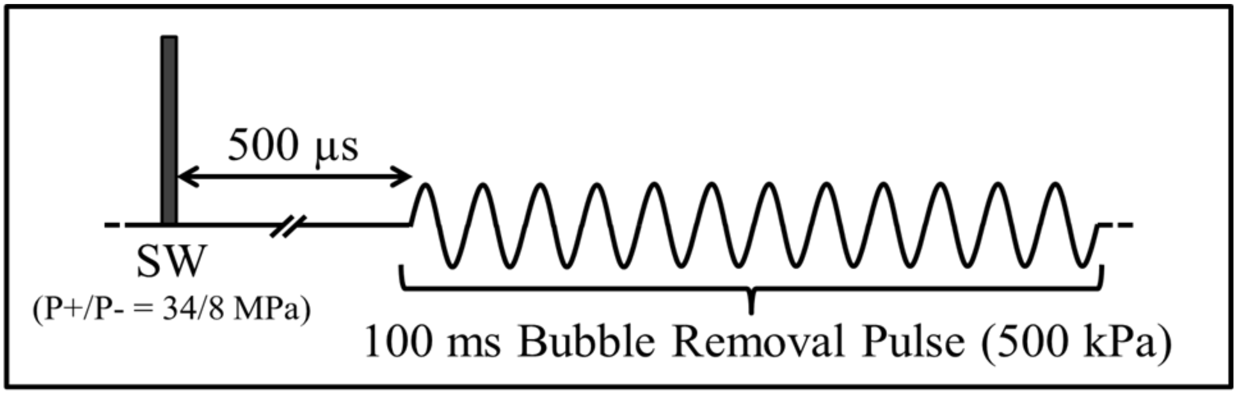

Fig. 6.3 Pulse timing utilized for SWL treatments incorporating bubble removal pulses. A 500 μs delay was imposed between the SW and bubble removal pulse in order to allow SW-induced cavitation to undergo an uninhibited growth-collapse cycle. Bubble removal pulses had a frequency of 370 kHz, duration of 100 ms, and amplitude of 500 kPa.

6.2.2 Treatment Schemes

To test the efficacy of active bubble removal in SWL, six different treatment schemes were applied to five model stones each. These included: (1) SWL at 120 SW/min and (2) SWL at 120 SW/min with bubble removal; (3) SWL at 60 SW/min and (4) SWL at 60 SW/min with bubble removal; (5) SWL at 30 SW/min and (6) SWL at 30 SW/min with bubble removal. Stones were treated until all debris had passed through the 2 mm holes of the basket in the finger cot assembly. The number of SWs required to achieve this complete comminution was recorded for each treatment.

6.2.3 Optical Cavitation Monitoring

In a separate set of experiments, the cavitation environment in the vicinity of the stone was optically monitored such as to correlate comminution efficacy to the extent of prefocal bubble excitation. An acrylic stone phantom, rather than BegoStone composites, was utilized for these imaging experiments in order to prevent stone debris from shielding our view of cavitation bubbles. In the same regard, the finger cot was removed from the stone holder assembly to provide an unobstructed imaging path. The entire treatment tank was maintained at a dissolved oxygen level 80% of saturation in this case, as the finger cot was no longer present to create a secluded treatment environment surrounding the stone. For each of the six treatment schemes, a sequence of 50 SWs was applied to the acrylic stone phantom. A single backlit image with 10 μs exposure was acquired 240 μs following the firing of each SW using a Point Grey Chameleon camera (Point Grey Research Inc., Richmond, BC, Canada). This timing was empirically determined to correspond to the point of maximum SW-induced prefocal bubble excitation.

6.3 Results

Stone comminution resulting from each treatment scheme is summarized in Fig. 6.4, while the corresponding level of prefocal bubble excitation is displayed in Fig. 6.5.

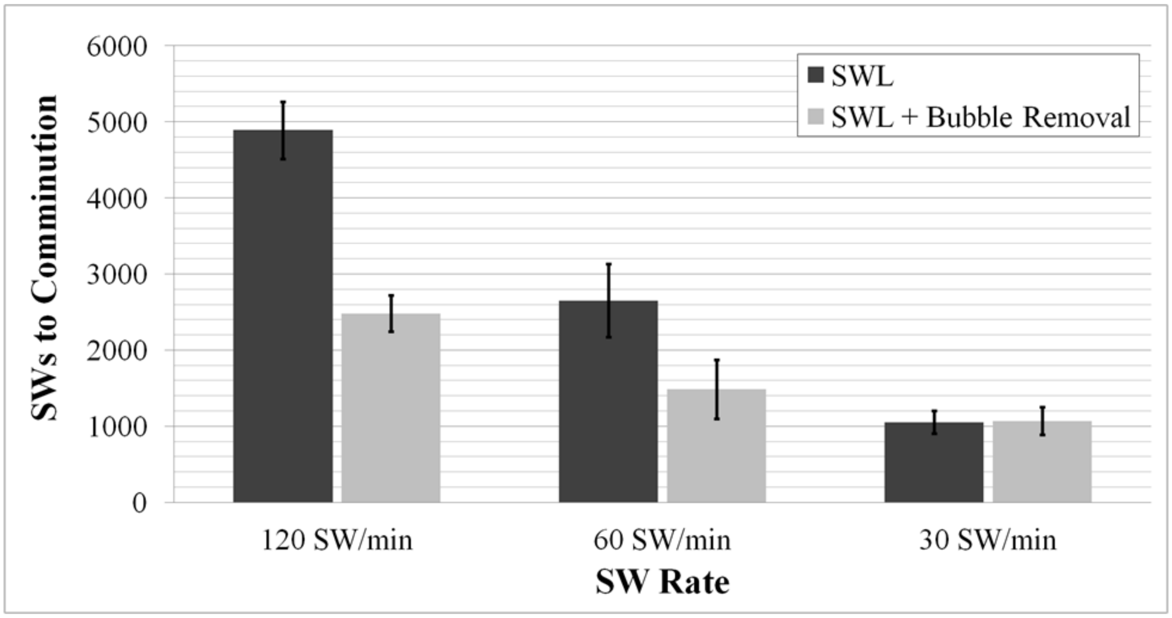

Fig. 6.4 Number of SWs required to achieve complete stone comminution (all debris <2 mm). The 'per-shock' efficiency of conventional SWL was observed to increase as the shock rate was decreased. The incorporation of bubble removal pulses resulted in a drastic reduction in the number of SWs required for complete treatment at both 120 SW/min and 60 SW/min, while bubble removal produced no detectable difference in comminution efficacy at the lower rate of 30 SW/min.

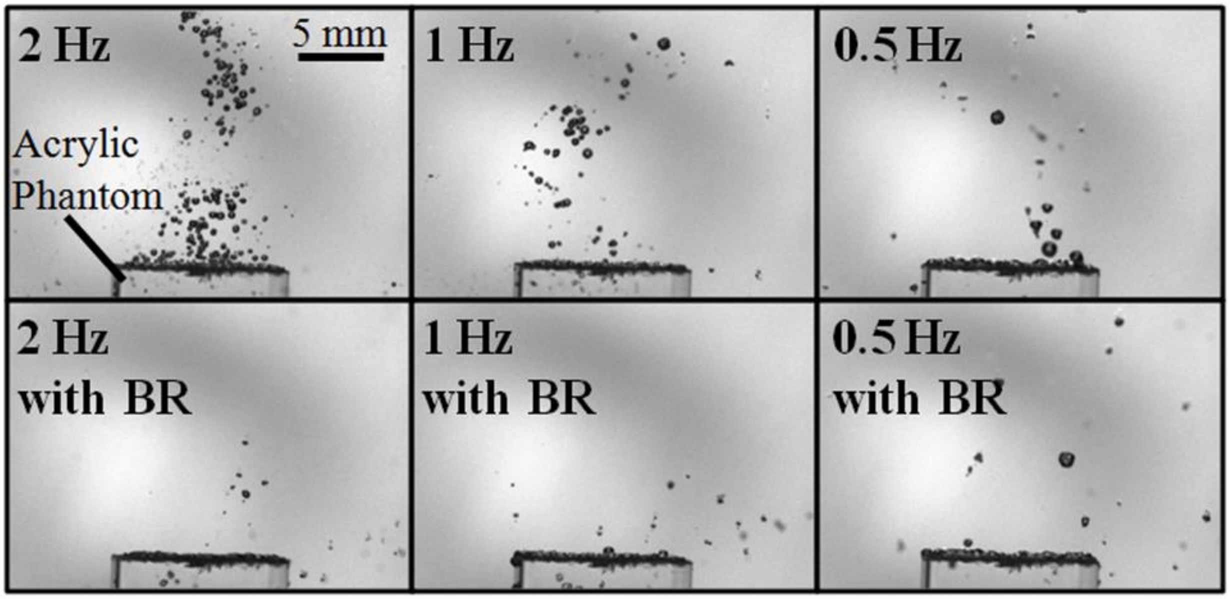

Fig. 6.5 Representative images capturing the degree of SW-induced prefocal bubble excitation for the six treatment schemes tested in this study. Each image corresponds to the 25th SW in a series of 50 SWs applied at the indicated rate. Cavitation along the SW axis was observed to decrease with decreasing rate in conventional SWL (top row). The introduction of bubble removal (BR) pulses drastically reduced this cavitation at rates of 120 SW/min and 60 SW/min, whereas minimal bubble excitation was produced along the SW axis at the lower rate of 30 SW/min with or without bubble removal.

6.3.1 SWL without Bubble Removal

Consistent with previous studies the number of SW required to achieve complete stone comminution in conventional SWL was observed to decrease with decreasing shock rate (*t-test*, $P < 0.0001$), indicating that the per-shock efficiency is higher when a lower rate is used. Correspondingly, the extent of SW-induced bubble excitation was found to decrease as the shock rate was lowered from 120 to 30 SW/min (Fig. 6.5, top row).

6.3.2 SWL with Bubble Removal

The introduction of bubble removal pulses resulted in a statistically significant reduction in the number of SWs required to achieve complete comminution at both 120 and 60 SW/min (*t-test*, $P \leq 0.003$). The most pronounced effect was observed at the highest utilized rate of 120 SW/min. Here, conventional SWL required 4893 ± 375 SW to achieve complete comminution, whereas incorporation of bubble removal pulses decreased the required number of SWs to 2482 ±

239 (*t-test* P < 0.0001). Imaging of the cavitation environment surrounding the stone at this rate shows a drastic reduction in bubble excitation along the SW axis with the addition of bubble removal pulses (Fig. 6.5, leftmost column). Incorporation of bubble removal pulses at 60 SW/min also produced a prominent effect, reducing the number of SWs required for complete comminution from 2652 ± 482 to 1487 ± 388 (*t-test*, P = 0.003). Analogous to the case of 120 SW/min, a decrease in bubble excitation along the SW axis is apparent with the addition of bubble removal pulses (Fig. 6.5, middle column).

The addition of bubble removal pulses in SWL applied at a lower rate of 30 SW/min did not produce any detectable effect on treatment efficacy, with complete comminution requiring 1054 ± 152 SW for conventional SWL and 1070 ± 182 SW for SWL with bubble removal (*t-test*, P = 0.88). Correspondingly, the degree of bubble excitation was minimal for these two cases (Fig. 6.5, rightmost column).

6.4 Discussion

The results documented in this chapter corroborate previous work regarding the role of cavitation in SWL rate dependent efficacy. Consistent with earlier studies [2-7], we observed the efficiency of SWL stone comminution to decrease as the rate of SW application was increased (Fig. 6.4). As was also observed by others [2, 15-17], optical monitoring of the cavitation environment in the vicinity of the stone showed that the size and density of the bubble population increased with increasing shock rate (Fig. 6.5). The introduction of bubble removal pulses drastically increased per-shock efficiency at rates of 120 SW/min and 60 SW/min (Fig. 6.4.), and corresponding images showed a pronounced reduction in bubble excitation along the SW propagation path (Fig. 6.5). This supports the idea that excitation of remnant bubble nuclei limits the efficacy of SWs [2, 17, 24, 25], and indicates that removing them from the field between successive SWs can drastically improve stone comminution. A similar result has been documented by Lautz, *et al.* [31], who used a jet of degassed water to remove cavitation nuclei from the coupling cushion of an electromagnetic lithotripter and improve stone fragmentation *iv-vitro*. In their study it was demonstrated that incorporation of the water jet between successive SWs resulted in a reduction in prefocal cavitation; correspondingly, hydrophone measurements indicated that attenuation of the SW's negative phase was mitigated when the jet was present.

Other recent work exploring the role of cavitation in SWL has further characterized rate dependent comminution as the result of bubble proliferation [22, 23]. It was found that inertial collapse and jetting of primary SW-induced bubbles produces a cloud of smaller daughter nuclei, with a single primary bubble giving rise to dozens of residual daughters. Furthermore, as bubbles proliferated from shot to shot, the amplitude of the negative phase of the SWs was observed to decline. At higher shock rates this proliferation of bubbles was more substantial, presumably due to the fact that there is less time for bubble dissolution between successive shocks. The authors of the study went on to conclude that it may take very few bubbles to seed a substantial cavitation cloud—and as such, substantial reduction of the tensile component of the SW—at rates used in clinical SWL. In this regard, the bubble removal pulses utilized in this study can be viewed as a means of mitigating the bubble proliferation phenomenon. If we can prevent the build-up of substantial cavitation by coalescing the daughter nuclei following each SW, the overall efficacy of the treatment should be much improved.

The bubble removal strategy presented in this dissertation offers a promising approach for enhancing the efficacy of SWL therapy. If per-shock efficiency can be maintained at high rates of SW application, treatments could be performed faster with more complete stone comminution. However, it should be noted that high shock rates are associated with increased collateral tissue damage, and an evaluation of the ability of bubble removal pulses to mitigate this damage remains for future work. In the present study bubble removal was observed to decrease the time to complete comminution by 49% and 44% at shock rates of 120 and 60 SW/min, respectively. These results were acquired using a relatively hard stone model (cystine-mimicking), and we anticipate similar improvements in comminution for more typical stone compositions such as calcium oxalate. Finally, while the results in this chapter offer promising results in an *in-vitro* setting, translation to an *in-vivo* model is a crucial next step in demonstrating the viability of bubble removal as an adjunct to SWL therapy. As is discussed further in Chapter 9, our future work will include an assessment of both stone comminution and collateral tissue effects resulting from the incorporation of bubble removal pulses in an *in-vivo* setting.

6.5 Conclusion

Active removal of residual bubble nuclei following a SW pulse can dramatically improve the *in-vitro* comminution efficacy of SWL at higher rates (120 SW/min and 60 SW/min). This supports the concept that remnant bubble nuclei that persist from shock to shock have deleterious effects on stone comminution, corroborating previous work regarding the role of cavitation in the rate dependent efficacy of SWL. Further development of this approach for active bubble removal could translate to faster and more complete SWL therapy.

6.6 References

[1] A. P. Duryea, W. W. Roberts, C. A. Cain, H. A. Tamaddoni, and T. L. Hall, "Acoustic bubble removal to enhance SWL efficacy at high shock rate: an in vitro study," *J Endourol*, vol. 28, pp. 90-5, Jan 2014.

[2] Y. A. Pishchalnikov, J. A. McAteer, J. C. Williams, Jr., I. V. Pishchalnikova, and R. J. Vonderhaar, "Why stones break better at slow shockwave rates than at fast rates: in vitro study with a research electrohydraulic lithotripter," *J Endourol*, vol. 20, pp. 537-41, Aug 2006.

[3] G. Vallancien, R. Munoz, M. Borghi, B. Veillon, J. M. Brisset, and M. Daudon, "Relationship between the frequency of piezoelectric shock waves and the quality of renal stone fragmentation. In vitro study and clinical implications," *Eur Urol,* vol. 16, pp. 41-44, 1989.

[4] H. Wiksell and A. C. Kinn, "Implications of cavitation phenomena for shot intervals in extracorporeal shock wave lithotripsy," *Br J Urol,* vol. 75, pp. 720-3, Jun 1995.

[5] A. Greenstein and H. Matzkin, "Does the rate of extracorporeal shock wave delivery affect stone fragmentation?," *Urology,* vol. 54, pp. 430-432, 1999.

[6] M. J. Weir, N. Tariq, and R. J. Honey, "Shockwave frequency affects fragmentation in a kidney stone model," *J Endourol,* vol. 14, pp. 547-50, Sep 2000.

[7] R. F. Paterson, D. A. Lifshitz, J. E. Lingeman, A. P. Evan, B. A. Connors, N. S. Fineberg, *et al.*, "Stone fragmentation during shock wave lithotripsy is improved by slowing the shock wave rate: studies with a new animal model," *J Urol,* vol. 168, pp. 2211-5, Nov 2002.

[8] K. Madbouly, A. M. El-Tiraifi, M. Seida, S. R. El-Faqih, R. Atassi, and R. F. Talic, "Slow versus fast shock wave lithotripsy rate for urolithiasis: a prospective randomized study," *J Urol,* vol. 173, pp. 127-30, Jan 2005.

[9] E. Yilmaz, E. Batislam, M. Basar, D. Tuglu, C. Mert, and H. Basar, "Optimal frequency in extracorporeal shock wave lithotripsy: prospective randomized study," *Urology,* vol. 66, pp. 1160-4, Dec 2005.

[10] K. T. Pace, D. Ghiculete, and M. Harju, "Shock wave lithotripsy at 60 or 120 shocks per minute: A randomized, double-blind trial," *The Journal of Urology,* vol. 174, pp. 595-599, 2005.

[11] J. Chacko, M. Moore, N. Sankey, and P. S. Chandhoke, "Does a slower treatment rate impact the efficacy of extracorporeal shock wave lithotripsy for solitary kidney or ureteral stones?," *J Urol,* vol. 175, pp. 1370-1373, 2006.

[12] Y. Kato, S. Yamaguchi, J. Hori, M. Okuyama, and H. Kakizaki, "Improvement of stone comminution by slow delivery rate of shock waves in extracorporeal lithotripsy," *Int J Urol,* vol. 13, pp. 1461-5, Dec 2006.

[13] D. Weiland, C. Lee, R. Ugarte, and M. Monga, "Impact of shockwave coupling on efficacy of extracorporeal shockwave lithotripsy," *J Endourol,* vol. 21, pp. 137-40, Feb 2007.

[14] M. J. Semins, B. J. Trock, and B. R. Matlaga, "The effect of shock wave rate on the outcome of shock wave lithotripsy: a meta-analysis," *J Urol,* vol. 179, pp. 194-7; discussion 197, Jan 2008.

[15] O. A. Sapozhnikov, V. A. Khokhlova, M. R. Bailey, J. C. Williams, Jr., J. A. McAteer, R. O. Cleveland, *et al.*, "Effect of overpressure and pulse repetition frequency on cavitation in shock wave lithotripsy," *J Acoust Soc Am,* vol. 112, pp. 1183-95, Sep 2002.

[16] P. Huber, K. Jochle, and J. Debus, "Influence of shock wave pressure amplitude and pulse repetition frequency on the lifespan, size and number of transient cavities in the field of an electromagnetic lithotripter," *Phys Med Biol,* vol. 43, pp. 3113-28, Oct 1998.

[17] Y. A. Pishchalnikov, O. A. Sapozhnikov, M. R. Bailey, I. V. Pishchalnikova, J. C. Williams, and J. A. McAteer, "Cavitation selectively reduces the negative-pressure phase of lithotripter shock pulses," *Acoust Res Lett Online,* vol. 6, pp. 280-286, Nov 3 2005.

[18] W. Sass, H. P. Dreyer, S. Kettermann, and J. Seifert, "The role of cavitational activity in fragmentation processes by lithotripters," *J Stone Dis,* vol. 4, pp. 193-207, Jul 1992.

[19] P. Zhong, I. Cioanta, F. H. Cocks, and G. M. Preminger, "Inertial cavitation and associated acoustic emission produced during electrohydraulic shock wave lithotripsy," *J Acoust Soc Am,* vol. 101, pp. 2940-50, May 1997.

[20] P. Zhong, H. L. Tong, F. H. Cocks, and G. M. Preminger, "Transient oscillation of cavitation bubbles near stone surface during electrohydraulic lithotripsy," *J Endourol,* vol. 11, pp. 55-61, Feb 1997.

[21] R. O. Cleveland, O. A. Sapozhnikov, M. R. Bailey, and L. A. Crum, "A dual passive cavitation detector for localized detection of lithotripsy-induced cavitation in vitro," *J Acoust Soc Am,* vol. 107, pp. 1745-58, Mar 2000.

[22] Y. A. Pishchalnikov, J. A. McAteer, I. V. Pishchalnikova, J. C. Williams, M. R. Bailey, and O. A. Sapozhnikov, "Bubble proliferation in shock wave lithotripsy occurs during inertial collapse," in *18th International Symposium on Nonlinear Acoustics*, 2008, pp. 460-463.

[23] Y. A. Pishchalnikov, J. C. Williams, and J. A. McAteer, "Bubble proliferation in the cavitation field of a shock wave lithotripter," *J Acoust Soc Am,* vol. 130, pp. EL87-93, Aug 2011.

[24] Y. A. Pishchalnikov, J. A. McAteer, M. R. Bailey, I. V. Pishchalnikova, J. C. Williams, and A. P. Evan, "Acoustic shielding by cavitation bubbles in shock wave lithotripsy (SWL)," in *17th International Symposium on Nonlinear Acoustics* 2005, pp. 319-322.

[25] Y. A. Pishchalnikov, J. A. McAteer, and J. C. Williams, Jr., "Effect of firing rate on the performance of shock wave lithotriptors," *BJU Int,* vol. 102, pp. 1681-6, Dec 2008.

[26] W. N. Simmons, F. H. Cocks, P. Zhong, and G. Preminger, "A composite kidney stone phantom with mechanical properties controllable over the range of human kidney stones," *J Mech Behav Biomed Mater,* vol. 3, pp. 130-3, Jan 2010.

[27] E. A. Gardner, J. B. Fowlkes, P. L. Carson, J. A. Ivey, and D. A. Ohl, "Bubble generation in excised canine urinary bladders using an electrohydraulic lithotripter " in *IEEE Ultrasonics Symposium*, 1993, pp. 905-908.

[28] A. J. Coleman, J. E. Saunders, and M. J. Choi, "An experimental shock wave generator for lithotripsy studies," *Phys Med Biol,* vol. 34, pp. 1733-42, Nov 1989.

[29] R. O. Cleveland, M. R. Bailey, N. Fineberg, B. Hartenbaum, M. Lokhandwalla, J. A. McAteer, *et al.*, "Design and characterization of a research electrohydraulic lithotripter patterned after the Dornier HM3," *Rev. Sci. Instrum.*, vol. 71, pp. 2514-2525, 2000.

[30] A. P. Duryea, W. W. Roberts, C. A. Cain, and T. L. Hall, "Optically triggered solid state driver for shock wave therapy," in *Int. Society for Therapeutic Ultrasound Symp.*, 2011, pp. 76-80.

[31] J. Lautz, G. Sankin, and P. Zhong, "Turbulent water coupling in shock wave lithotripsy," *Phys Med Biol,* vol. 58, pp. 735-48, Feb 7 2013.

Chapter 7

Active Removal of Residual Nuclei to Enhance Histotripsy Kidney Stone Erosion at High Pulse Rate

A majority component of this chapter is in-press in *IEEE Transactions on Ultrasonics, Ferroelectrics, and Frequency Control*. © 2015 IEEE. Reprinted, with permission, from [1].

7.1 Introduction

Chapters 2 and 3 of this dissertation present studies demonstrating the capability of histotripsy to effectively erode model urinary stones via a cavitational bubble cloud localized on the stone surface [2-4]. To reiterate briefly, stone comminution with histotripsy displays characteristics in stark contrast to those observed in shock wave lithotripsy (SWL). Whereas SWL comminutes stones in a progressive manner—first into large pieces and then to fragments of decreasing size [5]—debris resulting from histotripsy erosion is composed of tiny particulate dust from the onset of treatment [2-4]. Furthermore, because histotripsy stone treatment is a surface erosion phenomenon, the rate of erosion is dependent on the exposed stone surface area [4, 6]. These facts lend themselves to a natural synergism between SWL and histotripsy stone treatments (explored in Chapter 3), as fragments generated by SWL can be rapidly eroded to fine debris via histotripsy pulses after initial stone subdivision is achieved [4].

While histotripsy offers a promising adjunct to traditional SWL stone treatments, much room is available for the optimization of histotripsy pulse sequences for the application of stone erosion. Indeed, previous work has indicated that histotripsy stone erosion displays a rate-dependent efficacy, with histotripsy applied at low pulse repetition frequency (PRF) producing more efficient stone erosion in comparison to that applied at high PRF [6]. As discussed in detail in Chapter 6, a similar phenomenon is well documented in SWL, with testing both *in-vitro* [7-11] and *in-vivo* [12] showing a decrease in per-shock fragmentation efficiency with increasing shock rate. This is attributed to residual cavitation bubble nuclei that persist from one lithotripsy shock wave (LSW) to the next. While primary cavitation induced by an LSW has been identified as a crucial component of the stone comminution process [5, 13-18], its collapse is typically accompanied by fission into numerous microscopic residual daughter bubbles [19-22] which can persist on the order of a full second [21-24]. It has been shown that LSW propagation through a medium containing these residual daughters induces the selective attenuation of its negative tail [7, 25-27], reducing the energy that ultimately reaches the stone and compromising comminution efficiency. The use of higher shock rates reduces the time available for passive dissolution of residual bubble nuclei between successive LSWs, leading to more pronounced attenuative effects.

The work presented in Chapters 4 and 5 aimed to develop a strategy for the active removal of residual bubble nuclei following a cavitation event [28, 29]. It was demonstrated that the application of appropriately designed low-amplitude ultrasound pulses can stimulate the aggregation and subsequent coalescence of a population of residual bubbles, effectively removing them from the field. These pulses—which we term bubble removal pulses—are typically on the order of one millisecond in duration and have maximal nuclei consolidation effects near a mechanical index (MI) of 1 [28, 29]. In Chapter 6 this bubble removal strategy was applied to

SWL treatment of model stones *in-vitro* to enhance the per-shock efficiency when high shock rates are used.

In the present chapter, we incorporate bubble removal pulses into histotripsy treatment of model kidney stones in an effort to alleviate the rate-dependent efficacy previously observed for histotripsy stone erosion. Cystine-mimicking model stones were sonicated with histotripsy pulses applied at PRFs ranging from 1—500 Hz; at each rate, comminution was quantified with and without the incorporation of bubble removal pulses. It is our hope that this investigation will not only lead to drastic improvements in the efficiency of histotripsy stone erosion at high PRF, but also serve to expand our understanding regarding the complex role of cavitation in the stone comminution process.

7.2 Methods

7.2.1 Preparation of Model Urinary Stones

Composite stone phantoms formulated to mimic the tensile fracture strength of naturally occurring cystine calculi were cast from a mixture of BegoStone plaster (BEGO USA, Smithfield, RI), albumin (Carolina Biological Supply Co., Burlington, NC), and tap water. Following the methods of Simmons, *et al*. [30] the constituents were mixed with a mass ratio of 73% BegoStone, 24.5% water, and 2.5% albumin in order to achieve the desired stone properties. 0.6 mL aliquots of the resulting slurry were then distributed into the 1 cm diameter cylindrical wells of a Delrin (DuPont, Wilmington, DE) plastic mold and allowed to cure overnight. The next day, stones were removed from the mold and slowly heated to 90˚C in a low-temperature oven (Model 10GC, Quincy Lab Inc., Chicago, IL), where they were held for 12 hours to permit albumin polymerization. Finally, stones were allowed to cool back to room temperature and submersed in a beaker of tap water to hydrate. Prior to treatment, phantoms in the hydrated state were degassed overnight in a vacuum desiccator (Bel-Art Products, Wayne, NJ) to minimize any air trapped in the stone material. The end result of this process was the production of cylindrical model stones measuring 1 cm in diameter and having a hydrated mass of 1.01 ± 0.03 g (mean ± SD, n = 45).

7.2.2 Experimental Setup

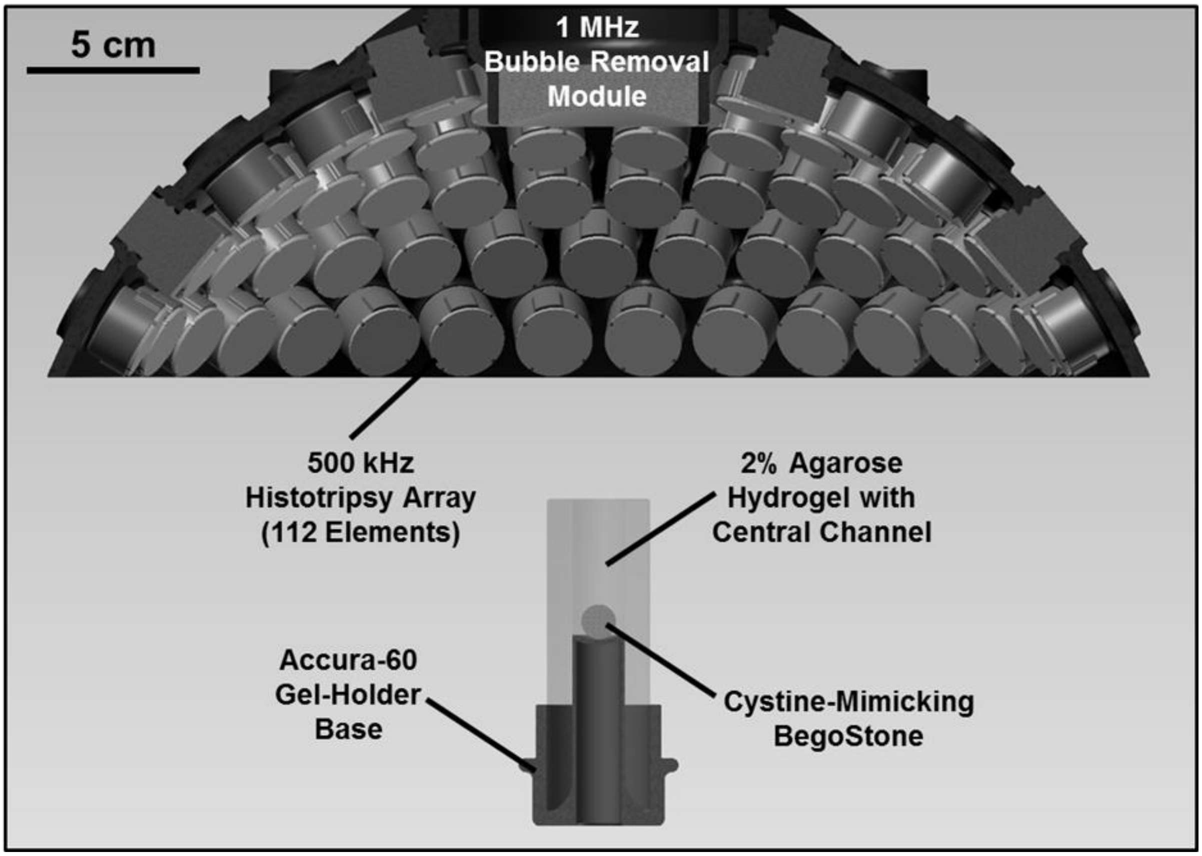

Fig. 7.1 Experimental setup used to study the effect of bubble removal pulses on histotripsy erosion of model kidney stones. Histotripsy treatment was delivered from a transducer composed of 112 individual 500 kHz modules arranged in a spherical cap pattern, while a separate 1 MHz transducer aligned confocally with the histotripsy array was used to generate bubble removal pulses. Cystine-mimicking BegoStones were positioned within an agarose hydrogel holder for treatment; this assembly was placed below the transducer such that sonication was performed in a top-down orientation.

The experimental setup used to study the impact of bubble removal pulse sequences on histotripsy erosion of model kidney stones is displayed in Fig. 7.1. All experiments were conducted in a water tank measuring 58 x 43 x 45 cm (L x W x H), which was filled with deionized water degased to physiologically relevant levels (dissolved oxygen content of 7.0 ± 0.3 mg/L at 21.2 ±

1.2 °C, corresponding to 77 ± 3% of saturation); this mimics the dissolved gas content of human urine, for example [31-33]. Dissolved oxygen levels were measured at the beginning and end of each treatment day (n = 18) using a Traceable Digital Oxygen Meter (Control Co., Friendswood, TX).

A 500 kHz histotripsy transducer constructed in-house was used to deliver histotripsy therapy to the model stones treated in this study. It consisted of 112 individual watertight modules arranged in a spherical cap pattern with a 150 mm radius of curvature and 270 mm aperture. This geometry was maintained via a scaffold fabricated from Accura 60 plastic (3D Systems Inc., Rock Hill, SC) on a stereolithography machine. Individual module housings were also fabricated from Accura 60 using stereolithography. Within each, two 1-MHz Pz36 disc elements (Ferroperm Piezoceramics A/S, Kvistgaard, Denmark) measuring 20 mm in diameter and 1.6 mm in thickness were stacked and driven in unison to produce a 500-kHz equivalent source. Epoxy adhesive (Hysol E-120 HP, Loctite Corporation, Rocky Hill, CT) was used to bond the individual Pz36 elements together, as well as mate the front face of each stack to a flat Accura-60 disc. The latter provided both electrical insulation and acoustic matching between the elements and water. A marine grade epoxy (TAP Epoxy System 314 Resin/143 Hardener, TAP Plastics Inc., San Leandro, CA) was used to pot the back of each module, ensuring complete electrical insulation from the surrounding water. Overall, this arrangement of 112 modules produced a focal zone having -6-dB beamwidths measuring 2.0 mm in the lateral dimension and 6.3 mm in the axial. These measurements were conducted at a pressure amplitude of 8 MPa (linear regime) using a fiber optic hydrophone with a 100-µm-diameter sensing tip [34]. The histotripsy transducer was driven using a pulse amplifier developed in our lab, which was designed to produce very short, intense bursts. More details regarding the acoustic output generated by this setup are provided in the subsequent section.

A separate 1 MHz transducer—which we denote as the bubble removal module—was used to sonicate residual bubble nuclei produced by collapse of the histotripsy bubble cloud. It consisted of a single 1 MHz PZT-4 disc element (Steiner & Martins Inc., Miami, FL) measuring 50 mm in diameter and 2 mm in thickness. This frequency was selected based on our previous observation that bubble removal pulses of higher frequency (>500 kHz) produce more effective consolidation of residual nuclei following histotripsy bubble cloud collapse [29]. Similar to the histotripsy modules, the PZT-4 element was sealed within a stereolithography-fabricated Accura-60 housing. In this case the front face of the housing contained an acoustic lens having a focal length of 175 mm; this design was utilized to center the beam of the bubble removal module coincident with the histotripsy focus when the module was held within a central port in the histotripsy transducer scaffold (Fig. 7.1). The PZT-4 element was matched to the lens using an epoxy (1C-LV Hysol, Loctite Corporation, Rocky Hill, CT) filled 50 mesh copper screen (McMaster-Carr, Aurora, OH) to achieve the proper thickness and impedance. This arrangement produced an acoustic field with -6-dB beamwidths measuring 7.0 mm in the lateral dimension and exceeding 100 mm in the axial; as such, the bubble removal field fully encompassed the focal zone generated by the histotripsy transducer. These field scans were performed at a pressure amplitude of 300 kPa (linear regime) using an HNR-0500 needle hydrophone (Onda Corporation, Sunnyvale, CA). The bubble removal module was driven using a 1 MHz sinusoid from an ENI AP400B controllable power amplifier (Electronic Navigation Industries Inc., Rochester, NY); further details on the acoustic output are presented in the subsequent section.

Cystine-mimicking BegoStone cylinders were held within a gel-holder assembly designed to maintain stone position within the focal zone while minimizing attenuation of incident acoustic pulses (Fig. 7.1). The gel-holder was constructed from Accura 60 plastic and contained a concave pedestal onto which stone phantoms were ultimately placed. An optically transparent 2% agarose hydrogel (LabScientific MB Grade AG-SP, LabScientific Inc., Livingston, NJ) was cast surrounding this pedestal, creating a central channel measuring 15 mm in diameter and 40 mm in height. Stone phantoms were free to move/rotate within the channel during sonication; however, the dimensions were such that the full extent of the histotripsy focal zone was always maintained on the stone surface. As indicated in Fig. 7.1, the gel-holder assembly was positioned below the histotripsy transducer and stones were sonicated in a top-down orientation. Alignment of the therapy focus to the stone was maintained on an inter-trial basis via two lasers laterally positioned at the known geometric focal location.

7.2.3 Acoustic Pulse Sequence

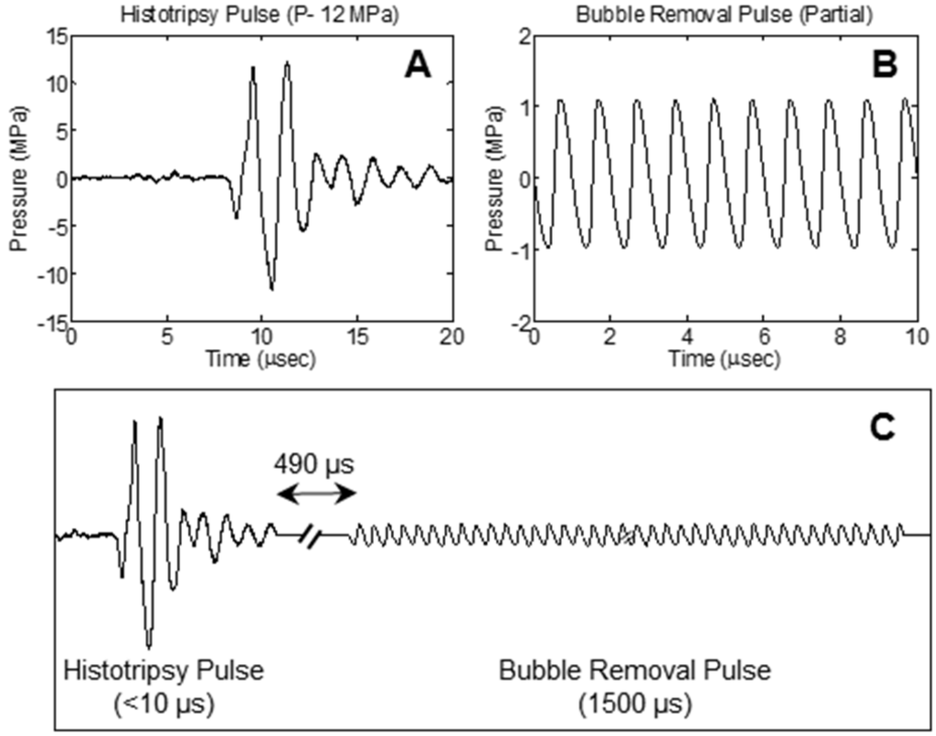

Fig. 7.2 General pulse scheme used to study the effect of bubble removal pulses on histotripsy erosion of model kidney stones. (A) Representative waveform acquired from the 500 kHz histotripsy transducer at low power (below the cavitation threshold). The histotripsy pulse P- used for stone treatments is estimated to be 45 MPa. (B) Partial segment of the 1500 µs bubble removal pulse; all bubble removal pulses had a center frequency of 1 MHz, and MI set to either 0 or 1. (C) Overall timing of the experimental pulse scheme. A 500 µs delay was imposed following histotripsy pulse firing to allow the bubble cloud to collapse in an unimpeded manner.

Two general types of acoustic pulses were utilized in this study, as represented in Fig. 7.2(A-B): 1) Histotripsy pulses generated by the 500 kHz histotripsy transducer were used to initiate a cavitational bubble cloud at the surface of the stone phantom, generating erosion damage consistent with our previous work [2-4]; 2) Bubble removal pulses produced by the 1 MHz bubble removal module were used to sonicate residual nuclei following histotripsy bubble cloud collapse, stimulating their coalescence and removal from the field. The overall timing of this pulse scheme is displayed in Fig. 7.2(C), with specifics provided henceforth.

Histotripsy pulses used in this study were very short (approximately 5 µs), had a center frequency of 500 kHz, and a peak-negative pressure (P-) of 45 MPa. The representative waveform displayed in Fig. 7.2(A), which was measured using the same fiber optic hydrophone used to perform histotripsy field scans, demonstrates the general shape of a histotripsy pulse. However, it was acquired at a lower P- of 12 MPa, as calibration at higher amplitudes can result in instantaneous cavitation on the fiber tip. The therapy P- of 45 MPa reported here was estimated via extrapolation based on the observation that P- increases extremely linearly with the transducer driving voltage. In order to investigate the effect of pulse rate on the efficacy of histotripsy stone erosion, PRFs of 1, 10, 100, and 500 Hz were tested.

A partial segment of a representative bubble removal pulse is displayed in Fig. 7.2(B), acquired using the same HNR-0500 needle hydrophone used to perform bubble removal module field scans. All bubble removal pulses had a center frequency of 1 MHz, duration of 1500 µs, and amplitude corresponding to an MI of either 0 (i.e., no bubble removal) or 1. The latter setting was selected based on our previous work demonstrating that the efficacy of the bubble removal process peaks near an MI of 1 [29]. Following histotripsy pulse firing, a 500 µs delay was imposed to allow for unimpeded bubble cloud collapse prior to sonication with the bubble removal pulse. This delay, combined with the fixed 1500 μs bubble removal pulse duration, limited the maximum investigated histotripsy PRF to 500 Hz.

7.2.4 Model Stone Treatment and Damage Quantification

Five model stones were treated with each parameter combination investigated in this study. In order to achieve an accurate comparison of stone erosion across all cases, a preliminary investigation was conducted to determine the number of pulses required to produce similar degrees of damage at each rate. This was deemed preferable to applying treatment for a set time duration or a set number of pulses, as the histotripsy PRFs explored in this study span a 500-fold range and have highly variable comminution outcomes. For example, 10,000 pulses applied at a PRF of 1 Hz (166.7 minutes) may erode nearly the entire model stone, whereas 10,000 pulses applied at a PRF of 500 Hz (20 seconds) may not produce any perceptible damage. For this reason, the following treatment durations were used for each respective PRF in order to produce more similar degrees of stone erosion: (A) PRF= 1 Hz: 2,000 pulses (33.3 minutes); (B) PRF= 10 Hz: 5,000 pulses (8.3 minutes); (C) PRF= 100 Hz: 20,000 pulses (3.3 minutes); (D) PRF= 500 Hz: 50,000 pulses (1.7 minutes).

To quantify the effect of histotripsy erosion, stone mass was measured before and after treatment. These measurements correspond to the hydrated mass of the stone, and care was taken to gently blot any standing water off the stone surface prior to their acquisition. Pre- and post-treatment stone mass was used to quantify both an average treatment rate (mass eroded/treatment time) and average treatment efficiency (mass eroded/number of pulses applied) for a given parameter set.

7.2.5 High Speed Imaging

High speed images for stone treatments conducted with each parameter set were acquired using a Photron Fastcam SA1.1 high speed camera (Photron USA Inc., San Diego, CA) equipped with a 200 mm macro lens (AF Micro-Nikkor 200mm f/4D IF-ED, Nikon Corporation, Tokyo, Japan). A large-area, high-power LED light source (Bridgelux 50C10K, Bridgelux Inc., Livermore, CA) was used to backlight the experiments such that bubbles generated in the field were visible as dark shadows on the optical images. A 39-frame sequence was recorded immediately following histotripsy pulse firing at a frame rate of 20 kfps and exposure time of 49 μs, such that the entirety of the pulse scheme detailed in Fig. 7.2(C) was imaged.

7.3 Results

7.3.1 Erosion Rate and Efficiency

The erosion efficiency (mg/1000 pulses) and erosion rate (mg/min) resulting from histotripsy treatment of model stones with and without the incorporation of bubble removal pulses are displayed in Fig. 7.3. Consistent with previous work in Chapters 2 and 3 [2-4], all histotripsy treatments were observed to erode fine particulate debris from the stone surface from the onset of treatment, with no subdivision of the stone into large fragments (à la SWL) ever produced. All treatments generated a statistically significant reduction in stone mass relative to control stones (*t-test*, $P < 0.02$), which were handled in the same manner as treated stones but not exposed to ultrasound. The treatment parameters utilized in this study resulted in only partial erosion of model stones, as is exemplified in Fig. 7.4.

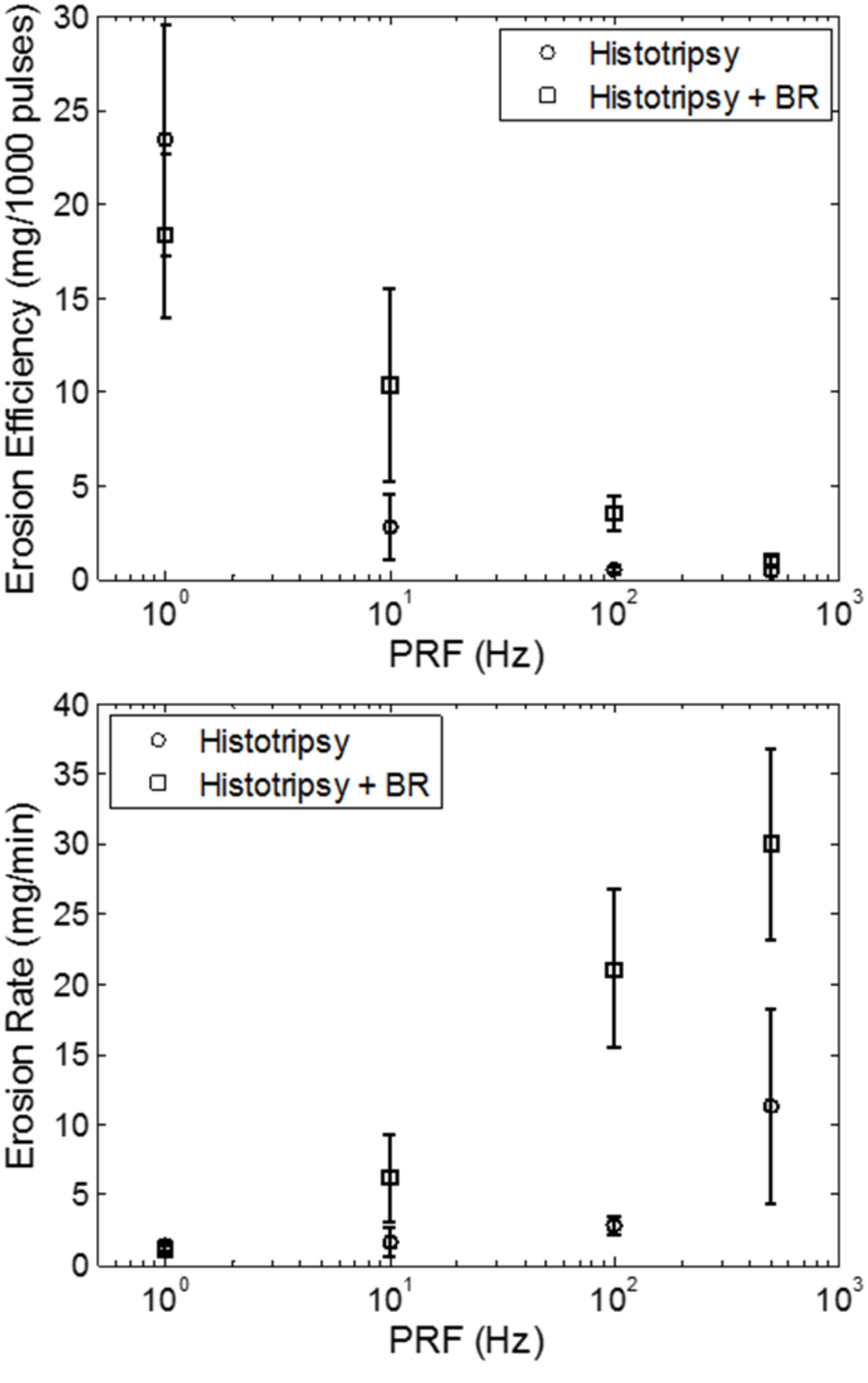

Fig. 7.3 Erosion efficiency (top panel) and erosion rate (bottom panel) resulting from histotripsy treatment of model stones without and with the incorporation of bubble removal (BR) pulses. Maximum erosion efficiency was produced at the lowest tested PRF of 1 Hz, while the highest rate of erosion was generated at the highest tested PRF of 500 Hz; a 10-fold increase in PRF does not correspond to a 10-fold increase in erosion rate, however. The introduction of bubble removal pulses resulted in a drastic enhancement in erosion for PRFs of 10 Hz and above.

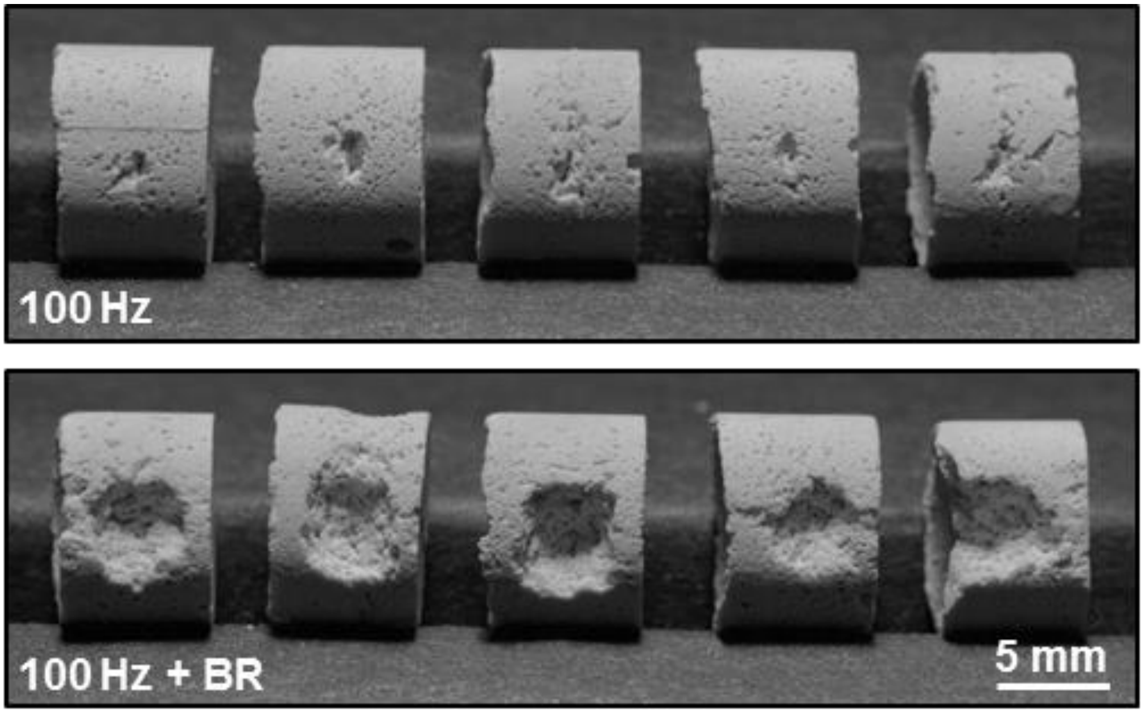

Fig. 7.4 Results of five trials performed for histotripsy stone erosion at 100 Hz PRF without (top panel) and with (bottom panel) the incorporation of bubble removal (BR) pulses. In each case material was eroded from the surface of the stone in the region targeted by the histotripsy focus. However, the introduction of bubble removal pulses allowed for an erosion rate of 21.1 ± 5.6 mg/min over the 3.3 minute treatment duration, in comparison to 2.8 ± 0.7 mg/min for histotripsy-only.

Without the incorporation of bubble removal, the efficiency of histotripsy stone erosion (Fig. 7.3, top panel) displayed an extreme dependence on PRF. Maximum efficiency was achieved for the lowest tested PRF of 1 Hz, which eroded 23.4 ± 6.2 mg/1000 pulses. All higher PRFs showed a significant drop in efficiency relative to this value (*t-test*, P < 0.0001). Specifically, application of histotripsy at 10 Hz resulted in an efficiency reduction to 2.8 ± 1.7 mg/1000 pulses. PRFs of 100 and 500 Hz produced efficiencies of 0.5 ± 0.1 and 0.4 ± 0.2 mg/1000 pulses, which were not statistically different from one another (*t-test*, P = 0.45). Alternatively, the erosion characteristics resulting from histotripsy treatment can be expressed as a temporal rate (Fig. 7.3, lower panel). In this case the rate of histotripsy stone erosion is observed to reach a maximum of 11.3 ± 6.9 mg/min at the highest tested PRF of 500 Hz (*t-test*, P < 0.03). Treatment at the lower PRFs of 1, 10, and 100 Hz produced erosion rates of 1.4 ± 0.4, 1.7 ± 1.0, and 2.8 ± 0.7 mg/min, respectively. Clearly, a 10-fold increase in PRF does not translate to a 10-fold increase in rate of erosion.

The incorporation of bubble removal pulses resulted in drastic enhancement of histotripsy stone erosion for PRFs of 10 Hz and above. At the lowest tested PRF of 1 Hz—in which case residual bubble nuclei had a full second for passive dissolution—a statistically significant difference in erosion was not observed in comparing histotripsy only vs. histotripsy with bubble removal (*t-test*, P = 0.17). At all PRFs above 1 Hz, however, the addition of bubble removal pulses produced a significant increase in erosion relative to their histotripsy-only counterpart (*t-test*, P < 0.015). Specifically, at PRFs of 10, 100, and 500 Hz erosion (both efficiency and rate) increased 3.7-, 7.5-, and 2.7-fold. Fig. 7.4 shows the outcome of the five stone erosion trials performed at a PRF of 100 Hz without (top panel) and with (bottom panel) bubble removal. In each case stone material was eroded from the surface in the region targeted by the histotripsy focus; however, the incorporation of bubble removal pulses allowed for an average erosion rate of 21.1 mg/min over the 3.3 minute treatment time, in comparison to the 2.8 mg/min rate produced by histotripsy in isolation.

7.3.2 High Speed Imaging

Representative high speed images showing histotripsy bubble cloud dynamics for low PRF (1 Hz) and high PRF (100 Hz) treatments are displayed in Fig. 7.5. Each image sequence corresponds to the 100th pulse in a series applied at each respective rate, with t = 0 μs indicating the time of pulse arrival at the stone. At the low rate of 1 Hz, bubble cloud dynamics are extremely similar across the histotripsy-only (Fig. 7.5, top panel, upper row) and histotripsy with bubble removal (Fig. 7.5, top panel, lower row) cases. In each, prefocal cavitation upon histotripsy pulse arrival is minimal and cloud collapse occurs as a coherent unit against the stone surface 200-250

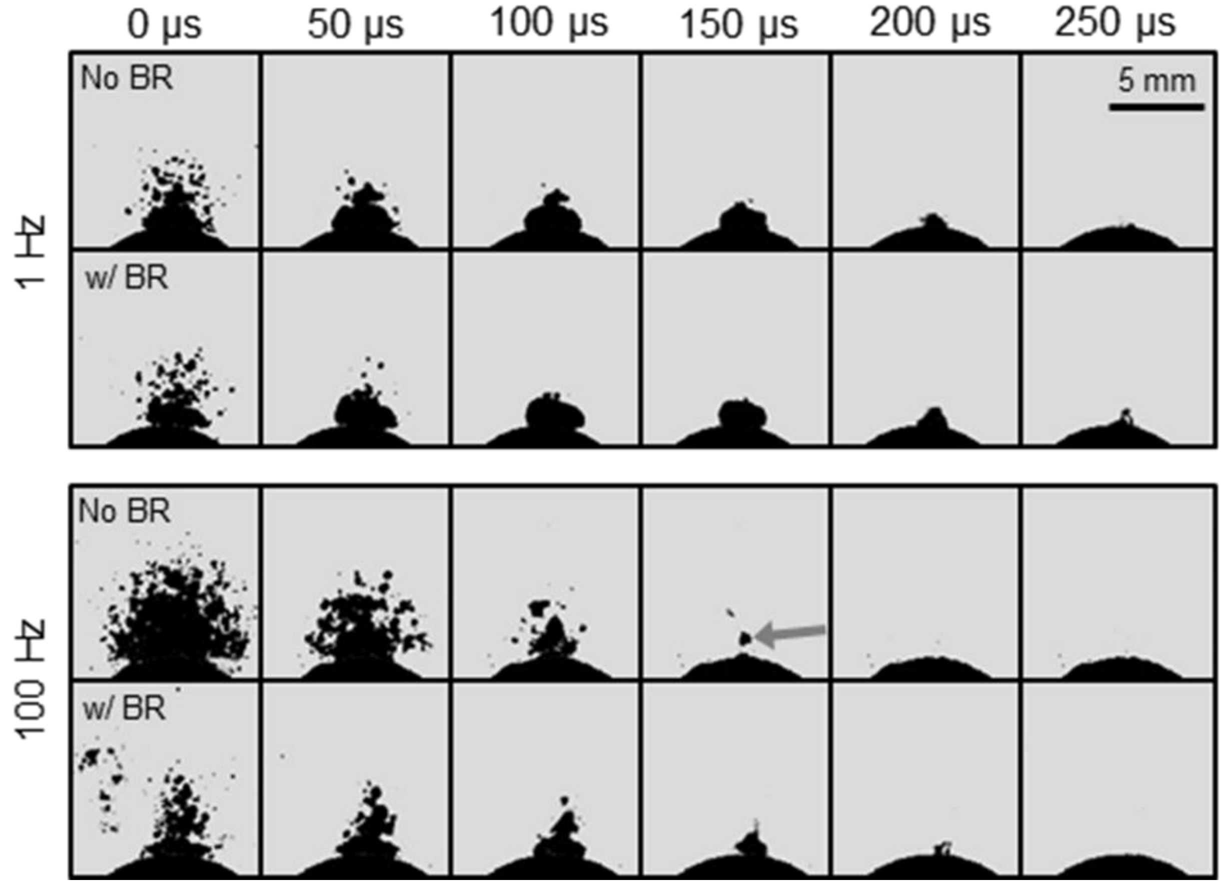

Fig. 7.5 Histotripsy bubble cloud dynamics at PRFs of 1 and 100 Hz. Each sequence corresponds to the 100th histotripsy pulse in a series, with t = 0 µs indicating the time at which the pulse arrives at the stone. For a given PRF, the top row of images displays the bubble cloud time-course for the histotripsy-only case, whereas the bottom row of images shows the cloud dynamics when bubble removal (BR) pulses are incorporated. In the absence of bubble removal, histotripsy applied at the high PRF of 100 Hz generates enhanced prefocal cavitation, reduction of the bubble cloud lifespan, and translation of the point of cloud collapse to a location above the stone (see arrow).

µs following initiation. Cloud dynamics at the high PRF of 100 Hz display markedly different characteristics when no bubble removal pulses are applied (Fig. 7.5, bottom panel, upper row). In this case, prefocal cavitation upon histotripsy pulse arrival is much more extensive, and the bubble cloud displays a shorter lifetime collapsing in the time window of 150-200 µs. Furthermore, cloud collapse appears more disparate rather than a cohesive unit, and the final collapse point resides prefocal to the stone surface (seen in the frame at 150 µs). Incorporation of bubble removal pulses in histotripsy applied at a PRF of 100 Hz results in cloud dynamics more closely approximating those observed at 1 Hz (Fig. 7.5, bottom panel, lower row). Here, the extent of prefocal cavitation upon histotripsy pulse arrival is greatly reduced relative to the case of 100 Hz without bubble removal, although some bubble excitation is still observed in the periphery. The lifetime of the cloud is roughly 200 μs, falling in a range intermediate to that for 100 Hz without bubble removal and the 1 Hz cases. Finally, the ultimate point of cloud collapse resumes its position adjacent to the stone surface (as seen in the frame at 200 μs).

7.4 Discussion

In Chapters 4 and 5 of this dissertation we presented work on a novel strategy for actively removing the microscopic remnant bubble nuclei that persist following primary cavitation collapse; here, we incorporate this bubble removal strategy in histotripsy model kidney stone erosion to mitigate the rate-limiting effects of these residual bubbles. When histotripsy is applied in isolation, the efficiency of stone erosion displays a precipitous drop-off for tested PRFs above 1 Hz. This is likely a result of the remnant bubble nuclei produced by primary cavitation collapse persisting on the order of one second [21-24]; as such, the lowest tested rate of 1 Hz is expected to afford the majority of residual bubbles sufficient time for passive dissolution between histotripsy pulses. Further support for this idea is offered by the observation that introducing bubble removal pulses did not produce a statistically different outcome in erosion at this lowest tested PRF. Contrastingly, at PRFs of 10 Hz and above the incorporation of bubble removal in histotripsy therapy resulted in pronounced improvements in erosion efficiency. At 10, 100, and 500 Hz, the extent of erosion was observed to increase 3.7-, 7.5-, and 2.7-fold relative to the respective histotripsy-only cases.

As discussed in Chapters 4 and 5, the bubble removal strategy utilized in this study is thought to achieve the aggregation and subsequent coalescence of residual bubble nuclei through an interplay of the Bjerknes forces. Our preliminary work has suggested that it is the secondary

Bjerknes force that is the major contributor to this bubble consolidation phenomenon, with this dominance manifesting in higher bubble removal frequencies producing enhanced nuclei consolidation effects [29]. Although not yet fully optimized, the 1 MHz bubble removal pulse scheme utilized in this study represents a compromise between the use of high frequency to maximize bubble aggregation and focal volume size to cover the region of interest. One of the practical limitations in moving to higher frequency is a reduction in focal coverage. Here, the 1 MHz bubble removal module produced a focal zone with a -6-dB beamwidth measuring 7.0 mm in the lateral direction. While this is certainly large enough to encompass the 2.0 mm -6-dB lateral beamwidth of the histotripsy transducer, it is possible that some residual bubble nuclei could escape to the periphery of the 15 mm diameter treatment channel. This is especially possible at the higher PRFs tested in this study, which are expected to generate some degree of fluid flow within the treatment channel. As such, one possible explanation for the failure of bubble removal pulses to achieve complete recovery of erosion efficiency is the persistence of residual nuclei outside the bubble removal focus. Evidence of this can be observed in the first frame corresponding to a PRF of 100 Hz with bubble removal in Fig. 7.5.

In Ch. 6 of this dissertation, bubble removal pulses were incorporated in SWL treatment of model stones to augment comminution efficacy at high shock rate. The trends in histotripsy stone erosion observed in the present chapter are consistent with both this work and previous investigations performed by others in the field of SWL. To reiterate briefly, residual bubble nuclei have been implicated as the primary contributor to the rate-dependent efficacy observed for stone comminution in SWL. Extensive testing has documented that LSWs applied at low rate produce a greater per-shock fragmentation efficiency in comparison to those applied at high rate [7-12]. These results are corroborated by an abundance of clinical data [35-41], which indicates that SWL performed at shock rates of 1-1.5 Hz produces more successful treatment outcomes than that at 2 Hz. It is the persistence of residual cavitation nuclei between successive LSWs that is responsible for these effects. While the lifespan of primary cavitation bubbles generated by an LSW is only on the order of 1 ms [42-45], their collapse has been shown to generate a large population of residual daughter bubbles—i.e. cavitation nuclei—that can persist on the order of 1 second [21-24]. When an LSW propagates through a medium containing these residual bubbles the tensile component of the waveform will cause them to grow, effectively removing energy from the LSW and leaving it behind in the form of kinetic and potential energy of the fluid surrounding the bubbles [26]. As such, the remnant nuclei induce the selective attenuation of an LSW's negative tail [7, 25-27] and reduce the energy that ultimately reaches the targeted stone, compromising comminution efficiency.

While the population of cavitation bubbles generated by an LSW is certainly different from a histotripsy bubble cloud, the ill-effects of residual cavitation nuclei experienced in SWL extend to histotripsy stone erosion therapy. Previous work has shown that the collapse of a histotripsy bubble cloud produces an extensive set of microscopic residual daughter bubbles [28, 46, 47]. Furthermore, in Chapter 5 propagation of an acoustic pulse through this population of remnant bubbles was observed to experience pronounced attenuation as measured by a hydrophone positioned distal to the histotripsy focus [29]. Similar to SWL, the expansion of remnant bubble nuclei induced by the histotripsy pulse will detract energy from the pulse directly; the expanded bubbles are likely to then provide a larger area for further scattering of the remainder of the histotripsy pulse. It is likely that the resulting pulse attenuation is partially responsible for the decreased efficiency of stone erosion observed at high PRF. Indeed, as represented in Fig. 7.5 the lifetime of histotripsy bubble clouds generated at high PRF was reduced relative to those produced at low PRF, suggesting a reduction in the pulse energy reaching the focal point in these cases.

A second major implication of residual bubble nuclei in histotripsy stone erosion is their influence on the location of bubble cloud collapse. As represented by the case of 100 Hz without bubble removal in Fig. 7.5, the point of cloud collapse was consistently observed to shift prefocal to the stone surface when high PRFs were utilized. Conversely, at the lowest tested PRF of 1 Hz the bubble cloud collapsed as a coherent unit against the stone surface with each histotripsy pulse applied. This suggests that remnant nuclei that persist in the field act to seed the point of cloud collapse away from the stone. A similar result was observed by Chitnis, *et al*. [48], who found that bubble clouds generated near a clean ceramic face collapsed onto the boundary; however, when the ceramic face contained a sparse bubble layer, cloud collapse shifted away from the surface and cavitation damage was mitigated. To the best of the author's knowledge this phenomenon has not been observed with respect to the effect of remnant bubble nuclei in SWL. Nevertheless, it appears to be an extremely important feature of efficient erosion in histotripsy therapy. The incorporation of bubble removal pulses facilitated the recovery of the collapse point toward the stone surface when high PRFs were utilized.

While the bubble removal pulses utilized in this study have not yet been fully optimized, they serve to demonstrate the drastic impact that residual cavitation nuclei can have on histotripsy kidney stone erosion. Furthermore, this strategy provides us with a tool through which we can begin to identify the aspects of histotripsy-induced cavitation that are crucial for the efficient erosion of a targeted structure. The results of this study suggest that, through appropriate manipulation of the cavitation environment surrounding the stone, the erosion efficiency achieved at low pulse rates can be recovered when high PRFs are utilized. It is important to note that these results were obtained in a simplified *in-vitro* setting, and as is discussed further in Chapter 9, our future work will focus on translating this approach to the more complex environment *in-vivo*. It is the author's hope that the treatment rates afforded by an optimized form of this bubble removal strategy will allow histotripsy stone erosion to offer a viable adjunct to SWL procedures.

7.5 Conclusion

Similar to SWL, histotripsy treatment of model kidney stones displays a rate-dependent efficacy in which pulses applied at low PRF achieve drastically higher erosion efficiency in comparison to those applied at high PRF. This is attributed to residual cavitation bubble nuclei that are generated by histotripsy bubble cloud collapse and persist from one pulse to the next. Such residual bubbles can cause direct attenuation of the incident acoustic waveform, as well as influence the resulting cavitation dynamics—seeding collapse of the bubble cloud prefocal to the targeted stone surface. The most direct approach to mitigating the effects of remnant bubbles is to simply wait long enough for their passive dissolution between successive pulses. While this may afford a high per-pulse efficiency, the temporal rate of stone erosion suffers. It is for this reason that we have developed an active means of bubble removal, using low-amplitude acoustic pulses to stimulate the aggregation and subsequent coalescence of residual nuclei. Although not yet fully optimized, the results of this study suggest that these bubble removal pulses offer great promise in recovering high per-pulse efficiency when high PRFs are utilized. The continued development of this approach will offer further insight into the qualities of cavitation that are paramount to effective stone comminution, while successful translation to an *in-vivo* model stands to drastically enhance the efficacy of histotripsy for the application of kidney stone treatment.

7.6 References

[1] A. P. Duryea, W. W. Roberts, C. A. Cain, and T. L. Hall, "Removal of residual cavitation nuclei to enhance histotripsy erosion of model urinary stones," *IEEE Trans Ultrason Ferroelectr Freq Control,* In-Press.

[2] A. P. Duryea, T. L. Hall, A. D. Maxwell, Z. Xu, C. A. Cain, and W. W. Roberts, "Histotripsy erosion of model urinary calculi," *J Endourol,* vol. 25, pp. 341-4, Feb 2011.

[3] A. P. Duryea, A. D. Maxwell, W. W. Roberts, Z. Xu, T. L. Hall, and C. A. Cain, "In vitro comminution of model renal calculi using histotripsy," *IEEE Trans Ultrason Ferroelectr Freq Control,* vol. 58, pp. 971-80, May 2011.

[4] A. P. Duryea, W. W. Roberts, C. A. Cain, and T. L. Hall, "Controlled cavitation to augment SWL stone comminution: mechanistic insights in vitro," *IEEE Trans Ultrason Ferroelectr Freq Control,* vol. 60, pp. 301-9, Feb 2013.

[5] S. Zhu, F. H. Cocks, G. M. Preminger, and P. Zhong, "The role of stress waves and cavitation in stone comminution in shock wave lithotripsy," *Ultrasound Med Biol,* vol. 28, pp. 661-71, May 2002.

[6] A. P. Duryea, W. W. Roberts, C. A. Cain, and T. L. Hall, "Optimization of histotripsy for kidney stone erosion," in *Ultrasonics Symposium (IUS), 2010 IEEE*, 2010, pp. 342-345.

[7] Y. A. Pishchalnikov, J. A. McAteer, J. C. Williams, Jr., I. V. Pishchalnikova, and R. J. Vonderhaar, "Why stones break better at slow shockwave rates than at fast rates: in vitro study with a research electrohydraulic lithotripter," *J Endourol,* vol. 20, pp. 537-41, Aug 2006.

[8] G. Vallancien, R. Munoz, M. Borghi, B. Veillon, J. M. Brisset, and M. Daudon, "Relationship between the frequency of piezoelectric shock waves and the quality of renal stone fragmentation. In vitro study and clinical implications," *Eur Urol,* vol. 16, pp. 41-44, 1989.

[9] H. Wiksell and A. C. Kinn, "Implications of cavitation phenomena for shot intervals in extracorporeal shock wave lithotripsy," *Br J Urol,* vol. 75, pp. 720-3, Jun 1995.

[10] A. Greenstein and H. Matzkin, "Does the rate of extracorporeal shock wave delivery affect stone fragmentation?," *Urology,* vol. 54, pp. 430-432, 1999.

[11] M. J. Weir, N. Tariq, and R. J. Honey, "Shockwave frequency affects fragmentation in a kidney stone model," *J Endourol,* vol. 14, pp. 547-50, Sep 2000.

[12] R. F. Paterson, D. A. Lifshitz, J. E. Lingeman, A. P. Evan, B. A. Connors, N. S. Fineberg, *et al.*, "Stone fragmentation during shock wave lithotripsy is improved by slowing the shock wave rate: studies with a new animal model," *J Urol,* vol. 168, pp. 2211-5, Nov 2002.

[13] M. Delius, W. Brendel, and G. Heine, "A mechanism of gallstone destruction by extracorporeal shock waves," *Naturwissenschaften,* vol. 75, pp. 200-1, Apr 1988.

[14] M. R. Bailey, "Control of Acoustic Cavitation with Application to Lithotripsy," DTIC Document 1997.

[15] N. Vakil and E. C. Everbach, "Transient acoustic cavitation in gallstone fragmentation: A study of gallstones fragmented *in vivo*," *Ultrasound in medicine & biology,* vol. 19, pp. 331-342, 1993.

[16] M. Delius, "Minimal static excess pressure minimises the effect of extracorporeal shock waves on cells and reduces it on gallstones," *Ultrasound in Medicine & Biology,* vol. 23, pp. 611-617, 1997.

[17] M. R. Bailey, R. O. Cleveland, T. Colonius, L. A. Crum, A. P. Evan, J. E. Lingeman, *et al.*, "Cavitation in shock wave lithotripsy: the critical role of bubble activity in stone breakage and kidney trauma," in *Ultrasonics, 2003 IEEE Symposium on*, 2003, pp. 724-727 Vol.1.

[18] X. Xi and P. Zhong, "Improvement of stone fragmentation during shock-wave lithotripsy using a combined EH/PEAA shock-wave generator—in vitro experiments," *Ultrasound in Medicine & Biology,* vol. 26, pp. 457-467, 2000.

[19] H. G. Flynn and C. C. Church, "A mechanism for the generation of cavitation maxima by pulsed ultrasound," *J Acoust Soc Am,* vol. 76, pp. 505-12, Aug 1984.

[20] C. E. Brennen, "Fission of collapsing cavitation bubbles," *Journal of Fluid Mechanics,* vol. 472, pp. 153-166, 2002.

[21] Y. A. Pishchalnikov, J. A. McAteer, I. V. Pishchalnikova, J. C. Williams, M. R. Bailey, and O. A. Sapozhnikov, "Bubble proliferation in shock wave lithotripsy occurs during inertial collapse," in *18th International Symposium on Nonlinear Acoustics*, 2008, pp. 460-463.

[22] Y. A. Pishchalnikov, J. C. Williams, and J. A. McAteer, "Bubble proliferation in the cavitation field of a shock wave lithotripter," *J Acoust Soc Am,* vol. 130, pp. EL87-93, Aug 2011.

[23] P. Huber, K. Jochle, and J. Debus, "Influence of shock wave pressure amplitude and pulse repetition frequency on the lifespan, size and number of transient cavities in the field of an electromagnetic lithotripter," *Phys Med Biol,* vol. 43, pp. 3113-28, Oct 1998.

[24] P. S. Epstein and M. S. Plesset, "On the stability of gas bubbles in liquid-gas solutions," *The Journal of Chemical Physics,* vol. 18, pp. 1505-1509, 1950.

[25] Y. A. Pishchalnikov, J. A. McAteer, and J. C. Williams, Jr., "Effect of firing rate on the performance of shock wave lithotriptors," *BJU Int,* vol. 102, pp. 1681-6, Dec 2008.

[26] Y. A. Pishchalnikov, O. A. Sapozhnikov, M. R. Bailey, I. V. Pishchalnikova, J. C. Williams, and J. A. McAteer, "Cavitation selectively reduces the negative-pressure phase of lithotripter shock pulses," *Acoust Res Lett Online,* vol. 6, pp. 280-286, Nov 3 2005.

[27] Y. A. Pishchalnikov, J. A. McAteer, M. R. Bailey, I. V. Pishchalnikova, J. C. Williams, and A. P. Evan, "Acoustic shielding by cavitation bubbles in shock wave lithotripsy (SWL)," in *17th International Symposium on Nonlinear Acoustics* 2005, pp. 319-322.

[28] A. P. Duryea, C. A. Cain, H. A. Tamaddoni, W. W. Roberts, and T. L. Hall, "Removal of Residual Nuclei Following a Cavitation Event using Low-Amplitude Ultrasound," *IEEE Trans Ultrason Ferroelectr Freq Control,* vol. 61, pp. 1619-26, Oct 2014.

[29] A. P. Duryea, H. A. Tamaddoni, C. A. Cain, W. W. Roberts, and T. L. Hall, "Removal of residual nuclei following a cavitation event: a parametric study," *IEEE Trans Ultrason Ferroelectr Freq Control,* In-Press.

[30] W. N. Simmons, F. H. Cocks, P. Zhong, and G. Preminger, "A composite kidney stone phantom with mechanical properties controllable over the range of human kidney stones," *J Mech Behav Biomed Mater,* vol. 3, pp. 130-3, Jan 2010.

[31] M. Chaigneau and G. Le Moan, "On the composition of gas dissolved in human urine," *C R Acad Sci Hebd Seances Acad Sci D,* vol. 267, pp. 1893-5, Nov 25 1968.

[32] J. B. Fowlkes, P. L. Carson, E. H. Chiang, and J. M. Rubin, "Acoustic generation of bubbles in excised canine urinary bladders," *J Acoust Soc Am,* vol. 89, pp. 2740-4, Jun 1991.

[33] E. Y. Hwang, J. B. Fowlkes, and P. L. Carson, "Variables controlling contrast generation in a urinary bladder model," *J Acoust Soc Am,* vol. 103, pp. 3706-16, Jun 1998.

[34] J. E. Parsons, C. A. Cain, and J. B. Fowlkes, "Cost-effective assembly of a basic fiber-optic hydrophone for measurement of high-amplitude therapeutic ultrasound fields," *J Acoust Soc Am,* vol. 119, pp. 1432-40, Mar 2006.

[35] K. Madbouly, A. M. El-Tiraifi, M. Seida, S. R. El-Faqih, R. Atassi, and R. F. Talic, "Slow versus fast shock wave lithotripsy rate for urolithiasis: a prospective randomized study," *J Urol,* vol. 173, pp. 127-30, Jan 2005.

[36] E. Yilmaz, E. Batislam, M. Basar, D. Tuglu, C. Mert, and H. Basar, "Optimal frequency in extracorporeal shock wave lithotripsy: prospective randomized study," *Urology,* vol. 66, pp. 1160-4, Dec 2005.

[37] K. T. Pace, D. Ghiculete, and M. Harju, "Shock wave lithotripsy at 60 or 120 shocks per minute: A randomized, double-blind trial," *The Journal of Urology,* vol. 174, pp. 595-599, 2005.

[38] J. Chacko, M. Moore, N. Sankey, and P. S. Chandhoke, "Does a slower treatment rate impact the efficacy of extracorporeal shock wave lithotripsy for solitary kidney or ureteral stones?," *J Urol,* vol. 175, pp. 1370-1373, 2006.

[39] Y. Kato, S. Yamaguchi, J. Hori, M. Okuyama, and H. Kakizaki, "Improvement of stone comminution by slow delivery rate of shock waves in extracorporeal lithotripsy," *Int J Urol,* vol. 13, pp. 1461-5, Dec 2006.

[40] D. Weiland, C. Lee, R. Ugarte, and M. Monga, "Impact of shockwave coupling on efficacy of extracorporeal shockwave lithotripsy," *J Endourol,* vol. 21, pp. 137-40, Feb 2007.

[41] M. J. Semins, B. J. Trock, and B. R. Matlaga, "The effect of shock wave rate on the outcome of shock wave lithotripsy: a meta-analysis," *J Urol,* vol. 179, pp. 194-7; discussion 197, Jan 2008.

[42] W. Sass, H. P. Dreyer, S. Kettermann, and J. Seifert, "The role of cavitational activity in fragmentation processes by lithotripters," *J Stone Dis,* vol. 4, pp. 193-207, Jul 1992.

[43] P. Zhong, I. Cioanta, F. H. Cocks, and G. M. Preminger, "Inertial cavitation and associated acoustic emission produced during electrohydraulic shock wave lithotripsy," *J Acoust Soc Am,* vol. 101, pp. 2940-50, May 1997.

[44] P. Zhong, H. L. Tong, F. H. Cocks, and G. M. Preminger, "Transient oscillation of cavitation bubbles near stone surface during electrohydraulic lithotripsy," *J Endourol,* vol. 11, pp. 55-61, Feb 1997.

[45] R. O. Cleveland, O. A. Sapozhnikov, M. R. Bailey, and L. A. Crum, "A dual passive cavitation detector for localized detection of lithotripsy-induced cavitation in vitro," *J Acoust Soc Am,* vol. 107, pp. 1745-58, Mar 2000.

[46] Z. Xu, T. L. Hall, J. B. Fowlkes, and C. A. Cain, "Optical and acoustic monitoring of bubble cloud dynamics at a tissue-fluid interface in ultrasound tissue erosion," *The Journal of the Acoustical Society of America,* vol. 121, pp. 2421-2430, 2007.

[47] T. Y. Wang, Z. Xu, T. L. Hall, J. B. Fowlkes, and C. A. Cain, "An efficient treatment strategy for histotripsy by removing cavitation memory," *Ultrasound Med Biol,* vol. 38, pp. 753-66, May 2012.

[48] P. V. Chitnis, N. J. Manzi, R. O. Cleveland, R. A. Roy, and R. G. Holt, "Mitigation of damage to solid surfaces from the collapse of cavitation bubble clouds," *Journal of Fluids Engineering,* vol. 132, p. 051303, 2010.

Chapter 8

Active Removal of Residual Nuclei to Enhance Histotripsy Soft Tissue Fractionation at High Pulse Rate

8.1 Introduction

The work presented in the preceding chapters of this dissertation documents the deleterious consequences of remnant bubble nuclei in kidney stone comminution, both in shock wave lithotripsy (SWL) and histotripsy. However, the ill effects of residual bubbles that persist following primary cavitation collapse are not limited to stone therapy, and their implications in histotripsy fractionation of soft tissue have been previously explored. Specifically, Wang, *et al.* [1] documented that the persistence of cavitation nuclei can limit the efficacy of histotripsy soft tissue fractionation when high pulse repetition frequencies (PRFs) are used. When applied at low PRF (< 10 Hz), the majority of remnant bubble nuclei generated by histotripsy bubble cloud collapse have sufficient time to dissolve between successive pulses. This permits each histotripsy pulse to nucleate cavitation at a randomized set of sites within the focal volume and produces highly efficient destruction of the targeted region. In contrast, when applied at high PRF (> 10 Hz) remnant bubble nuclei persist between successive histotripsy pulses and seed repetitive nucleation of cavitation at a discrete set of sites within the focus. This is referred to as the cavitation memory effect, and results in inefficient lesion formation. As a histotripsy lesion develops, sites with cavitation memory will become over-treated, while those without cavitation memory remain under-treated. Lesions generated in this fashion require an excess number of pulses to achieve complete destruction of the focal volume.

In the present chapter, we incorporate bubble removal sequences explored in Chapters 4 and 5 [2, 3] in histotripsy treatment of soft tissue-mimicking phantoms in an effort to alleviate the cavitation memory effect and improve the efficiency of lesion development at high pulse rates. Previous work has demonstrated that cavitation memory can be eliminated by waiting a sufficient duration between successive histotripsy pulses such that remnant nuclei can passively dissolve [1]. While this strategy produces a high per-pulse efficiency, the time-rate of lesion development suffers. We therefore seek to maintain the high per-pulse efficiency associated with low pulse rates when much higher PRFs are utilized. Red blood cell tissue-mimicking phantoms were treated at the high PRF of 100 Hz with and without the incorporation of bubble removal sequences, and the resulting lesion development was optically monitored and quantified. A series of reference treatments was also conducted at the very low PRF of 1 Hz in order to establish a point of comparison when cavitation memory is minimal. Finally, the results obtained from single-focal-spot treatments were extended to the treatment of a large volume, and optimal bubble removal parameters were utilized to homogenize a 10 x 10 mm region at high rate.

While the study presented in this chapter focuses on histotripsy soft tissue fractionation, the results offer preliminary insight into the application of our bubble removal strategy to soft tissue. This is an important aspect of this dissertation, as a major target of cavitation control for the enhanced efficacy of kidney stone treatment is the mitigation of collateral tissue damage associated with current SWL procedures [4-7]. The bulk of this investigation remains for future work, as is discussed further in Chapter 9. However, interpreting the results of the present study in this broader context offers a foundation on which this important work on active tissue protection can be based.

8.2 Methods

8.2.1 Tissue Phantom Preparation

Experiments conducted in this study utilized a red blood cell (RBC) tissue-mimicking phantom designed for the visualization and quantification of cavitation-induced damage [8]. Fresh bovine blood was obtained from a local abattoir (Dunbar Meats, Milan, MI) and immediately mixed with a citrate-phosphate-dextrose (CPD) anticoagulant solution (C7165, Sigma-Aldrich, St. Louis, MO) in a blood-to-CPD ratio of 9:1 (v:v). Blood samples were subsequently stored in a refrigeration unit at 4 ˚C prior to use, which was within 3 weeks of harvesting. RBC tissue-mimicking phantoms were prepared following the procedures detailed by Maxwell, *et al*. [8]. Briefly, a three-layer agarose hydrogel was constructed using powdered agarose (AG-SP, LabScientific, Livingston, NJ) and 0.9% saline in a 1:100 ratio (w:v). The outer layers of the construct were composed solely of this transparent agarose hydrogel, while the very thin (< 1 mm) center layer contained agarose hydrogel with RBCs embedded in a concentration of 5%. In this study, the RBC tissue-mimicking phantoms were cast in the form of right cylinders with outer dimensions measuring 6 cm in diameter and 9 cm in height. The RBC-layer was located in the center of the cylinder oriented parallel to the cylinder axis. A mold constructed from ABS plastic on a fused deposition modeling (FDM) machine (Dimension Elite, Stratasys Ltd., Eden Prairie, MN) was used to create this geometry. The top portion of the mold was detachable such that, following gel solidification, it could be removed to allow for unimpeded acoustic access to the RBC-layer (see Fig. 8.1). Cavitation-induced damage to this RBC-layer manifests in an optical change from translucent red to transparent and colorless as a result of RBC lysis, providing real-time visual feedback for histotripsy lesion development [8].

8.2.2 Experimental Setup

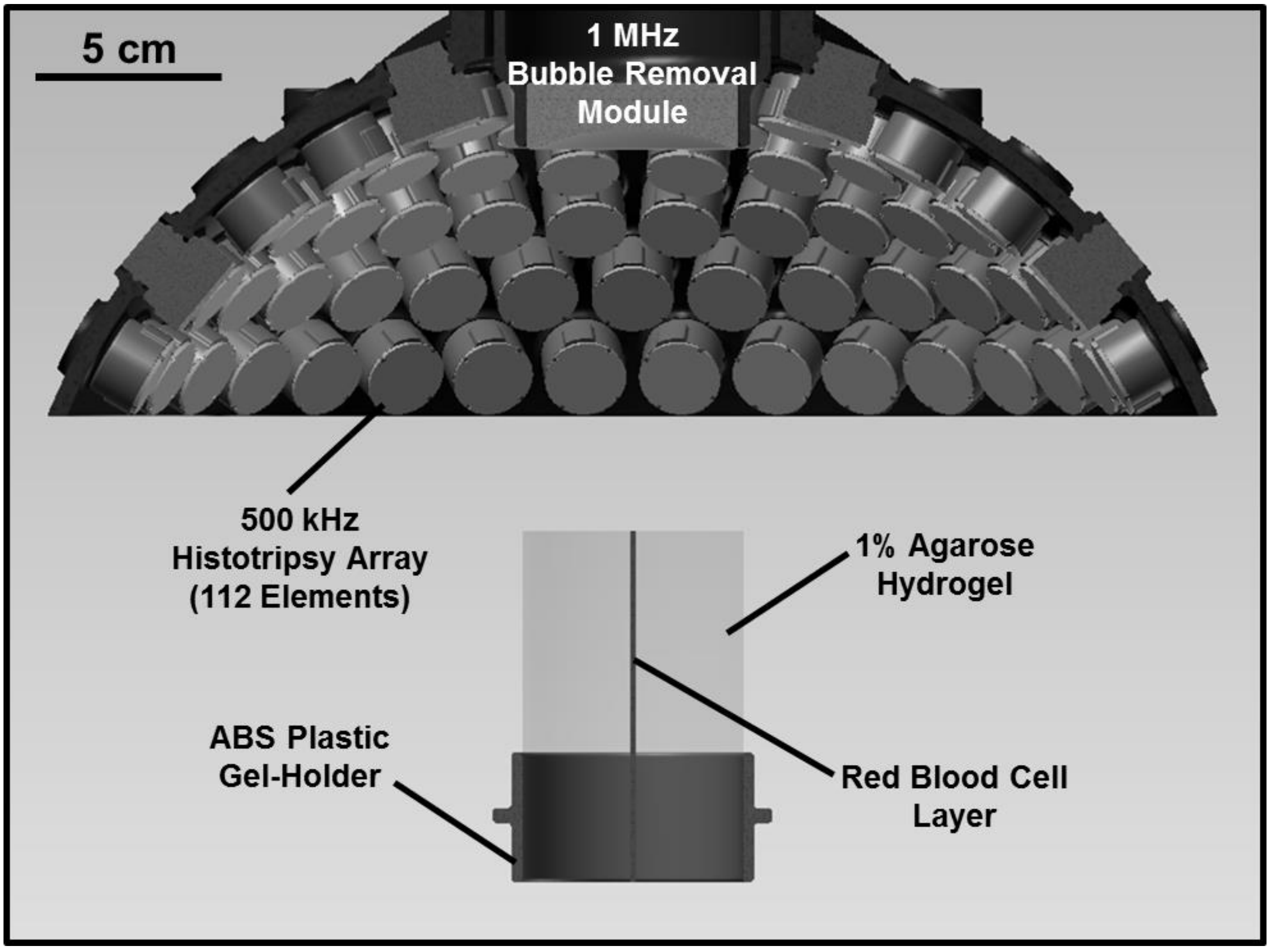

Fig. 8.1 Experimental setup used to study the effect of bubble removal pulses on histotripsy fractionation of soft tissue. Histotripsy treatment was delivered from a transducer composed of 112 individual 500 kHz modules arranged in a spherical cap pattern, while a separate 1 MHz transducer aligned confocally with the histotripsy array was used to generate bubble removal pulses. Treatments were performed on a tissue phantom constructed from 1% agarose hydrogel with a thin layer of red blood cells (RBCs) embedded within. This RBC layer was oriented parallel to the transducer axis such that the axial profile of histotripsy lesion development could be visualized.

The experimental setup used to study the impact of bubble removal sequences on histotripsy soft tissue fractionation is displayed in Fig. 8.1. All experiments were conducted in a water tank measuring 58 x 43 x 45 cm (L x W x H), which was filled with degased deionized water (dissolved oxygen content of 1.5 ± 0.2 mg/L at 23.0 ± 0.7 ˚C, corresponding to 16 ± 1% of saturation). Dissolved oxygen levels were measured at the beginning and end of each treatment day (n = 6) using a Traceable Digital Oxygen Meter (Control Co., Friendswood, TX).

The same 500 kHz histotripsy transducer detailed in Chapter 7 was used to deliver histotripsy therapy to the tissue phantoms treated in this study. Again, it consisted of 112 individual watertight modules arranged in a spherical cap pattern with a 150 mm radius of curvature and 270 mm aperture. This geometry was maintained via a scaffold fabricated from Accura 60 plastic (3D Systems Inc., Rock Hill, SC) on a stereolithography machine. Individual module housings were also fabricated from Accura 60 using stereolithography. Within each, two 1-MHz Pz36 disc elements (Ferroperm Piezoceramics A/S, Kvistgaard, Denmark) measuring 20 mm in diameter and 1.6 mm in thickness were stacked and driven in unison to produce a 500-kHz equivalent source. Epoxy adhesive (Hysol E-120 HP, Loctite Corporation, Rocky Hill, CT) was used to bond the individual Pz36 elements together, as well as mate the front face of each stack to a flat Accura-60 disc. The latter served to provide both electrical insulation and acoustic matching between the elements and water. A marine grade epoxy (TAP Epoxy System 314 Resin/143 Hardener, TAP Plastics Inc., San Leandro, CA) was used to pot the back of each module, ensuring complete electrical insulation from the surrounding water. Overall, this arrangement of 112 modules produced a focal zone having -6-dB beamwidths measuring 2.0 mm in the lateral dimension and 6.3 mm in the axial. These measurements were conducted at a pressure amplitude of 8 MPa (linear regime) using a fiber optic hydrophone with a 100-µm-diameter sensing tip [9]. The histotripsy transducer was driven using a pulse amplifier developed in our lab, which was designed to produce very short, intense bursts. More details regarding the acoustic output generated by this setup are provided in the subsequent section.

Again consistent with Chapter 7, a separate 1 MHz transducer—which we denote as the bubble removal module—was used to sonicate residual bubble nuclei produced by collapse of the histotripsy bubble cloud. It consisted of a single 1 MHz PZT-4 disc element (Steiner & Martins Inc., Miami, FL) measuring 50 mm in diameter and 2 mm in thickness. This frequency was selected based on our previous observation that bubble removal sequences of higher frequency (>500 kHz) produce more effective consolidation of residual nuclei following histotripsy bubble cloud collapse [3]. Similar to the histotripsy modules, the PZT-4 element was sealed within a stereolithography-fabricated Accura-60 housing. In this case the front face of the housing contained an acoustic lens having a focal length of 175 mm; this design was utilized to center the beam of the bubble removal module coincident with the histotripsy focus when the module was held within a central port in the histotripsy transducer scaffold (Fig. 8.1). The PZT-4 element was matched to the lens using an epoxy (1C-LV Hysol, Loctite Corporation, Rocky Hill, CT) filled 50 mesh copper screen (McMaster-Carr, Aurora, OH) to achieve the proper thickness and impedance. This arrangement produced an acoustic field with -6-dB beamwidths measuring 7.0 mm in the lateral dimension and exceeding 100 mm in the axial; as such, the bubble removal field fully encompassed the focal zone generated by the histotripsy transducer. These field scans were performed at a pressure amplitude of 300 kPa (linear regime) using an HNR-0500 needle hydrophone (Onda Corporation, Sunnyvale, CA). The bubble removal module was driven using a class-D amplifier developed in our lab; further details on the acoustic output are presented in the subsequent section.

As indicated in Fig. 8.1, the tissue-mimicking phantom was positioned below the histotripsy transducer such that the RBC layer was oriented vertically within the water tank (i.e. RBC layer parallel to the transducer axis). This allowed for visualization of the axial profile of histotripsy lesion development. Alignment of the histotripsy focus to the RBC layer was achieved via ultrasound imaging (not pictured in Fig. 8.1). An imaging probe (GE 11L with GE Logiq P6 system, GE Healthcare, Waukesha, WI) was oriented orthogonal to the RBC plane such that the layer showed as a thin hyperechoic strip on the ultrasound image. A test treatment was then performed in which a histotripsy bubble cloud was generated within the tissue phantom. This bubble cloud also showed as a hyperechoic zone in the image, and its location was marked with a cursor on the imager screen. In all subsequent treatments, the RBC layer was aligned to this cursor location prior to sonication.

Histotripsy lesion development in the RBC tissue-mimicking phantom was monitored using a Photron Fastcam SA1.1 high speed camera (Photron USA Inc., San Diego, CA) equipped with a 200 mm macro lens (AF Micro-Nikkor 200mm f/4D IF-ED, Nikon Corporation, Tokyo, Japan). A large-area, high-power LED light source (Bridgelux 50C10K, Bridgelux Inc., Livermore, CA) was used to backlight the experiments such that bubbles generated in the phantom were visible as dark shadows on the optical images. Consistent with previous work [1, 8, 10], damage to the RBC layer showed as an optical change from translucent to transparent, allowing for real time monitoring of lesion development via this setup. Two images were acquired for each histotripsy pulse, each with an exposure time of 49 µs. The first image was taken 50 µs prior to histotripsy pulse firing to capture the RBC phantom without cavitation bubbles. For the very first pulse, this frame corresponded to the intact background that was used to normalize all frames in our image processing algorithm (Section 8.2.4); for all subsequent pulses, this frame corresponded to the lesion resulting from the preceding pulse. The second image was acquired 120 µs following histotripsy pulse firing, which was empirically determined to capture the histotripsy bubble cloud near the point of maximum expansion.

8.2.3 Acoustic Pulse Sequence

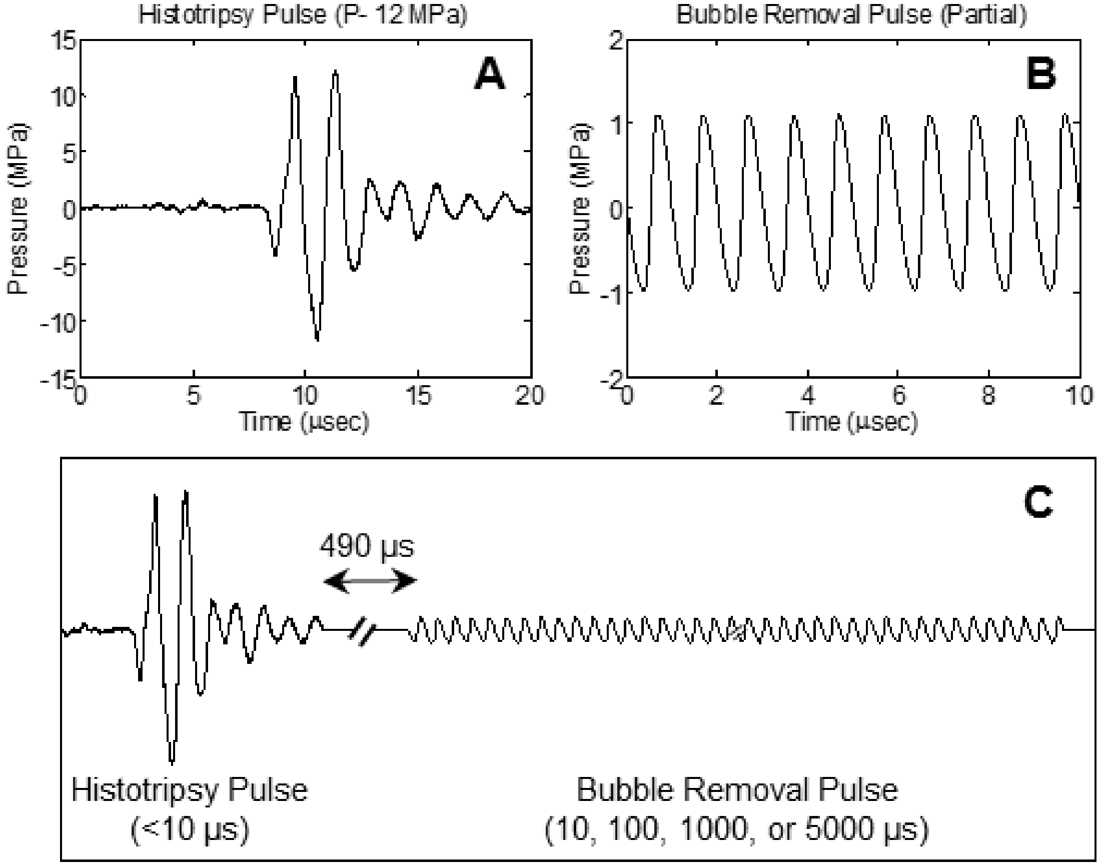

Fig. 8.2 General pulse scheme used to study the effect of bubble removal pulses on histotripsy soft tissue fractionation. (A) Representative waveform acquired from the 500 kHz histotripsy transducer at low power (below the cavitation threshold). The histotripsy pulse P- used for tissue phantom treatments is estimated to be 33 MPa. (B) Partial segment of the bubble removal pulse; all bubble removal pulses had a center frequency of 1 MHz, and amplitude set to either 0 or 1 MPa. (C) Overall timing of the experimental pulse scheme. A 500 µs delay was imposed following histotripsy pulse firing to allow the bubble cloud to collapse in an unimpeded manner. Bubble removal pulse durations of 10, 100, 1000, and 5000 µs were investigated.

Paralleling the work in Chapter 7, two general types of acoustic pulses were utilized in this study, as represented in Fig. 8.2(A-B): 1) Histotripsy pulses generated by the 500 kHz histotripsy transducer were used to initiate a cavitational bubble cloud to mechanically fractionate the tissue phantom; 2) Bubble removal sequences produced by the 1 MHz bubble removal module were used to sonicate residual nuclei following histotripsy bubble cloud collapse, stimulating their removal from the field. The overall timing of this pulse scheme is displayed in Fig. 8.2(C), with specifics provided henceforth.

Histotripsy pulses used in this study were very short (approximately 5 μs), had a center frequency of 500 kHz, and a peak-negative pressure (P-) of 33 MPa. The representative waveform displayed in Fig. 8.2(A), which was measured using the same fiber optic hydrophone used to perform histotripsy field scans, demonstrates the general shape of a histotripsy pulse. However, it was acquired at a lower P- of 12 MPa, as calibration at higher amplitudes can result in instantaneous cavitation on the fiber tip. The therapy P- of 33 MPa reported here was estimated via extrapolation based on the observation that P- increases extremely linearly with the transducer driving voltage. As previous work has established that histotripsy lesion development characteristics are highly dependent on pulse repetition frequency (PRF) [1], histotripsy PRFs of 1 and 100 Hz were tested. The low PRF of 1 Hz serves as a reference for lesion development when cavitation memory effects are minimal, while the high PRF of 100 Hz provides a scenario in which remnant bubble nuclei persist between successive pulses and cavitation memory is pronounced. 500 histotripsy pulses were applied to generate each lesion in this study.

A partial segment of a representative bubble removal sequence is displayed in Fig. 8.2(B), acquired using the same HNR-0500 needle hydrophone used to perform bubble removal module field scans. All bubble removal sequences had a center frequency of 1 MHz and amplitude of either 0 (i.e., no bubble removal) or 1 MPa. The latter setting was selected based on the results of a coarse amplitude investigation. To investigate the effect of pulse duration, bubble removal sequences of 10, 100, 1000, and 5000 cycles were tested. In all cases, a delay of 500 μs was imposed following histotripsy pulse firing to allow for unimpeded bubble cloud collapse prior to sonication with the bubble removal sequences (Fig. 8.2(C)). Eight histotripsy lesions were generated with each parameter combination tested in this study.

8.2.4 Histotripsy Lesion Development Quantification

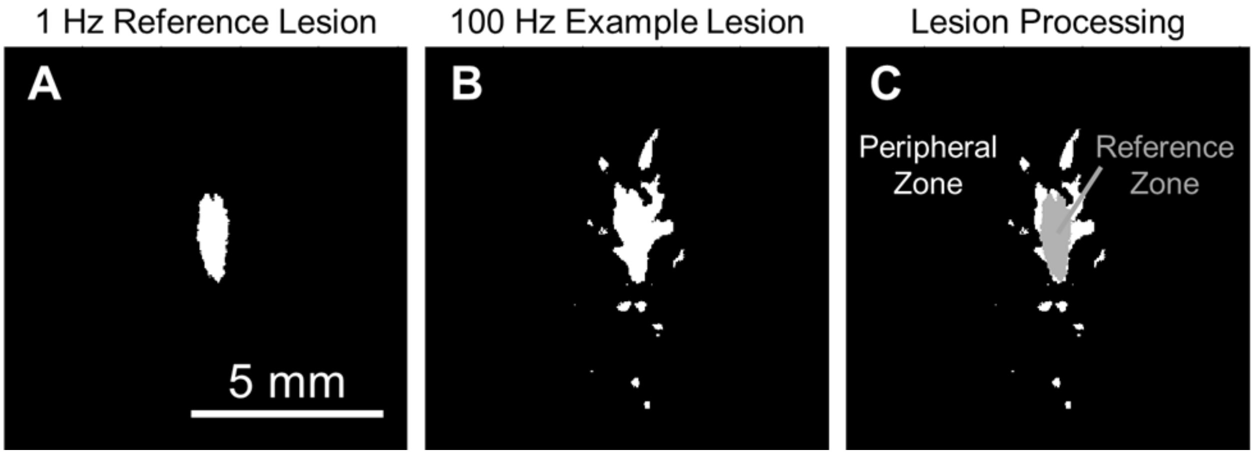

Fig. 8.3 Image processing to quantify the course of lesion development. (A) Because the goal of this work is to recover the efficacious lesion development characteristics associated with low PRF when much higher PRFs are used, the results of this study were analyzed in the context of a 1 Hz reference lesion. This reference lesion represents an average lesion generated at the very low rate of 1 Hz (see text for details). (B) For a given lesion of interest, the corresponding image frame was normalized and thresholded to produce a binary image. A two-dimensional cross correlation was then performed to register the lesion with the 1 Hz reference for damage quantification. (C) Damage occurring within the area encompassed by the 1 Hz reference was defined as reference zone damage, while that falling outside of the 1 Hz reference was defined as peripheral zone damage. The lesion images corresponding to each of the 500 pulses in a given treatment were analyzed in this fashion such that the course of lesion development could be quantified.

Because the goal of this work is to recover the efficacious histotripsy lesion generation characteristics associated with low PRF (e.g. 1 Hz) when much higher PRFs are used (e.g. 100 Hz), the results of this study were analyzed in the context of a 1 Hz reference lesion. This reference lesion represents the average outcome of eight treatments conducted at the very low rate of 1 Hz, and was generated using the following algorithm: 1) The image frames containing the final lesions produced from the eight 1 Hz treatments were normalized, dividing by an image of the untreated field of view acquired prior to each respective treatment. 2) Each normalized image was converted to binary by setting pixels that resided above a threshold value to 1 and those below the threshold to 0; this threshold was selected as 1.5 for all cases. 3) The spatial location of binary lesions #2-8 were registered with that of binary lesion #1 by performing a two-dimensional cross correlation to determine the appropriate amount to shift each image. 4) All eight registered binary images were summed, and the 1 Hz reference lesion was defined as the collection of pixels with values >4 (i.e. the set of sites where damage was present in over half of the eight individual lesions). This reference lesion was also a binary image, with pixels exceeding the 4-count threshold set to 1 and all others set to 0. Fig. 8.3(A) shows the result.

As discussed with respect to the optical setup in Section 8.2.2, a lesion image was acquired corresponding to each histotripsy pulse in a given treatment. These frames were normalized and thresholded using an algorithm analogous to that described above to create a set of binary images. Each resulting binary image was then registered to the 1 Hz reference lesion, again using a two-dimensional cross correlation between the reference lesion and the final lesion of interest to determine the appropriate translation. An example of the result of this processing for a lesion produced after 500 pulses at a PRF of 100 Hz without bubble removal is displayed in Fig. 8.3(B). As indicated in Fig 8.3(C), pixels that coincided with those of the 1 Hz reference lesion were defined as reference zone damage; those that were located outside the 1 Hz reference lesion were defined as peripheral zone damage. All 500 lesion images corresponding to a given treatment were analyzed in this way such that lesion development within the reference and peripheral zones could be quantified.

8.2.5 Volume Treatments

As an extension of this investigation, the bubble removal parameters identified to produce optimal histotripsy lesion development in the single-focus case were utilized to conduct histotripsy volume treatments within the RBC tissue-mimicking phantom. For these experiments the RBC-layer was constructed perpendicular to the axis of the cylindrical phantom, while the cylinder axis was maintained parallel to that of the transducer as shown in Fig. 8.1. This allowed for visualization of the lateral profile of the histotripsy lesion. A 10 x 10 mm region was treated within this lateral plane; in all cases, the transducer was maintained stationary while the tissue phantom was translated via a motorized positioning system (Anaheim Automation Inc., Anaheim, CA) through a series of 10 mm motion paths with 0.25 mm spacing. Histotripsy was applied continuously at a PRF of 100 Hz as the tissue phantom was mechanically scanned through this pattern. In order to vary the treatment dose, the speed of the positioning system was set to 1, 2, or 3 mm/s. For each dose four trials were conducted with and without the incorporation of optimal bubble removal sequences. Following treatment the tissue phantom was placed on a light box and photographed using a digital SLR camera (Rebel XT, Canon U.S.A. Inc., Melville, NY). Resulting images were processed in Matlab using the following algorithm: Each image was first converted to grayscale and then thresholded at six standard deviations above the background mean to create a binary image. Pixels residing below the threshold—which corresponded to unfractionated RBC phantom—were summed to quantify the area of intact structure remaining within the 10 x 10 mm target zone.

8.3 Results

8.3.1 Single-Focal-Spot Lesions

Representative lesions resulting from 500 pulse histotripsy treatments in the RBC tissue-mimicking phantom are displayed in Fig. 8.4, while lesion development within the reference and peripheral zones is quantified in Fig. 8.5 and Fig. 8.6, respectively. All treatments tested in this study produced lesions characterized by a completely fractionated central zone with varying degrees of damage in the periphery. The shape of the central lesion, extent of peripheral damage, and overall time-course of development were all highly dependent on the treatment parameters. As discussed in Section 8.2.4, because the goal of this work is to recover the efficacious histotripsy lesion generation characteristics associated with low PRF (1 Hz) when much higher PRF (100 Hz) is used, the lesions generated in this study were analyzed in the context of a 1 Hz reference lesion (Fig. 8.3).

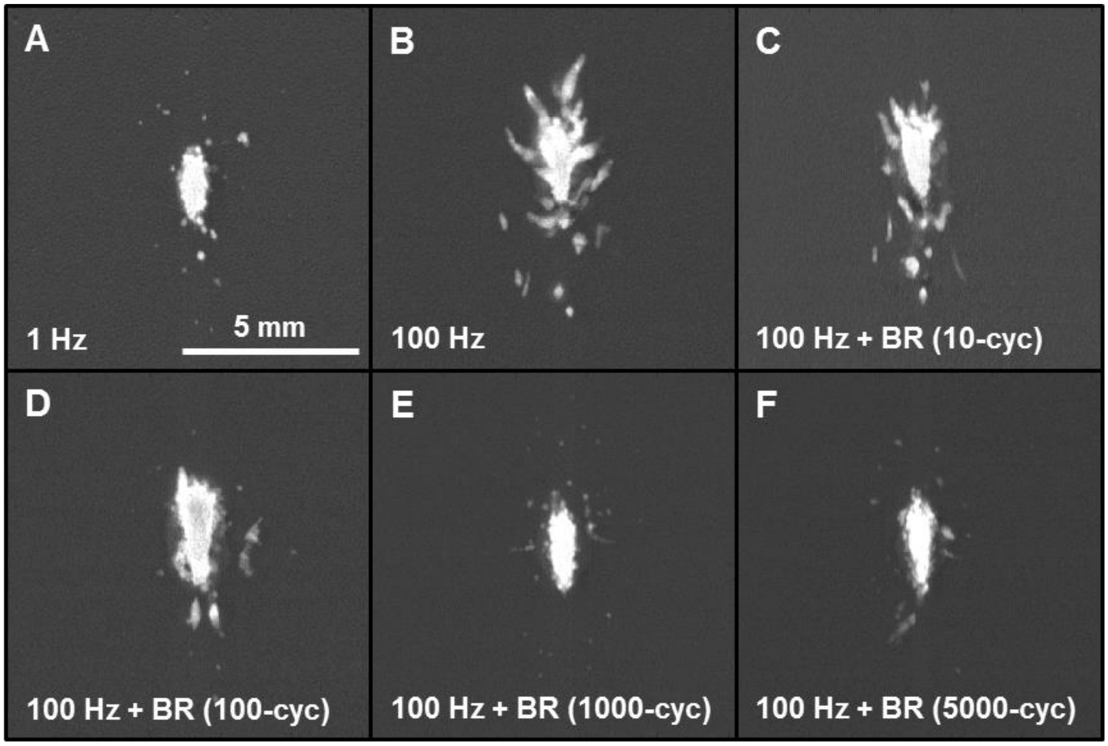

Fig. 8.4 Representative lesions in the RBC tissue-mimicking phantom following 500 histotripsy pulses. All treatments tested in this study produced lesions characterized by a completely fractionated central zone with varying degrees of damage in the periphery. (A) The very low PRF of 1 Hz generated ellipsoidal-shaped lesions with smooth boundaries and minimal peripheral damage. (B) Treatment at the high PRF of 100 Hz produced heterogeneously-shaped lesions with jagged boundaries and increased peripheral damage. (C/D) At 100 Hz PRF, the incorporation of relatively short duration bubble removal sequences of 10 and 100 cycles resulted in final lesions with appearance intermediate to that observed at 1 Hz and 100 Hz without bubble removal. (E/F) Longer bubble removal sequences of 1000 and 5000 cycles allowed final lesions generated at 100 Hz to closely approximate those produced at the low rate of 1 Hz.

Without the incorporation of bubble removal sequences histotripsy lesion development showed a marked dependence on pulse rate. At the very low PRF of 1 Hz, histotripsy generated extremely homogeneous ellipsoidal-shaped lesions with smooth boundaries (Fig. 8.4(A)) and minimal damage in the peripheral zone (Fig. 8.6(A)). In contrast, treatment at the high PRF of 100 Hz produced more heterogeneous lesions with jagged boundaries (Fig. 8.4(B)) and increased damage in the peripheral zone (Fig. 8.6(B)). The rate of lesion development within the reference zone—when evaluated as a function of pulse number—was significantly greater at the low PRF of

1 Hz (Fig. 8.5(A)) compared to the high PRF 100 Hz (Fig. 8.5(B)). Indeed, the number of histotripsy pulses required to achieve 50% damage within the reference zone was significantly lower at 1 Hz in comparison to 100 Hz (*t-test*, P < 0.001) , with respective values of 65 ± 27 (mean ± SD) and 164 ± 57. This metric of per-pulse efficiency is displayed in Fig. 8.7.

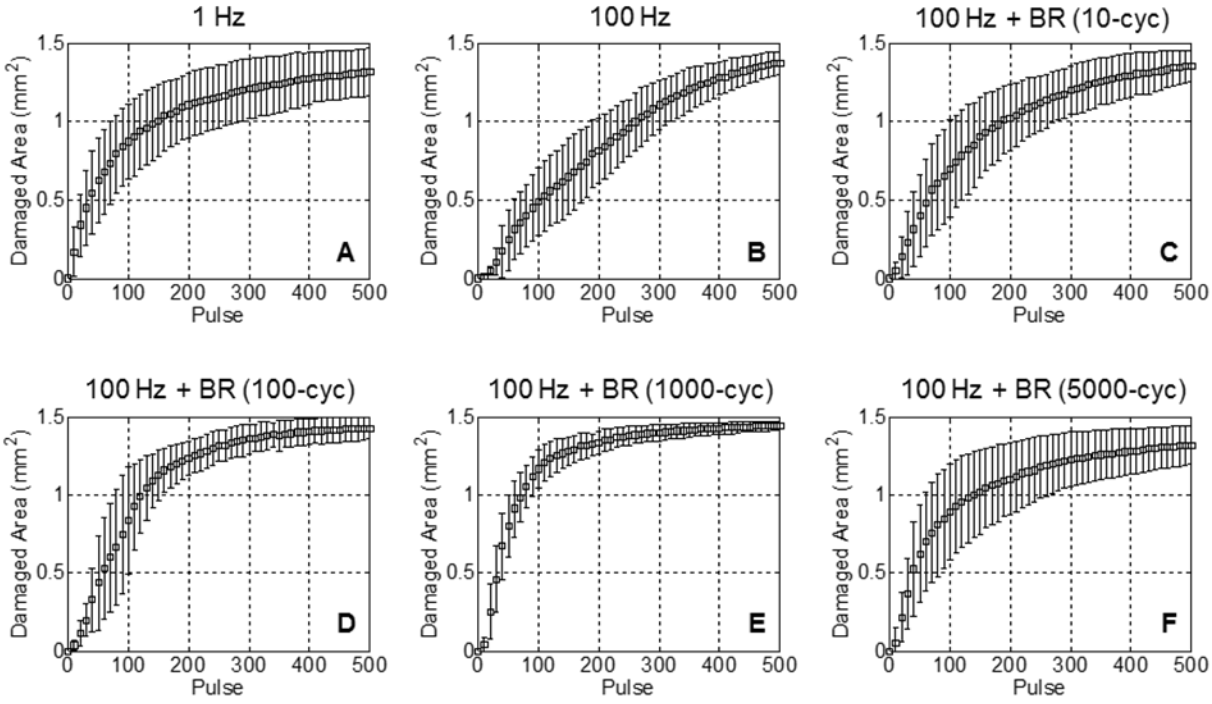

Fig. 8.5 Lesion development within the reference zone over 500 histotripsy pulses. Each curve shows the mean ± SD over eight treatments. (A) The low PRF of 1 Hz produced lesions with a relatively high per-pulse efficiency. (B) At the much higher PRF of 100 Hz, lesion generation showed a reduction in per-pulse efficiency. (C-F) With the incorporation of bubble removal sequences, the efficiency of lesion development at the high PRF of 100 Hz was improved, more closely approximating that observed at the low pulse rate of 1 Hz. Optimal lesion development was observed with the incorporation of a 1000 cycle bubble removal sequence, which produced a per-pulse efficiency exceeding that observed at 1 Hz.

The incorporation of bubble removal sequences in 100 Hz histotripsy treatments resulted in lesion generation characteristics that more closely approximated those achieved at the low PRF of 1 Hz, with the significance of the impact dependent on the bubble removal sequence duration. Relatively short bubble removal sequences of 10 and 100 cycles had moderate impact on lesion development characteristics, producing final lesions with appearance intermediate to that observed at 1 Hz and 100 Hz without bubble removal (Fig. 8.4(C) and Fig. 8.4(D)). In each case, the extent of damage within the peripheral zone was reduced relative to that observed at 100 Hz without bubble removal (Fig. 8.6(C) and Fig. 8.6(D)), while lesion development within the reference zone showed an increase in per-pulse efficiency (Fig. 8.5(C) and Fig. 8.5(D)). Treatments performed with 10 cycle bubble removal sequences required 104 ± 50 pulses to achieve 50% damage within the reference zone, while those with 100 cycle bubble removal sequences required 87 ± 31 pulses (Fig. 8.7). Both of these values represent a statistically significant reduction relative to the case of 100 Hz without bubble removal (*t-test*, $P < 0.04$).

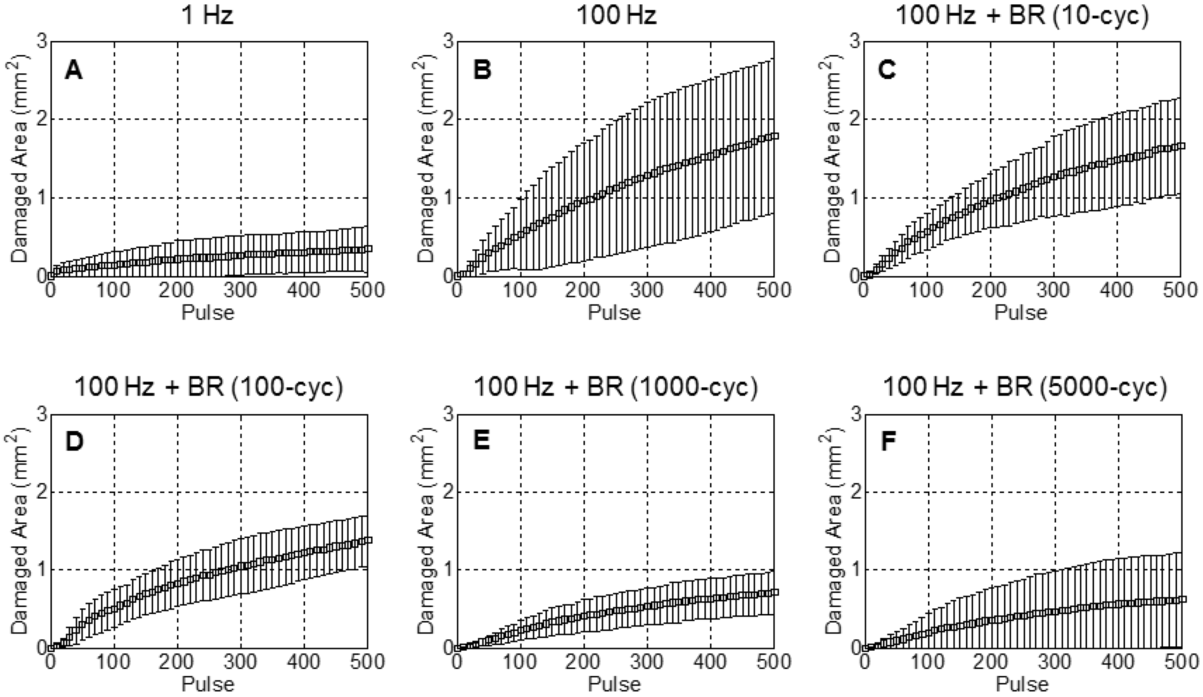

Fig. 8.6 Lesion development within the peripheral zone over 500 histotripsy pulses. Each curve shows the mean ± SD over eight treatments. (A) The low PRF of 1 Hz produced lesions with minimal peripheral zone damage. (B) At the much higher PRF of 100 Hz, the extent of damage observed in the peripheral zone increased substantially. (C-F) With the incorporation of bubble removal sequences, the degree of damage in the peripheral zone produced at 100 Hz PRF was reduced. Bubble removal sequences of 1000 and 5000 cycles mitigated peripheral zone damage to levels commensurate with that observed at 1 Hz.

Bubble removal sequences of 1000 and 5000 cycles had a drastic impact on lesion development at 100 Hz PRF, producing characteristics markedly similar to those observed at the much lower pulse rate of 1 Hz. Final lesions produced following these respective treatment schemes were ellipsoidal-shaped with smooth boundaries (Fig. 8.4(E) and Fig. 8.4(F)), closely approximating that produced following treatment at the low PRF of 1 Hz (Fig. 8.4(A)). In each case, damage in the peripheral zone was drastically reduced relative to 100 Hz without the incorporation of bubble removal sequences (Fig. 8.6(E) and Fig. 8.6(F)), again commensurate with that produced at the low PRF of 1 Hz. Lesion development within the reference zone was also augmented for each case (Fig. 8.5(E) and Fig. 8.5(F)), with per-pulse efficiencies that matched (5000 cycle bubble removal) or even exceeded (1000 cycle bubble removal) that produced at the low PRF of 1 Hz. Specifically, with the incorporation of 1000 cycle bubble removal sequences 46 ± 16 pulses were required to achieve 50% damage within the reference zone; using 5000 cycle bubble removal sequences 69 ± 32 pulses were necessary to reach this same level. Both of these values again represent statistically significant reductions relative to the case of 100 Hz without bubble removal (*t-test*, $P < 0.001$).

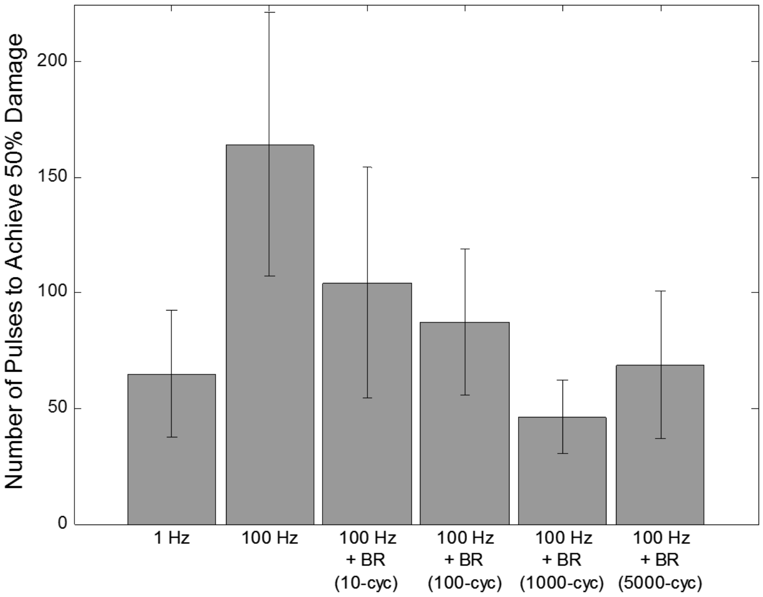

Fig. 8.7 Number of histotripsy pulses required to achieve 50% fractionation within the reference zone, provided as a metric for the per-pulse efficiency of histotripsy lesion development. The low PRF of 1 Hz generated a high efficiency, requiring an average of only 65 pulses to reach the 50% damage level. Treatment at the high PRF of 100 Hz was much less efficient, with an average of 164 pulses needed for 50% damage. The incorporation of bubble removal sequences resulted in a reduction in the number of pulses required to reach the 50% damage level for all cases tested. Optimal efficiency was achieved with the incorporation of a 1000 cycle bubble removal sequence, which required an average of only 46 pulses to reach the 50% threshold.

8.3.2 Volume Treatments

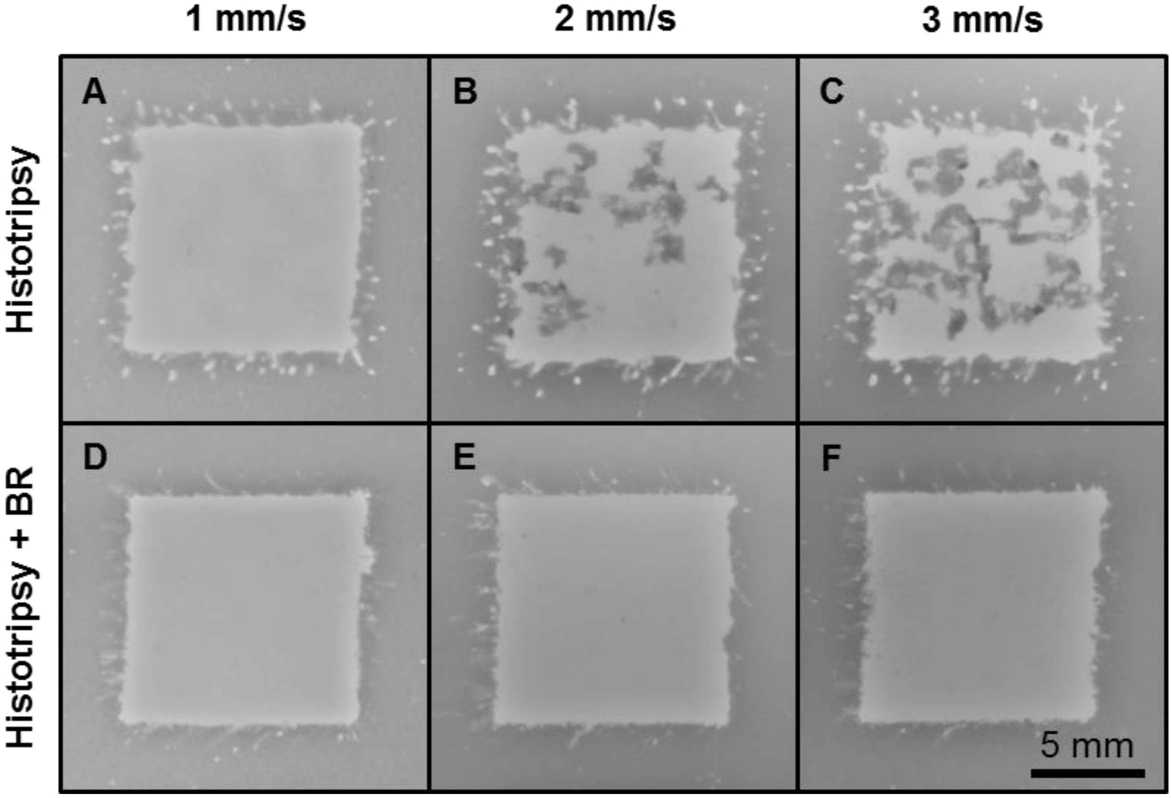

Fig. 8.8 Representative volume treatments in the RBC tissue-mimicking phantom. (A-C) Without the incorporation of bubble removal sequences, as the linear scan speed was increased—i.e. as the histotripsy dose was lowered—the extent of intact tissue phantom structure remaining in the target zone increased. Speeds of 1, 2, and 3 mm/s resulted in average residual structure areas of 5.2, 24.1, and 40.5 mm^2, respectively. (D-F) With the incorporation of 1000 cycle bubble removal sequences, all histotripsy doses resulted in near-complete homogenization of the target zone. In this case speeds of 1, 2, and 3 mm/s produced average residual structure areas of 0.9, 4.0, and 3.8 mm^2, with the majority of this intact structure located on the perimeter of the target zone.

As an extension of this investigation, the 1000 cycle bubble removal sequence identified to produce optimal histotripsy lesion development for the single-focal-location case was utilized to conduct volume treatments within the RBC tissue-mimicking phantom (described in Section 8.2.5). Representative images showing the 10 x 10 mm target zone following treatment are displayed in Fig. 8.8. Without the incorporation of bubble removal (Fig. 8.8, top row), as the histotripsy dose was reduced the area of intact phantom structure within the target zone was observed to increase (*t-test*, $P < 0.02$). Specifically, at linear scan speeds of 1, 2, and 3 mm/s, histotripsy treatment at 100 Hz PRF left behind 5.2 ± 2.8, 24.1 ± 7.9, and 40.5 ± 4.6 mm^2 of intact structure within the 10 x 10 mm target zone. With the incorporation of bubble removal (Fig. 8.8, bottom row), all histotripsy doses investigated resulted in near-complete homogenization of the target zone. The majority of remaining intact structure in these cases resided on the perimeter of the targeted volume, with scan speeds of 1, 2, and 3 mm/s producing residual structure areas of 0.9 ± 1.0, 4.0 ± 1.1, and 3.8 ± 1.6 mm^2, respectively. Each of these values represents a statistically significant reduction in comparison to its histotripsy-only counterpart (*t-test*, $P < 0.03$).

8.4 Discussion

This chapter demonstrates a unique strategy for mitigating the efficiency-limiting effects of residual bubble nuclei in histotripsy soft tissue fractionation, using low-amplitude ultrasound pulses to stimulate their removal from the target medium. When histotripsy is applied in isolation, lesion generation characteristics in the tissue-mimicking RBC phantom are highly dependent on PRF. At the low PRF of 1 Hz, histotripsy lesion development displays a high per-pulse efficiency and the general appearance of final lesions is highly reproducible, having an ellipsoidal shape with smooth boundaries and minimal peripheral damage. In contrast, treatment at the high PRF of 100 Hz results in a pronounced reduction in the per-pulse efficiency of lesion development, and final lesions have a more heterogeneous structure with jagged boundaries and substantial damage in the periphery. With the introduction of bubble removal sequences, the efficacious lesion development characteristics associated with the low pulse rate of 1 Hz can be maintained when the much higher PRF of 100 Hz is used. The impact of this bubble removal strategy is dependent on the sequence duration, with the longer bubble removal sequences of 1000 and 5000 cycles achieving efficiencies and final lesion structures comparable to those observed at 1 Hz.

The bubble removal strategy utilized in this study was developed in the work presented in Chapters 4 and 5 of this dissertation [2, 3]. Through the application of low-amplitude ($MI \leq 1$)

ultrasound pulse sequences on the order of 1 ms in duration, the aggregation and subsequent coalescence of remnant bubble nuclei can be stimulated. This effect is attributed to a combination of the forces exerted by the acoustic field on individual bubbles (primary Bjerknes force) [11-16] and the forces exerted by bubbles on one another (secondary Bjerknes force) [11, 12, 15, 17]; the latter is hypothesized to be the dominant facilitator of the process [2, 3]. Sonication of the remnant nuclei generated by histotripsy bubble cloud collapse with a bubble removal sequence can consolidate the population from thousands of microscopic daughter bubbles to a countably small number of residuals. However, it is important to note that these effects have been previously studied in water, where remnant bubble nuclei are free to translate and the bubble consolidation process experiences minimal impedance.

The present study offers an interesting extension of our previous work, as the medium of interest is a tissue-mimicking phantom composed of agarose hydrogel. In a separate set of fast-frame high speed imaging experiments not detailed in this chapter, we monitored the bubble consolidation process within the agarose construct to evaluate the feasibility of bubble removal in this setting. It was observed that, after a minimal number of histotripsy pulses (< 10), the medium had undergone a sufficient degree of fractionation such that bubble nuclei could be driven through the agarose matrix and consolidation achieved. Interestingly, following only 10 histotripsy pulses the target volume is far from fully fractionated, suggesting that only a minimal degree of porosity is required to achieve the translation of these microscopic bubbles. Currently, the porosity of biological tissue to these microscopic bubbles is unknown, and will most likely be dependent on the specific tissue type. Very preliminary work examining the bubble removal process in fibrinogen constructs suggests that fibrous tissues such as blood clots may have very low impedance to the translation of bubble nuclei. As is discussed further in Chapter 9, a more rigorous examination of this topic will be a component of our future work.

Fast-frame monitoring of residual bubble nuclei within the first 10 histotripsy pulses of a treatment produced a second interesting result. While the translation of remnant nuclei was constrained by the intact agarose hydrogel at this point in the treatment, they did not persist over the entire duration of a given bubble removal sequence. Rather, they were observed to progressively disappear as they were sonicated by a given bubble removal sequence. This suggests that, in addition to removing nuclei via coalescence, bubble removal sequences may destabilize these bubbles in some way that leads to enhanced dissolution. The mechanism underlying this effect is currently unknown. However, this observation suggests that bubble removal sequences may provide a means of actively modulating the incidental cavitation threshold in a target medium, thus setting the stage for the active protection of tissue structures. This important extension of this work is discussed further in Chapter 9.

With respect to histotripsy soft tissue fractionation, the results of this study corroborate previous work by Wang, *et al.* [1] in which the implications of remnant bubble nuclei were explored. In their study, it was shown that the persistence of residual bubbles between successive histotripsy pulses results in the repetitive nucleation of cavitation at a discrete set of sites within the focal volume. This effect—referred to as cavitation memory—limits the efficiency of histotripsy soft tissue fractionation, resulting in the overtreatment of sites with cavitation memory while those without remain undertreated. Development of a histotripsy lesion in this manner requires an excess number of pulses to achieve complete homogenization of the focal volume. One straightforward strategy for mitigating the memory effect is to simply wait a sufficient time between successive histotripsy pulses such that remnant bubble nuclei can passively dissolve.

Indeed, Wang, *et al*. demonstrated that the correlation coefficient between histotripsy cavitation patterns in successive pulses decreases exponentially as the time between pulses increases from 2-200 ms; correspondingly, the lesion development efficiency improves [1]. While this passive approach offers a means of augmenting per-pulse efficiency, the time-rate of treatment suffers when low PRFs are used. For this reason it is desirable to maintain the high efficiency associated with low pulse rates when much higher PRFs are utilized. The active approach provided by bubble removal sequences affords us with this capability, enabling high per-pulse efficiency to be maintained at high pulse rate.

While the cavitation memory effect limits the efficacy of histotripsy lesion development, it is possible that the persistence of a minimal subset of remnant bubble nuclei may augment the therapy. An interesting outcome of this study is the observation that histotripsy delivered at 100 Hz PRF with 5000 cycle bubble removal sequences closely matched the per-pulse efficiency achieved at the low PRF of 1 Hz, while histotripsy delivered at 100 Hz PRF with 1000 cycle bubble removal sequences exceeded it. One possible explanation for this observation is that the longer-duration 5000 cycle bubble removal sequence results in near-complete elimination of residual bubble nuclei, allowing lesion development to behave markedly similar to the 1 Hz case in which memory effects are expected to be negligible [1, 18]. In contrast, the shorter-duration 1000 cycle bubble removal sequence may not achieve complete consolidation of remnant bubbles, leaving behind a minimal number of coalesced seeding nuclei. These nuclei—which are likely to be randomly distributed following each bubble removal sequence—may then augment the subsequent histotripsy pulse. It is likely that the benefit gleaned from these residual bubbles is dependent on the histotripsy pulse amplitude, with pulses at or just below the cavitation threshold experiencing maximal benefit. Previous work has indicated that cavitation memory may indeed be beneficial in cavitation-based therapies that lack sufficient headroom to consistently generate primary cavitation with each pulse, and the persistence of bubble nuclei may enhance the cavitation process in such cases [19-22]. This idea has also been utilized in previous histotripsy studies to enhance tissue fractionation [23-25]. In the present work, our estimated P- of 33 MPa only marginally exceeds the previously measured inertial cavitation threshold in water [26], suggesting that the histotripsy pulses employed here may indeed benefit from a strategic seeding of the target medium. This concept may provide a useful tool in cases in which pulse headroom is limited, and as such warrants further study.

A natural extension of the single-focal-spot lesion development characterized in this study is the treatment of a large volume, as many applications of histotripsy soft tissue fractionation require the homogenization of a target zone much larger than a single histotripsy focus. In such cases the implications of cavitation memory remain pronounced, and the inhomogeneous tissue disruption that results from the persistence of remnant bubble nuclei can manifest in islands of structurally intact tissue persisting within the treatment volume [27, 28]. This phenomenon was observed in the volume treatments conducted in the RBC tissue-mimicking phantom in the present study (Fig. 8.8), with the extent of intact structure observed to increase with increasing scan rate (i.e. with decreasing histotripsy dose). If such volume treatments are being conducted with an electronically phasable array, the memory effect can be mitigated via strategic steering of the histotripsy focus [29]. Rather than treating adjacent points sequentially, it would be beneficial for successive treatment points to reside sufficiently far away from one another such that remnant nuclei do not influence the distribution of cavitation activity. However, in cases in which a steerable array is either not available or not feasible, the bubble removal strategy explored in this chapter can provide a means of enhancing the efficacy of large volume treatments (Fig. 8.8). The enhanced lesion development efficiency afforded by bubble removal sequences (Fig. 8.5) permits the complete homogenization of a point within the target volume with a reduced histotripsy dose. Furthermore, the highly-reproducible lesion shape generated with bubble removal sequences (Fig. 8.4(E) and Fig. 8.4(F)) allows for improved treatment planning with respect to the scan path of the histotripsy transducer. The combination of these characteristics manifests in the capability of faster histotripsy treatment of large target volumes with a reduced probability of residual intact structure.

While this chapter presents an exciting strategy for mitigating the effects of residual bubble nuclei to enhance histotripsy soft tissue fractionation, several limitations exist. This preliminary work utilized the RBC tissue-mimicking phantom due to its ability to provide real-time feedback of the histotripsy lesion development process. However, the results obtained in this phantom must be validated in biological tissues. As discussed in Chapter 9 future work will focus on this effort, evaluating the bubble removal process in *ex-vivo* tissue followed by eventual *in-vivo* application. With previous studies demonstrating that the RBC phantom is an excellent predictor of the outcomes observed in soft tissue [1, 8, 10], we fully expect this process to translate to biological settings to enhance the efficacy of histotripsy when high pulse rates are used.

8.5 Conclusion

Microscopic residual bubble nuclei produced by primary cavitation collapse can limit the efficacy of histotripsy soft tissue fractionation by imposing cavitation memory to the target medium. Sites within the focal volume at which remnant nuclei persist between pulses will experience the repetitive nucleation of cavitation activity and become overtreated, while those without remnant nuclei remain undertreated and require an excess number of pulses for complete homogenization. This effect manifests in histotripsy treatment at low PRF achieving significantly greater per-pulse efficiency in comparison to high PRF, as low pulse rates afford remnant bubbles with sufficient time to dissolve. The bubble removal sequences explored in this chapter provide a means of actively mitigating the ill-effects of bubble nuclei and allow the histotripsy lesion development characteristics observed at the high PRF of 100 Hz to closely match those achieved at the very low PRF of 1 Hz. This includes not only the high per-pulse efficiency of lesion development, but also the homogeneous, reproducible shape of final lesions. Both of these characteristics are highly desirable when planning and conducting histotripsy treatment of a large target volume, and a major potential application of this strategy is enhancing the speed and completeness of volume ablation. These results also provide a preliminary evaluation of the bubble removal process in soft tissue-like structures, suggesting that the extension of bubble removal to the active protection of tissue will be a feasible component of our future work.

8.6 References

[1] T. Y. Wang, Z. Xu, T. L. Hall, J. B. Fowlkes, and C. A. Cain, "An efficient treatment strategy for histotripsy by removing cavitation memory," *Ultrasound Med Biol,* vol. 38, pp. 753-66, May 2012.

[2] A. P. Duryea, C. A. Cain, H. A. Tamaddoni, W. W. Roberts, and T. L. Hall, "Removal of Residual Nuclei Following a Cavitation Event using Low-Amplitude Ultrasound," *IEEE Trans Ultrason Ferroelectr Freq Control,* vol. 61, pp. 1619-26, Oct 2014.

[3] A. P. Duryea, H. A. Tamaddoni, C. A. Cain, W. W. Roberts, and T. L. Hall, "Removal of residual nuclei following a cavitation event: a parametric study," *IEEE Trans Ultrason Ferroelectr Freq Control,* In-Press.

[4] G. Karalezli, O. Gogus, Y. Beduk, C. Kokuuslu, K. Sarica, and O. Kutsal, "Histopathologic effects of extracorporeal shock wave lithotripsy on rabbit kidney," *Urol Res,* vol. 21, pp. 67-70, Jan 1993.

[5] R. Newman, R. Hackett, D. Senior, K. Brock, J. Feldman, J. Sosnowski, *et al.*, "Pathologic effects of ESWL on canine renal tissue," *Urology,* vol. 29, pp. 194-200, Feb 1987.

[6] M. Delius, G. Enders, Z. R. Xuan, H. G. Liebich, and W. Brendel, "Biological effects of shock waves: kidney damage by shock waves in dogs--dose dependence," *Ultrasound Med Biol,* vol. 14, pp. 117-22, 1988.

[7] L. R. Willis, A. P. Evan, B. A. Connors, Y. Shao, P. M. Blomgren, J. H. Pratt*, et al.*, "Shockwave lithotripsy: dose-related effects on renal structure, hemodynamics, and tubular function," *J Endourol,* vol. 19, pp. 90-101, Jan-Feb 2005.

[8] A. D. Maxwell, T.-Y. Wang, L. Yuan, A. P. Duryea, Z. Xu, and C. A. Cain, "A tissue phantom for visualization and measurement of ultrasound-induced cavitation damage," *Ultrasound in medicine & biology,* vol. 36, pp. 2132-2143, 10/28 2010.

[9] J. E. Parsons, C. A. Cain, and J. B. Fowlkes, "Cost-effective assembly of a basic fiber-optic hydrophone for measurement of high-amplitude therapeutic ultrasound fields," *J Acoust Soc Am,* vol. 119, pp. 1432-40, Mar 2006.

[10] L. Kuang-Wei, K. Yohan, A. D. Maxwell, W. Tzu-Yin, T. L. Hall, X. Zhen*, et al.*, "Histotripsy beyond the intrinsic cavitation threshold using very short ultrasound pulses: microtripsy," *Ultrasonics, Ferroelectrics, and Frequency Control, IEEE Transactions on,* vol. 61, pp. 251-265, 2014.

[11] F. G. Blake, "Bjerknes Forces in Stationary Sound Fields," *The Journal of the Acoustical Society of America,* vol. 21, pp. 551-551, 1949.

[12] E. A. Neppiras, "Subharmonic and Other Low-Frequency Emission from Bubbles in Sound-Irradiated Liquids," *The Journal of the Acoustical Society of America,* vol. 46, pp. 587-601, 1969.

[13] L. A. Crum and A. I. Eller, "Motion of Bubbles in a Stationary Sound Field," *The Journal of the Acoustical Society of America,* vol. 48, pp. 181-189, 1970.

[14] L. A. Crum, "The motion of bubbles in a stationary sound field," *The Journal of the Acoustical Society of America,* vol. 46, p. 1411, 1969.

[15] T. G. Leighton, *The Acoustic Bubble*. San Diego, CA: Academic Press Inc, 1997.

[16] T. G. Leighton, A. J. Walton, and M. J. W. Pickworth, "Primary Bjerknes forces," *European Journal of Physics,* vol. 11, p. 47, 1990.

[17] L. A. Crum, "Bjerknes forces on bubbles in a stationary sound field," *The Journal of the Acoustical Society of America,* vol. 57, pp. 1363-1370, 1975.

[18] Z. Xu, T. L. Hall, J. B. Fowlkes, and C. A. Cain, "Optical and acoustic monitoring of bubble cloud dynamics at a tissue-fluid interface in ultrasound tissue erosion," *The Journal of the Acoustical Society of America,* vol. 121, pp. 2421-2430, 2007.

[19] M. Delius and W. Brendel, "A model of extracorporeal shock wave action: tandem action of shock waves," *Ultrasound Med Biol,* vol. 14, pp. 515-8, 1988.

[20] P. Huber, J. Debus, K. Jochle, I. Simiantonakis, J. Jenne, R. Rastert, *et al.*, "Control of cavitation activity by different shockwave pulsing regimes," *Phys Med Biol,* vol. 44, pp. 1427-37, Jun 1999.

[21] M. Arora, L. Junge, and C. D. Ohl, "Cavitation cluster dynamics in shock-wave lithotripsy: part 1. Free field," *Ultrasound Med Biol,* vol. 31, pp. 827-39, Jun 2005.

[22] A. M. Loske, F. E. Prieto, F. Fernandez, and J. van Cauwelaert, "Tandem shock wave cavitation enhancement for extracorporeal lithotripsy," *Phys Med Biol,* vol. 47, pp. 3945-57, Nov 21 2002.

[23] Z. Xu, J. B. Fowlkes, E. D. Rothman, A. M. Levin, and C. A. Cain, "Controlled ultrasound tissue erosion: the role of dynamic interaction between insonation and microbubble activity," *J Acoust Soc Am,* vol. 117, pp. 424-35, Jan 2005.

[24] Z. Xu, J. B. Fowlkes, and C. A. Cain, "A new strategy to enhance cavitational tissue erosion using a high-intensity, Initiating sequence," *IEEE Trans Ultrason Ferroelectr Freq Control,* vol. 53, pp. 1412-24, Aug 2006.

[25] J. E. Parsons, C. A. Cain, G. D. Abrams, and J. B. Fowlkes, "Pulsed cavitational ultrasound therapy for controlled tissue homogenization," *Ultrasound Med Biol,* vol. 32, pp. 115-29, Jan 2006.

[26] A. D. Maxwell, C. A. Cain, T. L. Hall, J. B. Fowlkes, and Z. Xu, "Probability of Cavitation for Single Ultrasound Pulses Applied to Tissues and Tissue-Mimicking Materials," *Ultrasound in Medicine & Biology,* vol. 39, pp. 449-465, 2013.

[27] W. W. Roberts, T. L. Hall, K. Ives, J. S. Wolf, Jr., J. B. Fowlkes, and C. A. Cain, "Pulsed cavitational ultrasound: a noninvasive technology for controlled tissue ablation (histotripsy) in the rabbit kidney," *J Urol,* vol. 175, pp. 734-8, Feb 2006.

[28] T. Y. Wang, Z. Xu, F. Winterroth, T. L. Hall, J. B. Fowlkes, E. D. Rothman, *et al.*, "Quantitative ultrasound backscatter for pulsed cavitational ultrasound therapy-histotripsy," *IEEE Trans Ultrason Ferroelectr Freq Control,* vol. 56, pp. 995-1005, May 2009.

[29] T. L. Hall, *Histotripsy: Non-Invasive Ultrasound Surgery*: University of Michigan., 2007.

Chapter 9

Summary and Future Work

9.1 Summary

This dissertation demonstrates that appropriate control of the cavitation environment surrounding a kidney stone can markedly enhance the comminution process. More specifically, two major approaches are investigated to augment traditional SWL procedures, including cavitation-enhancing histotripsy pulses and cavitation-suppressing bubble removal pulses. It is our hope that this work will provide a foundation for an augmented non-invasive stone therapy that incorporates each of these two modalities developed for improved cavitation control.

1) Histotripsy for Stone Erosion: Histotripsy has been shown effective for eroding model stones to tiny particulate debris via a cavitational bubble cloud localized on the stone surface [1-5]. Whereas SWL comminutes stones in a progressive manner—first into large pieces and then to smaller and smaller fragments as more shock waves are applied [6]—histotripsy produces this fine debris from the onset of treatment [1, 2, 4]. Furthermore, because histotripsy is a surface erosion phenomenon, the rate of erosion is dependent on the area of exposed stone [3, 4]. In this way histotripsy and SWL are highly synergistic. While SWL is extremely effective for the initial subdivision of a stone, its efficacy falls off as fragments are reduced to smaller size [6, 7]. The erosion efficiency of histotripsy, however, is enhanced as a stone is fragmented and has greater exposed surface area [3, 4]. Indeed, a truncated SWL exposure followed with histotripsy treatment was observed to produce enhanced comminution in comparison to either modality in isolation [4]. Benefit was also gleaned by applying a histotripsy pretreatment prior to SWL [4], and it is likely that stone surface defects initiated by histotripsy cavitation provide sites from which cracks can nucleate during the SWL comminution process. Interleaving histotripsy pulses between successive shock waves would be the preferred means of combining these modalities, as it should afford the complementary effects of a combined therapy without added treatment time. However, the effects of unmitigated remnant bubble nuclei are likely to limit the efficacy of stone comminution with this interleaved scheme [4].

2) Bubble Removal for Eliminating Remnant Nuclei: While cavitation is a crucial component of the stone comminution process, the persistence of microscopic remnant nuclei generated by primary cavitation collapse can limit the per-pulse efficiency of both histotripsy and SWL [8-16]. This motivated the development of a novel ultrasonic pulse sequence for the active removal of these residual bubbles [17, 18]. These sequences, which we term bubble removal pulses, are typified by low amplitude (MI ~ 1) and moderate duration (~ 1 ms). When used to sonicate the population of remnant bubbles produced by primary cavitation collapse, bubble removal pulses stimulate the aggregation and subsequent coalescence of bubble nuclei; this consolidates a population of thousands of remnant bubbles down to a countably small number of residuals. In this way the field can be actively cleared prior to the delivery of a subsequent therapy pulse, providing a ‘clean-slate’ for the initiation of cavitation activity. It is hypothesized that the bubble coalescence process is the result of an interplay of the primary and secondary Bjerknes forces, with the latter being the dominant contributor [17, 18]. Parametric investigation indicates that higher pulse frequencies (~ 2 MHz) are likely to maximize this force and produce more effective consolidation [18]. When applied to SWL [19] or histotripsy [5] stone comminution, bubble removal pulses were shown to enhance the per-pulse efficiency of treatment when high pulse rates were utilized. A similar result was observed for the application of bubble removal to histotripsy treatment of a soft-tissue-mimicking phantom, and histotripsy lesion development at high pulse rates was augmented.

While this dissertation demonstrates the feasibility of cavitation control for enhanced kidney stone comminution in an *in-vitro* setting, much work remains to facilitate the successful *in-vivo* translation of these concepts. The remainder of this chapter details the key components of our future work that will permit the continued development of both histotripsy and bubble removal pulses for augmented stone comminution procedures.

9.2 Future Work

9.2.1 Histotripsy Phasing Strategies for Enhanced Stone Erosion

As the histotripsy stone comminution process is a surface erosion phenomenon dependent on exposed stone area [3, 4], it stands to reason that the natural focal patterns of the histotripsy transducers used to-date are not optimal for this application. Rather, an enlarged focal zone better-suited for more complete stone coverage should lead to enhanced erosion rates and minimize the probability of untreated fragments of significant size. Such focal enlargement can be achieved through two main approaches: (1) A reduction in transducer center frequency, and (2) strategic phasing of a steerable array. A preliminary exploration of the latter is in progress using the 500-kHz 112-element histotripsy array detailed in Chapters 7 and 8 and the *in-vitro* model stone setup depicted in Fig. 7.1.

Three distinct phasing strategies are under evaluation as part of this initial work. These include: (1) Sector vortex [20, 21], in which array elements are subdivided into four equivalent quadrants with phase delays of 0°, 90°, 180°, and 270°, respectively; this phasing strategy produces an annular focal field with a -6-dB beamwidth of 4.6 mm when applied to the 112-element histotripsy array. (2) Rapid scanning, in which the histotripsy array focus is sequentially steered to the points of a 3 x 3 grid with 3 mm spacing; a 15 µs delay is imposed between successive points as dictated by the limits of the array's driving system. (3) Genetic algorithm [22], in which said algorithm is utilized to determine the phase delays required to generate a focal zone with -6-dB beamwidth of specified size; a 4.6 mm beamwidth should be tested for a direct comparison with the sector vortex strategy. As a preliminary assessment, phasing strategies were delivered to model stones at a repetition frequency of 1 Hz for 16.7 minutes, and the transducer driving voltage was adjusted such that the peak-negative pressure in the field was 40 MPa in all cases (estimated via linear extrapolation). Resulting stone erosion was compared to treatments performed using the array's natural focus, which has a -6-dB beamwidth of 2.0 mm. Natural focus treatments were also performed at a pulse repetition frequency of 1 Hz for 16.7 minutes, with an estimated peak-negative field pressure of 40 MPa.

Preliminary results have been obtained for the sector vortex, rapid scanning, and natural focus cases. The genetic algorithm, while already developed [22], has not yet been implemented in stone erosion experiments. Histotripsy treatment using the natural focus eroded 9.1 ± 4.5 mg of stone material. Corresponding high speed imaging showed that each pulse generated a bubble cloud localized on the stone surface, although this cavitation activity only covered a subset of the stone. Sector vortex phasing generated a substantial increase in stone erosion relative to the natural focus (*t-test*, $P < 0.001$), eroding 72.5 ± 9.3 mg. High speed imaging again showed that each pulse generated a bubble cloud localized on the stone surface, with enhanced coverage in comparison to the natural focal pattern. Rapid scanning of the histotripsy focus did not produce a significant difference in erosion relative to the natural focus (*t-test*, $P = 0.49$), with 6.9 ± 2.1 mg eroded over the course of treatment. In this case high speed imaging showed extensive prefocal cavitation, with minimal cavitation generated on the stone surface.

This ongoing work indicates that strategic phasing of a histotripsy array transducer can significantly enhance stone treatment. However, the timing of the relative field components appears to be an important consideration, and these preliminary results suggest that it is desirable to deliver the sound energy within a narrow time window in order to avoid bubble shielding. Such effects are likely responsible for the observation that the sector vortex approach (all sound delivered within 1.5 μs) substantially enhances erosion relative to the natural focus, whereas the rapid scanning approach (15 μs between successive points) has minimal effect. Continued work on this topic will further investigate this phenomenon, as well as explore additional approaches (e.g. the genetic algorithm) for focal enlargement via strategic array phasing.

9.2.2 Bubble Removal to Augment SWL-Histotripsy Combined Therapy

Chapter 3 of this dissertation demonstrates that histotripsy-induced cavitation can provide an adjunct to the SWL stone comminution process [4]. When applied prior to SWL, histotripsy cavitation generates extensive pitting on the stone surface; it is likely that these surface defects act to precondition stones for increased susceptibility to shock waves, providing sites at which cracks can initiate. When applied following primary stone subdivision with SWL, histotripsy rapidly erodes the large exposed stone surface area to fine particulate debris; this action is highly complementary to the SWL comminution process, which shows a reduced efficacy for fragments of small size [6, 7].

Rather than applying SWL and histotripsy therapies independent and subsequent to one another, it would be ideal to interleave histotripsy pulses between successive shock waves. At the typical clinical shock rate of 1 Hz, there is a full second between successive shock waves during which no therapy is administered. This presents a large time window during which histotripsy could be applied to enhance stone comminution without adding additional time to the procedure. In this type of interleaved treatment scheme, one would expect both the aforementioned comminution enhancements to be at play: During the initial stages, surface defects induced by histotripsy cavitation erosion are likely to facilitate the formation and growth of cracks within the stone matrix; following primary stone subdivision, the increase in exposed surface area should augment histotripsy therapy and enhance the cavitation erosion process. However, the results in Chapter 3 showed that the degree of stone comminution resulting from an interleaved scheme was reduced relative to cases in which SWL and histotripsy were applied in isolation subsequent to one another. The onset of stone subdivision was also noted to require an increased number of shock waves during the interleaved treatment in comparison to SWL-only. Correspondingly, an increase in prefocal cavitation was observed on high speed imaging when comparing interleaved treatment to traditional SWL.

These results regarding combined SWL-histotripsy treatment suggest that the implications of remnant bubble nuclei are an important consideration in designing an interleaved pulse scheme. When histotripsy pulses are applied between successive shock waves, they will seed the medium with residual daughter bubbles that reduce the efficacy of subsequent shocks. For this reason there is an inherent trade-off associated with an interleaved scheme. To maximize the histotripsy therapeutic effect, we would like to apply a maximal number of histotripsy pulses between shock waves; however, to minimize bubble shielding effects on subsequent shock waves, a sufficient wait time must be imposed following a histotripsy burst to allow for passive dissolution of remnant nuclei.

To realize the full potential of an interleaved SWL-histotripsy therapy, bubble removal pulses should be incorporated to actively relieve the ill-effects of remnant bubble nuclei. This future work will represent the culmination of the strategies explored in this dissertation: cavitation-enhancing histotripsy pulses will augment SWL stone comminution as described previously, while cavitation-suppressing bubble removal pulses will alleviate the compromising effects of remnant bubbles. In addition to promoting enhanced synergy between SWL and histotripsy, as demonstrated in Chapters 6 and 7 the incorporation of bubble removal should also augment the per-pulse efficiency of each individual therapy [5, 19]. Overall, it is expected that this combined approach will generate rates of stone comminution far-exceeding those achieved by any one modality in isolation.

This future work also offers the opportunity to further optimize the bubble removal process. While a preliminary parametric investigation was performed in Chapter 5 [18], optimizing bubble removal sequences via experimentation is a cumbersome undertaking. For this reason future efforts should utilize mathematical simulation to more efficiently assess the extensive parameter space associated with these pulses. A simulation for predicting the behavior of microscopic bubbles resulting from the primary and secondary Bjerknes forces has already been created [23], although not yet implemented for bubble removal pulse design. This simulation should be used to design a bubble removal source that is compatible with the dual-mode setup presented in Chapter 3. The relative sizes of residual bubble nuclei generated by cavitation collapse in SWL and histotripsy should also be further investigated and considered in this design.

9.2.3 Bubble Removal for Active Protection of Peripheral Tissues

The work in this dissertation primarily focuses on cavitation control for enhanced efficiency of kidney stone comminution. However, another aspect of stone treatment that stands to benefit from strategic cavitation control is procedure safety. Traditional SWL treatments carry the inherent risk of collateral tissue damage, especially when large shock wave doses (> 3000) are applied [24-27]. Cavitation is almost certainly a major contributor to this damage, as methods of cavitation suppression using static overpressure [28, 29], modified lithotripter waveforms [30, 31], and induced vasoconstriction [32, 33] have all been shown to greatly reduce tissue injury. With this in mind, we believe that the cavitation control strategies developed in this dissertation—specifically, bubble removal pulse sequences—can be adapted to actively protect tissues adjacent to a target stone.

Chapter 8 offers preliminary insight to the application of bubble removal sequences to soft tissue. In this case bubble removal was utilized to alleviate the cavitation memory effect and increase the efficiency of histotripsy lesion development in a tissue-mimicking phantom. However, when interpreted in a broader context, these results provide a foundation on which future work pertaining to active tissue protection can be built. Of particular interest are the fast-frame high speed imaging experiments discussed in Section 8.4. To reiterate briefly, it was observed that after a minimal number of histotripsy pulses (< 10), the agarose construct had undergone a sufficient degree of fractionation such that bubble nuclei could be driven through the medium and consolidation achieved. This result suggests that only a minimal degree of porosity is required to achieve the translation of these microscopic bubbles, as the agarose hydrogel is far from fully fractionated following only 10 histotripsy pulses. The porosity of biological tissue to microscopic cavitation nuclei is currently unknown, and this should be addressed as the bubble removal strategy is developed for the application of active protection. It is likely that the degree of bubble mobility will be a function of tissue type, and as introduced in Section 8.4, preliminary work suggests that fibrous tissues such as blood clots may have a low impedance to the translation of bubble nuclei.

Further investigation on this topic should first assess the bubble removal process in a variety of tissue-mimicking environments. Fibrin gels with a range of concentrations will be useful in this regard, as they maintain sufficient optical clarity such that the effect of bubble removal sequences can be monitored via high speed imaging. A follow up study in *ex-vivo* tissues should also be performed; in this case, ultrasound imaging feedback will be required to monitor the bubble nuclei behavior.

A second relevant result discussed in Section 8.4 is the behavior of remnant bubble nuclei within the first 10 pulses of a histotripsy treatment—i.e. when translation is constrained by the intact agarose hydrogel. In this case bubble nuclei were observed to progressively disappear as they were sonicated by a bubble removal sequence, suggesting that bubble removal pulses may be capable of destabilizing microscopic bubbles in some way that leads to their enhanced dissolution. The mechanism underlying this effect is currently unknown, and certainly warrants future study. If we can understand and optimize this process, bubble removal sequences could provide a means of actively increasing the incidental cavitation threshold in a target tissue by removing any preexisting nuclei. Application of this approach to tissues surrounding a kidney stone could significantly lower the risk of collateral tissue injury associated with incidental nucleation of cavitation activity.

Several valuable tools are at our disposal to further study the concept of nuclei destabilization for active threshold modulation. Most notably, our lab has recently developed frequency compounding transducers capable of synthesizing near-monopolar pulses (positive or negative) [34]. This affords us with the capability to isolate the aspects of a waveform that may lead to the destabilization effect detailed above. As previous research in the field of SWL has documented that the positive shock front of a lithotripsy waveform induces the fragmentation of preexisting bubble nuclei to smaller daughter bubbles [35], one hypothesis in this regard is that a train of positive monopolar pulses may progressively fragment bubble nuclei to the point of enhanced dissolution. This strategy would provide a means of active bubble removal that does not require bubble mobility within the medium, making it ideal for the application of active tissue protection. However, a potential drawback to this approach is the fact that—with our current frequency compounding transducers—the monopolar nature of the pulse exists explicitly within a tight focal volume, dictated by the highest frequency utilized in the array. It may therefore be difficult to protect a large region of interest in this way. Future work should evaluate the feasibility of enhanced bubble dissolution via monopolar pulses; if promising, careful planning of future frequency compounding transducer designs should enhance focal coverage for this specific application.

9.2.4 *In-Vivo* Validation of Strategies for Cavitation Control

While the studies presented in this dissertation provide proof of concept for cavitation control to enhance kidney stone comminution, it is important to note that they were performed in a simplified *in-vitro* environment. As such, i*n-vivo* validation of these concepts in a live animal model will be a crucial next step in their development. This is especially true for the assessment of bioeffects associated with stone treatment—as well as our ability to mitigate them. The use of a live animal model is essential for such studies as small focal regions of cell disruption can be very difficult to detect otherwise. A general protocol for acute studies utilizing a porcine model follows.

The same cystine-mimicking artificial stones used in Chapters 3, 6, and 7 of this dissertation can be implanted percutaneously in the upper pole of 45-55 kg pigs. Upon closer examination of the collecting system of these animals, the stone size may need to be modified relative to the 1 cm diameter cylinders utilized in previous *in-vitro* studies. The implantation method described by Paterson [36] with modifications suggested by Maynes [37] should be used with a single stone placed in the upper pole of both the left and right kidneys. A minimum delay time of two hours should be imposed between implantation and experiment to allow any air introduced during implantation to dissolve. Only the left kidney (treated first) will be used in these experiments due to the potential for vasoconstriction to reduce injury for secondary treatments [38]. The right kidney will not be exposed to ultrasound therapy, but should be examined to establish the degree of injury caused during stone implantation. SWL and histotripsy can be delivered using the system described in Ch. 3, which will require minor modification to spatially accommodate the animal. Furthermore, as discussed in Section 9.2.2, an optimized bubble removal source should be designed for compatibility with this system. Preliminary targeting will be performed using an ultrasound imaging probe inserted within the electrode port of the SWL reflector; treatments may need to be interrupted periodically to check alignment of the focus to the target stone. Following sonication, harvested kidneys will be grossly dissected and the collecting system and renal pelvis flushed to remove all stone debris. Fragments should be washed and sieved to determine resulting size distributions, and kidney tissue should be processed for histology to determine the extent of injury.

Through use of this general *in-vivo* protocol, the following aspects of cavitation control for enhanced stone comminution can be investigated: (1) Effectiveness of histotripsy stone erosion and potential for collateral tissue damage resulting from histotripsy-induced cavitation. (2) Histotripsy to augment SWL stone comminution and the potential for collateral tissue damage resulting from an interleaved pulse scheme. (3) Bubble removal sequences to mitigate cavitation nuclei shielding effects in a biological setting, both for SWL and histotripsy. (4) Active protection of tissue structures surrounding a target stone using bubble removal sequences optimized for this purpose. Successful translation of these aspects of cavitation control to the *in-vivo* setting will represent a major milestone for the strategies established in this dissertation. It is the author's hope that the continued development of these ideas will one day serve to alleviate the major limitations preventing SWL from realizing its full potential as a first-line treatment for the non-invasive removal of kidney stones.

9.3 References

[1] A. P. Duryea, A. D. Maxwell, W. W. Roberts, Z. Xu, T. L. Hall, and C. A. Cain, "In vitro comminution of model renal calculi using histotripsy," *IEEE Trans Ultrason Ferroelectr Freq Control*, vol. 58, pp. 971-80, May 2011.

[2] A. P. Duryea, T. L. Hall, A. D. Maxwell, Z. Xu, C. A. Cain, and W. W. Roberts, "Histotripsy erosion of model urinary calculi," *J Endourol*, vol. 25, pp. 341-4, Feb 2011.

[3] A. P. Duryea, W. W. Roberts, C. A. Cain, and T. L. Hall, "Optimization of histotripsy for kidney stone erosion," in *Ultrasonics Symposium (IUS), 2010 IEEE*, 2010, pp. 342-345.

[4] A. P. Duryea, W. W. Roberts, C. A. Cain, and T. L. Hall, "Controlled cavitation to augment SWL stone comminution: mechanistic insights in vitro," *IEEE Trans Ultrason Ferroelectr Freq Control*, vol. 60, pp. 301-9, Feb 2013.

[5] A. P. Duryea, W. W. Roberts, C. A. Cain, and T. L. Hall, "Removal of residual cavitation nuclei to enhance histotripsy erosion of model urinary stones," *IEEE Trans Ultrason Ferroelectr Freq Control*, In-Press.

[6] S. Zhu, F. H. Cocks, G. M. Preminger, and P. Zhong, "The role of stress waves and cavitation in stone comminution in shock wave lithotripsy," *Ultrasound Med Biol*, vol. 28, pp. 661-71, May 2002.

[7] O. A. Sapozhnikov, A. D. Maxwell, B. MacConaghy, and M. R. Bailey, "A mechanistic analysis of stone fracture in lithotripsy," *J Acoust Soc Am*, vol. 121, pp. 1190-202, Feb 2007.

[8] T. Y. Wang, Z. Xu, T. L. Hall, J. B. Fowlkes, and C. A. Cain, "An efficient treatment strategy for histotripsy by removing cavitation memory," *Ultrasound Med Biol*, vol. 38, pp. 753-66, May 2012.

[9] Y. A. Pishchalnikov, J. A. McAteer, and J. C. Williams, Jr., "Effect of firing rate on the performance of shock wave lithotriptors," *BJU Int*, vol. 102, pp. 1681-6, Dec 2008.

[10] Y. A. Pishchalnikov, J. A. McAteer, J. C. Williams, Jr., I. V. Pishchalnikova, and R. J. Vonderhaar, "Why stones break better at slow shockwave rates than at fast rates: in vitro study with a research electrohydraulic lithotripter," *J Endourol,* vol. 20, pp. 537-41, Aug 2006.

[11] Y. A. Pishchalnikov, O. A. Sapozhnikov, M. R. Bailey, I. V. Pishchalnikova, J. C. Williams, and J. A. McAteer, "Cavitation selectively reduces the negative-pressure phase of lithotripter shock pulses," *Acoust Res Lett Online,* vol. 6, pp. 280-286, Nov 3 2005.

[12] G. Vallancien, R. Munoz, M. Borghi, B. Veillon, J. M. Brisset, and M. Daudon, "Relationship between the frequency of piezoelectric shock waves and the quality of renal stone fragmentation. In vitro study and clinical implications," *Eur Urol,* vol. 16, pp. 41-44, 1989.

[13] H. Wiksell and A. C. Kinn, "Implications of cavitation phenomena for shot intervals in extracorporeal shock wave lithotripsy," *Br J Urol,* vol. 75, pp. 720-3, Jun 1995.

[14] A. Greenstein and H. Matzkin, "Does the rate of extracorporeal shock wave delivery affect stone fragmentation?," *Urology,* vol. 54, pp. 430-432, 1999.

[15] M. J. Weir, N. Tariq, and R. J. Honey, "Shockwave frequency affects fragmentation in a kidney stone model," *J Endourol,* vol. 14, pp. 547-50, Sep 2000.

[16] Y. A. Pishchalnikov, J. A. McAteer, M. R. Bailey, I. V. Pishchalnikova, J. C. Williams, and A. P. Evan, "Acoustic shielding by cavitation bubbles in shock wave lithotripsy (SWL)," in *17th International Symposium on Nonlinear Acoustics* 2005, pp. 319-322.

[17] A. P. Duryea, C. A. Cain, H. A. Tamaddoni, W. W. Roberts, and T. L. Hall, "Removal of Residual Nuclei Following a Cavitation Event using Low-Amplitude Ultrasound," *IEEE Trans Ultrason Ferroelectr Freq Control,* vol. 61, pp. 1619-26, Oct 2014.

[18] A. P. Duryea, H. A. Tamaddoni, C. A. Cain, W. W. Roberts, and T. L. Hall, "Removal of residual nuclei following a cavitation event: a parametric study," *IEEE Trans Ultrason Ferroelectr Freq Control,* In-Press.

[19] A. P. Duryea, W. W. Roberts, C. A. Cain, H. A. Tamaddoni, and T. L. Hall, "Acoustic bubble removal to enhance SWL efficacy at high shock rate: an in vitro study," *J Endourol,* vol. 28, pp. 90-5, Jan 2014.

[20] C. A. Cain and S. Umemura, "Concentric-Ring and Sector-Vortex Phased-Array Applicators for Ultrasound Hyperthermia," *Microwave Theory and Techniques, IEEE Transactions on,* vol. 34, pp. 542-551, 1986.

[21] S. Umemura and C. A. Cain, "The sector-vortex phased array: acoustic field synthesis for hyperthermia," *Ultrasonics, Ferroelectrics, and Frequency Control, IEEE Transactions on,* vol. 36, pp. 249-257, 1989.

[22] H. A. Tamaddoni, A. P. Duryea, and T. L. Hall, "Non-focal acoustic lens designs for caviation bubble consolidation " in *The 168th Meeting of the Acoustical Society of America*, Indianapolis, IN, USA, 2014.

[23] H. A. Tamaddoni, A. P. Duryea, C. A. Cain, and T. L. Hall, "Experimental validation of a model for cavitation bubble consolidation," in *The 14th International Symposium on Therapeutic Ultrasound*, Las Vegas, Nevada, USA, 2014.

[24] G. Karalezli, O. Gogus, Y. Beduk, C. Kokuuslu, K. Sarica, and O. Kutsal, "Histopathologic effects of extracorporeal shock wave lithotripsy on rabbit kidney," *Urol Res,* vol. 21, pp. 67-70, Jan 1993.

[25] R. Newman, R. Hackett, D. Senior, K. Brock, J. Feldman, J. Sosnowski*, et al.*, "Pathologic effects of ESWL on canine renal tissue," *Urology,* vol. 29, pp. 194-200, Feb 1987.

[26] M. Delius, G. Enders, Z. R. Xuan, H. G. Liebich, and W. Brendel, "Biological effects of shock waves: kidney damage by shock waves in dogs--dose dependence," *Ultrasound Med Biol,* vol. 14, pp. 117-22, 1988.

[27] L. R. Willis, A. P. Evan, B. A. Connors, Y. Shao, P. M. Blomgren, J. H. Pratt*, et al.*, "Shockwave lithotripsy: dose-related effects on renal structure, hemodynamics, and tubular function," *J Endourol,* vol. 19, pp. 90-101, Jan-Feb 2005.

[28] M. Delius, "Minimal static excess pressure minimises the effect of extracorporeal shock waves on cells and reduces it on gallstones," *Ultrasound in Medicine & Biology,* vol. 23, pp. 611-617, 1997.

[29] J. A. McAteer, M. A. Stonehill, K. Colmenares, J. C. Williams, A. P. Evan, R. O. Cleveland*, et al.*, "SWL cavitation damage in vitro: Pressurization unmasks a differential response of foil targets and isolated cells," *The Journal of the Acoustical Society of America,* vol. 103, pp. 3038-3038, 1998.

[30] D. L. Sokolov, M. R. Bailey, and L. A. Crum, "Dual-pulse lithotripter accelerates stone fragmentation and reduces cell lysis in vitro," *Ultrasound Med Biol,* vol. 29, pp. 1045-52, Jul 2003.

[31] P. Zhong and Y. Zhou, "Suppression of large intraluminal bubble expansion in shock wave lithotripsy without compromising stone comminution: methodology and in vitro experiments," *J Acoust Soc Am,* vol. 110, pp. 3283-91, Dec 2001.

[32] L. R. Willis, A. P. Evan, B. A. Connors, R. K. Handa, P. M. Blomgren, and J. E. Lingeman, "Prevention of lithotripsy-induced renal injury by pretreating kidneys with low-energy shock waves," *J Am Soc Nephrol,* vol. 17, pp. 663-73, Mar 2006.

[33] R. K. Handa, M. R. Bailey, M. Paun, S. Gao, B. A. Connors, L. R. Willis, *et al.*, "Pretreatment with low-energy shock waves induces renal vasoconstriction during standard shock wave lithotripsy (SWL): a treatment protocol known to reduce SWL-induced renal injury," *BJU Int,* vol. 103, pp. 1270-4, May 2009.

[34] K. W. Lin, T. L. Hall, R. J. McGough, Z. Xu, and C. A. Cain, "Synthesis of monopolar ultrasound pulses for therapy: the frequency-compounding transducer," *IEEE Trans Ultrason Ferroelectr Freq Control,* vol. 61, pp. 1123-36, Jul 2014.

[35] Y. A. Pishchalnikov, J. A. McAteer, I. V. Pishchalnikova, J. C. Williams, M. R. Bailey, and O. A. Sapozhnikov, "Bubble proliferation in shock wave lithotripsy occurs during inertial collapse," in *18th International Symposium on Nonlinear Acoustics*, 2008, pp. 460-463.

[36] R. F. Paterson, J. E. Lingeman, A. P. Evan, B. A. Connors, J. C. Williams, Jr., and J. A. McAteer, "Percutaneous stone implantation in the pig kidney: a new animal model for lithotripsy research," *J Endourol,* vol. 16, pp. 543-7, Oct 2002.

[37] L. J. Maynes, P. J. Desai, C. W. Zuppan, B. J. Barker, G. J. Zimmerman, and D. D. Baldwin, "Comparison of a novel one-step percutaneous nephrolithotomy sheath with a standard two-step device," *Urology,* vol. 71, pp. 223-7, Feb 2008.

[38] B. A. Connors, A. P. Evan, L. R. Willis, J. R. Simon, N. S. Fineberg, D. A. Lifshitz, *et al.*, "Renal nerves mediate changes in contralateral renal blood flow after extracorporeal shockwave lithotripsy," *Nephron Physiol,* vol. 95, pp. p67-75, 2003.